AKADEMIA GÓRNICZO-HUTNICZA IM. STANISŁAWA STASZICA W KRAKOWIE

FIELD OF SCIENCE: Engineering and Technology

SCIENTIFIC DISCIPLINE: Mechanical Engineering

DOCTORAL DISSERTATION

Modeling of multiphase flow and heat transfer in an ejector-condenser system

Author: Tomasz Kuś, MSc, Eng

Supervisor: Paweł Madejski, PhD, DSc, Eng
Auxiliary supervisor: Michał Karch, PhD, Eng

Completed at: AGH University of Science and Technology,
Faculty of Mechanical Engineering and Robotics

Kraków, 2025

Project acknowledgement

The research leading to these results has received funding from the Norway Grants 2014-2021 via the National Centre for Research and Development. Work has been prepared within the frame of the project: "Negative CO2 emission gas power plant"-NOR/POLNORCCS/NEGATIVE-CO2-PP/0009/2019-00 which is co-financed by programme "Applied research" under the Norwegian Financial Mechanisms 2014-2021 POLNOR CCS 2019 - Development of CO2 capture solutions integrated in power and industry processes.

I would like to express my gratitude to Prof. Paweł Madejski
for his invaluable support and insightful guidance,
throughout the writing of this dissertation.

I also wish to thank Dr Michał Karch, my auxiliary supervisor,
for their helpful suggestions and kind assistance
during my doctoral studies.

I dedicate this dissertation to my parents.

Abstract

This work presents the results of a numerical investigation of a spray-ejector condenser, a liquid-driven, two-phase ejector operating as a direct contact condenser in a gas power plant with negative CO_2 emission. Computational Fluid Dynamics (CFD) based on the Finite Volume Method was used to model multiphase, turbulent flow with heat transfer and condensation occurring in the presence of inert gas. The study aims to develop a reliable numerical model for investigating thermal–flow phenomena and performance analysis to ensure efficient steam condensation from exhaust gases. A review of the current state of ejector technology and available numerical techniques enabled the formulation of the research hypotheses and the selection of the most suitable modeling approaches. A steady-state, axisymmetric CFD model was developed using the Euler–Euler Mixture approach to account for the two-phase, three-component flow. Different RANS-based turbulence models were investigated, and the Realizable k-ε model with two-layer wall treatment was selected. A thermally-driven condensation model was applied, where the condensation mass flow rate was determined from the local heat balance. This approach allowed for simulating direct contact condensation of steam in the presence of CO_2. Various types and values of boundary conditions were tested to assess their influence on model stability and the distribution of key flow and thermal quantities along the flow path. The impact of key modeling parameters, such as the assumed average droplet diameter and different assumed Nusselt number values, was investigated to determine their effect on the predicted condensation intensity. The performance of the basic geometrical design was assessed using the calibrated CFD model, based on pressure, temperature, and steam mass flow rate profiles along the flow path, as well as non-dimensional parameters. The calibrated model agreed well with experimental data, with deviations of up to 3.7% for suction pressure, outlet temperature, and compression ratio, and up to 15.6% for expansion ratio, depending on the operating conditions. The obtained condensation efficiency ranged from 61.6% to 83.9%, which was considered insufficient. The impact of the selected geometrical parameters of the motive nozzle and mixing chamber geometry on the performance was investigated to support further model improvement. A final geometrical design, supported by the developed CFD results and enabling complete steam condensation, was implemented in a gas power plant with negative CO_2 emissions.

Table of content

Nomenclature

Roman symbols

a – interaction area density	m^{-1}
$\boldsymbol{a}$ – surface area vector	m^2
b_i – element of the residual vector $\boldsymbol{b}$	
$\boldsymbol{b}$ – residual vector of the linear system	
c_{ij} – element of the coefficient matrix $\mathbf{C}$ in row i, column j	
$\mathbf{C}$ – coefficient matrix of the linear system	
C_p – specific heat at constant pressure	$J\ kg^{-1}\ K^{-1}$
C_{1-4} – empirical coefficients in the Nusselt number correlation	
$C_{\varepsilon 1}$, $C_{\varepsilon 2,}$ C_μ – coefficients in turbulence model equations	
CR – compression ratio	
d – diameter	m
$\boldsymbol{d}^v$– vector of central coefficients for the discretized velocity equation	
$\mathbf{D}$ – mean strain rate tensor	s^{-1}
E – specific total energy	$J\ kg^{-1}$
ER – mass entrainment ratio	-
f_2 – dumping function in turbulence model	
$\boldsymbol{f_b}$ – body force vector	$N\ m^{-3}$
f_μ – dumping function in turbulence eddy viscosity formulation	
$\dot{g}$ – mass flow rate of boiling/condensation per unit volume	$kg\ m^{-3}\ s^{-1}$
h – heat transfer coefficient,	$W\ m^{-2}\ K^{-1}$
H – specific total enthalpy	$m^2\ s^{-2}$
H_{st} – specific static enthalpy	$m^2\ s^{-2}$
$\mathbf{I}$ – unit tensor	
$\boldsymbol{J^\varphi}$ – flux of the transported scalar property	*variable*
k – turbulent kinetic energy,	$J\ kg^{-1}$
k_0 – ambient value of turbulent kinetic energy [1]	$J\ kg^{-1}$
l – length scale	m
L – phase change heat	J/kg
$\dot{m}$ – mass flow rate	$kg\ s^{-1}$
$\dot{m}_f$ – mass flux across the cell face f	$kg\ s^{-1}$
Nu – Nusselt number	
p – pressure	Pa

p_{lift} – pressure lift	Pa
P_k – turbulent kinetic energy production term per unit volume	W m^{-3}
P_ε – turbulent dissipation production term per unit volume	W m^{-3}
Pr – Prandtl number	
Q – heat transfer per unit volume	W m^{-3}
Re – Reynolds number	
$\dot{\boldsymbol{q}}$ – heat flux vector	W m^{-2}
$\boldsymbol{r}$ – radial position vector in cylindrical coordinates	m
$\boldsymbol{s_M}$ – momentum source term per unit volume	N m^{-3}
S_E – energy source term per unit volume	W m^{-3}
S_k – turbulent kinetic energy source term per unit volume	W m^{-3}
S_M – mass source term per unit volume	Kg s^{-1} m^{-3}
S_P – volume fraction source term	s^{-1}
S_ε – turbulent dissipation source term per unit volume	W m^{-3}
S_φ – scalar variable φ source term	*variable*
Sc – Schmidt Number	
t – time	s
T – temperature	K
T_s – saturation temperature	K
$\mathbf{T}$ – viscous stress tensor	Pa
$\mathbf{T_{RANS}}$ – Reynolds stress tensor	Pa
u_* – friciton velocity	m s^{-1}
v – velocity	m s^{-1}
$\boldsymbol{v}$ – velocity (vector)	m s^{-1}
$\boldsymbol{v_d}$ – diffusion velocity (vector)	m s^{-1}
V – volume	m^3
x_i – element of the unknowns vector $\boldsymbol{x}$	
$\boldsymbol{x}$ – unknowns vector of the linear system	
y – wall distance	m
y^+ – non-dimensional wall distance	

Greek symbols

α – volume fraction	
Γ – diffusion coefficient	m^2 s^{-1}
ϑ – the instantaneous value of a flow variable	-

ε – turbulent dissipation rate	J kg^{-1} s^{-1}
ε_0 – the ambient value of turbulent dissipation rate [1]	J kg^{-1} s^{-1}
φ – general scalar quantity	*variable*
η – condensation efficiency	%
λ – thermal conductivity	W m^{-1} K^{-1}
μ – dynamic viscosity	Pa s
ν – kinematic viscosity	m^2 s^{-1}
ξ – expansion ratio	
ρ – density	kg m^{-3}
$\boldsymbol{\sigma}$ – stress tensor	Pa
σ_k, σ_ε – model coefficients	
τ – turbulent time scale	s
τ_e – large-eddy time scale	s
τ_w – wall shear stress	Pa
τ_0 – specific time scale	s
$\tau_{\theta\theta}$ – stress in circumferential direction	Pa
φ – general scalar quantity	
ω – under-relaxation factor	

Subscripts

c – continuous phase

$CD3$ – third-order central differencing

CO_2 – carbon dioxide

d – dispersed phase

f – face

FOU – first-order upwind

g – gas

i – phase *i*

j – phase j

m – mixture

mot – motive side (liquid inlet)

$MUSCL3$ – third-order MUSCL scheme

o – value at the cell center

out – ejector outlet (discharge side)

p - particle

s – steam

suc – suction side (gas inlet)

t – turbulent

w – water (liquid)

$\boldsymbol{x}$ – vector of unknows of the linear system

$x,\ y,\ z$ – directions in Cartesian coordinate system

$z,\ r,\ \theta$ – directions in cylindrical coordinate system

Superscripts

cv – corrected value

n – current iteration/time step

$*$ – intermediate value

$'$ – fluctuating component

Abbreviations and Acronyms

CCS/CCU – Carbon Capture Storage / Utilization

CD – Central Differencing

CFD – Computational Fluid Dynamics

DCC – Direct Contact Condensation

DNS – Direct Numerical Simulation

FOU – First Order Upwind

FVM – Finite Volume Method

HEM – Homogeneous Equilibrium Model

LES – Large Eddy Simulation

LPL – Low-Pressure Lift

MMP – Mixture Multiphase (model)

MUSCL – Monotonic Upstream-centered Schemes for Conservation Laws

nLPL – new Low-Pressure Lift

NVD – Normalized Variable Diagram

NXP – Nozzle Exit Position

OP – Operating Point

RANS – Reynolds-Averaged Navier–Stokes

RSM – Reynolds Stress Model

SEC – Spray-Ejector Condenser

SOU – Second-Order Upwind

1. Introduction

Many countries and international organizations, including the European Union, have adopted the ambitious policy to reduce significantly greenhouse gas emissions. The overarching goal of the European Union policy is to achieve climate neutrality by 2050, as outlined formally in the European Green Deal [2]. One of the key intermediate targets is the "Fit for 55" package, which aims to reduce greenhouse gas emissions by at least 55% by 2030, compared to the 1990 levels. Among anthropogenic greenhouse gases, carbon dioxide is the most significant contributor [3].

To stimulate sustainable development across the energy, transport, industry, and agricultural sectors, several regulations and financial mechanisms have been introduced to accelerate decarbonization. One of the most important is the Emissions Trading System (EU ETS), which uses market-based instruments to incentivize emission reductions. The system, based on tradable emission permits with a progressively declining cap, has generated revenues that have increased sevenfold since 2017 [4]. These funds are often used for climate-related investments to support the "green transition" process.

These ecological, political, and economic drivers create a favorable environment for the development of carbon-free technologies, particularly in the power-generation sector, which accounts for around 40% of global CO_2 emissions from fossil fuel combustion [5]. Despite ongoing efforts to develop modern low-emission technologies, global energy-related CO_2 emissions increased by 2.5% from 2019 to 2023, reaching a record of 37.4 Gt in 2023 [6,7]. In Poland, where nearly three-quarters of electricity is still generated in fossil fuel-based power plants, the greenhouse gas emissions from the power sector have declined by approximately 3% between 2021 and 2022 and by 14% between 2005 and 2022 [8]. Nevertheless, Poland remains among the European Union countries with the highest CO_2 emissions per capita.

Energy-related CO_2 emissions can be reduced through increased reliance on renewable and nuclear energy sources and by applying CCUS technology (Carbon, Capture, Utilization and Storage). These systems reduce emissions by capturing CO_2 from fossil-fuel power plants and storing it or converting it into useful products [9]. Importantly, The CCUS technology can be applied to existing power plant infrastructure [10], which is particularly relevant for countries like Poland, where lignite and coal will remain significant components of the energy mix for years [11].

Among CCUS methods, gas-based technologies are gaining increasing attention due to their lower greenhouse gas emissions. In addition, gas combustion produces fewer pollutants such as NO_x, SO_x and particulate matter. Combustion in an oxygen-enriched atmosphere enables efficient CO_2 separation from the exhaust gases. Oxyfuel combustion is therefore considered a promising CCUS solution, particularly in terms of power generation efficiency [12].

To separate CO_2 from exhaust gases, a condensation system is required. Traditional steam systems employ surface condensers, whereas ejectors are applied to remove non-condensable gases from turbine condensers [13] or to compress the working fluid using thermal energy in refrigeration systems. In response to the limitations of surface condensers, particularly in oxy-fuel applications, direct contact condensers have recently gained interest and are being developed for integration with such systems. Two-phase ejectors are particularly promising in this context due to efficient mass, momentum, and energy exchange, enabling them to function as practical gas–liquid mixers. This research focuses on the development a two-phase ejector condenser using numerical modeling techniques. The device is designed to entrain exhaust gases and condense steam, creating favorable conditions for effective CO_2 separation in a gas power plant.

2. State of the art

This chapter provides a comprehensive overview of the current state of development in ejector technologies, with a particular focus on modeling strategies. It discusses various research approaches applied to the modeling of ejector operation, ranging from simplified analytical and numerical methods to advanced CFD simulations, and highlights their applicability, strengths, and limitations. Special attention is given to modeling two-phase ejectors, including challenges related to turbulence, multiphase flow, and phase change mechanisms. Finally, the research gap concerning the modeling and understanding of phenomena in the liquid-driven, two-phase ejector condenser is identified.

2.1. Investigation of ejector performance

In the literature, ejectors are often referred to as jet pumps, educators, or injectors [14–17]. Due to their simple construction and reliable operation, ejectors are applicable in various industries, such as refrigeration, chemical processing, and power systems. Most current research focuses on supercritical ejectors in refrigeration systems, where they operate as heat compressors, replacing the standard compressors [18–20], or as an expansion devices that reduce compression work and improve evaporation performance [21]. To increase energy efficiency and thus decrease fossil fuel consumption, ejector-based combined power and cooling systems are being developed [22,23], including those integrated with solar energy [24]. In fossil fuel-based power plants, ejectors are typically applied for the removal of non-condensable gases and for maintaining a vacuum in the surface condensers [25]. Although ejectors can also efficiently function as mixers, their use as direct contact heat exchangers in power systems is rarely considered.

One of the key challenges is the proper design of the ejector, which depends on the operating conditions and the properties of the working fluid. While fundamental components such as the suction chamber with motive nozzle, mixing chamber, and diffuser remain unchanged, recent research increasingly focuses on optimizing these parts to enhance performance. Studies on the motive nozzle design aim to optimize its shape and nozzle exit position (NXP) [26] to ensure proper acceleration of the motive fluid and the creation of a low-pressure zone for effective entrainment. The mixing chamber diameter should provide sufficient phase mixing while minimizing friction losses. Therefore, the length and diameter of the mixing chamber are key parameters in

performance-oriented design studies [27]. Regarding the diffuser, investigations concern pressure recovery and typically examine its diameter, length and angle.

Appropriate modeling techniques can support ejector geometry development and performance optimization. Moreover, simulation results can help deepen the understanding of the relevant thermal-flow mechanisms. Depending on the system's complexity and the required level of accuracy, different approaches are used to model ejector operation, ranging from simple analytical models to advanced numerical simulations.

2.2. Analytical and numerical models of ejector

The modeling difficulty increases with the complexity of the phenomena, and more sophisticated computational methods become necessary to achieve accurate predictions. Ejectors can be categorized according to the growing challenges in modeling as follows: one-phase ejectors, two-phase ejectors, and two-phase ejectors with phase change [28,29].

The following approaches can be distinguished in ejector modeling: zero-dimensional (0D) models, one-dimensional (1D) models, and multidimensional CFD models [30]. Zero-dimensional models treat the object as a single entity, ignoring spatial variations and focusing on the global parameters. One-dimensional models offer more detailed descriptions, allowing for variations in flow properties, typically along the flow path. Both 0D/1D models can be analytical or numerical and are based on significant simplifications compared to multidimensional models, especially regarding turbulence and interfacial interactions. These models are helpful for initial design and performance due to their computational efficiency and reasonable accuracy. Multidimensional CFD models overcome the limitations of 0D/1D approaches but require increased computational effort and model complexity.

Challenges in modeling one-phase ejectors relate to turbulent flow, working fluid properties, and possible operation in subsonic and supersonic regimes [31]. The key phenomena influencing the momentum exchange are turbulence, possible shock formation, and boundary layer interactions [32]. Zero-dimensional and one-dimensional models perform well for one-phase ejectors, particularly under on-design conditions. Schillaci et al. [33] used a 0D model to predict the performance of air ejectors in on- and off-design conditions. Results were verified against CFD RANS-based simulations. The model worked well for sonic flow in the nozzle throat but performed poorly when the

sonic line moved downstream, and the flow became subsonic. Croquet et al. [34] developed a thermodynamic 1D model to simulate the supersonic air ejector performance for different operating conditions and determine the basic dimensions. Agreement with CFD results included a 2% difference in isentropic and mixing efficiencies and a 37% standard deviation in the entertainment ratio for double choking operation. Kumar et al. [35] developed a 1D model of the R141b ejector, treating the working fluid as an ideal gas and introducing the Fanno flow assumption and variable heat capacity ratio. The error was within 4% for the entertainment ratio compared to experimental results. Marum et al. [36] developed a 1D model based on the CFD results to calculate the friction loss coefficient and predict efficiency. The model reproduces the efficiency curve well compared to the CFD results previously validated against experimental data. Chen et al. [37] proposed a 1D model to predict gas ejector performance at critical and subcritical operation modes for different working fluids and geometries. The performance was calculated with a maximum error of 18% for critical and 20% for subcritical modes. The zero-dimensional model of the R1233zd(E) one-phase ejector was developed by Mastrowski et al. [38] in the refrigeration system. Results were validated by experimental measurements achieving the following relative errors: 4.5%, 7.1%, and 13.7%, respectively for pressure ratio, mass entrainment ratio, and ejector efficiency.

More advanced methods, such as CFD, are also used to investigate one-phase ejector operation, both to validate 0D/1D models and gain deeper insight into the complex turbulence interactions. RANS-based eddy viscosity models dominate turbulence modeling, especially the SST k-ω and various k-ε models. Śmierciew et al. [39] applied axisymmetric and 3D CFD models of gas ejectors coupled with the SST k-ω model to conduct the geometrical model design procedure. Results were experimentally validated, and the axisymmetric model produced results similar to those of the 3D model. Xiao et al. [40] investigated different turbulent approaches (Standard k-ε, RNG k-ε, Realizable k-ε and SST k-ω) using the CFD to evaluate their agreement with experimental data for a supersonic steam ejector. The Realizable k-ε and the SST k-ω were recommended for further investigation. Hemidi et al. [41] developed CFD model of a one-phase supersonic air ejector governed by the compressible, steady-state, axisymmetric form of the Navier-Stokes equations, closed with k-ε and SST k-ω turbulence models. In general, the k-ε was indicated as better, but the accuracy of modeling strongly depended on the operating conditions.

2.3. Modeling of two-phase ejector operation

Modeling of the two-phase ejectors is incomparably more difficult than in the case of single-phase ejectors. In addition to all the challenges described for single-phase ejectors, two-phase ejectors introduce additional complexities related to interfacial interactions, including heat and mass transfer phenomena. Depending on the boundary conditions and geometrical design, different flow regimes can occur even for the same pair of phases. Moreover, thermodynamic and transport-related, non-equilibrium effects may arise, expressed by superheated or subcooled states or differences in temperature or velocity between phases [42].

Despite the significant complexity of phenomena in two-phase ejectors, advanced versions of 0D/1D models are widely used due to their robustness and efficiency. Most research is focused on developing 0D/1D numerical or analytical models describing the operation of two-phase ejectors working with refrigerants such as CO_2 (R744). Taleghani et al. [43] developed a zero-dimensional thermodynamic model of a two-phase R744 ejector based on real fluid properties and dynamic and thermal equilibrium assumptions. The motive mass flow rate was achieved with 10-15% accuracy. Banasiak et al. [44] developed a one-dimensional model of an R744 two-phase ejector for expansion work recovery. Transcritical flow with delayed flashing over the motive nozzle was calculated using the Delayed Equilibrium Model and homogeneous nucleation theory. The relative errors were 2.7% and 1.8% on average for pressure lift and critical mass flow rate, respectively. Simplified 0D/1D models of two-phase ejectors are also commonly used for modeling their operation with other refrigerants [45,46].

Numerical research on two-phase liquid-driven ejectors remains relatively limited, creating a notable gap in the field. Wang et al. [47] developed a one-dimensional slug-flow model for condensing ejectors with liquid and vapor as the primary fluid, considered separately. The model showed good agreement with experimental results. A one-dimensional model of a water–steam ejector for use in a high-temperature heat pump system was proposed by Khass et al. [48]. The pseudofluid approach incorporated mechanical and thermal non-equilibrium through source terms that account for mass, momentum, and energy transport.

2.4. CFD modeling of two-phase ejector

Compared to simplified 0D/1D models, two or three-dimensional CFD simulations offer enhanced capabilities for capturing the local flow properties and predicting more realistic fluids behavior. A key advantage of CFD for simulating two-phase ejector operation is its reduced reliance on empirical correlations. CFD allows accurate capture of multiphase interactions, turbulent structures, and phase-change processes such as boiling, condensation, or evaporation.

2.4.1. Turbulence modeling

Applied turbulence models significantly influence predicted ejector efficiency [43]. Similar to one-phase ejectors, the most popular are two-equation eddy viscosity models, including various modifications of k-ε and k-ω. Palacz et al. [49] applied Realizable k-ε formulation and the Homogeneous Equilibrium Model (HEM) in a developed 3D CFD model to evaluate the model's accuracy. The reported error was below 10% for motive and entrained mass flow rates. A CFD simulation of a CO_2 two-phase ejector was presented by Smołka et al. [50] to reproduce compressible, high-speed flow. The RNG k-ε model, together with the homogeneous equilibrium approach, was applied. Kandakure et al. [51] investigated the axisymmetric turbulent flow in the water–air ejector using the k-ε model to assess the effect of geometrical and operating parameters on the hydrodynamic behavior. The Realizable k-ε model was also implemented by Hassani et al. [52] in the analysis of a water-jet ejector. Good agreement with experimental data was achieved, with 11.2% and 7.4% deviations for flow ratio and maximum discharge pressure, respectively. Haida et al. [53] used a CFD approach incorporating the Realizable k-ε turbulence model to investigate the flow behavior in a CO_2-based two-phase ejector. The resulting CFD predictions were used as a reference for evaluating a simplified ejector model. Other CFD-based studies confirm the versatility of the Realizable k-ε model in two-phase ejector analysis [54–57].

2.4.2. Multiphase modeling

Two different multiphase modeling approaches can be distinguished in CFD simulations of two-phase ejectors: the Euler–Lagrange and Euler–Euler. The Euler–Lagrange approach focuses on tracking individual particles (droplets, bubbles) and modeling their distribution and interactions [58,59]. In the context of two-phase ejector simulations, this method is occasionally used for cases involving liquid injection or gas–

solid flow [60–62], but its high computational cost and increased complexity significantly limit its application.

The Euler–Euler approach is commonly used due to its balance between accuracy, computational efficiency, and versatility. All phases are treated as interpenetrating continua, and the volume fraction concept is introduced to describe the distribution of each phase within the computational domain. In CFD simulations of the two-phase ejectors using this approach, two distinct modeling strategies can be identified: the two-fluid and the pseudofluid. The two-fluid model solves a separate set of conservation equations for mass, momentum and energy for each phase, allowing for more complex interactions between the phases. The simplified model treats the phases as a single pseudo-fluid, and solves governing equations for averaged properties. Although flow is typically assumed to be homogeneous, additional submodels can be incorporated to account for transport and thermodynamic non-equilibrium effects such as slip velocity, surface tension forces, or phase change.

Due to its robustness, sufficient accuracy and low computational cost, the pseudofluid model has become widely used in numerical studies of two-phase ejectors, particularly in water–air and air–water applications. Assari et al. [63] applied the steady-state Mixture and two-fluid Eulerian model to simulate multiphase parallel flow in a water–air ejector. The difference in flow ratio was approximately 6%, and the pressure distributions obtained from both models were similar. The Mixture model proved to be more efficient and presented better agreement with experimental data. Yuan et al. [64] used the Mixture model with non-equilibrium transport effects to investigate the influence of operating pressures on the performance of the water–air ejector. Balamurugan et al. [65] developed a CFD model of air–water ejectors using the Mixture approach to examine hydrodynamics characteristics across different geometric configurations. The Mixture modeling approach has been successfully applied in simulations of two-phase ejectors operating with refrigerants, further confirming its versatility across various fluid systems. Giacomelli et al. [66] numerically investigated a CO_2 liquid-driven two-phase flashing ejector using two pseudofluid approaches: The Homogeneous Equilibrium Model (HEM) and the Mixture model. Both models treat the phases as compressible and metastable. The Mixture model predicted the mass-flow rates more accurately, with a 19% error in entrainment ratio, compared to 48% for the HEM. Zheng et al. [67] developed a CFD model of a liquid-driven two-phase ejector in which the Mixture model was used to

simulate the multiphase flow. The primary fluid was liquefied natural gas, and the secondary fluid was boil-off gas. Kabur et al. [68] modeled CO_2 two-phase flow in ejector using the Thermodynamic Equilibrium Model based on the mixture approach. The reported relative errors in mass flow range from 15.7% to 21.7% for the motive stream and from 0.1% to 12.4% for the suction stream. CO_2 two-phase flow in an ejector was numerically calculated using a non-homogeneous Mixture model combined with submodels for boiling and cavitation by Yazdani et al. [69]. Lee et al. [70] developed a CFD model of a two-phase R600a ejector using a homogeneous Mixture approach, accounting for non-equilibrium compressible flashing flow in the motive nozzle. The reported relative errors were within 10% for the primary mass flow rate and 16% for the secondary suction pressure.

2.4.3. Phase change modeling

Accurately capturing phase change dynamics remains a significant challenge for two-phase ejectors, as these phenomena considerably affect ejector performance. The phase change process introduces complex interfacial interactions and affects the overall flow structure. Mass transfer rates in two-phase ejectors are particularly high, especially in the gas–liquid ejectors where the jet is highly turbulent, and the flow pattern after the mixing process becomes strongly homogeneous [71–74].

In the multiphase flow through the ejectors, condensation may occur in two distinct modes: an equilibrium condensation due to contact with a cooling medium and high-speed non-equilibrium condensation, typically occurring in the convergent-divergent supersonic nozzle [75–79]. The former, known as direct contact condensation (DCC), remains especially challenging to describe theoretically and is not yet fully understood [80].

One commonly used modeling approach is based on a thermally driven concept, in which the mass transfer is determined by the heat balance between the phases and their interfaces [81–83]. The accuracy of such models strongly depends on appropriate values for interfacial parameters, particularly the interfacial area density (for dispersed flow related to bubble or droplet size) and the heat transfer coefficient, which is often estimated using the Nusselt number correlations. These thermally driven models have shown good agreement with experimental data in steam jet condensation simulations [84,85].

CFD studies focusing on condensing ejectors with DCC are scarce. Most are limited to liquid-driven ejectors operating in subsonic modes. Zhou et al. [86] developed a 3D

CFD steam–water ejector model using a two-resistance, thermally-driven condensation model, where the interfacial area density depends on steam volume fraction and bubble diameter. The maximum relative errors in temperature and pressure predictions compared to experimental data were 10.5% and 22.0%, respectively. Koirala et al. [87] presented a CFD model of a water–steam ejector to analyze thermal–flow phenomena with DCC using the two-fluid Eulerian model coupled with a thermal phase change model. There was a noticeable difference between the simulation results and the experimental data, as the relative error in the entrainment ratio ranged from 19% to 68%, depending on the entrainment pressure. Vieira et al. [88] applied a different approach based on the Lee model [82], combined with Ranz–Marshall correlation for the Nusselt number [83], in a 2D axisymmetric simulation of a gas–liquid ejector with DCC. The maximum relative error for outlet temperature was 6.4% compared to experimental data.

One crucial aspect in CFD modeling of condensing two-phase ejectors is the influence of inert gas, which substantially impacts the efficiency of the direct contact condensation process. The number of studies addressing the effect of non-condensable gas on DCC, particularly in the case of condensation on water droplets, remains very limited [89]. The negative impact on the condensation heat transfer coefficient has been confirmed experimentally by Ma et al. [90,91] and computationally by Wang et al. [91]. Mikielewicz et al. [92] showed analytically that the presence of inert gas weakens the condensation process. Zhang et al. [93] conducted a numerical study on the influence of the inlet mass fraction of non-condensable gas on DCC effectiveness in a convergent tube. Increasing this mass fraction from 0.1 to 0.2 reduced the condensation heat transfer coefficient by as much as 50%.

2.5. Research gap

The majority of the presented numerical research, including both 0D/1D models and CFD simulations, focuses on two-phase ejectors operating in gas–gas or gas–liquid configuration. Most of these studies are related to refrigeration systems, especially CO_2-based cycles, where ejectors function as heat compressors. Numerical research on liquid-driven, two-phase ejectors is significantly less common than gas-driven systems. Available investigations mainly address water–gas ejectors used for vacuum generation in power and chemical industries and thermal desalination systems [46]. The amount of CFD studies on liquid–gas two-phase ejectors that account for DCC remains very limited. The role of inert gases in this type of condensation process is not yet fully understood.

This lack of understanding poses a significant challenge for accurate modeling and highlights the need for further research.

This research gap indicates that current modeling techniques are not yet fully suited to accurately simulate liquid-driven two-phase ejectors in the presence of inert gases. The main challenges concern multiphase flow and phase change modeling, while turbulence modeling methods are more mature and commonly used across different working fluids. The accuracy of the Mixture model in predicting the behavior of a two-phase ejector operating with refrigerants, where the spontaneous condensation occurs, has been confirmed by both numerical and experimental studies. To the best of the author's knowledge, no studies have been conducted on applying the Mixture model to liquid-driven, water–steam ejectors, where direct contact condensation occurs in the presence of inert gases. Moreover, research using thermally-driven phase change models has focused mainly on condensation occurring on the steam jet. The number of publications applying this group of models to predict ejector performance also remains limited, creating an opportunity for further research on the condensation process involving non-condensable gases.

3. Thesis, aim, and scope of the research

The existing need to develop a two-phase ejector operating as a condenser, supported by the analysis of current technologies, modeling techniques, and the identified research gap, provides the foundation for the research hypothesis presented in this chapter. Scientific aims have been defined to develop a reliable numerical model and to gain a deeper understanding of the phenomena related to the ejector operation. The scope of the research is outlined to support the achievement of these objectives. Practical goals are also presented in reference to the broader project framework within which this study was conducted.

3.1. Research hypothesis

The formulated hypotheses directly relate to assessing two-phase ejector performance under various operating conditions and analyzing turbulent, multiphase flow with direct contact condensation. Due to the identified research gap in CFD modeling of the water-driven condensing ejectors, the selected multiphase modeling technique will be verified in terms of its accuracy, robustness, and practical applicability. The hypotheses are as follows:

1. The developed CFD results for the two-phase ejector condenser, accounting for steam condensation in the presence of inert gas, enable the analysis of thermal and flow phenomena and the evaluation of condensation efficiency within the ejector-condenser system under varying boundary conditions.
2. The application of the Euler–Euler Mixture approach for modeling multiphase flow with condensation in the presence of inert gas is sufficient and enables obtaining reliable results when simulating the operation of a two-phase ejector-condenser.
3. The results of CFD modeling allow for the assessment of the ejector-condenser system's performance and the proposal of geometry modifications to ensure complete condensation of water vapor contained in flue gases after oxy-fuel combustion.

3.2. Scientific aims of the research

From a scientific point of view, the key objective is to develop a numerical model that enables both quantitative and qualitative analysis of the phenomena in the two-phase ejector-condenser. Particular attention is given to a proper understanding of the heat and

mass transfer mechanisms occurring in the flow through the ejector. The scientific aims are defined as follows:

1. Development of a reliable numerical model of a two-phase ejector, considering turbulent, multiphase flow with heat transfer and condensation phenomena.
2. Analysis of the condensation in the presence of inert gas using the developed CFD model based on the Euler-Euler approach.

3.3. Scope of the research

This section outlines the extent of the numerical research focused on modeling multiphase flow in a two-phase ejector condenser. The study covers multiple aspects of developing a reliable CFD model, including reviewing the relevant modeling approaches, formulating the numerical model, analyzing and verifying results. The research includes the following key aspects:

1. Review and selection of appropriate modeling techniques suitable for the simulation of the two-phase ejector condenser.
2. Development of a two-dimensional axisymmetric CFD model representing turbulent, multiphase, two-component flow with direct contact condensation, applied to a basic geometric configuration.
3. Analysis of the influence of boundary conditions, including their type (specified as velocity or pressure), magnitude, and inert gas content in exhaust gas mixture, on the predicted pressure, temperature, and velocity distributions, as well as on condensation intensity.
4. Calibration and sensitivity analysis of selected physical and numerical parameters, including droplet diameter, Nusselt number, turbulence model, and numerical convection discretization schemes.
5. Analysis of the results obtained using final model setup under nominal conditions and comparison with experimental data.
6. Evaluation of the influence of selected geometrical parameters of the motive nozzle and mixing chamber on the thermal–flow performance of the spray-ejector condenser.
7. Assessment of the ejector condenser performance for the final geometrical model, in terms of flow performance and condensation efficiency.

3.4. Practical aims of the research

The results presented in this thesis were developed within the frame of the project "Negative CO_2 emission gas power plant" co-financed by programme "Applied research" under the Norwegian Financial Mechanisms 2014-2021 POLNOR CCS 2019, in which the spray-ejector condenser system is one of the crucial parts. The project aims to develop an innovative technology, along with a demonstration plant, that enables the use of sewage sludge for electricity production while achieving a positive environmental impact [94]. Negative CO_2 emission is achieved through the synergy between the use of renewable energy sources (sewage sludge) and CCS/CCU system. The project utilized various computational approaches to model the operation of the gas power plant under different scenarios and to design its critical components, including the spray-ejector condenser. A zero-dimensional thermodynamic analysis of the negative CO_2 emission gas power plant using Aspen Plus, Aspen Hysys, and Ebsilon software, enabling a comparison of results between different tools and providing the input data for a more detailed analysis of the system's critical components [95].

Due to the significant role of the ejector condenser in the CO_2 separation system, both numerical and analytical models, as well as experimental investigations, were carried out to ensure a comprehensive understanding of multiphase turbulent flow with condensation in the presence of inert gas. Results obtained from the one-dimensional numerical model were used to define the basic geometrical model parameters and to provide an initial estimation of condensation efficiency and compression performance [96].

Computational investigations of thermal and flow processes in the ejector condenser, alongside the analysis of measurement and experimental techniques, supported the development of a jet-type flow condenser test rig at AGH University [97,98]. The experimental setup enabled precise measurements of flow parameters at the inlets and outlets and detailed monitoring of pressure and temperature along the entire flow path. Moreover, qualitative flow investigations using optical methods can be carried out on the setup to identify characteristic flow patterns [99]. The results and observations provided a basis for validating the CFD model and assessing its accuracy and reliability in simulating multiphase flow.

The thesis practically aims to develop and apply the CFD model of the ejector condenser to identify a suitable geometric design that meets the technical requirements

dictated by the operation of a negative-emission gas power plant. The practical objectives are as follows:

1. Evaluation of the applicability of the developed CFD model for performance analysis of the spray-ejector condenser under realistic operating conditions.
2. Investigation of the influence of selected geometrical parameters and operating conditions on the performance of the ejector condenser to provide input for further geometry development.
3. Assessment of the feasibility of implementing the developed solution in a gas power plant with negative CO_2 emissions.

4. Spray-ejector condenser

This chapter focuses on the spray-ejector condenser as the research object, for which a numerical model will be developed. General background information on the operation of this type of ejector is presented to provide a better understanding. The non-dimensional parameters describing thermal–flow performance, which will be used in the analysis, are defined. The role of the ejector-condenser within a negative-emission gas power plant and its operating environment is also described. Finally, the geometrical parameters of the developed model are presented.

4.1. General characteristics of the two-phase ejector

Two-phase ejectors are highly diverse devices capable of operating under various conditions, design configurations, and phase combinations. They can simultaneously handle liquid and vapor phases, including phase transitions between them. Their ability to operate across different pressure regimes, including both subsonic and supersonic flows, enables complex flow behavior and interactions.

Four main phase combinations can be distinguished: liquid–gas, gas–liquid, solid–gas, and gas–solid. The latter two are typically used for transporting particles, where a high-pressure gas or liquid acts as a driving medium. Liquid–gas and gas–liquid ejectors are commonly applied in mixing and compression processes, which often involve phase change or chemical reactions due to high heat and mass transfer [100]. These configurations can be applied as mixers and condensers in heat and power systems.

In analyzing two-phase ejector performance, several non-dimensional parameters are employed to evaluate and compare the efficiency under various design and operating conditions. These parameters provide insight into how effectively the ejector compresses, entrains, and mixes the working fluids. The most important are compression ratio CR, pressure lift p_{lift}, mass entrainment ratio ER, and expansion ratio ξ. An additional indicator, condensation efficiency η, is defined to assess the thermal performance of the ejector condenser.

The compression ratio CR is defined as the ratio of the outlet (discharge) pressure p_{out} to the suction (gas inlet) pressure p_{suc} (Equation (4.1)). It indicates the ability of the ejector to compress the lower-pressure fluid.

$$CR = \frac{p_{out}}{p_{suc}} \tag{4.1}$$

The pressure lift p_{lift} represents the difference between ejector outlet pressure p_{out} and the suction pressure p_{suc} , as presented in Equation (4.2).

$$p_{lift} = p_{out} - p_{suc} \tag{4.2}$$

The expansion ratio ξ is defined as the ratio of motive fluid pressure p_{mot} to the suction pressure p_{suc}, describing how the motive fluid expands as it passes through the ejector nozzle (Equation (4.3)).

$$\xi = \frac{p_{mot}}{p_{suc}} \tag{4.3}$$

The mass entrainment ratio ER is expressed in terms of mass flow rates of the motive fluid $\dot{m}_{mot}$ and the entrained fluid on the gas side $\dot{m}_{suc}$, according to Equation (4.4). It provides insight into how effectively the ejector draws the secondary fluid.

$$ER = \frac{\dot{m}_{mot}}{\dot{m}_{suc}} \tag{4.4}$$

The condensation efficiency η indicates how much steam has been condensed, and is calculated by comparing the steam mass flow rate at the ejector outlet $\dot{m}_{out}$ and at the gas inlet $\dot{m}_{suc}$, as presented in Equation (4.5)

$$\eta = (1 - \frac{\dot{m}_{out}}{\dot{m}_{suc}}) \cdot 100\% \tag{4.5}$$

4.2. Ejector-condenser system – the object of the research

The object of the study is the ejector condenser, which is one of the critical components of a gas power plant with negative CO_2 emission [101,102]. The operational environment of the ejector condenser is illustrated in the process flow diagram of a negative CO_2 emission gas cycle in Figure 4.1. The primary function of the ejector is to entrain the exhaust gas mixture from the turbine outlet and condense the steam contained in it. Condensation of steam enables carbon dioxide separation in the separator. The schematic of the ejector is shown in Figure 4.2. Condensation occurs through direct contact between subcooled motive water and steam in the presence of CO_2. The boundary conditions at the ejector inlet are defined based on the operating parameters of the negative-emission gas power plant.

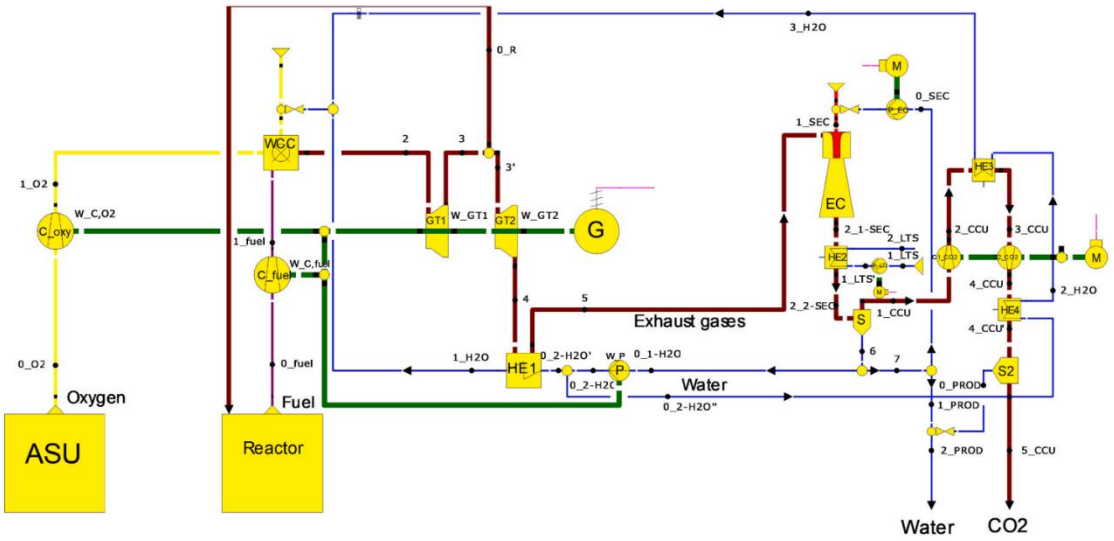

Figure 4.1. Process flow diagram of a negative CO_2 emission gas cycle. C_{oxy} – Oxygen Compressor; C_{fuel} – Gas Fuel Compressor; WCC – Wet Combustion Chamber; GT1, GT2 – Gas Turbines; G – Electricity Generator; EC – Spray-Ejector Condenser (Ejector Condenser); HE1, HE2, HE3, HE4 – Heat exchangers; P – water pump; P_{EC} – SEC water pump; M – motor; S – separator; $C1_{CO2}$, $C2_{CO2}$ – CO_2 compressors. [102].

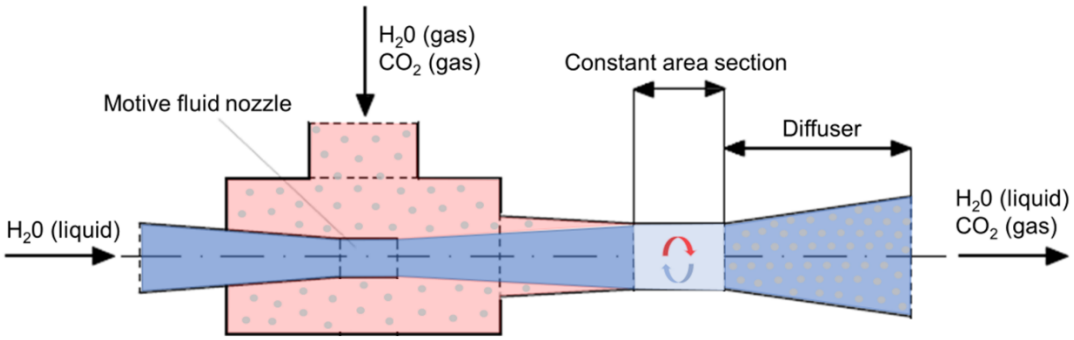

Figure 4.2. Schematic of the two-phase ejector driven by water, with a mixture of steam and CO_2 as an exhaust gas [102].

A schematic view of the ejector with key geometrical parameters is presented in Figure 4.3, and a 3D model for visualization purposes is shown in Figure 4.4. The specific dimensions for two geometrical configurations, LPL (Low-Pressure Lift) and nLPL (new Low-Pressure Lift), are summarised in Table 4.1. The LPL configuration was developed using zero-dimensional and one-dimensional numerical modeling as part of the collaborative work within the project framework [102]. This variant was designed to operate under nominal conditions of the negative-emission gas power plant and ensure high condensation efficiency and a moderate pressure lift effect. The nLPL represents a modified version of the LPL geometry, developed to improve overall performance based on the results and observations obtained from CFD simulations and experimental observations.

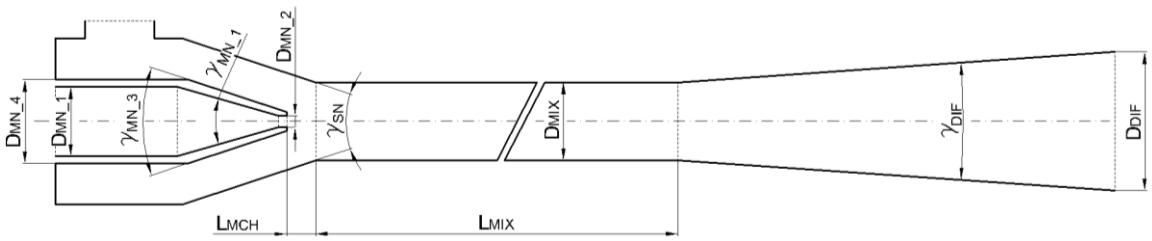

Figure 4.3. Schematic of the spray-ejector condenser with key geometrical parameters.

Table 4.1. Geometrical parameters of the LPL and nLPL spray-ejector condenser configurations.

Parameter	LPL	nLPL
D_{MN_1}[mm]	25.4	25.4
D_{MN_2}[mm]	3.0	3.6
D_{MN_4}[mm]	40.0	40.0
D_{DIF} [mm]	100.0	56.2
D_{MIX} [mm]	25.4	29.7
L_{MIX} [mm]	1050.0	550.0
L_{MCH} [mm]	25.0	25.0
γ_{MN_1} [°]	30.0	30.0
γ_{MN_3} [°]	45.0	45.0
γ_{SN} [°]	45.0	45.0
γ_{DIF} [°]	10.0	10.0

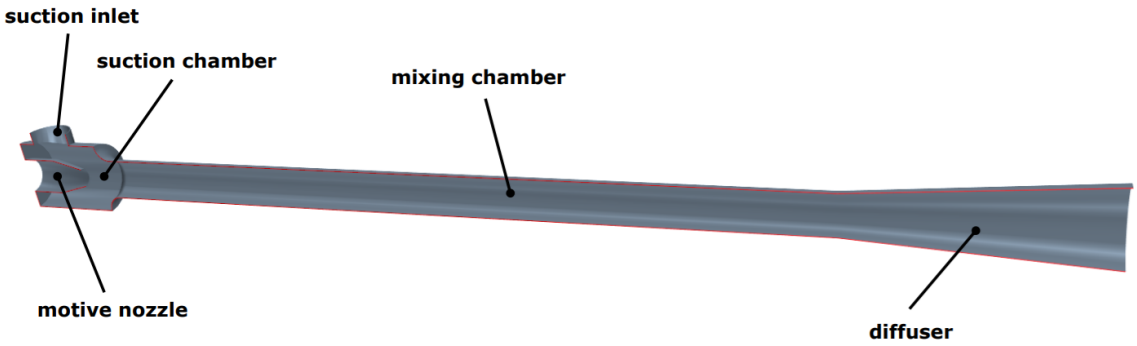

Figure 4.4. 3D model of the spray-ejector condenser in the LPL configuration.

5. Mathematical description of the flow in a two-phase ejector condenser

Conducting thermal-flow analysis in the spray-ejector condenser requires the development of a steady-state numerical model that accounts for turbulent, multiphase flow with condensation. The model should include governing equations capable of capturing all key physical phenomena. This section presents the integral form of the conservation equations for mass, momentum, and energy, along with appropriate closure relations. Particular emphasis is placed on turbulence modeling using the RANS approach and phase change modeling using thermally-driven models. The meaning of key terms in the transport equations and the simplifications introduced based on the axisymmetry and homogeneity assumptions of the mixture model are also discussed.

5.1. Governing equations for CFD modeling

Governing equations for the unsteady flow are formulated as differential equations representing the conservation laws of mass, momentum (linear), and energy of a moving fluid (Equation (5.1), Equation (5.2), and Equation (5.3), respectively):

$$\frac{\partial \rho}{\partial t} + \nabla \cdot (\rho \boldsymbol{v}) = 0 \tag{5.1}$$

$$\frac{\partial (\rho \boldsymbol{v})}{\partial t} + \nabla \cdot (\rho \boldsymbol{v}\boldsymbol{v}) = -\nabla \cdot (p\mathbf{I}) + \nabla \cdot \mathbf{T} + \boldsymbol{f_b} \tag{5.2}$$

$$\frac{\partial (\rho E)}{\partial t} + \nabla \cdot (\rho E \boldsymbol{v}) = \boldsymbol{f_b} \cdot \boldsymbol{v} + \nabla \cdot (\boldsymbol{v} \cdot \boldsymbol{\sigma}) - \nabla \cdot \dot{\boldsymbol{q}} + S_E \tag{5.3}$$

The Finite Volume Method (FVM) transforms the partial differential equations into an integral form suitable for numerical implementation in CFD modeling. The resulting integral formulations of the conservation of mass (continuity), momentum, and energy are presented in Equation (5.4), Equation (5.5), and Equation (5.6), respectively.

$$\frac{\partial}{\partial t}\int_V \rho \, dV + \oint_A \rho \boldsymbol{v} \cdot d\boldsymbol{a} = \int_V S_M \, dV \tag{5.4}$$

$$\frac{\partial}{\partial t}\int_V \rho \boldsymbol{v} dV + \oint_A \rho (\boldsymbol{v}\boldsymbol{v}) \cdot d\boldsymbol{a} = -\oint_A p\mathbf{I} \cdot d\boldsymbol{a} + \oint_A \mathbf{T} \cdot d\boldsymbol{a} + \int_V \boldsymbol{f}_\mathbf{b} dV + \int_V \boldsymbol{s}_M \, dV \tag{5.5}$$

$$\frac{\partial}{\partial t}\int_V \rho E \, dV + \oint_A \rho H \boldsymbol{v} \cdot d\boldsymbol{a} = -\oint_A \dot{\boldsymbol{q}} \cdot d\boldsymbol{a} + \oint_A \mathbf{T} \cdot \boldsymbol{v} \, d\mathbf{a} + \int_V \boldsymbol{f}_\mathbf{b} \cdot \boldsymbol{v} \, dV + \int_V S_E \, dV \tag{5.6}$$

In the Mixture Multiphase Model (MMP), transport equations for mass, momentum and energy are computed for the entire mixture using volume-averaged or mass-averaged mixture properties. The conservation equations of mass, momentum, and energy for phase i for the Mixture approach are presented respectively in Equation (5.7), Equation (5.8), and Equation (5.9). The additional term includes the diffusion velocity $\boldsymbol{v}_{d,i}$ which accounts for slip velocity effects and contributes to additional momentum and energy fluxes resulting from the relative motion between phases.

$$\frac{\partial}{\partial t}\int_V \rho_m \, dV + \int_A \rho_m \boldsymbol{v}_m \cdot d\boldsymbol{a} = \int_V S_M \, dV \tag{5.7}$$

$$\begin{aligned}\frac{\partial}{\partial t}\int_V \rho_m \boldsymbol{v_m} \, dV + \int_A \rho_m (\boldsymbol{v_m}\boldsymbol{v_m}) \cdot d\boldsymbol{a} = -\int_A p\mathbf{I} \cdot d\boldsymbol{a} + \int_A \mathbf{T}_m \cdot d\boldsymbol{a} \\ + \int_V \boldsymbol{f}_\mathbf{b} dV + \int_V \boldsymbol{s} dV - \sum \alpha_i \rho_i \boldsymbol{v}_{d,i} \boldsymbol{v}_{d,i} \cdot d\boldsymbol{a}\end{aligned} \tag{5.8}$$

$$\begin{aligned}\frac{\partial}{\partial t}\int_V \rho_m E_m \, dV + \int_A \left(\rho_m H_m \boldsymbol{v}_m + \sum\nolimits_i \alpha_i \rho_i H_i \boldsymbol{v}_{d,i} \right) \cdot d\mathbf{a} = -\int_A \dot{\boldsymbol{q}} \cdot d\mathbf{a} \\ + \int_A (\mathbf{T}_m \cdot \boldsymbol{v}_m) \cdot d\mathbf{a} + \int_V \boldsymbol{f}_\mathbf{b} \cdot \boldsymbol{v}_m \cdot dV + \int_V S_E \, dV\end{aligned} \tag{5.9}$$

The phase distribution is determined by solving a separate volume fraction transport equation for each phase, as presented in Equation (5.10).

$$\begin{aligned}\frac{\partial}{\partial t}\int_V \alpha_i \, dV + \int_A \alpha_i \boldsymbol{v}_m \cdot \, d\boldsymbol{a} = \int_V \left(S_{P,i} - \frac{\alpha_i}{\rho_i}\frac{D\rho_i}{Dt} \right) dV + \\ \int_A \frac{\mu_t}{\mathrm{Sc}_t \rho_m} \nabla \alpha_i \cdot \, d\boldsymbol{a} - \int_V \frac{1}{\rho_i} \nabla \cdot \left(\alpha_i \rho_i \boldsymbol{v}_{d,i} \right) dV\end{aligned} \tag{5.10}$$

Equation (5.11) presents the momentum conservation equation in the axisymmetric formulation of the Mixture model.

$$\begin{aligned}\frac{\partial}{\partial t}\int_A \rho_m \boldsymbol{v}_m \cdot \boldsymbol{r} \, dA + \oint_{\partial A} \rho_m (\boldsymbol{v}_m \boldsymbol{v}_m) \cdot \boldsymbol{r} \, ds = -\oint_{\partial A} p\mathbf{I} \cdot \boldsymbol{r} \, ds + \oint_{\partial A} \mathbf{T}_m \cdot \boldsymbol{r} \, ds \\ + \int_A \frac{1}{r} \begin{bmatrix} 0 \\ p - \tau_{\theta\theta} \\ 0 \end{bmatrix} \cdot \boldsymbol{r} \, dA + \int_A \boldsymbol{f}_\mathbf{b} \, dA + \int_A \boldsymbol{s}_M \, dA\end{aligned} \tag{5.11}$$

The components of the mixture velocity vector $\boldsymbol{v}_m$ in cylindrical coordinates $z,\ r,\ \theta$ are given in Equation (5.12).

$$\boldsymbol{v}_m = \left(\boldsymbol{v}_{m,z}, \boldsymbol{v}_{m,r}, \boldsymbol{v}_{m,\theta}\right)^T \tag{5.12}$$

Quantities in the Mixture model can be averaged using either volume and mass. The mixture properties such as density ρ_m, dynamic viscosity μ_m, and thermal conductivity λ_m are volume-averaged using phase volume fractions, as presented in Equation (5.13), Equation (5.14), and Equation (5.15), respectively.

$$\rho_m = \sum_{i=1}^{n} \rho_i \alpha_i \tag{5.13}$$

$$\mu_m = \sum_{i=1}^{n} \mu_i \alpha_i \tag{5.14}$$

$$\lambda_m = \sum_{i=1}^{n} \lambda_i \alpha_i \tag{5.15}$$

In contrast, velocity $\boldsymbol{v}_m$ and specific heat capacity $C_{p\,m}$ are mass-averaged using phase volume fractions and densities, as shown in Equation (5.16) and Equation (5.17).

$$C_{p\,m} = \frac{1}{\rho_m} \sum_{i=1}^{n} C_{p\,i} \alpha_i \rho_i \tag{5.16}$$

$$\boldsymbol{v}_m = \frac{1}{\rho_m} \sum_{i=1}^{n} \boldsymbol{v}_i \alpha_i \rho_i \tag{5.17}$$

The mixture total enthalpy H_m is determined by adding the kinetic energy term to the mass-averaged static enthalpy, as presented in Equation (5.18). The total energy E_m required in the energy equation of the Mixture model (Equation (5.9) is calculated by subtracting the pressure work term from the total enthalpy, as presented in Equation (5.19).

$$H_m = H_{st,m} + \frac{\left|\boldsymbol{v}_m\right|^2}{2} = \frac{1}{\rho_m} \sum_{i=1}^{n} H_{st,i} \alpha_i \rho_i + \frac{\left|\boldsymbol{v}_m\right|^2}{2} \tag{5.18}$$

$$E_m = H_m - \frac{p}{\rho_m} \tag{5.19}$$

For the case considered in the study, the conservation equations of mass, momentum, and energy for an axisymmetric, steady-state Mixture model with a homogeneous velocity approach and temperature-dependent material properties are presented in Equation (5.20), Equation (5.21), and Equation (5.22), respectively. In the energy equation (Equation (5.22)), the source term accounts for the energy release or absorption associated with the phase change process.

$$\int_A \rho_m \boldsymbol{v}_m \cdot d\boldsymbol{a} = 0 \tag{5.20}$$

$$\begin{aligned} \oint_{\partial A} \rho_m (\boldsymbol{v}_m \boldsymbol{v}_m) \cdot \boldsymbol{r}\, ds = -\oint_{\partial A} p\mathbf{I} \cdot \boldsymbol{r}\, ds + \oint_{\partial A} \mathbf{T}_m \cdot \boldsymbol{r}\, ds + \\ + \int_A \frac{1}{r} \begin{bmatrix} 0 \\ p - \tau_{\theta\theta} \\ 0 \end{bmatrix} \cdot \boldsymbol{r}\, dA + \int_A \boldsymbol{f}_\mathbf{b}\, dA \end{aligned} \tag{5.21}$$

$$\int_A \rho_m H_m \boldsymbol{v}_m \cdot d\mathbf{a} = -\int_A \dot{\boldsymbol{q}} \cdot d\mathbf{a} + \int_A (\mathbf{T}_m \cdot \boldsymbol{v}_m) \cdot d\mathbf{a} + \int_\mathrm{V} (\boldsymbol{f}_\mathbf{b} \cdot \boldsymbol{v}_m) \cdot dV + \int_\mathrm{V} S_E\, dV \tag{5.22}$$

Three phases are considered in the developed model: water, steam, and carbon dioxide. The volume fraction transport equations of each phase are presented in Equation (5.23), Equation (5.24), and Equation (5.25).

$$\int_A \alpha_w \boldsymbol{v}_m \cdot\, d\boldsymbol{a} = \int_\mathrm{V} \left(S_{P,w} - \frac{\alpha_w}{\rho_w} \boldsymbol{v}_m \cdot \nabla \rho_w \right) dV + \int_A \frac{\mu_t}{\mathrm{Sc}_t \rho_m} \nabla \alpha_w \cdot\, d\boldsymbol{a} \tag{5.23}$$

$$\int_A \alpha_s \boldsymbol{v}_m \cdot\, d\boldsymbol{a} = \int_\mathrm{V} \left(S_{P,s} - \frac{\alpha_s}{\rho_s} \boldsymbol{v}_m \cdot \nabla \rho_s \right) dV + \int_A \frac{\mu_t}{\mathrm{Sc}_t \rho_m} \nabla \alpha_s \cdot\, d\boldsymbol{a} \tag{5.24}$$

$$\int_A \alpha_{CO_2} \boldsymbol{v}_m \cdot\, d\boldsymbol{a} = -\int_\mathrm{V} \left(\frac{\alpha_{CO_2}}{\rho_{CO_2}} \boldsymbol{v}_m \cdot \nabla \rho_{CO_2} \right) dV + \int_A \frac{\mu_t}{\mathrm{Sc}_t \rho_m} \nabla \alpha_{CO_2} \cdot\, d\boldsymbol{a} \tag{5.25}$$

5.2. Turbulent flow modeling using RANS approach

Turbulence models can be generally classified into three categories: Direct numerical simulations (DNS), Reynolds-Averages Navier-Stokes equations (RANS), and Large Eddy simulations (LES), as illustrated in Figure 5.1.

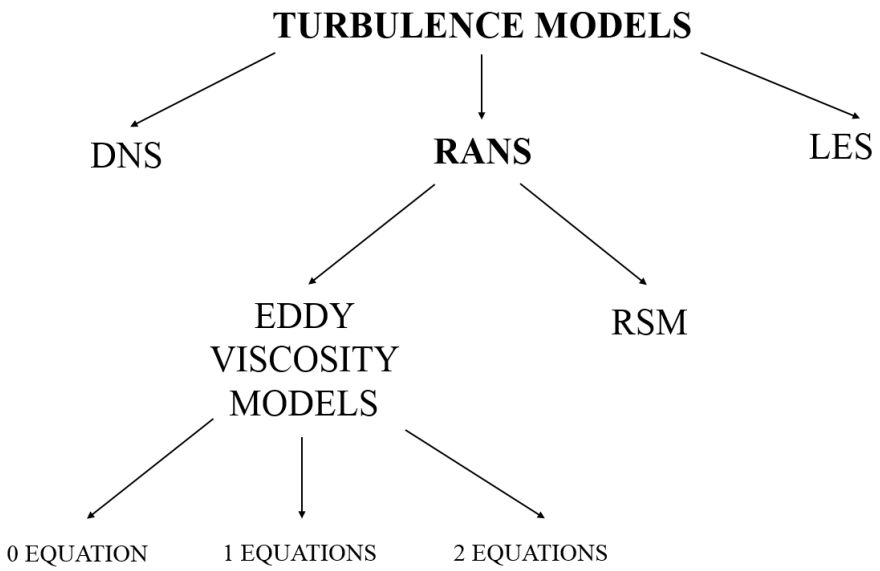

Figure 5.1. Classification of turbulence models used in CFD modeling.

In the DNS approach, the Navier-Stokes equations are solved without any simplifications, which leads to the resolution of all turbulence scales. As a consequence, this method requires extremely fine computational grids [103] with the minimum cell size less than the most minor scales of turbulence [104]. In the LES approach, only large-scale eddies are directly computed from Navier-Stokes equations, as they contain the most turbulent kinetic energy. Smaller turbulent structures are filtered out and modeled. The separation between resolved and modeled eddies depends on the filter width used in the simulation. Finally, the RANS-based models use the Reynolds decomposition, where Navier-Stokes equations are time-averaged. This leads to additional nonlinear Reynolds stress terms, which should be modeled. A comparison of the advantages and disadvantages of the discussed approaches is presented in Figure 5.2. RANS methods rely on turbulence modeling techniques, typically involving empirically selected closure assumptions. They enable the simulation of turbulent flows in complex geometrical domains at moderate computational cost and with acceptable accuracy. Due to these benefits, RANS-based models are widely used in engineering applications, including power engineering, aerospace, and marine industries.

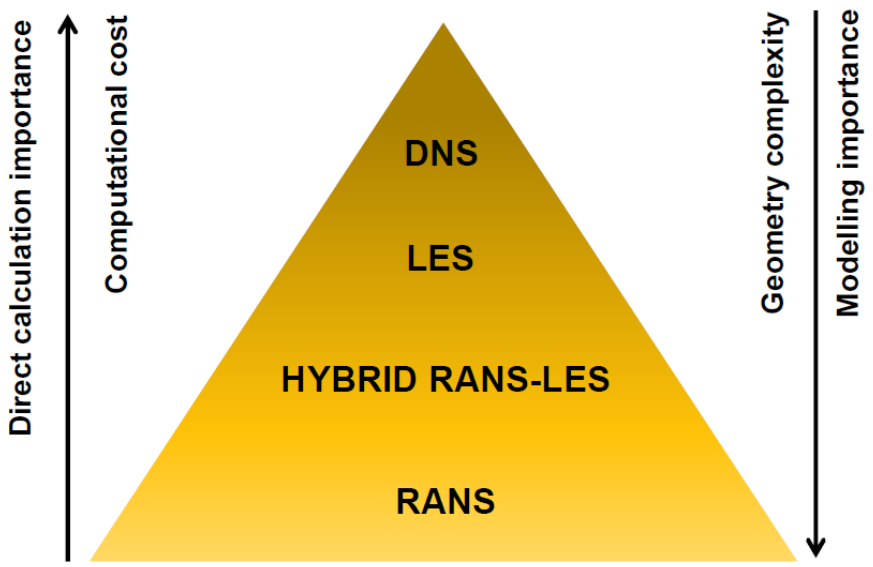

Figure 5.2. Strengths and weaknesses of the different turbulence modeling strategies.

Reynolds decomposition in RANS approaches is based on the separation of instantaneous quantities of turbulent flow (such as pressure, velocity, and energy) denoted by ϑ, into a steady mean value $\bar{\vartheta}$ and a fluctuating component $\bar{\vartheta}'$, as expressed in Equation (5.26).

$$\vartheta(x,y,z,t) = \bar{\vartheta}(x,y,z) + \vartheta'(x,y,z,t) \tag{5.26}$$

The governing equations (Equation (5.1), Equation (5.2), Equation (5.3)), after applying Reynolds decomposition, give the Reynolds-averaged equations representing the transport of mean mass, momentum and energy transport equations as presented in Equation (5.27), Equation (5.28), and Equation (5.29), respectively.

$$\frac{\partial \rho}{\partial t} + \nabla \cdot (\rho \bar{\boldsymbol{v}}) = 0 \tag{5.27}$$

$$\frac{\partial (\rho \bar{\boldsymbol{v}})}{\partial t} + \nabla \cdot \left(\rho (\bar{\boldsymbol{v}}\, \bar{\boldsymbol{v}})\right) = -\nabla \cdot \bar{p}\mathbf{I} + \nabla \cdot \left(\bar{\mathbf{T}} + \mathbf{T}_{RANS}\right) + \boldsymbol{f}_{\mathbf{b}} \tag{5.28}$$

$$\frac{\partial (\rho \bar{E})}{\partial t} + \nabla \cdot (\rho \bar{E} \bar{\boldsymbol{v}}) = -\nabla \cdot \bar{p}\bar{\boldsymbol{v}} + \boldsymbol{f}_{\mathbf{b}} \bar{\boldsymbol{v}} + \nabla \cdot (\bar{\mathbf{T}} + \mathbf{T}_{RANS})\bar{\boldsymbol{v}} - \nabla \cdot \bar{\boldsymbol{q}} \tag{5.29}$$

A new term, called Reynolds stress tensor $\mathbf{T}_{RANS}$, appears in the momentum and energy transport equations. These additional stresses arise from fluctuating momentum exchange between neighbouring stream surfaces, significantly enhancing both heat transfer and diffusion in turbulent flows. The mathematical formulation of $\mathbf{T}_{RANS}$ is provided in Equation (5.30)

$$\mathbf{T}_{RANS} = -\rho \begin{pmatrix} \overline{v_x' v_x'} & \overline{v_x' v_y'} & \overline{v_x' v_z'} \\ \overline{v_x' v_y'} & \overline{v_y' v_y'} & \overline{v_y' v_z'} \\ \overline{v_x' v_z'} & \overline{v_x' v_y'} & \overline{v_z' v_z'} \end{pmatrix} + \frac{2}{3}\rho k \mathbf{I} \tag{5.30}$$

Similar to the DNS method, a direct computation of the Reynolds stress tensor $\mathbf{T}_{RANS}$ is possible. Reynolds Stress Model (RSM) solve transport equations for each component of the tensor, naturally allowing for the inclusion of turbulence anisotropy. More details about the RSM model can be found in [105].

In the eddy viscosity models, the Reynolds stress tensor $\mathbf{T}_{RANS}$ is calculated using the turbulent viscosity concept μ_t. Turbulent eddy viscosity is analogous to molecular viscosity, but unlike the latter, it is not a physical property of the fluid. Instead, it emerges from fluid motion and depends on the local turbulence structure at a given point in the velocity field. The Boussinesq approximation, used to express stress tensor as a function of mean flow quantities, is presented in Equation (5.31).

$$\mathbf{T}_{RANS} = 2\mu_t \mathbf{D} - \frac{2}{3}\left(\mu_t \nabla \cdot \bar{\boldsymbol{v}}\right)\mathbf{I} \tag{5.31}$$

The most popular RANS eddy-viscosity models solve the additional transport equations to determine the turbulent viscosity μ_t. Two-equation models solve equations for the turbulent kinetic energy k and a second turbulence variable. The most common are the k-ω and k-ε, including their various modification. The k-ω model solves two transport equations: one for turbulent kinetic energy k and the other for the specific dissipation rate ω. One of the most widely used modifications is the k-ω *SST* model, which combines k-ε and k-ω models using a blending function to improve accuracy in both near-wall and free-shear flows. A detailed description of the k-ω family of models can be found in [106].

In the k-ε model, the turbulent eddy viscosity is determined using Equation (5.32). The model solves two transport equations: for turbulent kinetic energy k and for turbulent dissipation rate ε, as presented for steady-state conditions in Equation (5.33) and Equation (5.34).

$$\mu_t = \rho C_\mu f_\mu k\, \tau \tag{5.32}$$

$$\nabla \cdot (\rho k \bar{\boldsymbol{v}}) = \nabla \left[\left(\mu + \frac{\mu_t}{\sigma_k} \right) \nabla k \right] + P_k - \rho(\varepsilon - \varepsilon_o) + S_k \tag{5.33}$$

$$\nabla \cdot (\rho \varepsilon \bar{\boldsymbol{v}}) = \nabla \left[\left(\mu + \frac{\mu_t}{\sigma_\varepsilon} \right) \nabla \varepsilon \right] + \frac{1}{\tau_e} C_{\varepsilon 1} P_\varepsilon - \rho C_{\varepsilon 2} f_2 \left(\frac{\varepsilon}{\tau_e} - \frac{\varepsilon_0}{\tau_0} \right) + S_\varepsilon \tag{5.34}$$

Significant improvement over the standard *k*-*ε* model is achieved through its modified version, known as the Realizable *k*-*ε* model. It can accurately predict complex flow, including separation, recirculation and adverse pressure gradient. The modifications introduced in the turbulent dissipation rate transport equation are derived from the dynamic equation of the mean-square vorticity fluctuation [107]. The realizability condition of the model is enforced by relating the critical coefficient of the model C_μ to the mean strain rate. In Simcenter Star-CCM+ software, the model is implemented through the dumping function introduced in Equation (5.32) and Equation (5.34), taking the value 1 in the standard *k*-*ε* model. In the Realizable *k*-*ε* formulation, the dumping function for the turbulent dissipation rate transport equation f_2 is defined by Equation (5.35). The dumping function for the turbulent eddy viscosity f_μ is more complex and can be found in [108].

$$f_2 = \frac{k}{k + \sqrt{\nu \varepsilon}} \tag{5.35}$$

Calculating the viscous-affected layer using the k-ε models is possible by applying a two-layer approach. The turbulent kinetic energy equation is solved throughout the entire computational domain, whereas the turbulent dissipation rate ε is specified as a function of the wall distance in the near-wall region, as presented in Equation (5.36). The blended smooth transition is applied between values to the wall and those farther away. More details on the implementation of the two-layer formulation within the two-equation model can be found in [109].

$$\varepsilon = \frac{k^{3/2}}{l_\varepsilon} \tag{5.36}$$

5.3. Modeling of the phase change

Thermally driven models' interfacial mass transfer prediction is based solely on the heat transfer calculations between the liquid and vapor phases to a saturated interface. The resulting energy balance determines the heat available for the phase change process, which is driven by thermal diffusion rather than concentration gradients. The boiling/condensation model, implemented in Simcenter STAR-CCM+, follows this thermally driven concept and operates within the mixture multiphase framework. The

local thermal imbalance between the bulk mixture temperature and the saturation temperature governs the rate of phase change. The total mass rate of boiling/condensation $\dot{g}^{ij}$ between phases *i* and *j* is determined from the sum of the heat fluxes transferred from the phases $Q_i^{(ij)}$ and $Q_j^{(ij)}$ to the interface, related to the latent heat of phase change L_{ij} according to the Equation (5.37):

$$\dot{g}^{ij} = \frac{Q_i^{(ij)} + Q_j^{(ij)}}{L_{ij}} \tag{5.37}$$

Heat fluxes $Q_i^{(ij)}$ and $Q_j^{(ij)}$ between the phases and interface in the boiling/condensation model based on the mixture approach are expressed in Equation (5.38) and Equation (5.39).

$$Q_i^{(ij)} = h_i^{(ij)} a_{ij}^{(ij)} (T_{sat} - T_i) \tag{5.38}$$

$$Q_j^{(ij)} = h_j^{(ij)} a_{ij}^{(ij)} (T_{sat} - T_i) \tag{5.39}$$

The appropriate calculation of the heat transfer fluxes requires well-defined interfacial area density, which defines the effective phase interface area per unit volume and significantly influences the intensity of the phase change process. Phase interface depends on the flow regime and phase topology, but practically, it is estimated using simplified empirical models, e.g., assuming idealized particle geometry like “Spherical particle model” or “symmetric model” [110].

The temperature gradient $(T_{sat} - T_i)$ and the interfacial area density $a_{ij}^{(ij)}$, which appear in the expressions for the heat fluxes $Q_i^{(ij)}$ and $Q_j^{(ij)}$ (Equation (5.38) and Equation (5.39)) are identical in the homogeneous approach, where the bulk temperature of the mixture is assumed. These expressions differ only in the heat transfer coefficient *h*, which depends on the physical properties of the fluid and the definition of the Nusselt number. These equations used to calculate the heat transfer coefficient for phase *i* and j are presented in Equation (5.40) and Equation (5.41). It it worth noting that Nusslet number is defined separately for each phase, e.g., individually for contionus and dispersed phases.

$$h_i^{(ij)} = \frac{\lambda_i \, \mathrm{Nu}_i}{l_{ij}} \tag{5.40}$$

$$h_j^{(ij)} = \frac{\lambda_j \, \mathrm{Nu}_j}{l_{ij}} \tag{5.41}$$

One of the critical parameters is the interaction length scale l, which is usually related to the averaged droplet or bubble diameter d_p. It is determined by nozzle geometry, operating conditions, fluids properties, particularly pressure, viscosity, and specific gravity [111].

The Nusselt Number can determined using various methods, and the appropriate correlation for the multiphase flow depends on the flow pattern. For example, in stratified flows, the Hughes-Duffey correlation is used, where the condensation mass transfer is predicted based on turbulent properties using the surface renewal theory [112,113]. For the flows with dispersed–continuous flow regime (i.e. droplet- or bubble-laden flow), the Ranz–Marshall correlation is typically applied [114]. Based on boundary layer theory, this correlation describes convective heat transfer between a particle and the surrounding fluid (Equation (5.42)). It incorporates the particle Reynolds Number Re_p and the Prandtl number of the surrounding fluid (continuous phase) Pr_c, defined in Equation (5.43) and Equation (5.44), respectively. The Nusselt number coefficients C_{1-4} which appear in Equation (5.42) and were proposed initially by Ranz and Marshall can be tunned to reflect specific thermal–flow conditions. In case of water droplets, these coefficients have been refined by various authors [115–117].

$$\mathrm{Nu} = C_1 + C_2 \, \mathrm{Re}_p^{C_3} \, \mathrm{Pr}_c^{C_4} \tag{5.42}$$

$$\mathrm{Re}_p = \frac{\rho_c \left(v_c - v_p \right) d_p}{\mu_c} \tag{5.43}$$

$$\mathrm{Pr}_c = \frac{\mu_c \cdot C_{p\,c}}{\lambda_c} \tag{5.44}$$

6. Discretization of the flow domain using the Finite Volume Method

The Finite Volume Method (FVM) is the numerical approach for solving partial differential equations describing fluid flow and heat transfer. It transforms these equations into a system of linear algebraic equations through a discretization procedure. The computational domain is subdivided into a finite number of non-overlapping, small control volumes, within which the integral form of the governing equations is applied in a discrete form. The main advantage of FVM is its ability to handle arbitrary geometries using unstructured and structured meshes, making it particularly suitable for industrial applications. The chapter presents the fundamental concepts and procedures for discretizing the computational domain using FVM, including selecting control volumes, developing the numerical mesh, and applying discretization schemes. The solution strategy is also introduced by presenting the pressure–velocity coupling algorithms and techniques commonly used for solving the resulting systems of algebraic equations.

6.1. Definition of control volume and development of mesh

FVM focuses on local balances within each control volume rather than the entire continuum. The flexibility in shaping these control volumes allows for the easy generation of appropriate equations that determine the nodal values of the sought function. Depending on the selection of the control volume, two distinct approaches can be identified within the finite volume method:

- the control volume created around the grid node (vertex-centered approach)
- the control volume equivalent to the grid cell (cell-centered approach)

Examples of control volume definition using cell-centered (marked as 1) and vertex-centered (marked as 0) methods for both structural and unstructural meshes are presented in Figure 6.1. In the vertex-centered approach, control volumes are formed by connecting the centroids of cells that share a common node. The unknowns are stored at the vertices of the mesh. This approach works well on a structured mesh, offering high accuracy but less flexibility in handling complex geometries. In the cell-centered method, cells directly serve as control volumes, and the solution is stored at the centers of the cells. The fluxes of flow quantities are computed at the cell faces. The method is computationally efficient and performs well even on highly unstructured meshes, which is why it is widely used in commercial CFD software.

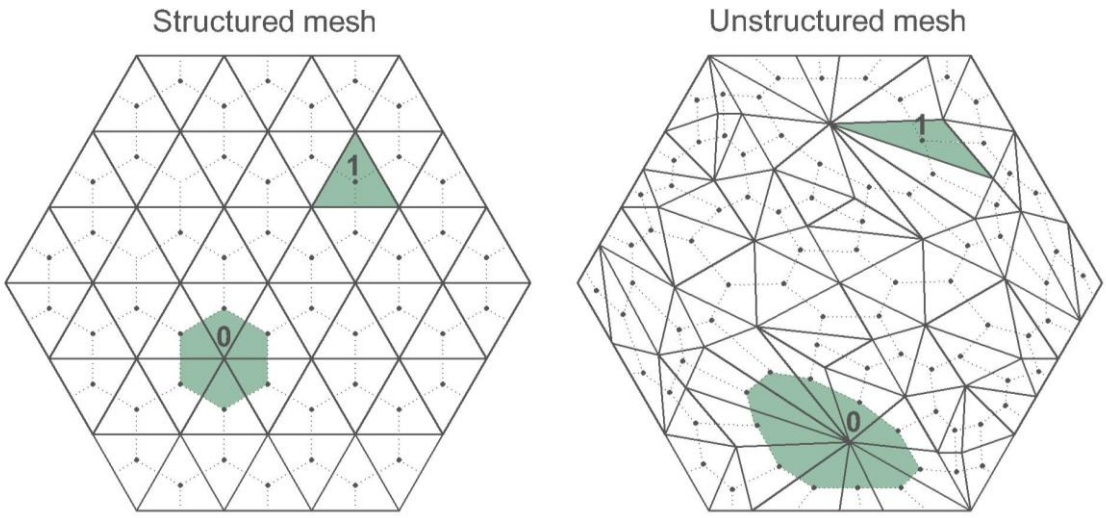

Figure 6.1. Two methods of defining control volume: vertex-centered (0) and cell-centered (1), depending on the mesh type (structured and unstructured).

The validity of the prepared mesh determines whether a converged and physically meaningful solution can be obtained. Beyond the physics of the process, several factors can influence the mesh validity:

- mesh quality,
- type of solver (coupled or segregated),
- under-relaxation factors,
- discretization scheme.

Mesh quality significantly impacts the convergence, stability, and, most importantly, the accuracy of the numerical solution. The mesh should be refined in high-gradient regions and provide a smooth transition between refined and coarse areas. To accurately calculate the convective and diffusive fluxes, the line connecting the centroids of neighboring cells should ideally pass near the centroid of the shared face and be approximately orthogonal to it. Additionally, layers near the walls require special attention, especially in regions with significant turbulence or heat transfer effects.

The non-dimensional wall distance y^+ represents the distance y from the wall to the center of the first mesh cell, relative to the viscous length defined by the friction velocity u^* and kinematic viscosity ν (Equation (6.1)).

$$y^+ = \frac{y u_*}{\nu} \tag{6.1}$$

The friction velocity u_* is determined using wall shear stress τ_w and the density of the fluid ρ according to Equation (6.2).

$$u_* = \sqrt{\frac{\tau_w}{\rho}} \tag{6.2}$$

The desirable value of the y^+parameter depends on the near-wall treatment strategy, specifically whether the viscous sublayer is resolved or modeled. For the Realizable k-ε model with the two-layer approach, accurate near-wall prediction requires $y^+ < 1$, while the standard wall functions can be applied for values of $y^+ > 30$, similarly to the k-ω SST model.

In Simcenter STAR-CCM+, the mesh cell quality can be evaluated using various indicators. The two most versatile are face validity and volume change. Face validity measures the correctness of the face normal relative to the attached cell centroid using an area-weighted approach. Ideally, face normals should point outward from the cell. A face validity of 1 indicates that all face normals are correctly oriented. If one or more face normals point inwards (towards the cell centroid), the cell is considered bad, as indicated by a face validity below 1. Based on face validity, a comparison between valid and invalid cells is presented in Figure 6.2. A face validity below 0.5 indicates a negative volume cell. Poor face validity can lead to convergence difficulties and numerical diffusion errors.

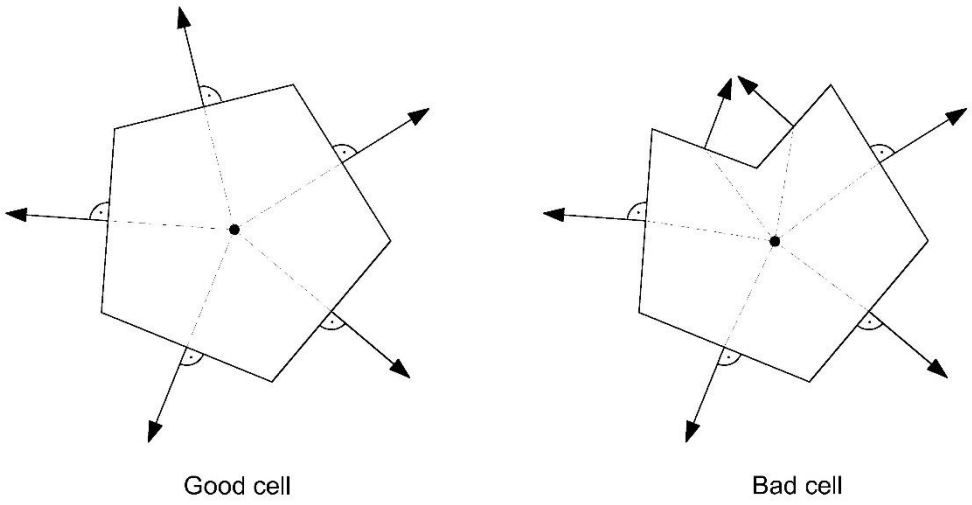

Figure 6.2. Face validity concept: good cell vs bad cell.

The volume change is also a key parameter used to evaluate the quality of the computational mesh. It measures the ratio between a cell's volume and the volume of its largest neighboring cell. The concept of volume change is presented in Figure 6.3, comparing the mesh structures for good and bad cells. When a cell has a volume equal to

or greater than its neighbors, the volume change value is 1. Cell volume should vary smoothly and gradually across the mesh to ensure accurate interpolation of flow variables. A volume change below 0.01 indicates a strongly disproportionate cell volume compared to its neighbors. Although moderate variations in mesh volume are essential for accurately capturing physics in regions with high gradient variations, excessive volume change can lead to numerical instability and reduced solution accuracy.

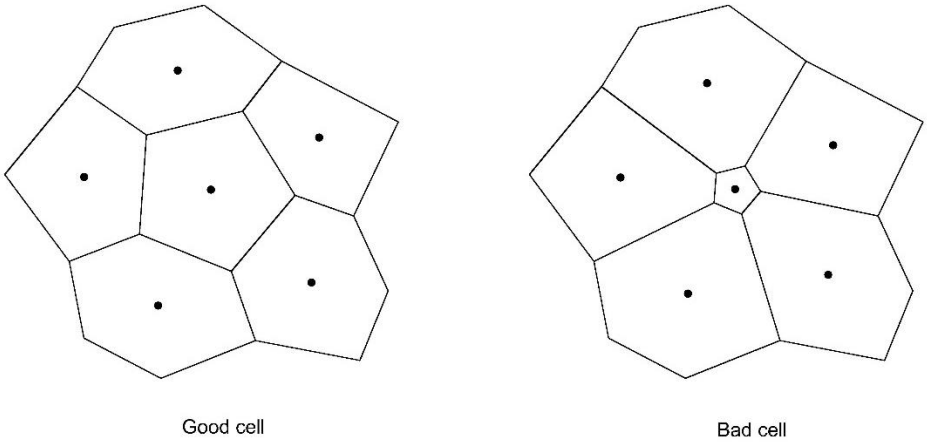

Figure 6.3. Volume change concept: good cell vs bad cell.

6.2. Discretization process

The general integral form of the scalar equation for property φ within the control volume V is presented in Equation (6.3). The equation comprises four essential terms representing key physical phenomena: temporal variation, convection, diffusion, and local generation of the transported property. The integral form is derived by integrating the transport differential equations over a finite control volume and applying Gauss's divergence theorem. This theorem transforms volume integrals containing divergence terms into surface integrals, simplifying the computation by evaluating the fluxes across the control volume instead of computing the divergence over the entire volume.

$$\underbrace{\frac{\partial}{\partial t}\int_V \rho\,\varphi\,dV}_{\textit{Transient term}} + \underbrace{\oint_A \rho\,\boldsymbol{v}\varphi\cdot d\boldsymbol{a}}_{\textit{Convective flux}} = \underbrace{\oint_A \Gamma\nabla\varphi\cdot d\boldsymbol{a}}_{\textit{Diffusive flux}} + \underbrace{\int_V S_\varphi\,dV}_{\textit{Source term}} \tag{6.3}$$

Surface and volume integrals are converted into discrete algebraic equations over control volumes and their surfaces by applying integration quadrature approximations. The discretization process of the generic transport equation for two polyhedral cells is illustrated in Figure 6.4. It highlights the geometric relationships between adjacent cells that are essential for approximating transport processes and serve as the foundation for the discretisation approach presented in the section.

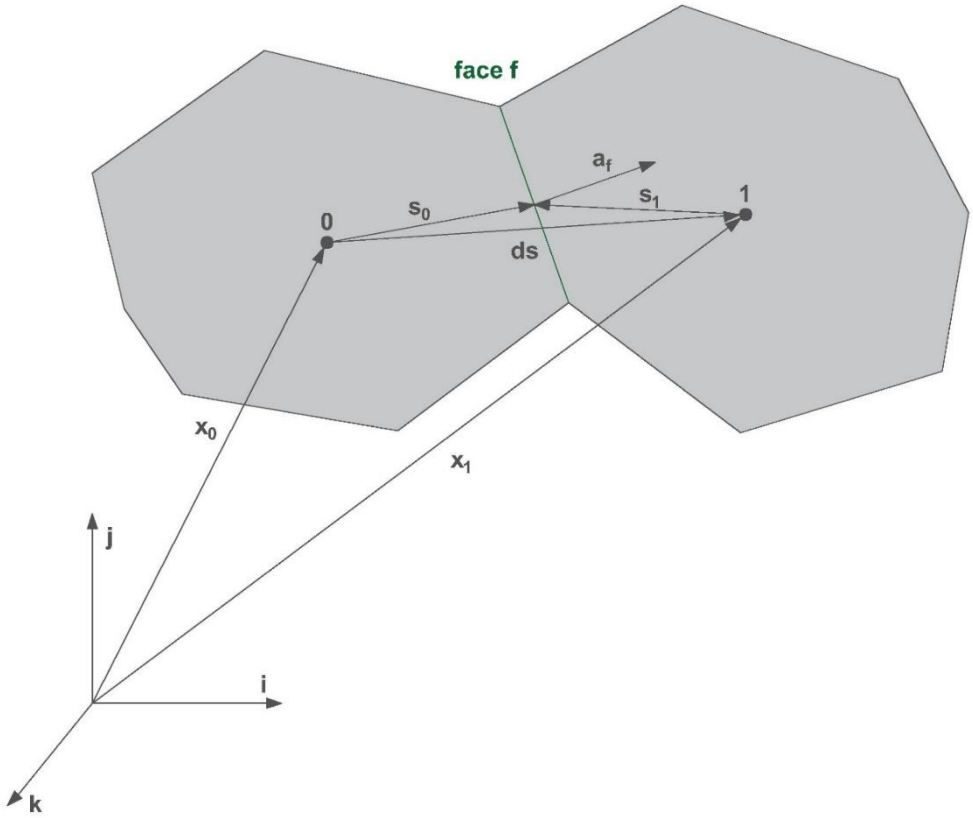

Figure 6.4. Two polyhedral computational cells illustrating the discretization process of a generic transport equation (x_0, x_1 – cell centroids, s_0, s_1 – vectors from centroids to the face centroid, $\boldsymbol{a_f}$ – face area vector).

The surface integrals, which describe transport phenomena arising from diffusion and convection, are computed using quadrature approximations. According to the second-order midpoint rule applied in the Simcenter STAR-CCM+, the surface integral is approximated as a sum of the products over all cell faces, where the value at each face center is multiplied by its corresponding surface area vector, as shown in Equation (6.4). The flux, denoted as $\boldsymbol{J^{\varphi}}$, represents either convective or diffusive transport of the property.

$$\int_A \boldsymbol{J}^{\varphi} \cdot d\boldsymbol{a} \approx \sum\nolimits_f \boldsymbol{J}_f^{\varphi} \cdot \mathbf{a}_f \tag{6.4}$$

The volume integral, appearing as the source term in the governing equations (Equation (6.3)), represents the processes of generation and dissipation of quantities. The integral is approximated by multiplying the mean value of the source term at the cell center by the cell volume, as presented in Equation (6.5). The approximation is second-order for both surface and volume integrals, achieved by the use of area-weighted cell face centers and volume-centered cell centers, respectively.

$$\int_V S_\varphi \, dV \approx S_{\varphi o} \cdot V_o \tag{6.5}$$

Application of approximate integration methods from Equation (6.4) and Equation (6.5) to Equation (6.3) leads to the following form of semi-discrete general transport equation (Equation (6.6))

$$\frac{\partial}{\partial t}\left(\rho \varphi V\right)_0 + \sum_f \left[\rho \varphi \left(\boldsymbol{v} \cdot \boldsymbol{a}\right)\right]_f = \sum_f \left(\Gamma \nabla \varphi \cdot \boldsymbol{a}\right)_f + \left(S_\varphi \cdot V\right)_0 \tag{6.6}$$

6.3. Convection discretization schemes

The convective term can be reformulated using the mass flow rate at the face $\dot{m}_f$ and the fluid property value at the face φ_f, as presented in Equation (6.7). These values can be calculated using different discretization methods, which significantly affect the stability and accuracy of the solution.

$$\left(\varphi \, \boldsymbol{v} \cdot \boldsymbol{a}\right)_f = \left(\dot{m} \varphi\right)_f = \dot{m}_f \varphi_f \tag{6.7}$$

The convective flux in a Second-Order Upwind (SOU) numerical scheme is computed based on the direction of the mass flow rate $\dot{m}_f$, according to Equation (6.8). The face values of transported property, $\varphi_{f,0}$ and $\varphi_{f,1}$, are obtained by linear interpolation from the cell center values on either side of the face, using the gradients reconstructed within the neighboring cells.

$$\left(\dot{m} \varphi\right)_f = \begin{cases} \dot{m}_f \varphi_{f,0} & \text{for } \dot{m}_f \geq 0 \\ \dot{m}_f \varphi_{f,1} & \text{for } \dot{m}_f < 0 \end{cases} \tag{6.8}$$

In the Hybrid MUSCL third-order/CD scheme, the convective flux is computed using χ, obtained from the Normalized Variable Diagram (NVD), as presented in Equation (6.9). In regions of non-smooth flows, the First-Order Upwind (FOU) scheme is applied, using the reconstructed value φ_{FOU}. For smooth flow conditions, a blended scheme is used, combining the third-order upwind (φ_{MUSCL3}) and third-order central-differencing (φ_{CD3}). The blending factor φ_{MUSCL3} determines the relative contribution of MUSCL3 and CD3 based on the physical characeristis of the flow.

$$\left(\dot{m} \varphi\right)_f = \begin{cases} \dot{m} \, \varphi_{FOU} & \text{for } \chi < 0 \quad or \quad \chi > 1 \\ \dot{m}_f \left(\sigma_{MUSCL3} \, \varphi_{MUSCL3} + \left(1 - \sigma_{MUSCL3}\right) \varphi_{CD3}\right) & \text{for } \; 0 < \chi \leq 1 \end{cases} \tag{6.9}$$

6.4. Pressure–velocity coupling using segregated solver

Based on the solution strategy for velocity–pressure coupling, the following solvers can be distinguished: coupled and segregated. A coupled solver simultaneously solves pressure and velocity fields derived from continuity and momentum equations. Despite the strong coupling, and thus, the high stability of the solution, the coupled solver can be overly demanding in terms of memory requirements to deal with practical engineering problems [118]. The segregated solver solves iteratively the main variables from the discretized governing equations in a sequential manner. Continuity and momentum equations are addressed independently, with each solved variable providing an updated input for the next equation. More time is needed to achieve solution convergence but the method is computationally economical. Typical application of segregated solver contains constant density flow, low and mildly compressible flows as well as flow with large velocity gradients produced by a boundary layer formation [119].

In the segregated-type solvers, the pressure-correction method is typically applied. This method introduces a pressure–velocity coupling algorithm in which the pressure-correction equation ensures the mass conservation within the velocity field. The pressure-correction equation is derived from continuity and momentum equations, enabling the prediction of the velocity field that satisfies the continuity equation based on the corrected pressure. Pressure as a variable can be obtained from the pressure-correction equations for the constant density flow, or directly from the equation of state when the density is variable [120].

Within the framework of the pressure-correction method, various algorithms have been developed over the past decades including SIMPLE, SIMPLEC, PISO, CLEAR or IDEAL. The first three are implemented in the Simcenter STAR-CCM+ software, which provides users with versatile tools for addressing diverse flow conditions. Only the SIMPLE algorithm can be applied for steady-state flows and is fully compatible with multiphase simulation [108].

In the SIMPLE iterative algorithm developed by Patankar and Spalding, convective fluxes per unit mass through cell faces are computed using initially estimated velocity components. The momentum equation is then solved with a guessed pressure field, resulting in an intermediate velocity field $\boldsymbol{v}^*$. Subsequently, the uncorrected mass fluxes $\dot{m}_f^*$ at cell faces are computed. The pressure correction equation, derived from the continuity equation, is solved to obtain a pressure correction field p^{cv}, which is then

used to update the solution variables. The pressure field is updated iteratively according to Equation (6.10).

$$p^{n+1} = p^{n} + \omega p^{cv} \tag{6.10}$$

The pressure at the boundaries is also updated. Subsequently, the face mass fluxes are corrected based on Equation (6.11).

$$\dot{m}_f^{n+1} = \dot{m}_f^{*} + \dot{m}_f^{cv} \tag{6.11}$$

The velocity field is updated using Equation (6.12). Finally, the density is recalculated to account for pressure changes. This iterative process of improving both the velocity and pressure fields is repeated until the solution reaches the required level of convergence.

$$\boldsymbol{v}_o^{n+1} = \boldsymbol{v}_o^{*} - \frac{V \nabla p^{cv}}{\boldsymbol{d}_o^{v}} \tag{6.12}$$

The under-relaxation factor ω in Equation (6.10) significantly influences the numerical stability and convergence of the solution. It controls the proportion of newly computed values incorporated in each iteration. Although the given example refers to pressure, the same principle applies to other key quantities in segregated solvers, such as velocity, pressure, energy, volume fraction, turbulent kinetic energy, and turbulent dissipation rate. Setting appropriate relaxation factors is particularly important in discretization schemes involving convection, which are often connected with strong gradients and complex interactions between neighboring cells. Optimal values are problem-dependent and are typically determined through the trial-and-error method.

6.5. Solution of discretized equations using the Algebraic Multigrid method

After discretizing the governing equations describing fluid flow, a linear system of algebraic equations must be solved. The system can be expressed in matrix form, as shown in Equation (6.13), where the coefficient matrix is denoted by **C,** the vector of unknowns by $\boldsymbol{x}$**,** and the residual vector by $\boldsymbol{b}$**.**

$$\mathbf{C}\boldsymbol{x} = \boldsymbol{b} \tag{6.13}$$

The Gauss–Seidel method is a point-iterative algorithm, in which the variables are updated sequentially, one at a time in each iteration, incorporating the most recently calculated and available values of other variables, as presented in Equation (6.14). The

row and column indices are represented by i and j, respectively. The dominance of elements lying on the main diagonal ensures the convergence of this method [121].

$$x_i^{(n)} = \sum_{j=1}^{i-1} \left(\frac{-c_{ij}}{c_{ii}} \right) x_j^{(n)} + \sum_{j=i+1}^{N} \left(\frac{-c_{ij}}{c_{ii}} \right) x_j^{(n-1)} + \frac{b_i}{c_{ii}} \tag{6.14}$$

Conventional point-iterative methods require considerable time to achieve convergence. Multigrid acceleration techniques have been developed to improve the convergence for large systems arising from highly refined meshes. To understand their operation, two types of error components should be distinguished: short-wavelength (high-frequency) and long-wavelength (low-frequency) errors. Point-iterative procedures effectively reduce short-wavelength errors, while long-wavelength components tend to converge slowly. Multigrid methods perform computations on a hierarchy of grids with different resolutions, allowing efficient reduction of both error types. High-frequency errors are damped on fine grids, whereas low-frequency errors, once transferred to a coarser grid, appear as high-frequency relative to the new resolution and are also eliminated.

The AMG solver available in SimCenter STARCCM+ follows the multigrid strategy to accelerate the convergence of linear system solutions. The Gauss–Seidel method is commonly used as a relaxation scheme to perform smoothing iterations at each level of the algebraic multigrid hierarchy. Switching between grid levels is typically performed using a regular pattern, most commonly the V-cycle, illustrated in Figure 6.5 . The cycle begins with relaxation sweeps on the most refined mesh. The residuals are then transferred to the next coarser level, where the process is repeated and continues until the coarsest level is achieved. The estimated error at the coarsest mesh is then used to correct the solution on the next finer level. Relaxation sweeps are again performed, and the corrected solution is successively transferred back to finer levels until the original mesh resolution is restored.

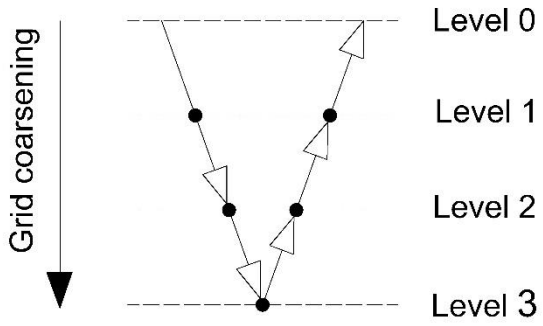

Figure 6.5. V-cycle in the Algebraic Multigrid method.

7. Numerical model of multiphase flow with condensation in the spray-ejector condenser

This chapter presents the development of the numerical model of multiphase flow with condensation in the spray-ejector condenser, including all assumptions, physical models, and numerical settings applied in the analysis. The structure follows the logical sequence of steps, starting with preparing the geometric model and numerical mesh, and continuing through the specification of boundary conditions, fluid properties, and selected physical models. Due to the extensive number of simulations, input data and model parameters are compiled in tables and consistently referenced throughout the appropriate sections. The theoretical background for the presented models and numerical methods is provided in Chapters 5 and 6.

7.1. Development of a two-dimensional geometric model

The spray-ejector condenser's axisymmetric geometrical model was developed using the 3D-CAD module available in Simcenter StarCCM+. The model is developed based on the dimensions presented in Table 4.1 (page 29). The choice of a two-dimensional axisymmetric approach for two-phase ejector modeling enabled a reduction in computational cost while maintaining enough accuracy in capturing key flow phenomena associated with two-phase ejector operation [39–41,51,88] .

Two geometrical variants of the ejector were analyzed: LPL and nLPL (a refined version of the LPL). Modifications in the LPL geometry aim to improve pressure performance and condensation effectiveness by adjusting key design parameters using numerical methods. Figure 7.1 and Figure 7.2 present views of the suction and mixing chambers, and the diffuser section of the LPL geometrical model, respectively.

Figure 7.1. Axisymmetric, geometrical model of the spray-ejector condenser - LPL variant, suction and mixing chambers.

Figure 7.2. Axisymmetric, geometrical model of the spray-ejector condenser - LPL variant, diffuser.

Different geometrical parameters were varied to investigate their influence on overall performance: mixing chamber diameter D_{MIX}, mixing chamber length L_{MIX}, the motive nozzle diameter D_{MN_2}, outer nozzle diameter D_{TIP}, and nozzle exit position L_{MCH} (NXP) as presented in Figure 7.3. Additionally, a modified configuration of the motive nozzle was considered, involving the introduction of a secondary nozzle placed directly downstream of the primary one, at a distance L_{MS} (Figure 7.4). Table 7.1 presents the specific values of the investigated geometrical parameters. Primary dimensions are marked in bold. For the mixing chamber diameter, an asterisk (*) indicates that the value was adjusted by slightly modifying the mixing chamber length. Otherwise, the diameter was changed by adjusting the outer diameter of the suction chamber. In the mixing chamber length investigation, the asterisk(*) refers to the case without the diffuser part.

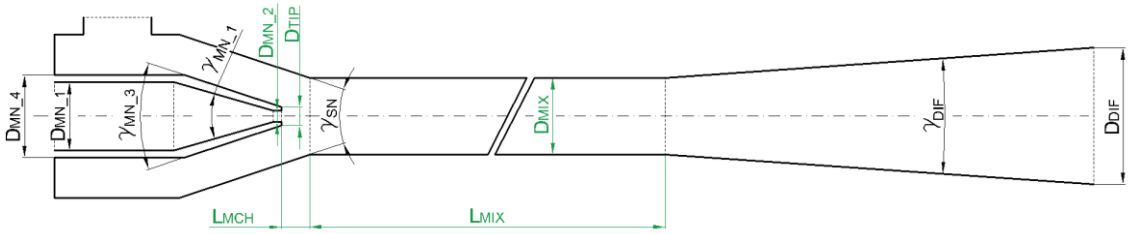

Figure 7.3. Investigated geometrical parameters (marked in green).

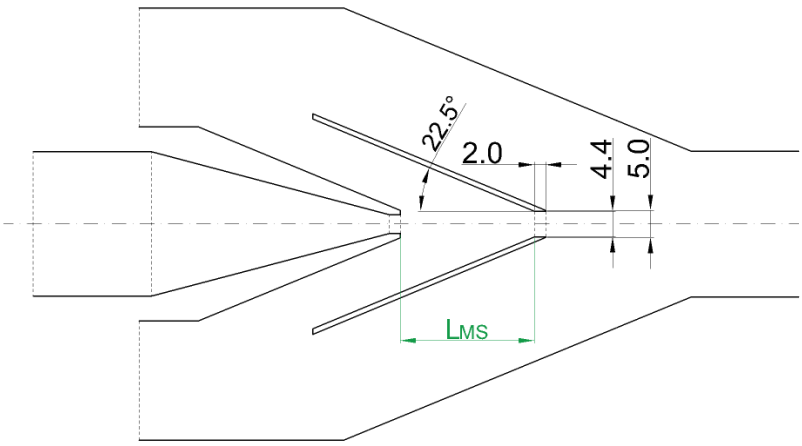

Figure 7.4. Multi-stage nozzle configuration.

Table 7.1. Tested Geometrical Parameters of the LPL Variant
*(Bold – primary dimensions, * – alternative variants)*

Parameter	Tested Values, mm
D_{MIX}	20, 20*, **25**, 30, 30*
L_{MIX}	550, 800, **1050**, 1050* 1300, 1550
L_{MCH} (NXP)	15, **25**, 30
D_{MN_2}	2.6, 2.8, **3.0**, 3.2, 3.6
D_{TIP}	**5**, 10, 15
L_{MS}	15(v2), 25(v1)

The nLPL geometrical model was developed, and views of the modified suction and mixing chambers, as well as the diffuser section, are presented in Figure 7.5 and Figure 7.6, respectively.

Figure 7.5. Axisymmetric, geometrical model of the spray-ejector condenser - nLPL variant, suction and mixing chambers.

Figure 7.6. Axisymmetric, geometrical model of the spray-ejector condenser - nLPL variant, diffuser.

7.2. Development of a mesh

The polygonal mesher available in Simcenter Star-CCM+ was used to generate numerical meshes for the axisymmetric model of the spray-ejector condenser. Prism layers were created in the near-wall regions to enable appropriate boundary treatment. In all considered cases, the mesh was locally refined in the trailing edge region (30% of the target surface size). The assumed mesh parameters for the developed geometrical models are summarised in Table 7.2. Mesh quality was evaluated using face validity and volume change indicators. For all meshes, face validity was equal to 1.0, and the volume change for nearly all cells ranged between 0.1 and 1.0, indicating good mesh quality. Regarding the non-dimensional wall distance y^+, values ranged from 7.3 to 0.1. However, for meshes selected for further analysis based on the mesh independence study, y^+ was below 0.5, allowing accurate near-wall resolution using the Realizable k-ε model with the two-layer approach.

Table 7.2. Mesh properties for the developed geometrical models. The bolded values indicate the mesh selected based on the mesh independence study for further parametric analysis.

Analysis (Section no.)	Mesh no.	Base size, mm	Number of elements	Inflation layers properties			Mesh indicators		Average wall *y*+
				Number of layers	Stretching factor	Total thickness	Face validity	Volume change	
Boundary conditions (8.1–8.3)	M1	2.00	14938	3	1.6	40	1	1.0-0.1 97% 0.1-0.01 3%	7.3
	M2	**1.25**	**28299**	**3**	**1.6**	**40**	**1**	**1.0-0.1 98% 0.1-0.01 2%**	**4**
	M3	0.70	60787	3	1.6	40	1	>0.01	1.7
Calibration of models (9.1–9.2)	M1	0.70	60787	3	1.6	40	1	1.0-0.1 98% 0.1-0.01 2%	1.7
	M2	0.53	174895	3	1.6	40	1	1.0-0.1 99% 0.1-0.01 1%	1.4
	M3	0.28	387221	3	1.6	40	1	1.0-0.1 99% 0.1-0.01 1%	0.7
	M4	**0.08**	**820643**	**3**	**1.6**	**40**	**1**	**1.0-0.1 99% 0.1-0.01 1%**	**0.3**
	M5	0.05	1302936	3	1.6	40	1	1.0-0.1 98% 0.1-0.01 2%	0.2
Performance analysis and verification (10.1–10.2)	**-**	**0.08**	**820643**	**3**	**1.6**	**40**	**1**	**1.0-0.1 99% 0.1-0.01 1%**	**0.3**
Analysis of geometrical design (11.1–11.5)	**-**	**0.08**	**820643**	**3**	**1.6**	**40**	**1**	**1.0-0.1 99% 0.1-0.01 1%**	**0.3**
Results for the final geometry (12)	M1	0.41	80205	3	1.6	40	1	1.0-0.1 98% 0.1-0.01 2%	3.3
	M2	0.29	130016	3	1.6	40	1	1.0-0.1 98% 0.1-0.01 2%	2.4
	M3	0.18	208323	3	1.6	40	1	1.0-0.1 98% 0.1-0.01 2%	1.3
	M4	0.12	335754	3	1.6	40	1	1.0-0.1 98% 0.1-0.01 2%	0.6
	M5	0.08	537990	3	1.6	40	1	1.0-0.1 99% 0.1-0.01 1%	0.3
	M6	**0.05**	**860784**	**3**	**1.6**	**40**	**1**	**1.0-0.1 99% 0.1-0.01 1%**	**0.2**
	M7	0.03	1376335	3	1.6	40	1	1.0-0.1 99% 0.1-0.01 1%	0.1

The meshes with increasing refinement in the suction and mixing chamber regions are presented in Figure 7.7, Figure 7.8, and Figure 7.9. Among them, Figure 7.9 also illustrates the final mesh selected for the analysis of the LPL geometrical model. The corresponding mesh in the diffuser section is presented in Figure 7.10. A view of the mesh in the suction chamber and the beginning of the mixing chamber, selected for the performance analysis of nLPL geometrical model, is presented in Figure 7.11.

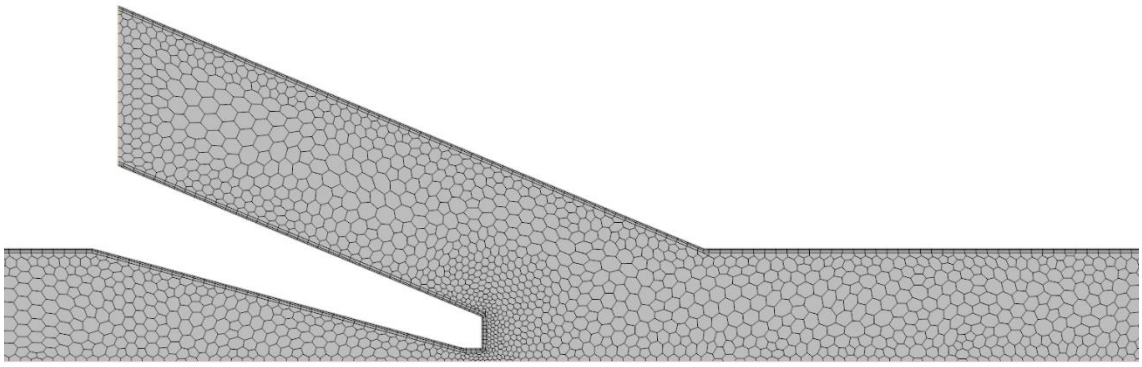

Figure 7.7. Mesh M2 applied in boundary conditions analysis (8.1–8.3) - suction chamber and beginning of the mixing chamber.

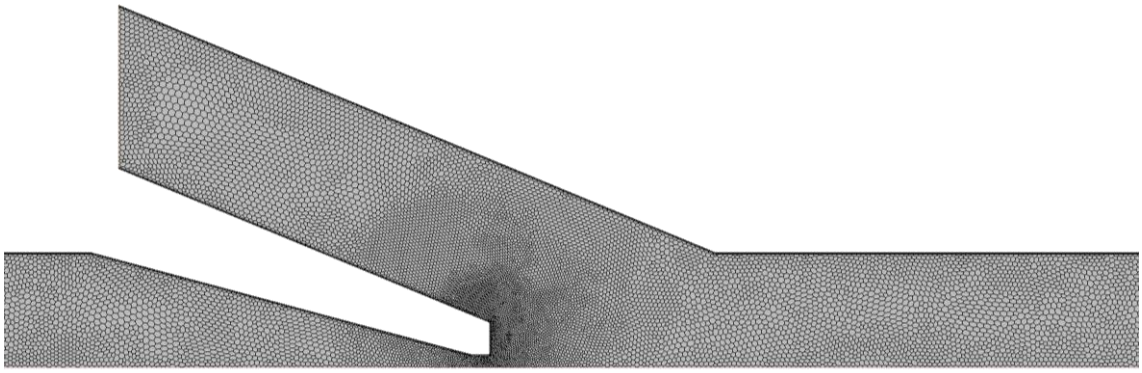

Figure 7.8. Mesh M2 applied in Calibration of models analysis (9.1–9.2) - suction chamber and beginning of the mixing chamber.

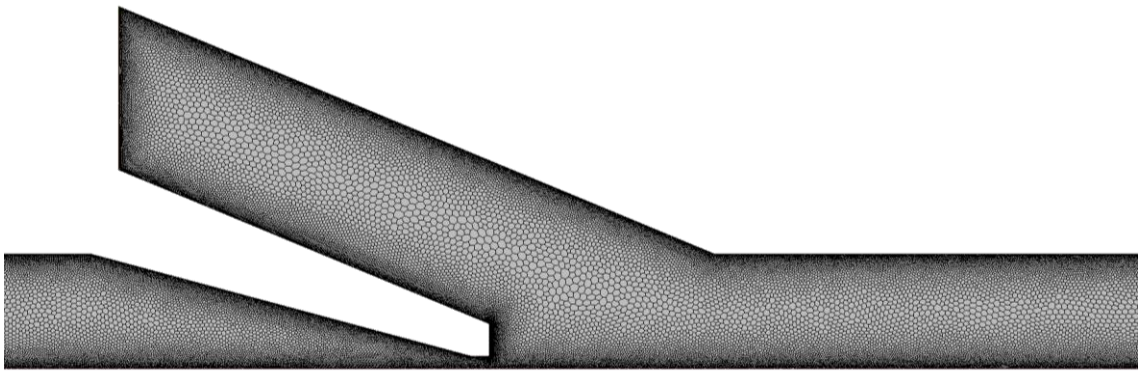

Figure 7.9. Mesh M4 selected for the analysis of the LPL geometrical model - suction chamber and beginning of the mixing chamber.

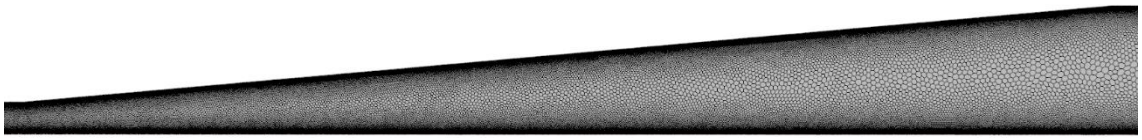

Figure 7.10. Mesh M4 selected for the analysis of the LPL geometrical model – diffuser.

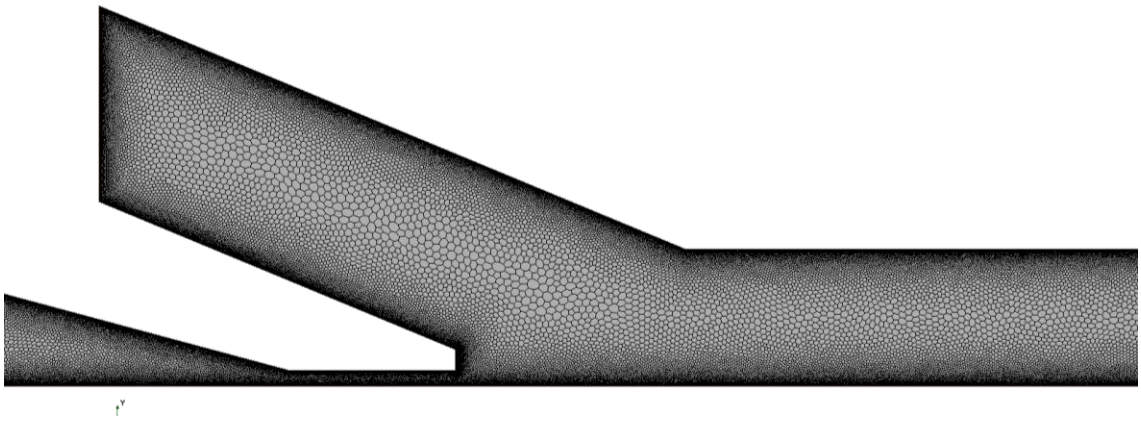

Figure 7.11. Developed Mesh (M6) for the analysis of the nLPL geometrical model - suction chamber and beginning of the mixing chamber.

7.3. Boundary conditions in axisymmetric model of spray-ejector condenser

The scheme of the boundary conditions applied in the CFD model of the spray-ejector condenser is presented in Figure 7.12. Mass flow or pressure boundary conditions were applied at the gas inlet (steam + CO_2). At the liquid inlet (water), either velocity or pressure was imposed, depending on the analysis. The outlet was defined as a pressure outlet. The boundary along the centerline was treated as axial symmetry, while the remaining surfaces were defined as no-slip walls.

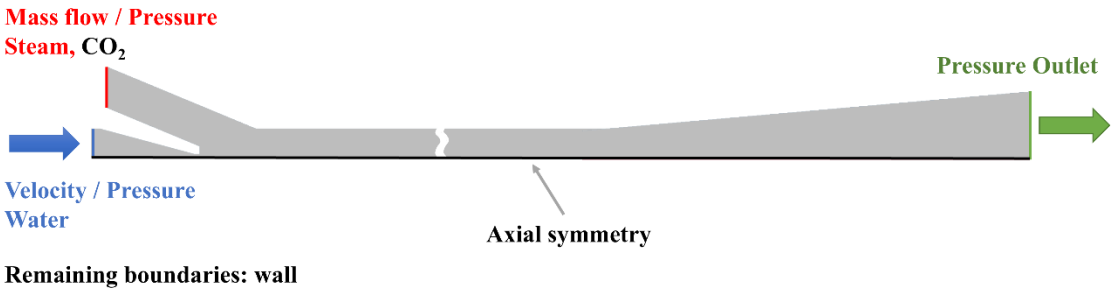

Figure 7.12. The scheme of boundary conditions applied in the CFD analysis of the spray-ejector condenser.

Boundary conditions evolved during the numerical model's development as more experimental and computational data became available. Table 7.3 presents the detailed values applied in the CFD analysis. In most simulations, the exhaust gas mass flow rate was assumed to be approximately 10 g/s, with a CO_2 mass fraction of 20%, corresponding to the nominal operating conditions.

Table 7.3. Boundary conditions details applied in the CFD analysis of the spray-ejector condenser.

Analysis	Section no.	Water inlet		Gas inlet			Outlet
		Velocity; Pressure	Temperature	Massflow; Pressure	Temperature	CO_2 mass content	Pressure
Boundary conditions	8.1	0.67 m/s; 12 bar	17.0°C	10 g/s ; 0.9 bar	150.0°C	20%	1.13 bar
	8.2	12 bar	17.0°C	0.81-0.90 bar	150.0°C	20%	1.13 bar
	8.3	0.67 m/s	17.0°C	10 g/s, 8 g/s	150.0°C	20%, 0%	1.13 bar
Calibration of models	9.1–9.2	0.69 m/s	34.4°C	10.2 g/s	119.4°C	20%	1.01 bar
Performance analysis and verification	10.1–10.2 (OP1–OP3)	0.69 m/s	34.4°C	10.2 g/s	119.4°C	20%	1.01 bar
		0.69 m/s	35.49°C	10.2 g/s	108.29 °C	39%	1.01 bar
		0.68 m/s	36.61°C	8.8 g/s	112.8	21%	1.01 bar
Analysis of geometrical design	11.1–11.5	0.69 m/s	34.4°C	10.2 g/s	119.4°C	20%	1.01 bar
Results for the final geometry	12	16 bar	30.0°C	9.88	102.0°C	20%	1.01 bar

7.4. Fluid properties

The fluid properties of steam and CO_2 were assumed to be temperature-dependent at a constant pressure of 1 bar. The properties of steam were derived from the IAPWS-97 formulation [122], while those of CO_2 were based on NIST data [123]. The properties were implemented using the tabulated data, with the linear-piecewise interpolation method applied between the data points. Figure 7.13 and Figure 7.14 present the temperature-dependent density and thermal conductivity of steam and CO_2, whereas isobaric heat capacity and dynamic viscosity are shown in Figure 7.15 and Figure 7.16.

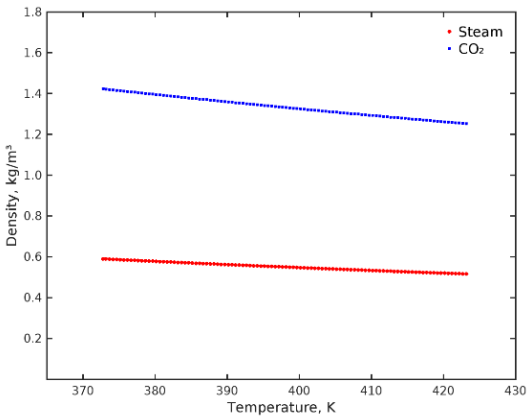

Figure 7.13. Density of steam and CO_2 as a function of temperature at 1 bar pressure.

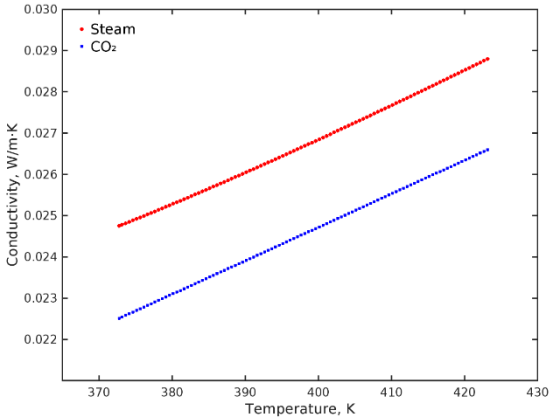

Figure 7.14. Thermal conductivity of steam and CO_2 as a function of temperature at 1 bar pressure

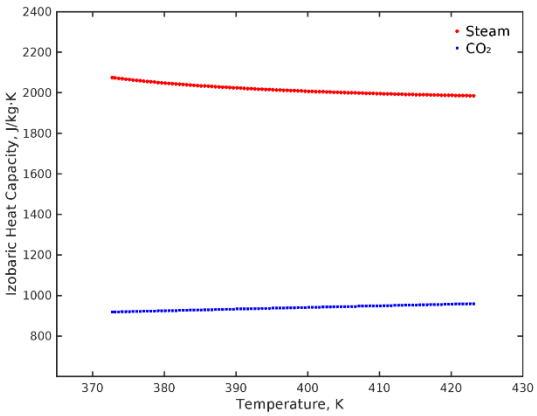

Figure 7.15. Izobaric heat capacity of steam and CO_2 as a function of temperature at 1 bar pressure.

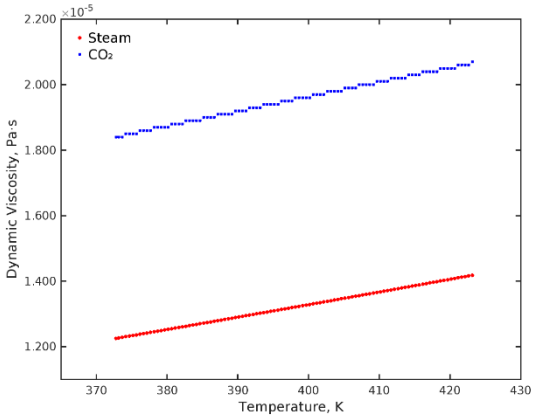

Figure 7.16. Dynamic viscosity of steam and CO_2 as a function of temperature at 1 bar pressure

7.5. Models and submodels applied in the analysis

This section focuses on the specific settings and implementations of the selected models and sub-models used in the numerical analysis. Each model's configuration has been tailored to address the complexity of the studied processes to ensure accurate and computationally efficient simulations.

7.5.1. Multiphase model

The Mixture Multiphase Model (MMP) was applied to calculate the multiphase flow involving three phases: water, steam, and CO_2. Fluid mixture properties such as density, viscosity, and thermal conductivity were determined using volume-averaging, while the specific heat capacity, enthalpy, and velocity were computed using mass-averaging (as presented in Section 5.1, page 32). The mixture's turbulent Prandtl and Schmidt numbers were assumed to be 0.9.

A homogeneous velocity (no-slip) approach was assumed, meaning that all phases share the same velocity field. The gas phase was considered continuous, while the liquid water was treated as dispersed. For the interfacial heat fluxes (Equation (5.38) and Equation (5.39), page 38), the interaction area density between steam (continuous phase) and water (dispersed phase) was calculated using a symmetric model, which works well for high particle loading conditions (Equation (7.1)).

$$a_{sw} = \frac{6\alpha_s \alpha_w}{l_{sw}} \tag{7.1}$$

The interaction length scale for the steam–water interactions $l_{s\,w}$, was assumed to be equal to the droplet diameter, and a constant value was applied. The range of the investigated values was estimated based on the outer diameter of the motive nozzle, fluid properties, and inlet pressure conditions, using the relations and data presented in [124–126]. The adopted values are summarised in Table 7.4.

Table 7.4. Assumed droplet diameters applied in the CFD analysis of the spray-ejector condenser.

Analysis	Section no.	Droplet diameter, mm
Boundary conditions	8.1–8.3	1.0
Calibration of models	9.1–9.2	0.4, 0.6, 0.8, 1.0, 1.5, 2.5
Performance analysis and verification	10.1–10.2	0.6
Analysis of geometrical design	11.1–11.5	0.6
Results for the final geometry	12	0.6

7.5.2. Turbulence model

Several turbulence models were investigated in terms of reliability and their influence on the ejector performance: *k-ω*, *k-ω* SST, RSM, and Realizable *k-ε*. Based on the literature review and modeling results, the Realizable k-*ε* model with the two-layer approach was selected for the final simulations due to its robustness, consistent predictive behavior, and numerical stability, as discussed in Section 9.2.2. The Shear Driven (Wolfstein) model [127] was used for the length scale function in the two-layer formulation. Wall treatment was set to all y^+, allowing the solver to automatically apply wall functions or near-wall resolution depending on local y^+ values. The turbulence model constants were used according to the default settings for the model, as summarized in Table 7.5.

Table 7.5. Coefficients applied in the Realizable *k-ε* model with the two-layer approach.

Coefficient	Value
C_μ	0.09
$C_{\varepsilon 1}$	1.44
$C_{\varepsilon 2}$	1.9
σ_k	1.0
σ_ε	1.2

7.5.3. Phase change model

The thermally driven Boiling/Condensation was employed to simulate direct contact condensation of steam in the presence of non-condensable gas (CO_2). The heat transfer coefficient, calculated separately on the steam and water side (Equation (5.40) and Equation (5.41) on page 39), is determined primarily by the Nusselt number. The Nusselt number values used in the CFD analysis of the spray-ejector condenser are summarized in Table 7.6. The effect of the assumed values on both the steam and water sides on the simulation results is discussed in Section 9.2.2. Finally, the Ranz–Marshall correlation extended with the Armenante–Kirwan approach $\mathrm{Nu}(\mathrm{Re}_t)$, was applied on the steam side to account for the effect of turbulent heat transfer, while a constant value of 2 was used on the water side representing pure conductive heat transfer.

Table 7.6. Nusselt number values applied in the CFD analysis of the spray-ejector condenser.

Analysis	Section no.	Nusselt number	
		Steam side	Water side
Boundary conditions	8.1–8.3	2	2
Calibration of models	9.1–9.2	Nu (Re_t), 2, 4, 8, 16, 32, 64	2, 4, 8, 16, 32, 64
Performance analysis and verification	10.1–10.2	Nu (Re_t)	2
Analysis of geometrical design	11.1–11.5	Nu (Re_t)	2
Results for the final geometry	12	Nu (Re_t)	2

The Ranz–Marshall correlation for the Nusselt number assumes that the relative velocity governs heat transfer between a particle and the surrounding fluid (Equation (5.42), page 39). Armenante and Kirwan [128] proposed a modified correlation for water droplets, suggesting that for small particles the relative velocity is negligible and the heat transfer occurs mainly due to turbulence. Equation (7.2) presents the modified Ranz-Marshall correlation based on the Armenante-Kirwan approach, which uses the turbulent Reynolds number Re_t and Prandtl number of continuous phase Pr_s (steam).

$$\mathrm{Nu} = 2 + 0.6\,\mathrm{Re}_t^{0.5}\,\mathrm{Pr}_s^{0.33} \tag{7.2}$$

The turbulent Reynolds number is calculated based on the turbulent dissipation rate ε, the average droplet diameter d_p and the kinematic viscosity of the steam ν_s, according to Equation (7.3).

$$\mathrm{Re}_t = \frac{\varepsilon^{1/3} \cdot d_p^{4/3}}{\upsilon_s} \tag{7.3}$$

The Prandtl number is determined based on the thermophysical properties of steam, as presented in Equation (7.4).

$$\mathrm{Pr}_s = \frac{\mu_s \cdot C_{p\,s}}{\lambda_s} \tag{7.4}$$

To account for the inert gas (CO_2) effect on the heat transfer coefficient, the correlation proposed by Borishanskiy et al. [129] was adopted. The presence of CO_2 reduces the local heat transfer coefficient h_{CO_2} compared to the reference value without non-condensable gases h. The reduction is expressed as a function of the CO_2 volume fraction α_{CO_2}, according to Equation (7.5).

$$\frac{h_{CO_2}}{h} = 1 - 0.25 \cdot \alpha_{CO_2}{}^{0.7} \tag{7.5}$$

The influence of CO_2 was also incorporated by adjusting the saturation temperature based on the partial pressure of steam p_s, as presented in Equation (7.6).

$$p_s = p \cdot \alpha_s \tag{7.6}$$

7.6. Numerical solution

A steady-state formulation was used for all simulations. For pressure–velocity coupling, the segregated solver was applied due to its suitability for constant-density and low-compressible flows, combined with favorable computational efficiency. The solution update was controlled using the SIMPLE algorithm, selected for its compatibility with the employed multiphase model. A multigrid strategy was employed with an Algebraic Multigrid (AMG) solver, using the Gauss–Seidel relaxation scheme. Switching between grid levels was performed using a V-cycle approach.

The order of discretization for convection schemes used in the applied solvers in the conducted analysis is presented in Table 7.6. Generally, a second-order scheme was used as the default. However, due to the investigation of applying Hybrid MUSCL Third-Order/Central Differencing (CD) for flow and energy solvers, as discussed in Section 9.2.3, a third-order scheme was applied for the energy solver. The relaxation factors used in the analysis are listed in Table 7.8.

Table 7.7. Discretization order of convection terms used in the simulations.

Solver	Convection discretization scheme	Section no.
Flow	2nd order	8.1–8.3, 9.1–9.2, 10.1–10.2, 11.1–11.5, 12
	3rd order	9.2.3
Turbulence	2nd order	all
Multiphase	2nd order	all
Energy	2nd order	8.1–8.3, 9.1–9.2,
	3rd order	9.1–9.2, 10.1–10.2, 11.1–11.5, 12

Table 7.8. Relaxation factors used in the simulations.

Relaxation factor	Value
Velocity	0.7
Pressure	0.3
k-ε Turbulence	0.9
k-ε Turbulent viscosity	1.0
Volume fraction	0.9
Energy	0.9

8. The influence of boundary conditions on model reliability and ejector operation

Correctly specified values at the boundary surfaces are essential for developing a reliable CFD model. The assumed types of boundary conditions significantly affect the numerical solution's stability and the accuracy of the obtained results. This section considers different combinations of pressure and velocity boundary conditions. In numerical investigations of two-phase ejectors, pressure specification at the boundaries is more commonly used, as it allows the calculation of velocities and mass flow rates. However, from the perspective of this study, the key parameter is the resulting pressure for a given mass flow rate (or velocity), which corresponds to the operating point of the gas power plant. Additionally, the influence of the assumed suction pressure and the CO_2 content in the exhaust gas on the ejector thermal–flow performance was investigated.

An initial mesh independence study was performed to select a mesh suitable for the investigation. The cross-sectional averaged temperature along the flow path for the considered meshes Mesh M1–M3 (respectively with 14938, 28299, and 60787 elements) is presented in Figure 8.1. Notable differences between temperature distributions are observed in the suction chamber and at the entrance of the mixing chamber. Further downstream, the discrepancies diminish, and the outlet temperature remains nearly unchanged for all cases. Based on the observations, Mesh M2 was found to be sufficient for investigating the impact of boundary conditions on the ejector operation.

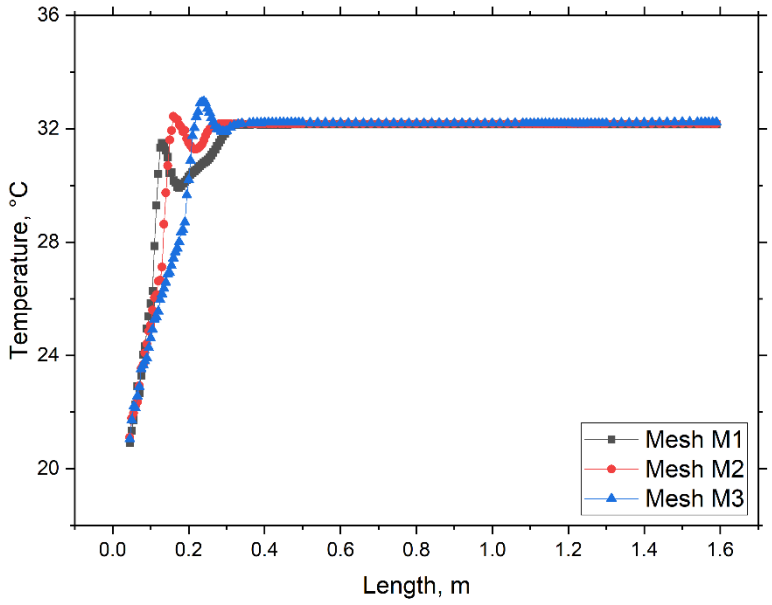

Figure 8.1. Cross-sectional averaged temperature along the flow path for initial meshes (M1–M3).

8.1. Suction pressure

This section discusses the influence of suction pressure on ejector performance. Table 8.1 presents the assumptions and results for calculating of the basic operating point. The assumed motive pressure at the water inlet was 12 bar, and the pressure at the gas inlet was set to 0.9 bar. Under these conditions, 25 g/s of exhaust gases are entrained, and the steam present in the exhaust gas mixture is fully condensed.

The effect of suction pressure on the entrained gas mass flow rate and the mass-averaged outlet temperature is presented in Figure 8.2. Higher suction pressure results in a greater entrained exhaust gas mass flow and a higher outlet temperature. An exhaust gas mass flow rate of 10 g/s is obtained at a suction pressure of 0.81 bar. The outlet temperature ranges from 33 °C to 54 °C, depending on the suction pressure and, consequently, on the amount of entrained gas.

Table 8.1. Results for basic operation mode (0.9 bar at the exhaust gas inlet, bolded – calculated values).

Quantities	Water Inlet	Exhaust inlet	Outlet
Pressure, bar	12.0	0.9	1.1
Velocity, m/s	**0.65**	**12.04**	**0.60**
Temperature, °C	17.0	150.0	**54.0**
Steam mass flow, g/s	**0.0**	**25.0**	**0.0**

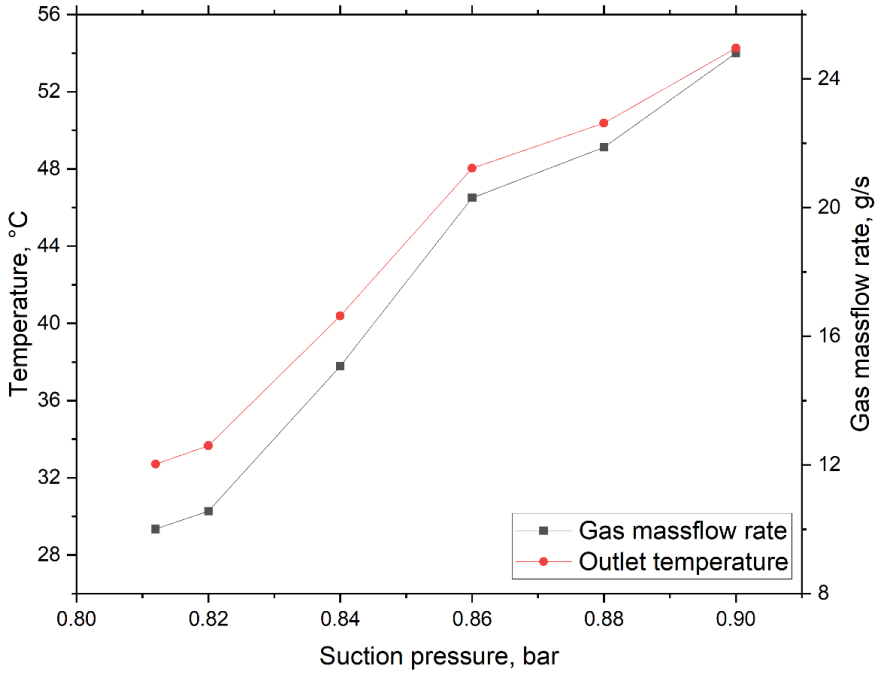

Figure 8.2. Effect of suction pressure on the entrained gas mass flow rate and mass-averaged outlet temperature.

Suction pressure significantly affects not only the boundary values but also flow characteristics along the flow path. The cross-sectional averaged pressure profiles along

the flow path for different suction pressures are presented in Figure 8.3. Although the pressure increases along the flow direction in all cases, the rate of this increase varies. For higher suction pressure, the pressure rise is smoother and more gradual, whereas for lower suction pressure, it becomes steeper and starts earlier.

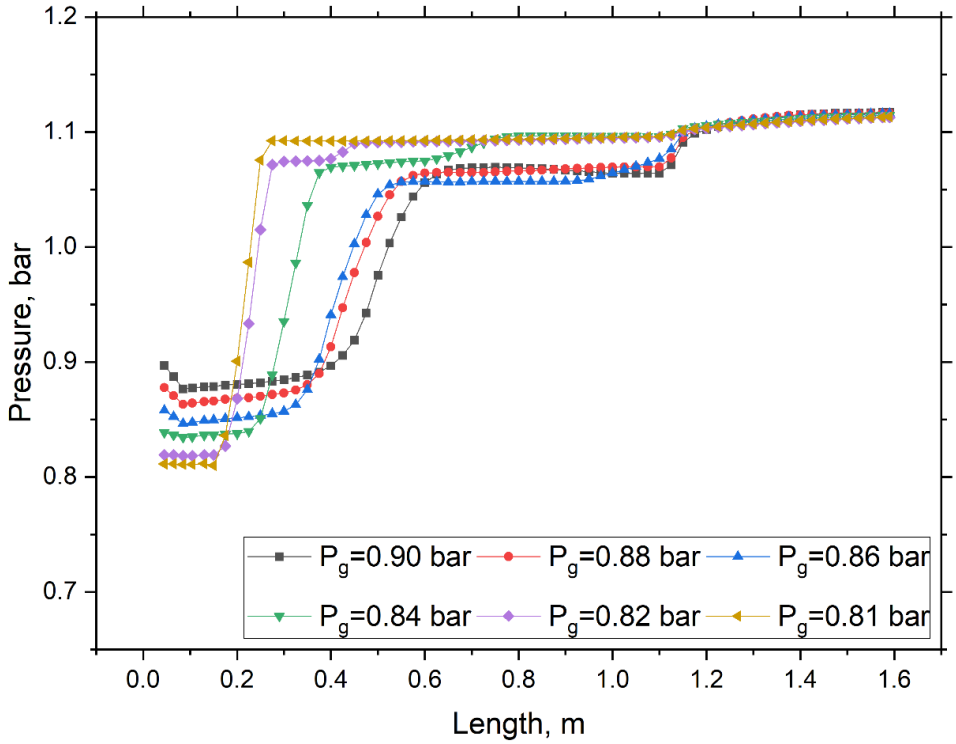

Figure 8.3. The influence of suction pressure on the cross-sectional averaged pressure along the flow path.

Considering the cross-sectional averaged velocity profiles along the flow path for different suction pressures (Figure 8.4), it can be observed that higher suction pressure results in significantly higher peak mixture velocities, which occur at the entrance of the mixing chamber. This effect is caused by the increased volumetric flow rate of the entrained exhaust gases. In all considered cases, the outlet mixture velocity remains low, ranging from approximately 0.2 to 0.5 m/s, which indicates a minimal gas volume fraction at the ejector outlet.

The effect of suction pressure on the thermal performance of the ejector is illustrated by the cross-sectional mass-averaged temperature and cross-sectional averaged steam mass flow along the flow direction, presented in Figure 8.4 and Figure 8.5, respectively. The mixture temperature throughout the domain generally increases with higher gas inlet

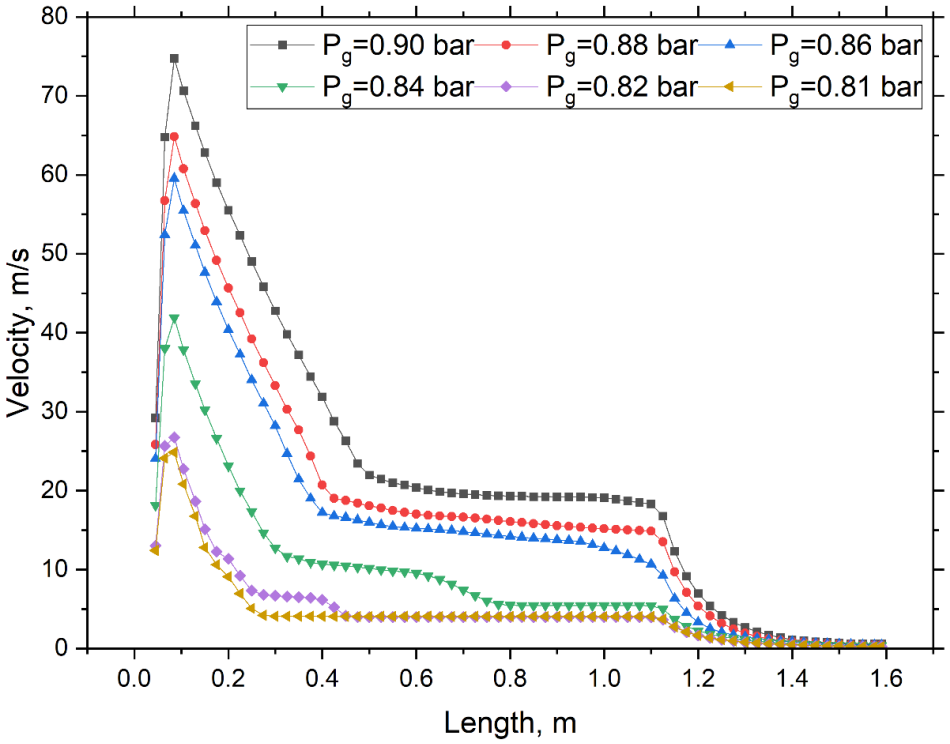

Figure 8.4. The influence of suction pressure on the cross-sectional averaged velocity along the flow path.

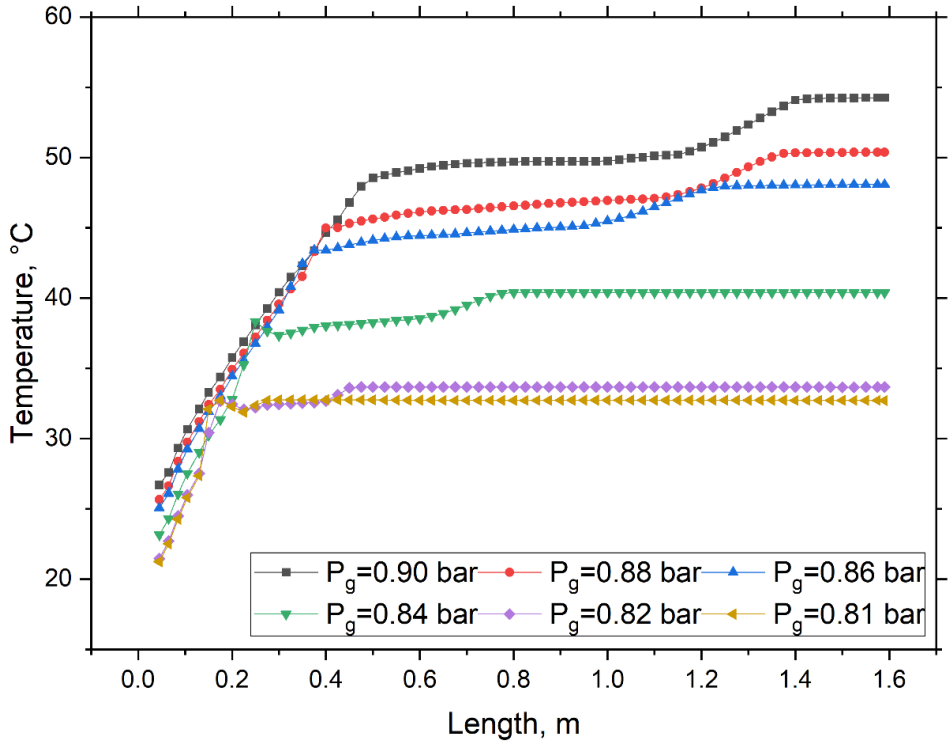

Figure 8.5. The influence of suction pressure on the cross-sectional mass-averaged temperature along the flow path.

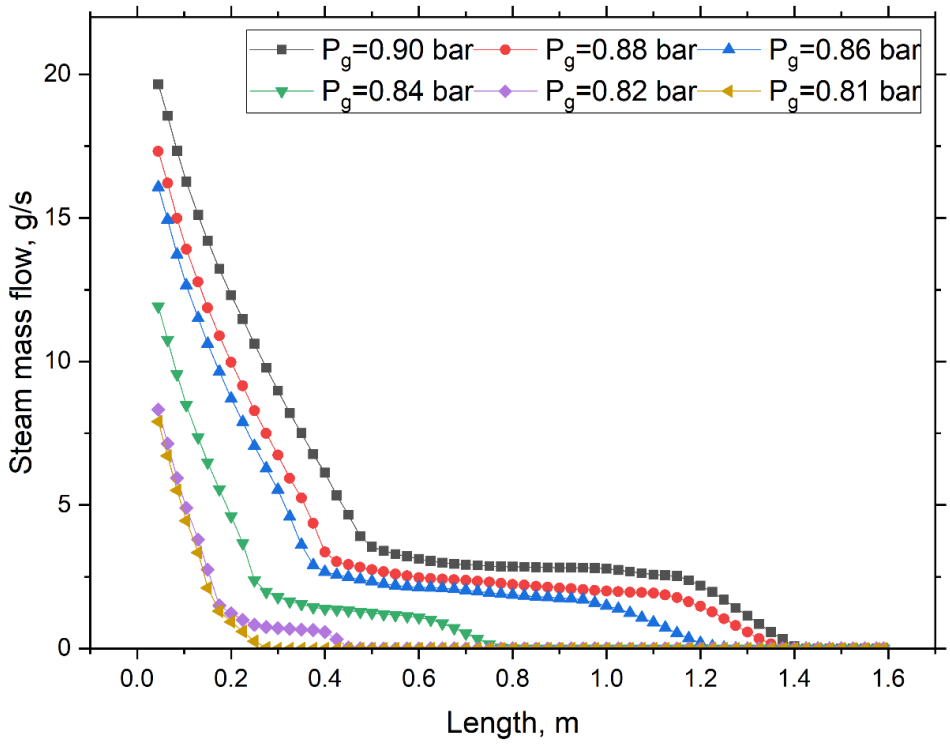

Figure 8.6. The influence of suction pressure on the cross-sectional averaged steam mass flow along the flow path.

pressure. Significant differences in outlet temperature are associated with the heat released due to condensation. The steam mass flow rate chart confirms that steam is fully condensed in all cases, with a greater total amount of condensed steam observed at higher suction pressures. However, condensation occurs more rapidly along the flow path at lower suction pressures, resulting in a faster temperature equalization.

The velocity distribution in the ejector for different gas inlet pressures is presented in Figure 8.7. Significant radial velocity gradients occur at the entrance of the mixing chamber, particularly at higher suction pressures. The highest velocity values are observed for the gas inlet pressure of 0.9 bar. The velocity distribution becomes more homogeneous as the flow develops along the ejector. Figure A. 1, included in Appendix A, illustrates the pressure distribution for the analyzed suction pressures.

Temperature variations in the radial direction are also evident in the scalar field for different gas inlet pressures, as presented in Figure 8.8. At a suction pressure of 0.90 bar, radial temperature gradients persist over half the mixing chamber length. In contrast, at 0.81 bar, a nearly uniform temperature field forms immediately after the streams meet.

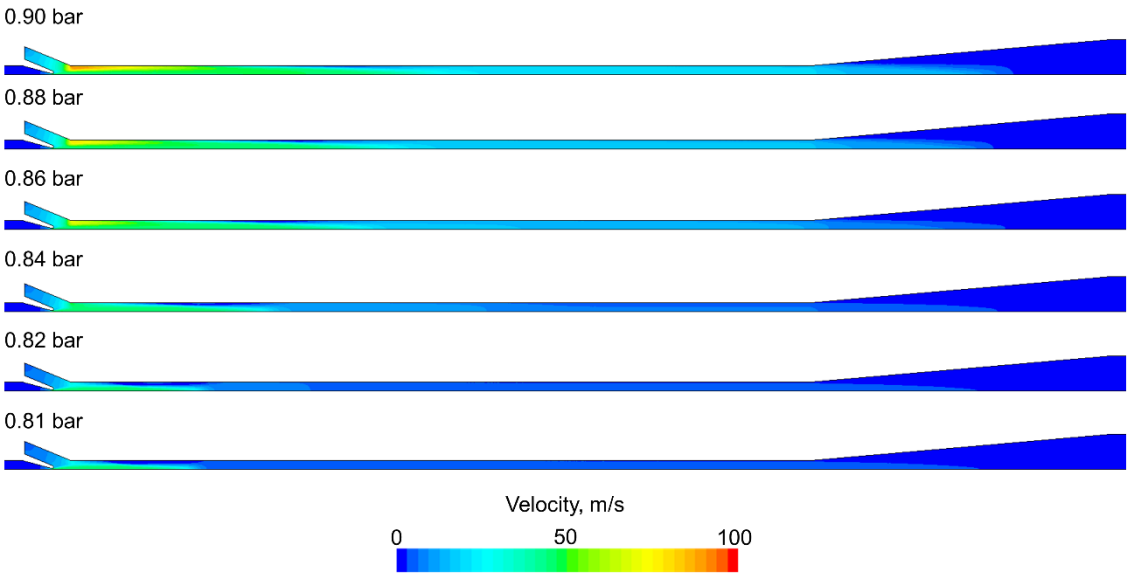

Figure 8.7. The influence of suction pressure on the velocity distribution in the spray-ejector condenser.

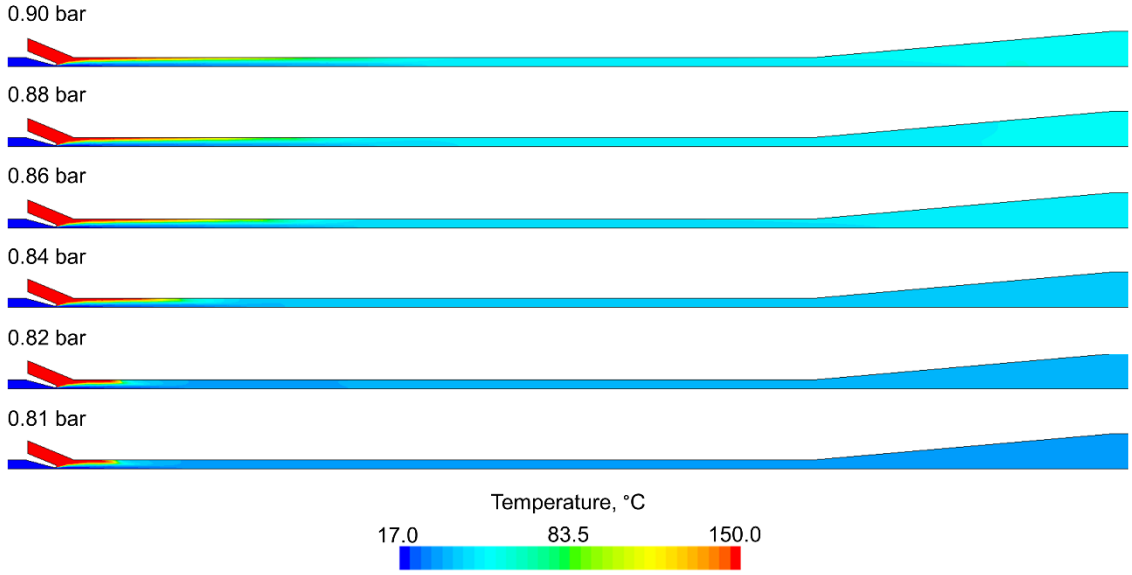

Figure 8.8. The influence of suction pressure on the temperature distribution in the spray-ejector condenser.

The impact of the suction pressure on the scalar fields of water and CO_2 volume fractions is presented in Figure 8.9 and Figure 8.10. The water jet region can be identified in all cases by higher volume fraction values along the axis, particularly at the entrance to the mixing chamber. The water volume fraction at the outlet varies between 0.1 and 0.3, depending on the suction pressure. This is related to the presence of CO_2, as higher suction pressure results in greater entrainment of the non-condensable gas. The CO_2 volume fraction varies significantly in both axial and radial directions. Lower suction pressure leads to a more rapid increase in CO_2 concentration due to more intensive

condensation. The highest CO_2 concentration, approximately 0.7–0.8, occurs in the diffuser region.

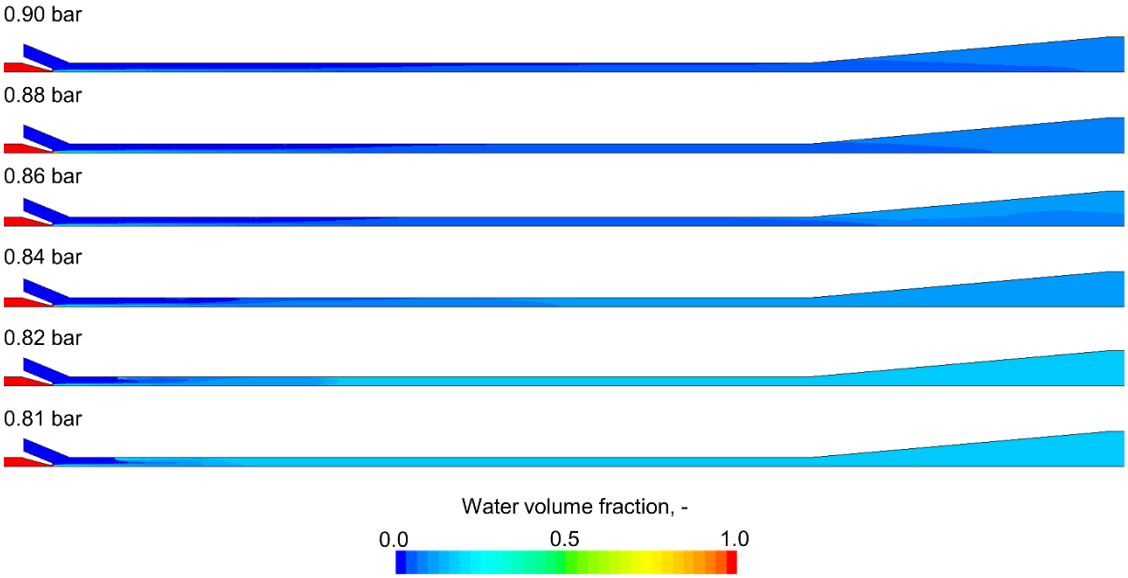

Figure 8.9. The influence of suction pressure on the water volume fraction distribution in spray-ejector condenser.

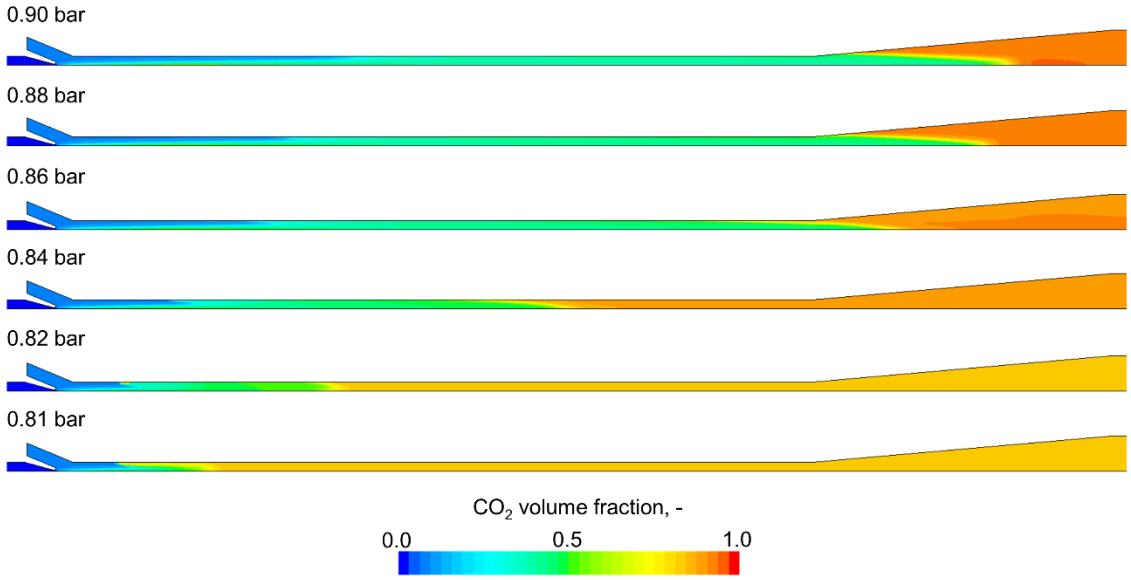

Figure 8.10. The influence of suction pressure on the CO_2 volume fraction distribution in the spray-ejector condenser.

8.2. Boundary conditions type

A pressure boundary condition was applied at the outlet to represent the atmospheric pressure. Four different combinations of inlet boundary conditions were considered in the analysis to evaluate their impact on ejector operation:

- velocity specified at both the gas and water inlets (Velocity Inlets),
- pressure specified at both inlets (Pressure Inlets),
- velocity specified at the water inlet and pressure specified at the gas inlet (Gas Pressure Inlet, Water Velocity Inlet),
- velocity specified at the gas inlet and pressure specified at the water inlet (Gas Velocity Inlet, Water Pressure Inlet).

The impact of the applied boundary conditions type on the cross-sectional averaged pressure along the flow path is presented in Figure 8.11. The Pressure profiles differ significantly between the considered cases. When the velocity is specified at the gas inlet, a rapid pressure increase is observed at the beginning of the mixing chamber. The lowest suction pressure is obtained when velocity boundary conditions are applied at both inlets.

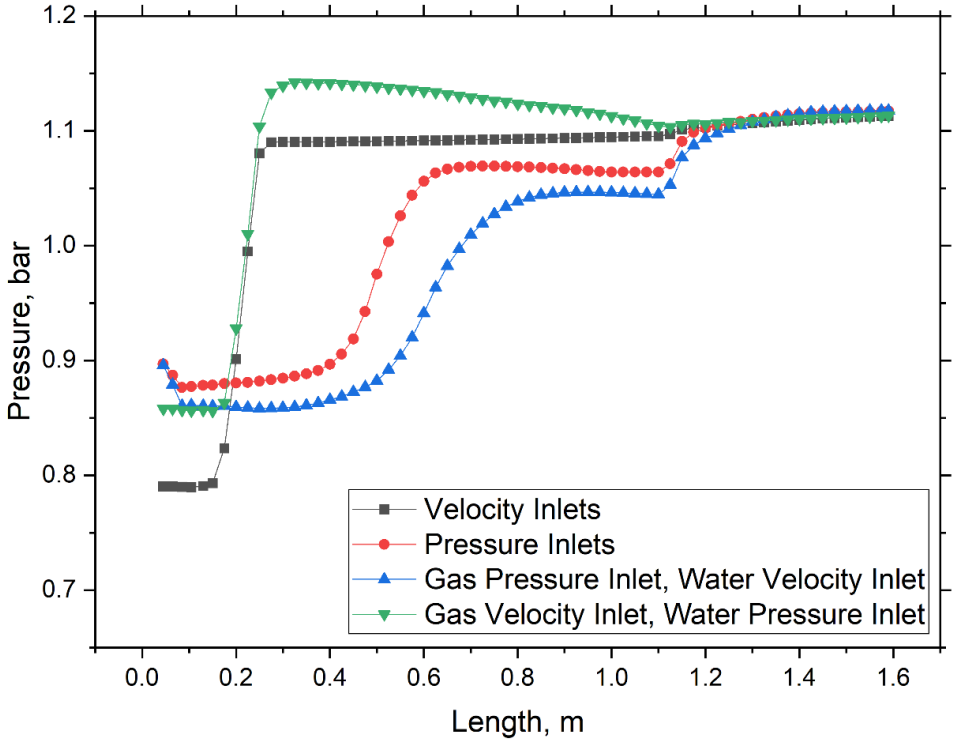

Figure 8.11. The influence of assumed boundary condition type on the cross-sectional averaged pressure along the flow path.

Distinct differences are observed in the cross-sectional velocity pressure along the flow path, as shown in Figure 8.12. The average velocity at the beginning of the mixing chamber is several times higher when either pressure or velocity boundary conditions are

applied at both inlets, indicating substantially higher volume flow rates of both liquid and gas. Furthermore, when the velocity is specified at the gas inlet, the type of boundary conditions applied to the water inlet has little influence on the pressure distribution.

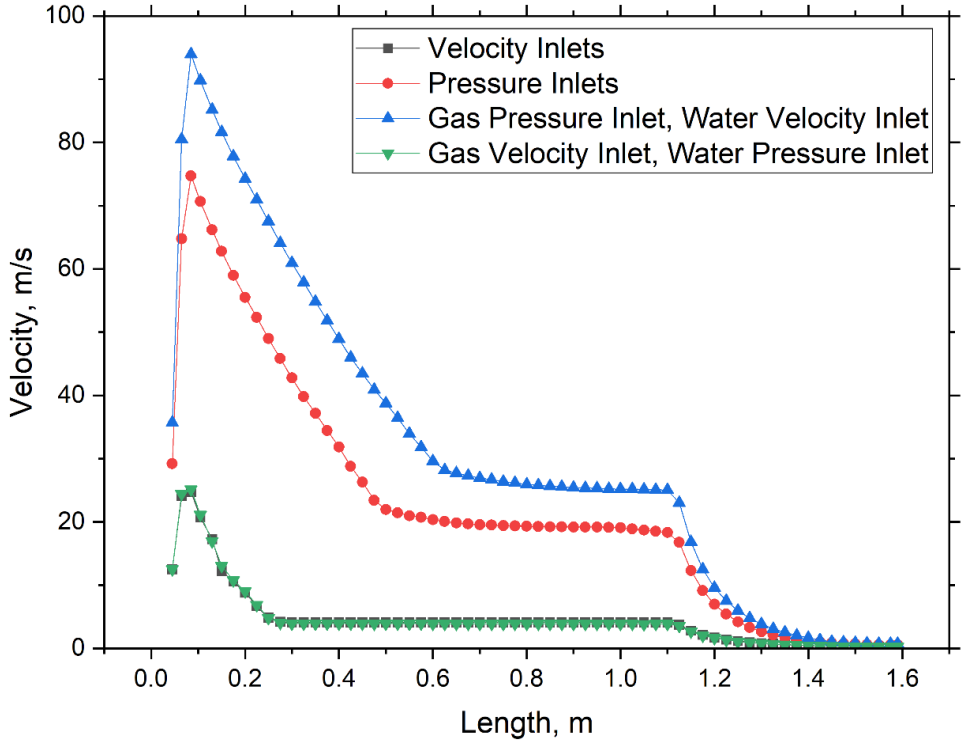

Figure 8.12. The influence of assumed boundary condition type on the cross-sectional averaged velocity along the flow path

The cross-sectional mass-averaged temperature and the cross-sectional averaged steam mass flow along the flow path for different types of applied boundary conditions are presented in Figure 8.13 and Figure 8.14. In cases where velocity is specified at the gas inlet, the profiles remain nearly identical, and steam is condensed rapidly, as indicated by both steam mass flow and temperature distributions. When pressure is applied at the gas inlet, significantly higher entrained steam mass flow rates are observed. In this case, the steam is fully condensed in the diffuser.

To sum up, the boundary condition applied at the gas inlet has the most significant impact on the thermal–flow performance of the ejector. Applying velocity boundary conditions at the gas inlet gives more reasonable and physically consistent results, better reflecting the expected behavior resulting from the operation of a negative-pressure gas power plant. Moreover, specifying the velocity at the gas inlet improves the numerical stability and robustness of the model. Therefore, this approach is recommended for further investigation.

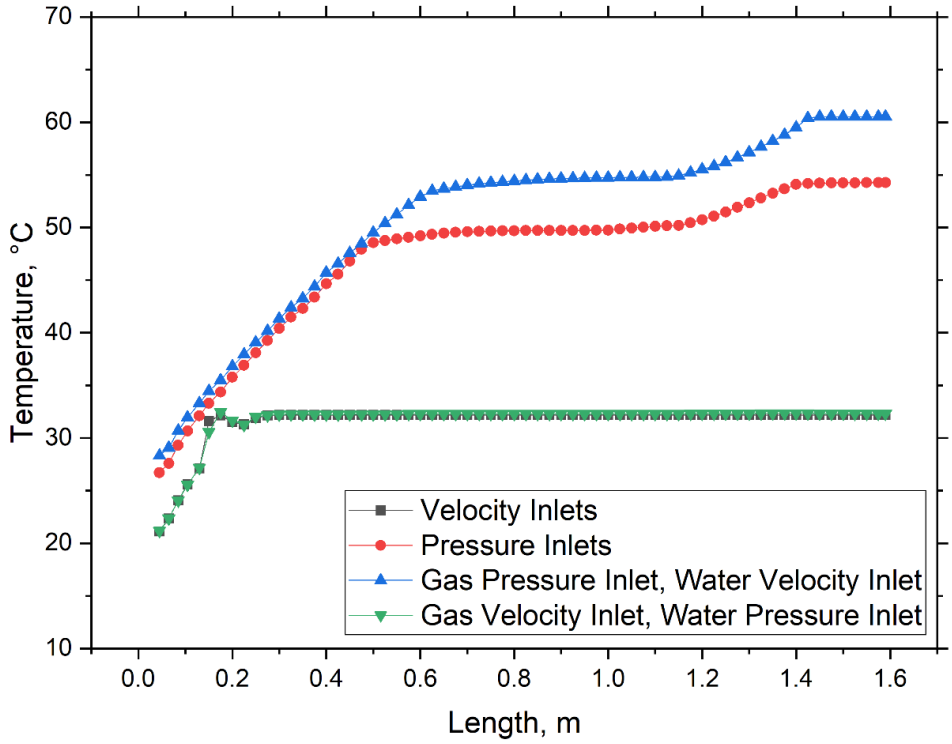

Figure 8.13. The influence of assumed boundary condition type on the cross-sectional mass-averaged temperature along the flow path.

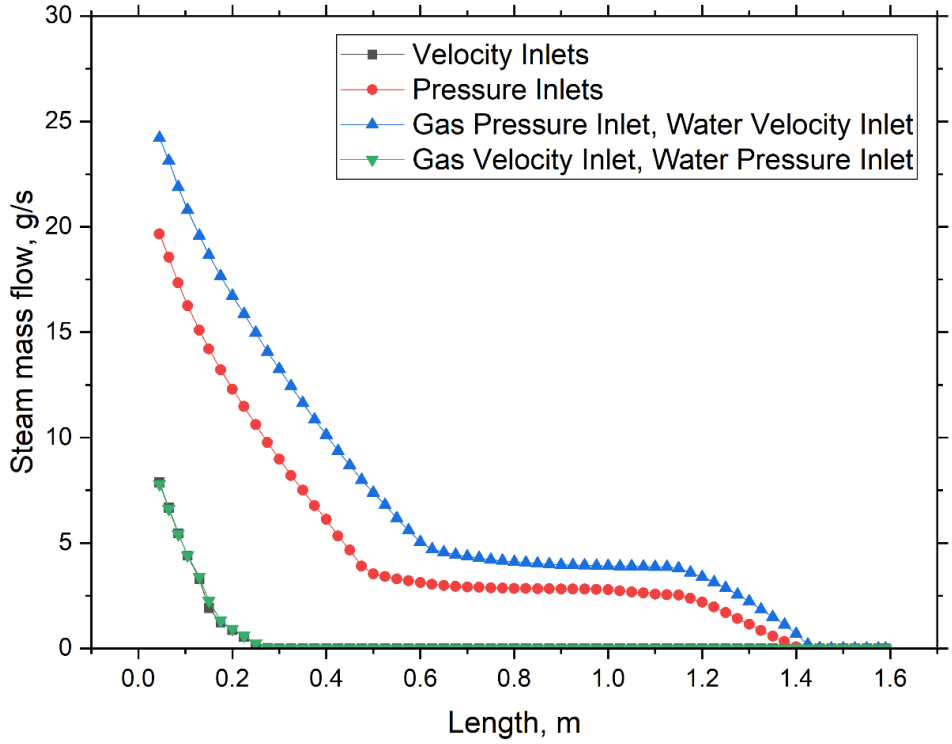

Figure 8.14. The influence of assumed boundary condition type on the cross-sectional averaged steam mass flow along the flow path.

8.3. CO_2 presence

The presence of CO_2 in the exhaust gas stream is expected to significantly affect flow phenomena and overall ejector performance. To compare the resulting flow characteristics and scalar fields, the case with CO_2 in the exhaust gas was analyzed alongside two reference cases with pure steam. In the first reference case, the steam mass flow was equal to the total mass flow rate of exhaust gas (steam + CO_2), whereas in the second, it corresponded to the steam flow rate from the CO_2-containing case.

The influence of CO_2 presence on the cross-sectional averaged pressure along the flow path is presented in Figure 8.15. In the pure steam cases, the pressure in the suction chamber exceeds 0.5 bar, whereas for the CO_2–steam mixture, it reaches nearly 0.8 bar. The pressure increases rapidly at the beginning, followed by an approximately linear rise toward the outlet. The pressure curves corresponding to the pure steam cases are nearly

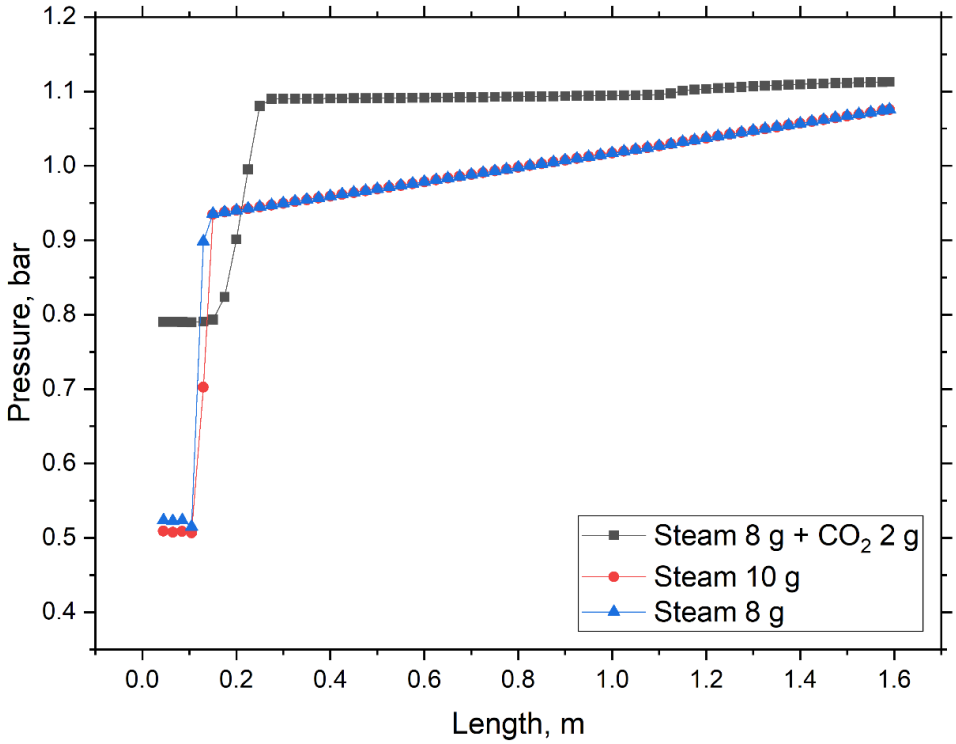

Figure 8.15. The influence of CO_2 presence on the cross-sectional averaged pressure along the flow path.

identical. The cross-sectional averaged velocity along the flow path for different configurations of the exhaust gas mass flow rate is presented in Figure 8.16. At the beginning of the mixing chamber, the highest mixture velocity (approximately 25 m/s) is observed for case with CO_2 and 10 g/s of steam, due to the higher volumetric flow rate of the exhaust gas. The difference between the cases with and without CO_2 is most

pronounced in the mixing chamber and diffuser, where significantly higher mixture velocity occurs in the CO_2 case (around 5 m/s compared to 0.3 m/s in the other cases).

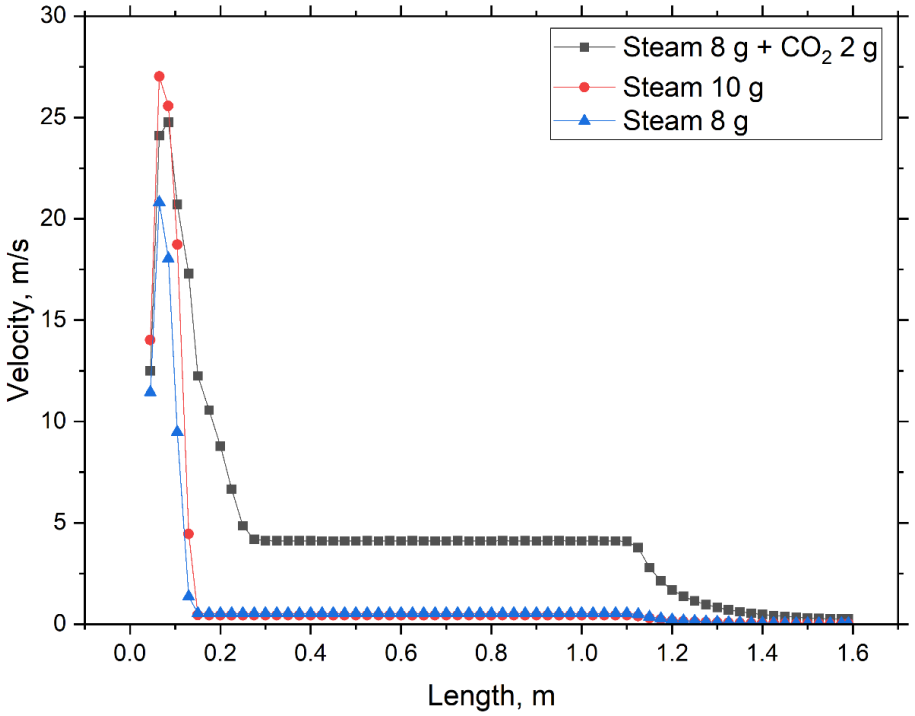

Figure 8.16. The influence of CO_2 presence on the cross-sectional velocity along the flow path.

The condensation process can be analyzed using the cross-sectional averaged steam mass flow along the flow path for considered exhaust gas compositions, as shown in Figure 8.17. Under the given operating conditions, the steam mass flow decreases rapidly

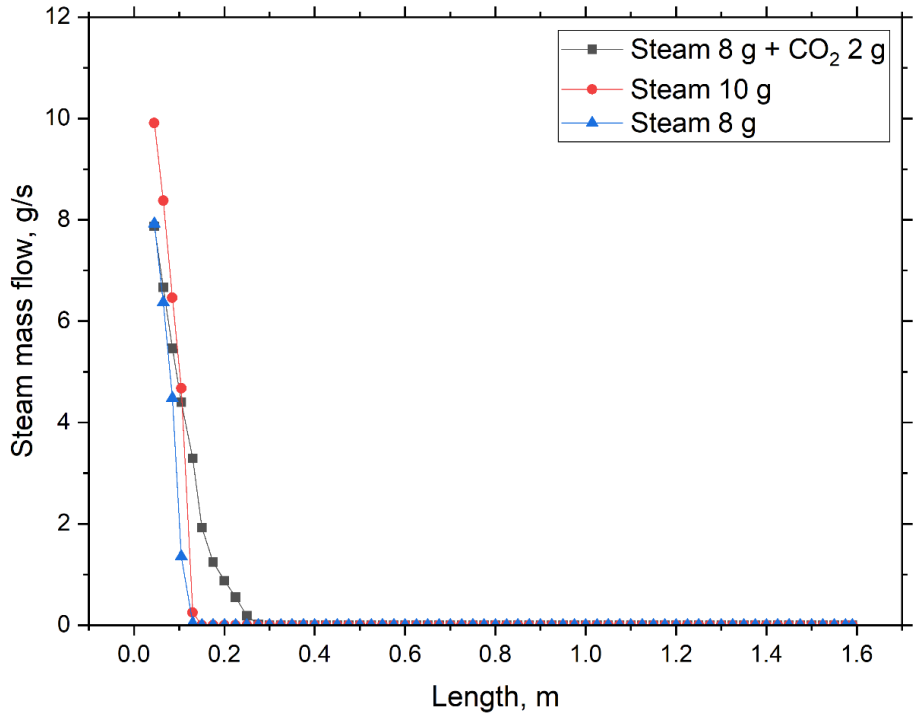

Figure 8.17. The influence of CO_2 presence on the cross-sectional averaged steam mass flow along the flow path.

at the initial section of the ejector, indicating high condensation intensity in all analyzed cases. The presence of CO_2 affects the condensation process, resulting in a slight delay in the location where condensation begins, compared to the pure steam cases.

The impact of the CO_2 presence on the temperature scalar field is presented in Figure 8.18. The entire domain exhibits a uniform temperature distribution, except for the suction chamber and the beginning of the mixing chamber. The average temperature of exhaust gas with CO_2 after mixing is lower than in the pure cases.

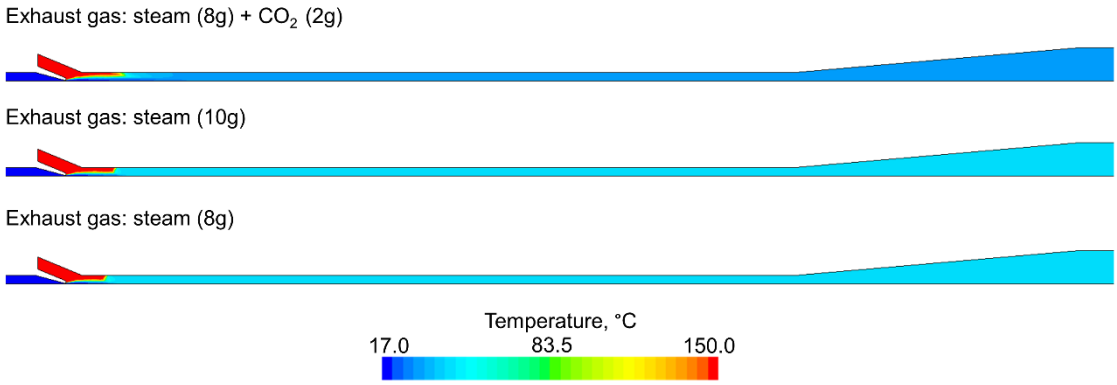

Figure 8.18. The influence of CO_2 presence on the temperature distribution in the spray-ejector condenser.

Figure 8.19 presents the influence of CO_2 presence on the water volume fraction distribution in the spray-ejector condenser. A volume fraction equal to 1.0 is observed in the mixing chamber and diffuser in the pure steam cases, indicating that no steam remains. In the case of steam–CO_2 mixture, the same region corresponds to a water volume fraction of approximately 0.2. Given that steam is fully condensed in all cases, these differences can be explained by Figure 8.20, which shows the CO_2 volume fraction field for the analyzed exhaust gas compositions. In the case with CO_2, the volume fraction reaches approximately 0.8, while in the pure steam cases it is, naturally, zero. The transition from the initial to the final CO_2 concentration occurs over a very short distance, similar to other scalar field distributions. Pressure and velocity distributions for different exhaust gas compositions are included in the Appendix (Figure A. 2 and Figure A. 3, respectively).

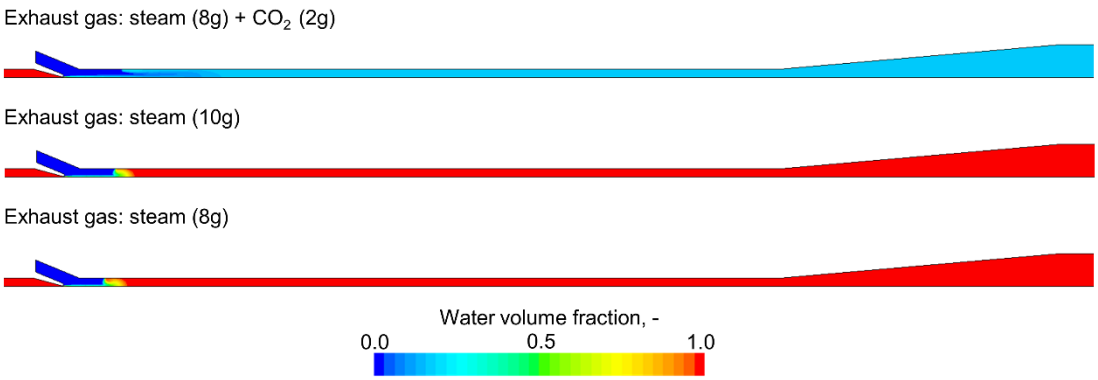

Figure 8.19. The influence of CO_2 presence on the water volume fraction distribution in spray-ejector condenser.

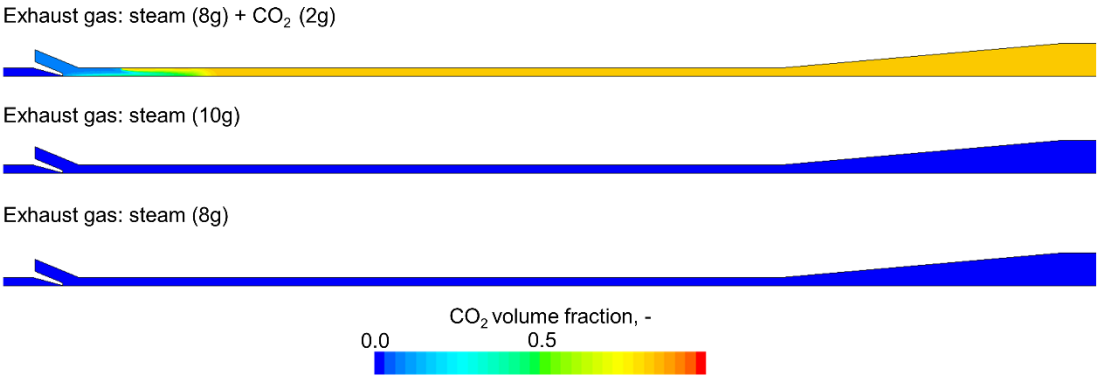

Figure 8.20. The influence of CO_2 presence on the CO_2 volume fraction distribution in spray-ejector condenser.

9. Calibration of selected model and sub-model properties and analysis of their impact on thermal-flow characteristics

Developing a reliable CFD model requires defining and selecting multiple models and parameters, especially when the underlying physical phenomena are complex. While some parameters marginally influence the solution, others strongly affect the thermal-flow behavior. This chapter discusses and analyses selected parameters that demonstrated a significant or interesting influence on the simulation results. The detailed mesh independence study was conducted based on flow quantities curves and non-dimensional parameters to establish a consistent foundation for model calibration.

9.1. Mesh independence study

The influence of the mesh refinement on the ejector operation was investigated based on the non-dimensional ejector performance indicators and pressure, velocity, and temperature profiles. Meshes M1–M5 with the following number of elements were considered: 60787, 174895, 387221, 820643, and 1302936. Table 7.2 (page 52) presents more detailed mesh properties.

Non-dimensional parameter values and outlet temperature as a function of mesh refinement are presented in Figure 9.1. The corresponding percentage changes with respect to element count are shown in Table 9.1. The compression and expansion ratios decrease as the mesh is refined. The mass entrainment ratio remains relatively stable, as velocity was specified at the inlets, and the observed variation is primarily due to numerical effects. Outlet temperature increases slightly and then reaches a stable value. The most considerable compression and expansion ratio variation is observed for meshes M1–M3, particularly between M2 and M3, where changes range from 10–12%. For finer meshes, the values stabilize, and the variation in parameter values drops to below 1%.

Table 9.1. Mesh independence test: Change in parameters due to mesh refinement (meshes M1–M5).

Mesh no.	Number of elements	Element ratio	Change of parameters			
			Mass entrainment ratio *ER*	Compression ratio *CR*	Expansion ratio ξ	Outlet temperature
M1	**60787**	-	-	-	-	-
M2	**172485**	2.84	1.8	4.2	3.4	0.1
M3	**387337**	2.25	0.0	11.7	10.2	0.8
M4	**820640**	2.12	0.0	0.1	0.3	0.0
M5	**1302918**	1.59	0.0	0.8	0.4	0.1

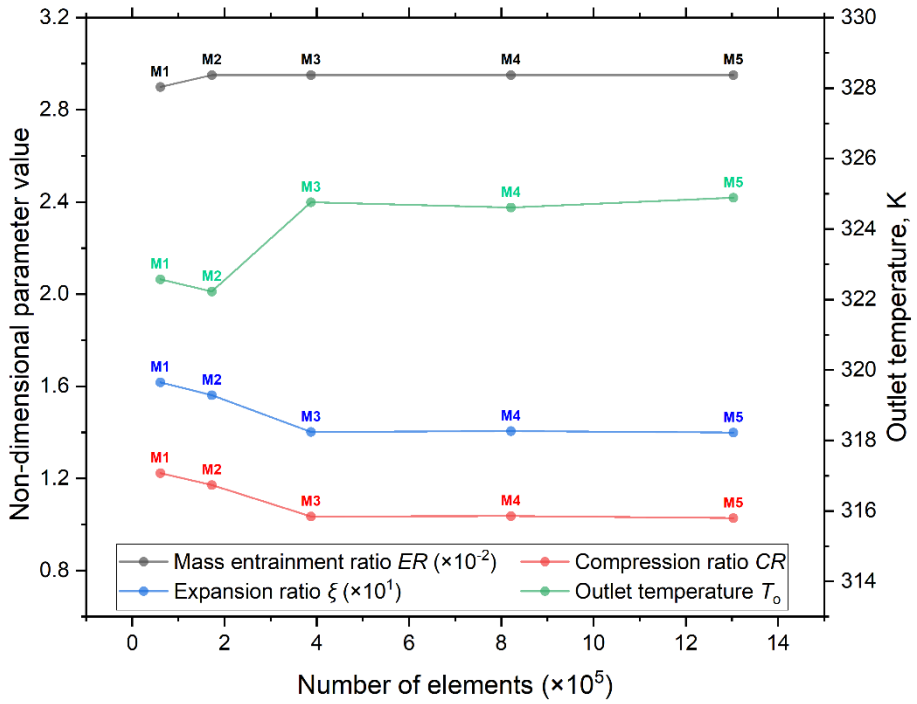

Figure 9.1. Mesh independence test: non-dimensional parameter values and outlet temperature as a function of mesh refinement (meshes M1–M5).

Figure 9.2 presents the cross-sectional averaged pressure along the flow path for meshes M1–M5. As the mesh is refined, the pressure in the suction chamber increases. Meshes M1 and M2 predict significantly lower pressure in the suction chamber compared to others (0.82 and 0.86 bar, respectively). The pressure profiles for meshes M3–M5 are

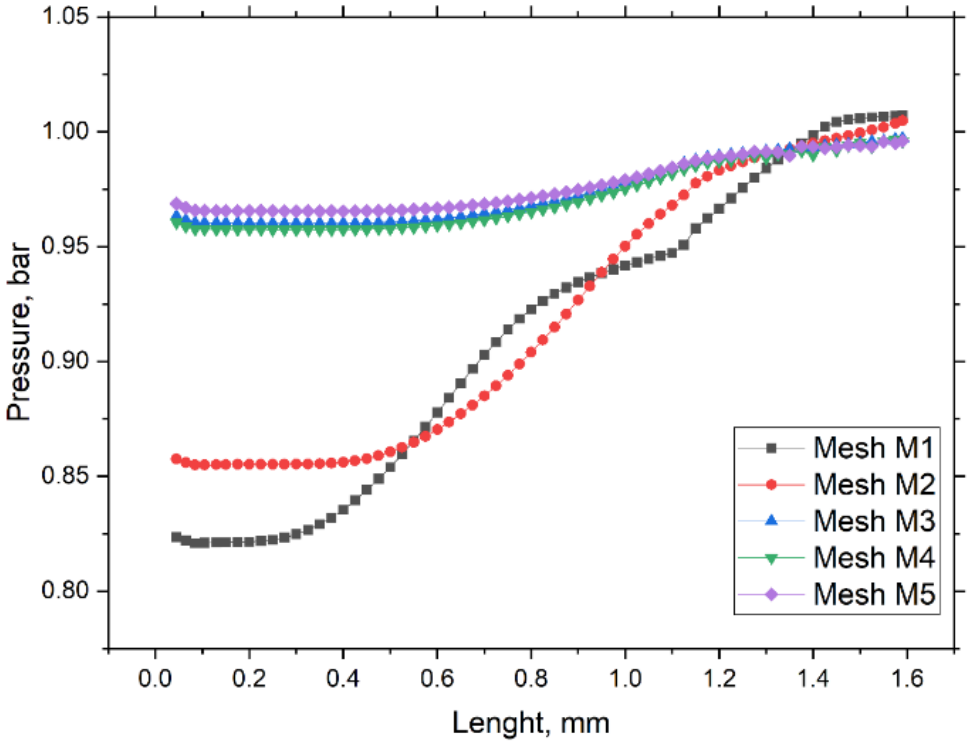

Figure 9.2. Effect of mesh refinement on the cross-sectional averaged pressure along the flow path (meshes M1–M5).

nearly identical. The impact of mesh refinement on the cross-sectional averaged velocity along the flow path for the considered meshes is presented in Figure 9.3. The maximum average velocity ranges from 32 to 34 m/s. The most noticeable differences are observed between meshes M1 and M2, although the variation is relatively small. At the ejector outlet, the average velocity of the mixture is 0.19 m/s for M1, 1.5 m/s for M2, and approximately 2.8 m/s for M3–M5.

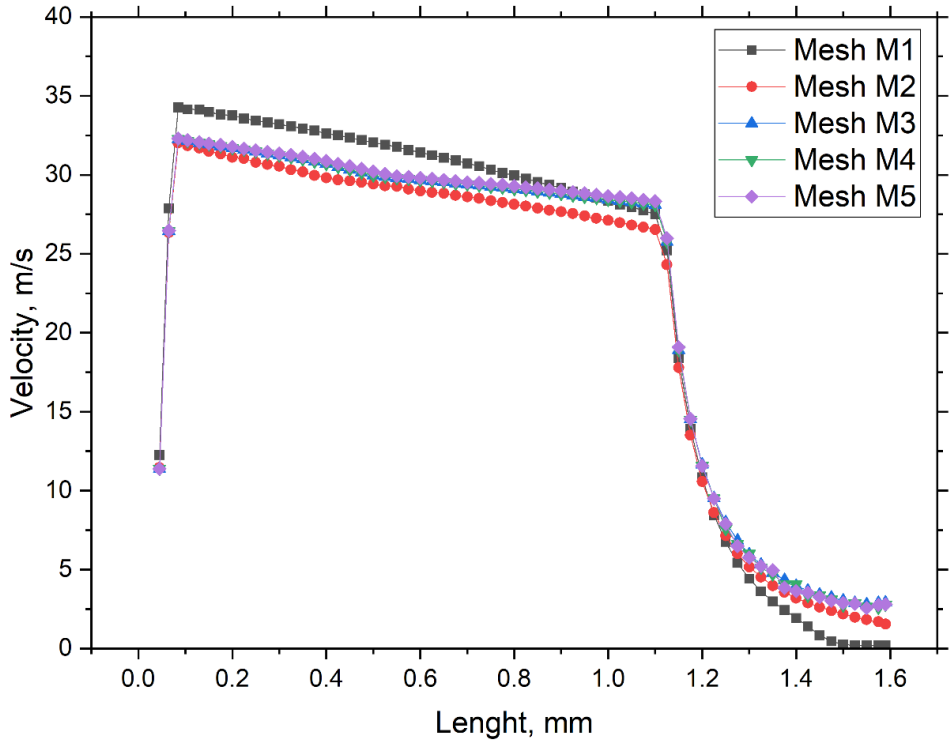

Figure 9.3. Effect of mesh refinement on the cross-sectional averaged velocity along the flow path (meshes M1–M5).

The cross-sectional mass-averaged temperature along the flow path for meshes M1–M5 is presented in Figure 9.4. A higher outlet mixture temperature is obtained for the more refined mesh (51.7°C for meshes M3–M5, compared to 49.0°C–49.4°C for M1–M2). Apart from this, the temperature profiles show no significant differences. Slightly larger fluctuations in the cross-sectional mass-averaged temperature within the diffuser are observed for finer meshes.

Based on the presented results and observations, and considering computational cost and numerical stability, Mesh M4 was selected for further analysis. It provides a grid-independent solution and a good compromise between result convergence and computational efficiency. Moreover, mesh indicators such as volume change and face validity (Table 7.2, page 52) confirm that the mesh meets all required quality criteria.

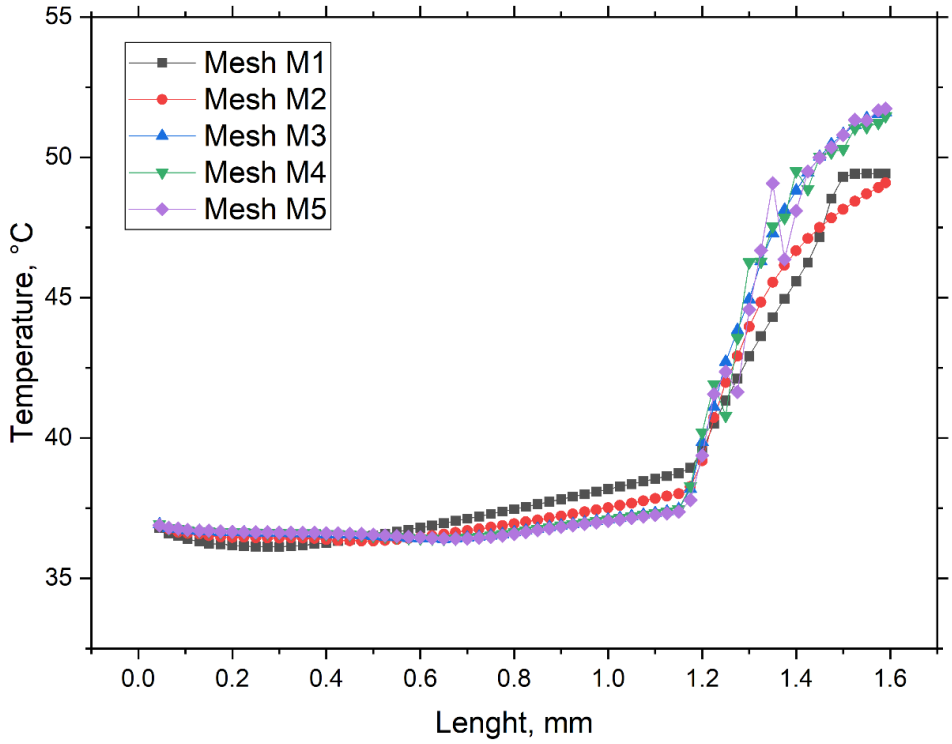

Figure 9.4. Effect of mesh refinement on the cross-sectional mass-averaged temperature along the flow path (meshes M1-M5).

9.2. Analysis of submodels and model properties

The droplet diameter and the applied Nusselt number model were analyzed, as they fundamentally define the model's heat transfer and condensation processes. Various turbulence models were tested to evaluate differences in overall flow behavior. Finally, the selected second and third-order numerical schemes for convective terms were applied and compared. The study identified the parameter values that resulted in the most physically consistent behavior. These were selected for further research, including experimental validation and geometrical analysis.

9.2.1. Droplet diameter

Five average droplet diameters were analyzed to assess their influence on thermal–flow performance: 0.4 mm, 0.6 mm, 1.0 mm, 1.5 mm, and 2.5 mm. The impact of the droplet diameter on the cross-sectional averaged pressure along the flow path is presented in Figure 9.5. In all considered cases, the pressure gradually increases in both the mixing chamber and the diffuser until it reaches the outlet pressure. The droplet diameter influences the pressure distribution along the flow path. However, the trend is complex and not straightforward. The lowest and nearly identical pressure values in the suction chamber (0.96 bar) are observed for droplet diameters of 1.0 and 1.5 mm. The remaining cases are associated with higher suction chamber pressures.

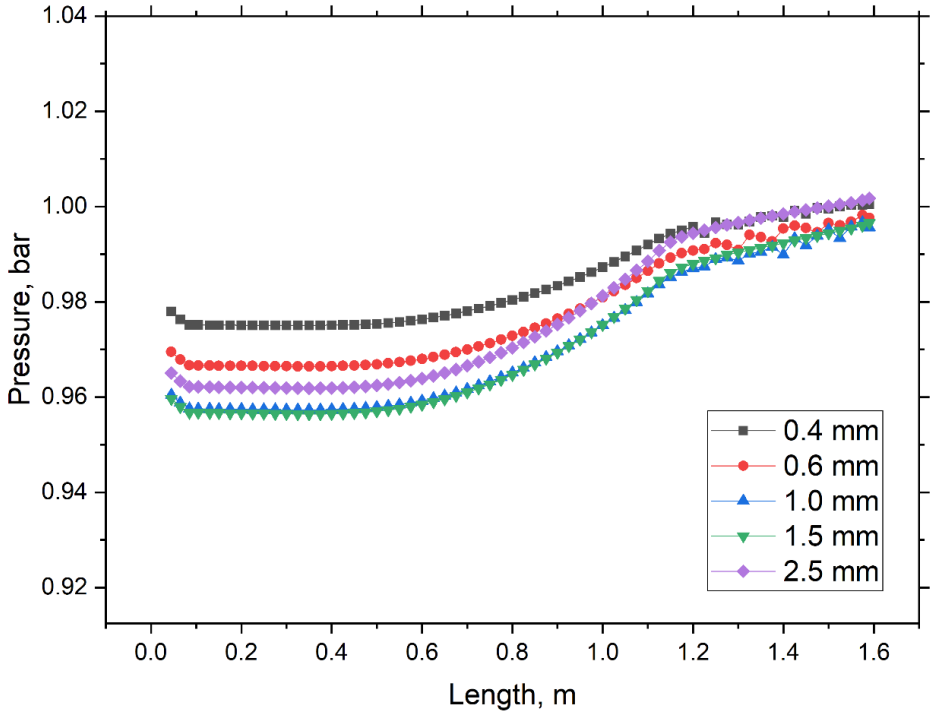

Figure 9.5. The influence of droplet diameter on the cross-sectional averaged pressure along the flow path.

The cross-sectional averaged velocity along the flow path for different droplet diameters is presented in Figure 9.6. As the droplet diameter decreases, differences in velocity profiles become more noticeable. Smaller droplets result in a more rapid decrease in velocity along the flow path. Furthermore, the outlet velocity of the mixture is lower for finer droplets, reaching 2.1 m/s for 0.4 mm and 4.3 m/s for 2.5 mm.

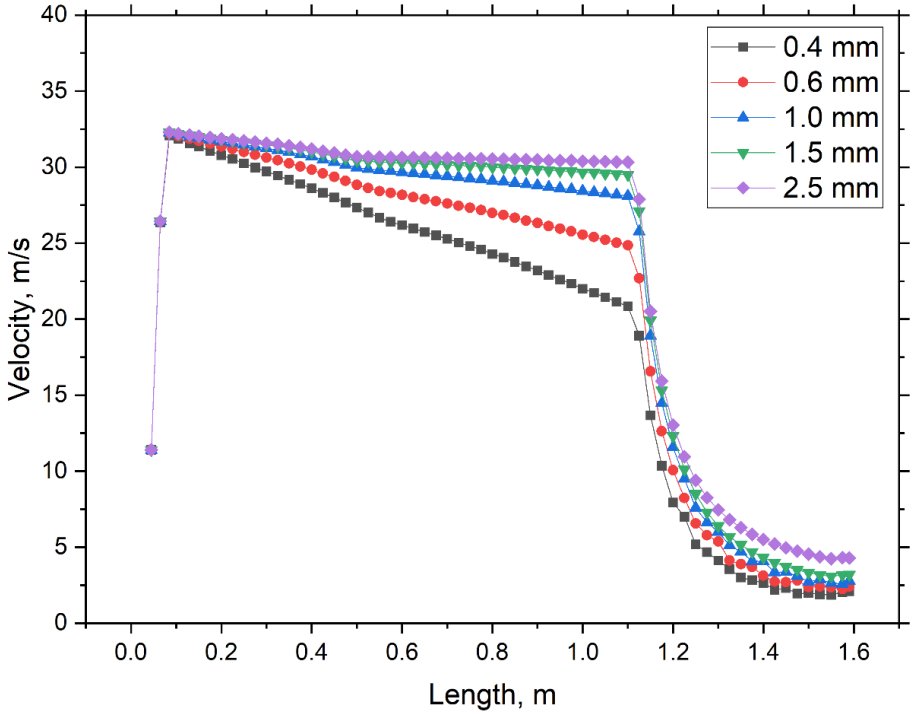

Figure 9.6. The influence of droplet diameter on the cross-sectional velocity along the flow path.

To investigate the influence of assumed droplet diameter on thermal performance, the cross-sectional mass-averaged temperature and cross-sectional steam mass flow rate along the flow path are presented in Figure 9.7 and Figure 9.8, respectively. The results indicate that a smaller droplet diameter leads to a more rapid decrease in steam mass flow rate along the flow path. Reduced droplet diameter enhances the steam condensation, which results in higher temperatures due to the heat released during the phase change process. For a constant motive water volume flow rate, decreasing the droplet diameter increases the total interfacial area available for heat and mass transfer, intensifying condensation.

The droplet diameter is a key parameter that strongly affects flow and thermal phenomena in the spray-ejector condenser. Among the investigated cases, a droplet diameter of 0.6 mm was considered the most appropriate for the analyzed operating conditions due to its moderate suction effect, condensation intensity, and stable numerical behavior.

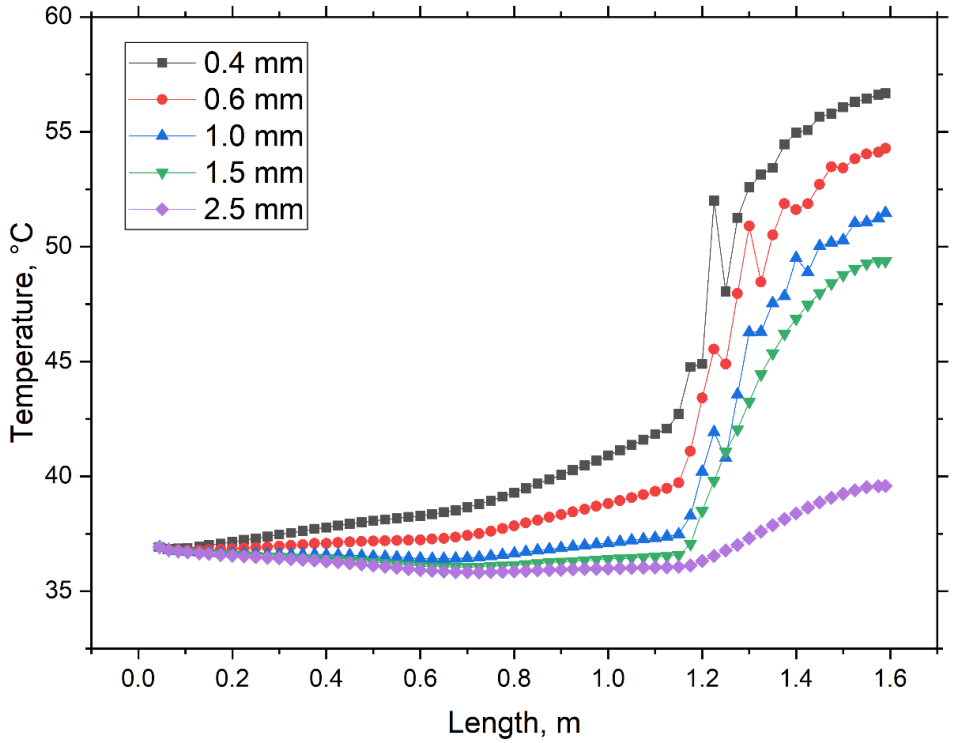

Figure 9.7. The influence of droplet diameter on the cross-sectional mass-averaged temperature along the flow path.

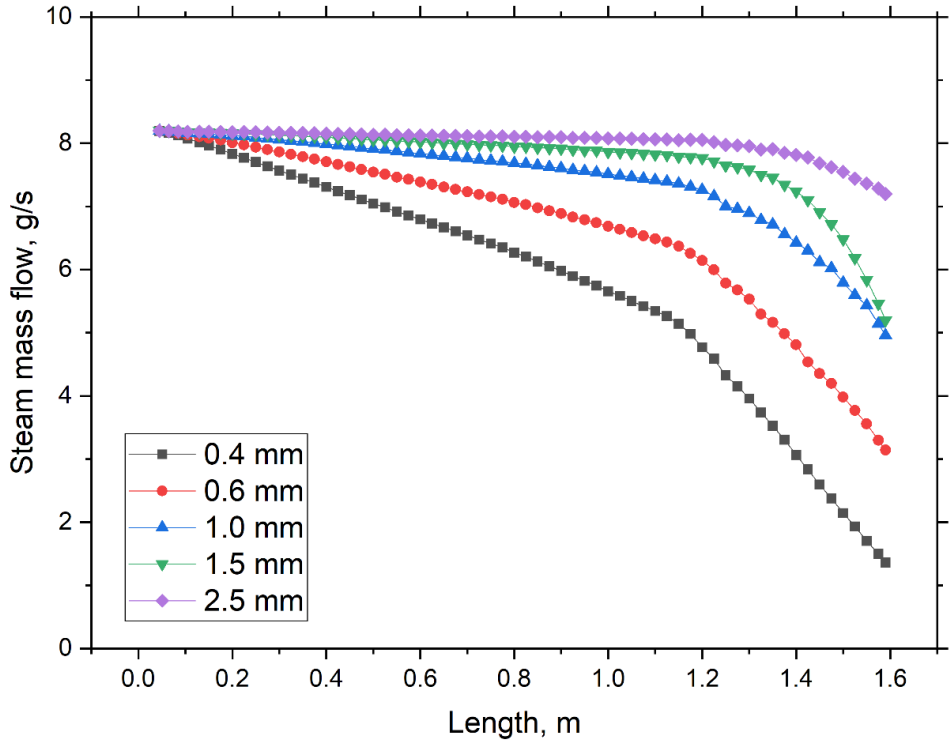

Figure 9.8. The influence of droplet diameter on the cross-sectional steam mass flow along the flow path.

9.2.1. Nusselt number

Varying the Nusselt number on either the steam or water side of the phase-change interface allowed for an analysis of the influence of the applied correlation and its parameters on the ejector performance. Twelve cases were investigated, including a reference case with a constant Nusselt Number of $\mathrm{Nu} = 2$ on both sides (steam and water). In the remaining cases, the Nusselt number was progressively doubled on only one side (steam or water), resulting in $\mathrm{Nu} = 4$, 8, 16, 32, and 64. A Nusselt number correlation based on a turbulent Reynolds Number, as described in Equation (7.2) (page 58), was also applied on the steam side and evaluated.

The cross-sectional averaged pressure along the flow path for various Nusselt numbers is presented in Figure 9.9. Since the differences between the cases are relatively small (less than 1%), the pressure axis was narrowed to illustrate the trends better. The lowest pressure is observed for the reference case ($\mathrm{Nu} = 2$) and the turbulent Reynolds number-based correlation. Increasing the Nusselt number on either the steam or water side raises the pressure profile, with a stronger effect on the water side. Figure 9.10 presents the influence of the Nusselt number on the cross-sectional velocity along the flow path. The curves for the reference case ($\mathrm{Nu} = 2$) and the turbulent Reynolds number-based correlation are nearly identical. Increasing the Nusselt number results in lower

average velocity along the flow path. Notably, a stronger effect is observed when the Nusselt number is increased on the water side. In this case, the average outlet velocity drops to approximately 14.6 m/s for $\mathrm{Nu} = 64$, compared to 25.9 m/s when the same value is applied on the steam side.

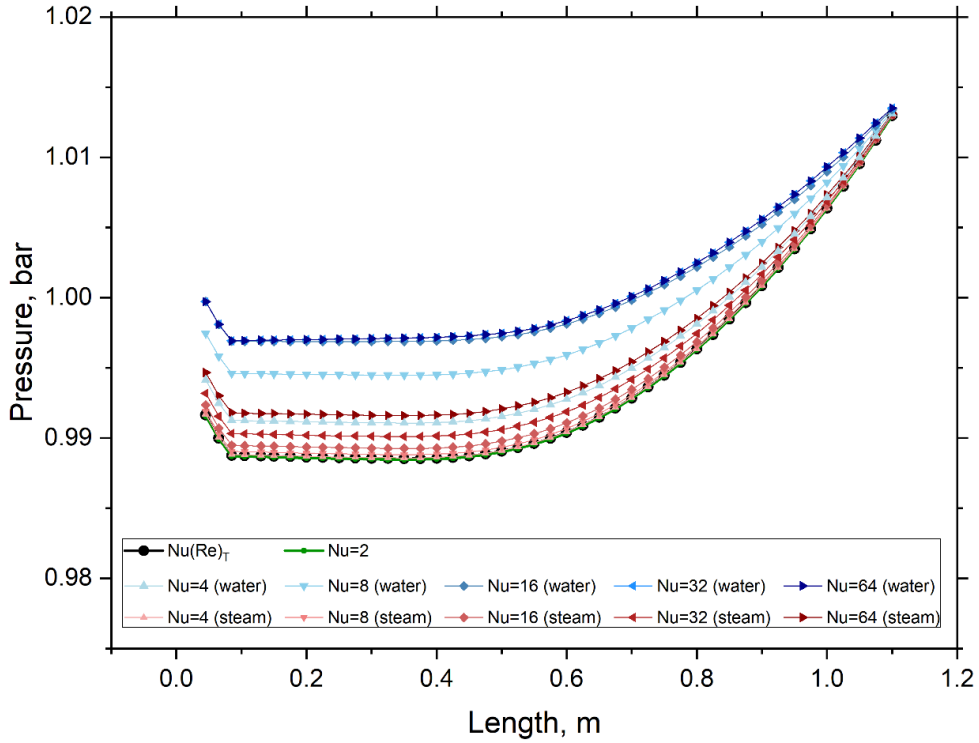

Figure 9.9. The influence of Nusselt Number on the cross-sectional averaged pressure along the flow path.

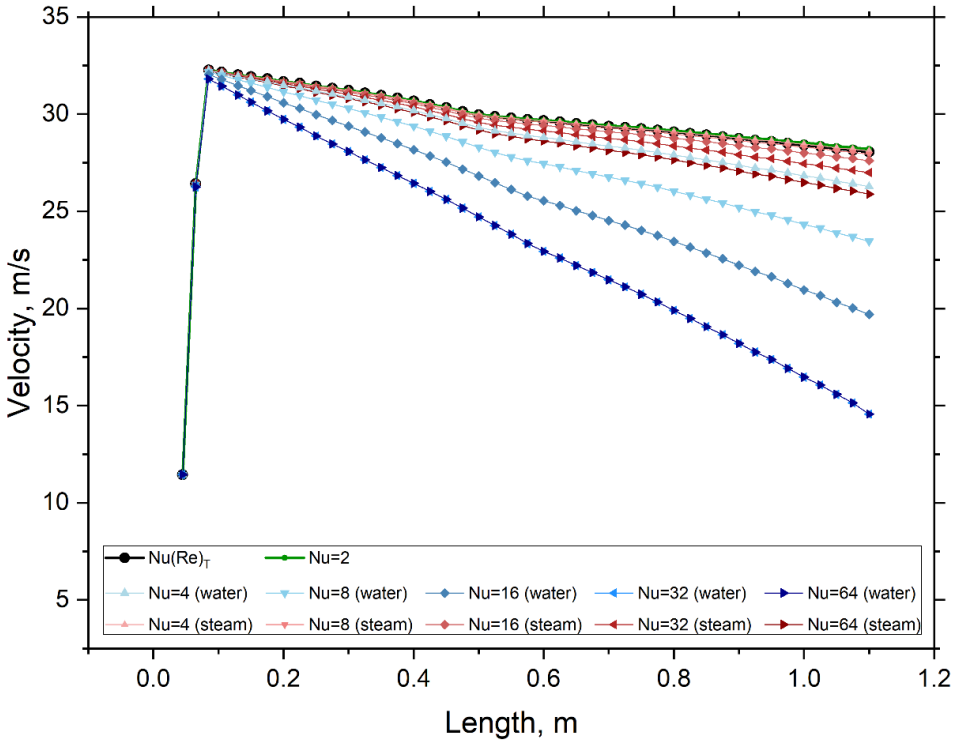

Figure 9.10. The influence of Nusselt Number on the cross-sectional velocity along the flow path.

The cross-sectional mass-averaged temperature and steam mass flow along the flow path for various Nusselt numbers are presented in Figure 9.11 and Figure 9.12, respectively. As the Nusselt number increases, the average mixture temperature rises, and the steam mass flow rate decreases along the flow path. This effect results from the correlation between the Nusselt number and the heat transfer coefficient, which governs the computed heat flux and, consequently, the condensation mass flow rate. Similarly to the pressure and velocity curves, a much greater influence on the thermal-flow performance is associated with the water side.

The results clearly show that the Nusselt number affects the ejector's thermal and flow performance. Its proper definition is essential for predicting the pressure lift and the condensation intensity. Assigning the Nusselt number on the steam side appears more physically justified, as it reduces the risk of overestimating the condensation rate. For further analysis, the correlation based on the turbulent Reynolds Number defined on the steam side is considered the most reasonable choice.

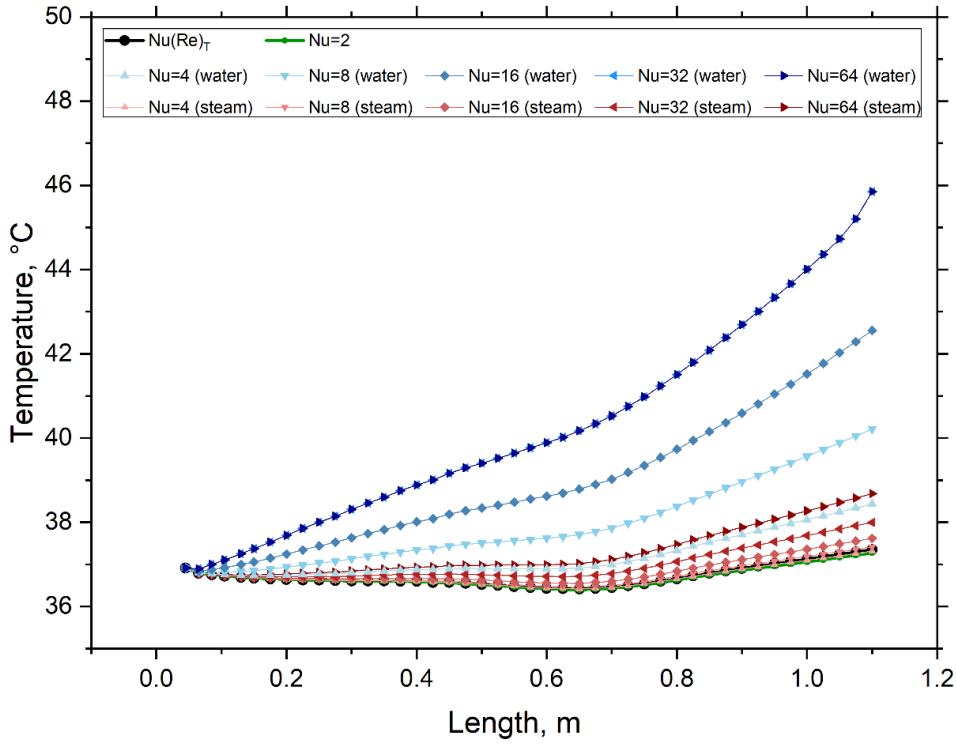

Figure 9.11. The influence of Nusselt Number on the cross-sectional mass-averaged temperature along the flow path.

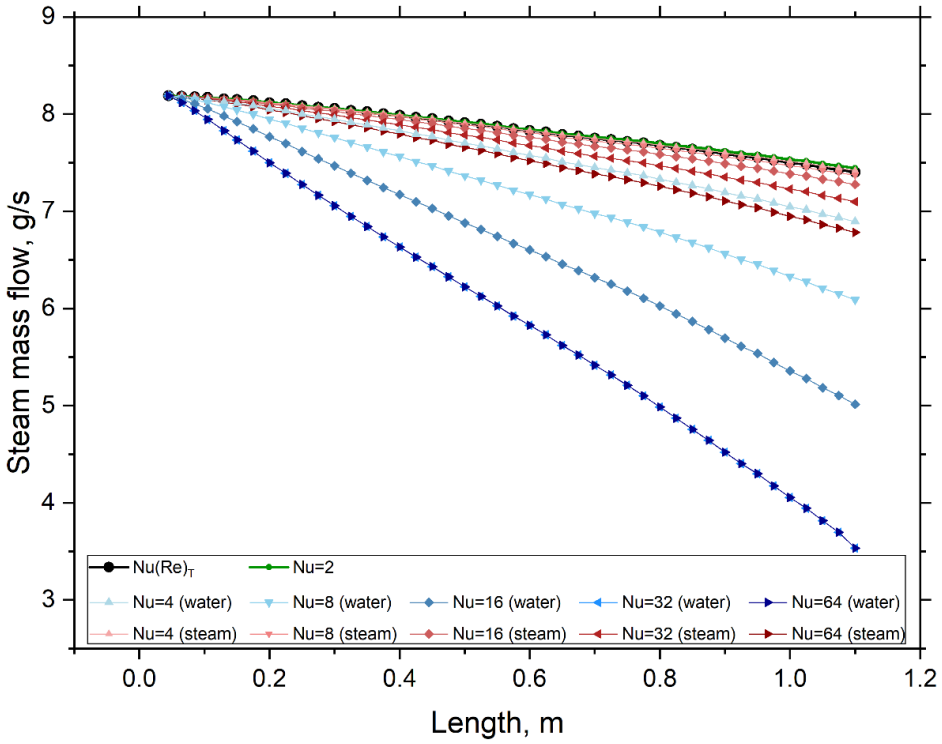

Figure 9.12. The influence of Nusselt Number on the cross-sectional steam mass flow along the flow path.

9.2.2. Turbulence model

Four RANS-based models were analyzed: Realizable *k-ε* (two-layer), *k-ω, k-ω* SST, and RSM. Figure 9.13 presents the impact of the turbulence model on the cross-sectional averaged pressure along the flow path. Similar trends in pressure increase are observed in all cases. The *k-ω* model predicts the lowest pressure in the suction chamber (approximately 0.97 bar), whereas the highest value (around 1.00 bar) is obtained using the *k-ω SST* model. The Realizable *k-ε* and RSM models provide similar predictions, with suction pressure close to 0.99 bar. The cross-sectional mass-averaged temperature along the flow path for various turbulence models is shown in Figure 9.14. Slight differences appear in the mixing chamber, and both inlet and outlet temperatures remain nearly identical across all cases. This confirms that turbulence modeling has a limited influence on thermal behavior for the considered operating conditions. Cross-sectional velocity and steam mass flow profiles showed no visible differences and are included in the Appendix (Figure B. 1 and Figure B. 2, respectively)

The results indicate that the applied turbulence model primarily affects the pressure distribution. Although the RSM model, which directly computes the Reynolds stresses, is theoretically expected to provide the most accurate predictions, the Realizable *k-ε* (two-layer) model produces nearly identical outcomes. Considering its numerical robustness,

widespread application in two-phase ejector simulations (Section 2.4.1), and consistency with the present results, the Realizable *k-ε* (two-layer) model was selected for further investigation.

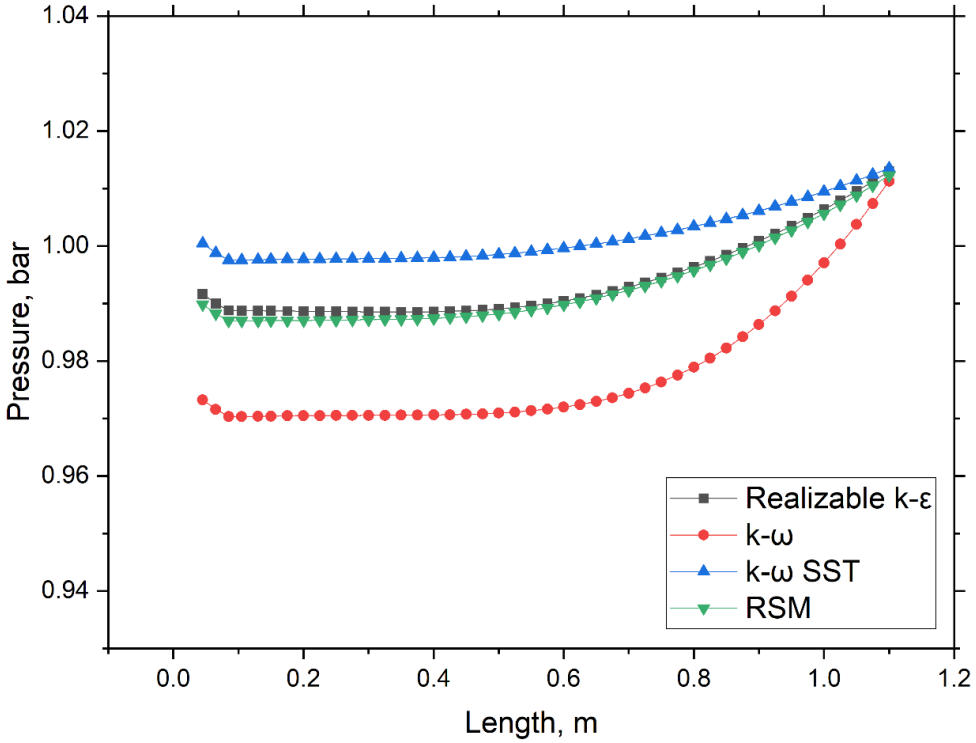

Figure 9.13. The influence of the turbulence model on the cross-sectional averaged pressure along the flow path.

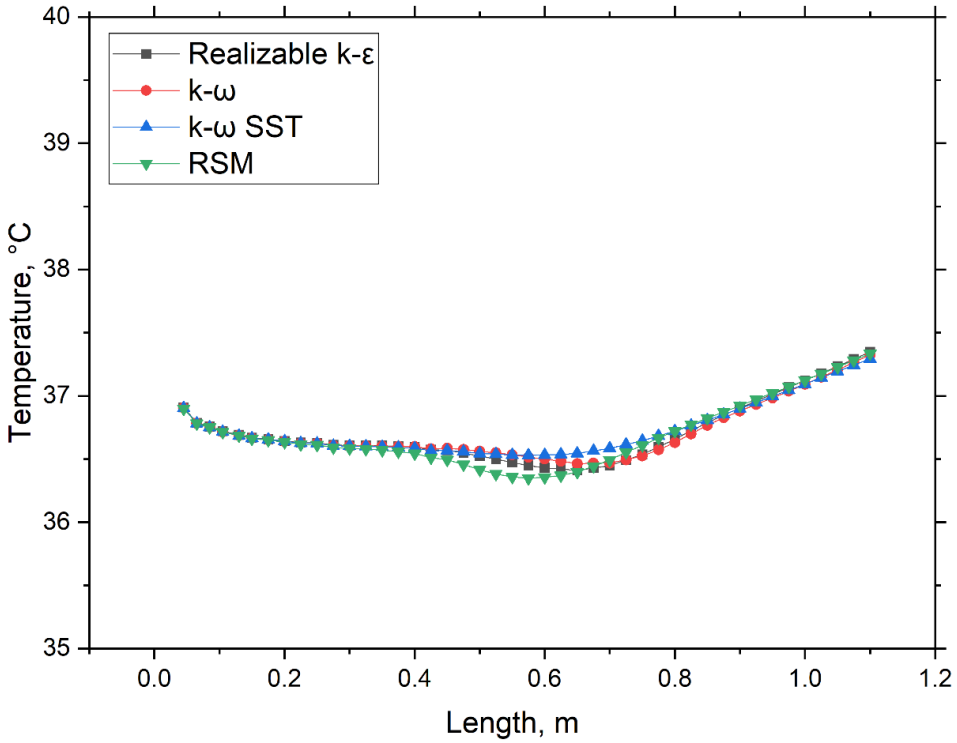

Figure 9.14. The influence of the turbulence model on the cross-sectional mass-averaged temperature along the flow path

9.2.3. Numerical convection schemes

The influence of the discretization scheme for convection terms on the ejector's thermal–flow behavior was analyzed by applying a third-order scheme separately for the flow and temperature solvers. A case with a second-order scheme for all solvers was used as the reference case. Figure 9.15 presents the impact of the numerical convection scheme on the cross-sectional averaged pressure along the flow path. While the overall variation is insignificant, applying a third-order scheme to the flow solver leads to slightly elevated pressure levels in the suction and mixing chambers. The pressure distribution remains unchanged when a third-order scheme is applied to the temperature solver.

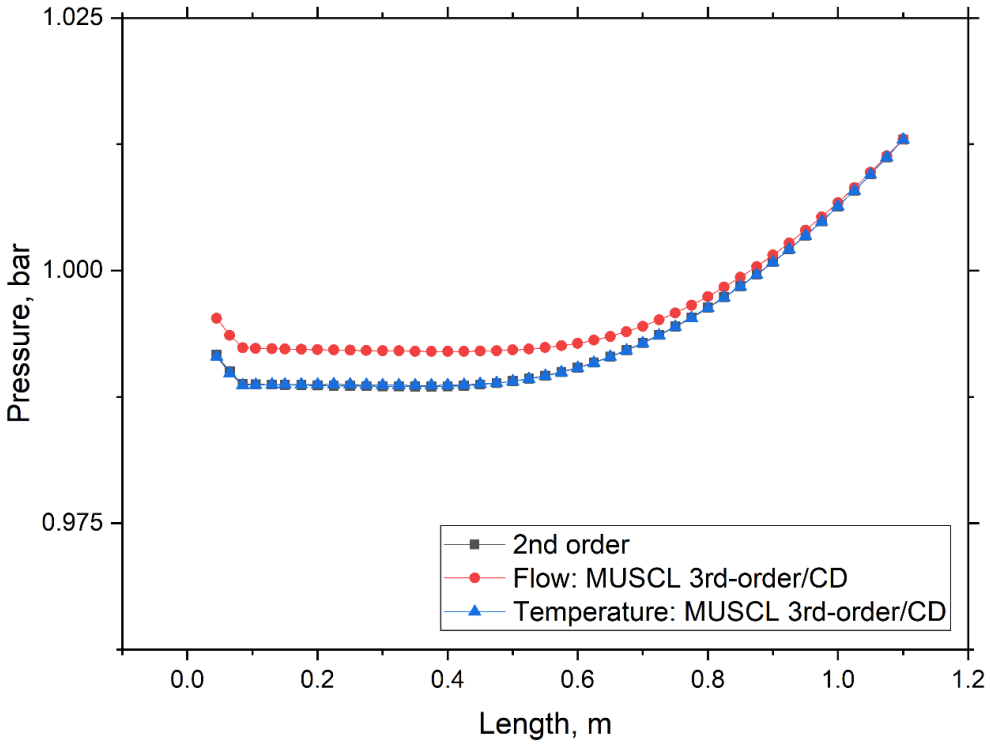

Figure 9.15. The influence of the numerical convection scheme on the cross-sectional averaged pressure along the flow path.

A smoother temperature profile can be observed after applying a third-order scheme for the temperature solver, as shown in Figure 9.16, which presents the cross-sectional mass-averaged temperature along the flow path. The outlet temperature is slightly lower for the third-order convection discretization scheme for the temperature solver (37.1°C vs. 37.3°C). Since no noticeable differences were observed in the cross-sectional average velocity and steam mass flow along the flow path, the corresponding figures are provided in the Appendix (Figure B. 3 and Figure B. 4, respectively).

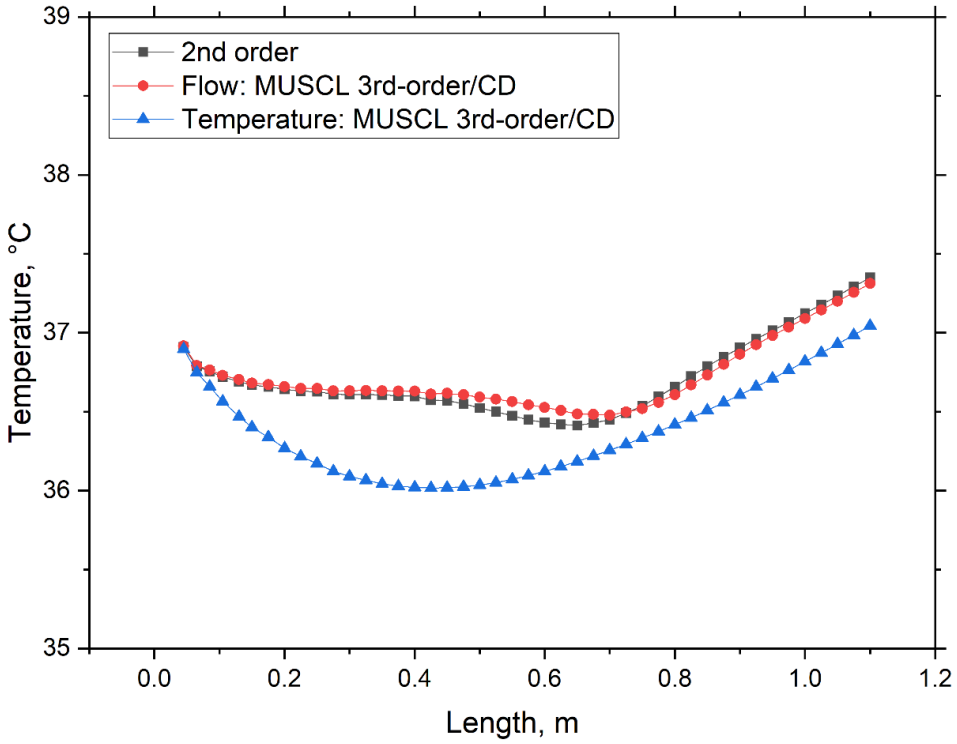

Figure 9.16. The influence of the numerical convection scheme on the cross-sectional mass-averaged temperature along the flow path.

Based on the numerical investigation's results, and aiming to improve the accuracy of thermal behavior prediction, a third-order convection scheme was adopted for the temperature solver. This setup was considered the most appropriate for capturing the thermal effects in the studied flow conditions while maintaining solution stability and convergence.

10. Analysis of the spray-ejector condenser operation

The final modeling results are presented for the developed LPL spray-ejector condenser operating under conditions representative of a negative-pressure gas power plant. The numerical model was developed using the final set of sub-models and parameter settings selected during the preceding stages of analysis. Three operating scenarios OP1, OP2, and OP3, were considered. They differ mainly in entrained fluid parameters such as mass flow rates, pressures, phase content, and temperature, as listed in Table 7.3 (page 55). Operating point OP1 corresponds to nominal conditions. OP2 represents a case with increased CO_2 mass fraction while maintaining the same total exhaust gas mass flow rate. In OP3, the total exhaust gas mass flow rate is reduced, with the CO_2 mass fraction unchanged compared to OP1.

The ejector's thermal–flow performance was evaluated using non-dimensional and dimensional parameters, which were compared against experimental data to verify the reliability of the developed model. Pressure and temperature distributions along the flow path were also analyzed and verified against measurements. Particular attention was given to the condensation process, with condensation efficiency identified as a key thermal performance parameter ensuring proper operation of the ejector condenser.

10.1. Ejector performance in reference to experimental data

Computational results were validated against data from the experimental direct contact jet condenser test rig installation developed at AGH University of Science and Technology as part of the project (Figure 10.1). The facility enables investigation of the ejector performance under various operating conditions, including boundary conditions, geometrical designs, and working fluids. A detailed description of the rig and apparatus is provided in [98]. In the numerical model, pressure and temperature probes were positioned near the ejector wall (Figure 10.2) following the experimental setup. Their exact locations are listed in Table 10.1. Pressure and temperature were measured at nine and eight points along the flow path, respectively.

The pressure and temperature distributions obtained from the experimental measurements are presented as average values with their extreme deviations. This approach is justified by the complex nature of direct contact condensation, which is associated with strong fluctuations in the measured parameters.

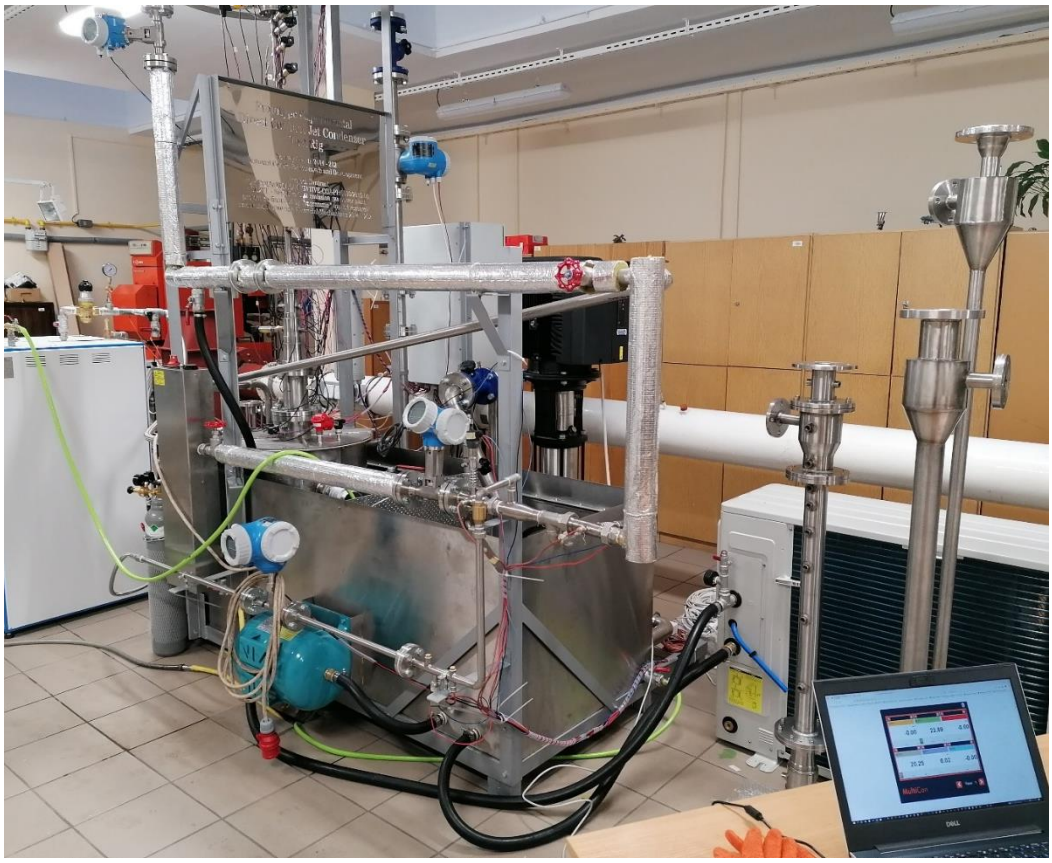

Figure 10.1. Experimental direct contact jet condenser test rig installation at AGH University of Science and Technology.

Figure 10.2. Arrangement of measurement probes in the numerical model, consistent with the experimental setup.

Table 10.1. Detailed locations of the pressure and temperature probes in the numerical model, consistent with the experimental setup).

Probe number	Distance from motive nozzle outlet, mm	Pressure measurement	Temperature measurement
1	0	✓	
2	25	✓	
3	88	✓	
4	138	✓	✓
5	213	✓	✓
6	313	✓	✓
7	463	✓	✓
8	663		✓
9	913		✓
10	1113	✓	✓
11	1338	✓	✓

The pressure distribution along the flow path obtained from the CFD model and experimental measurements for OP1 is presented in Figure 10.3. It follows the expected trend, starting with a sub-atmospheric pressure region in the suction chamber and continuing with a pressure increase through the mixing chamber towards the outlet. The overall pressure rise seems to be underestimated compared to the experimental data. The pressure profile predicted computationally is at or near the boundaries of the experimental range within the suction chamber and approximately the first half of the mixing chamber. The pressure computed by CFD in the suction chamber is 0.97 bar, whereas the experimental values range from 0.90 to 0.97 bar.

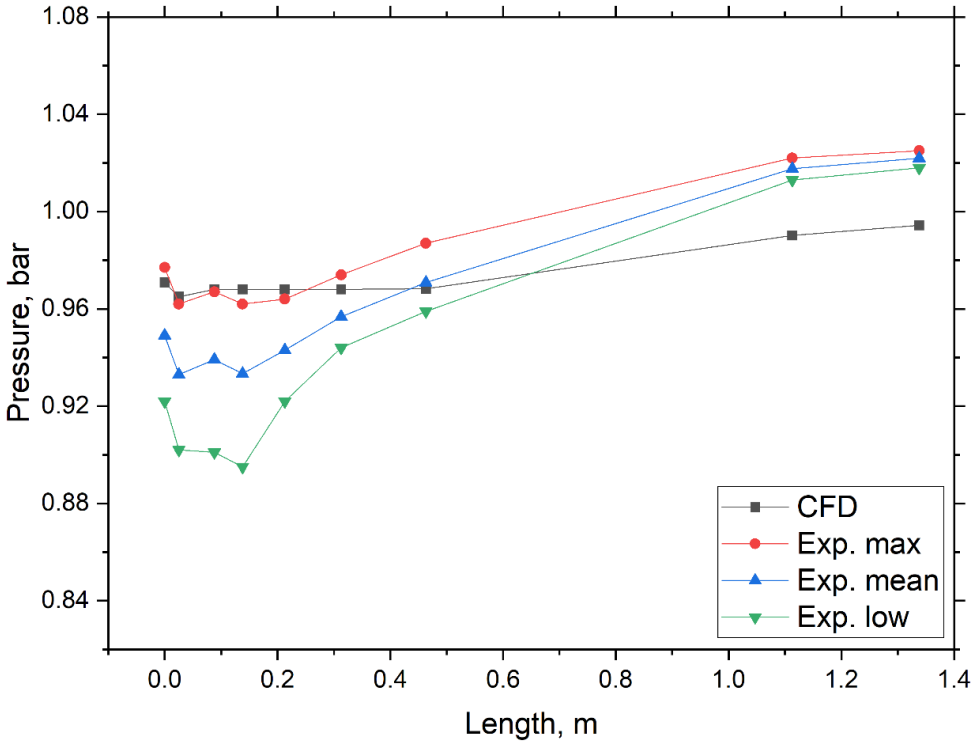

Figure 10.3. Pressure distribution along the flow path obtained from CFD and experimental measurements for OP1 (exhaust gas mass flow rate: 10.2 g/s, gas temperature: 119.4°C, CO_2 mass fraction: 20%).

Figure 10.4 presents the temperature distribution along the flow path for the considered cases. The CFD model predicts a significant temperature drop up to the middle of the diffuser, where the temperature stabilizes. It then increases before decreasing near the outlet, reaching a final value of 54.9°C. The experimentally measured outlet temperature ranges from 46.6°C to 61.6°C. The most pronounced discrepancies between the numerical and experimental results appear in the region where the exhaust gas and water come into contact. The thermal behavior in the mixing chamber is particularly complex, as confirmed by both computational and experimental observations.

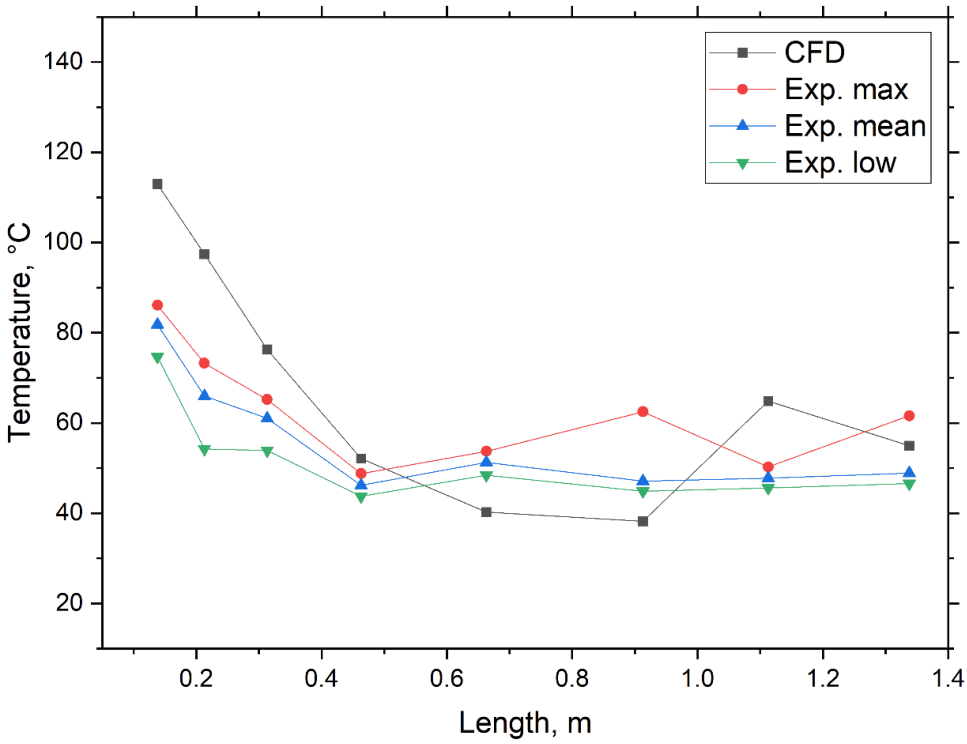

Figure 10.4. Temperature distribution along the flow path obtained from CFD and experimental measurements for OP1 (exhaust gas mass flow rate: 10.2 g/s, gas temperature: 119.4°C, CO_2 mass fraction: 20%).

The pressure distribution along the flow path derived from computational simulation and experimental measurements for OP2, in which the CO_2 mass content in the exhaust gas is higher, is shown in Figure 10.5. The CFD model predicts a relatively stable pressure profile in the suction chamber, extending nearly to the midpoint of the mixing chamber. The calculated pressure in the suction chamber is about 0.95 bar, while the experimental values range from 0.94 bar to 0.98 bar, with an average of about 0.96 bar. Although the outlet pressure values differ between the numerical and experimental results, the pressure rise dynamics in the second half of the mixing chamber and the diffuser appear similar. The temperature distribution along the flow path obtained from CFD and experimental measurements for OP2 is presented in Figure 10.6. The computed temperature profile rises in the final part of the mixing chamber and remains nearly constant in the diffuser, suggesting that condensation is not very intensive in this section. Good agreement between numerical and experimental data is observed, particularly in the suction chamber and diffuser regions. The calculated outlet temperature is 47.8°, while the average value from measurement is 46.6°C.

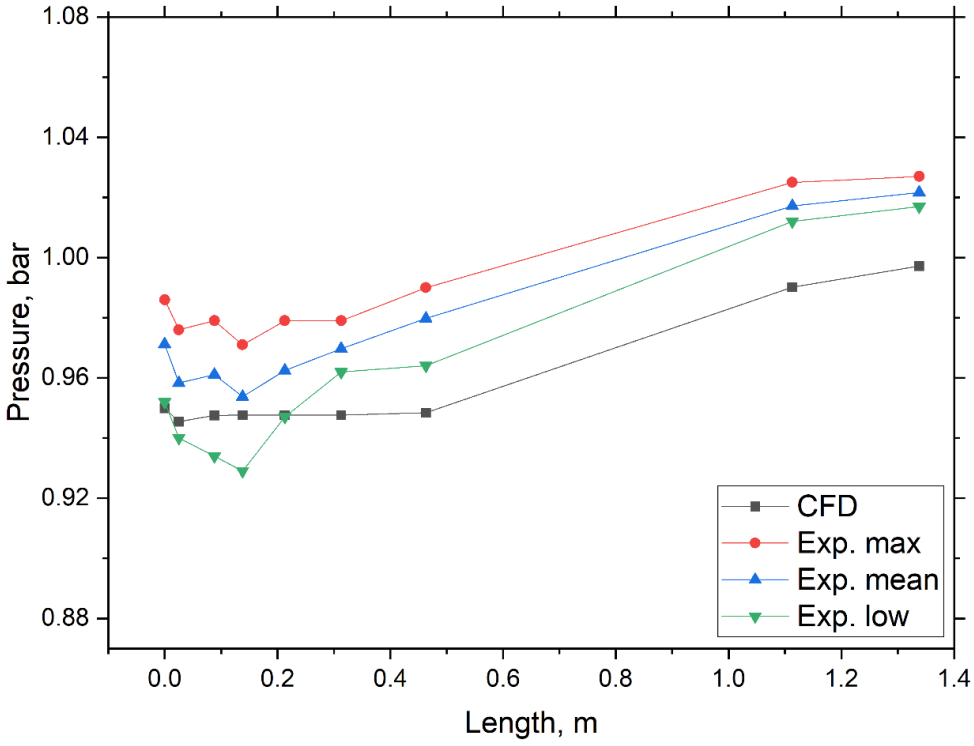

Figure 10.5. Pressure distribution along the flow path obtained from CFD and experimental measurements for OP2 (exhaust gas mass flow: 10.2 g/s; gas temperature: 108.3°C; CO_2 mass content: 39%).

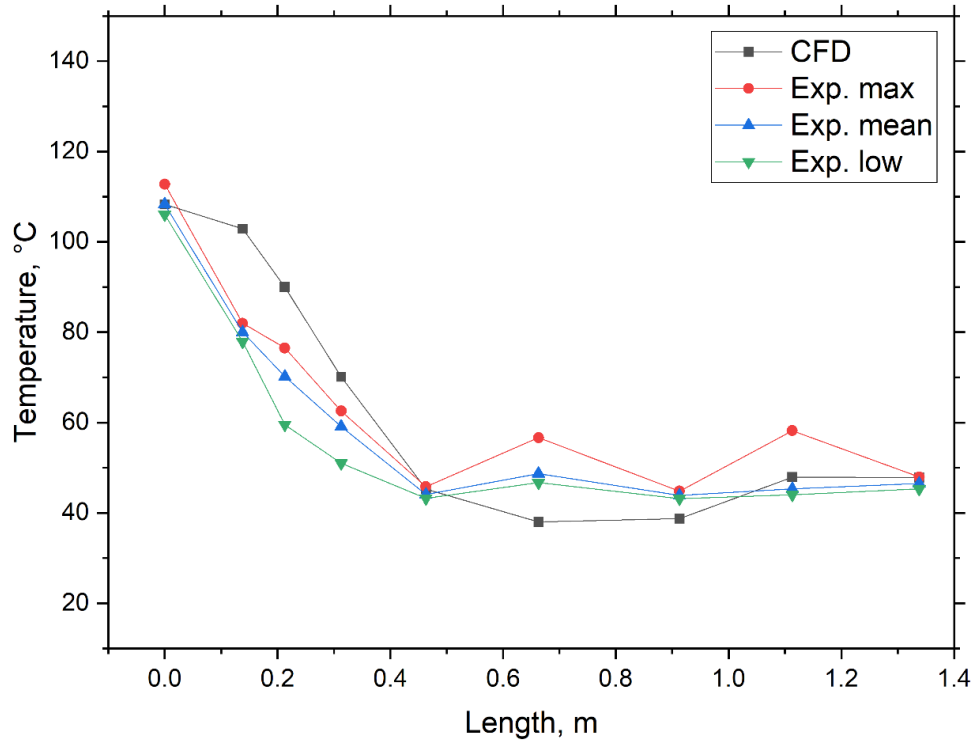

Figure 10.6. Temperature distribution along the flow path obtained from CFD and experimental measurements for OP2 (exhaust gas mass flow: 10.2 g/s; gas temperature: 108.3°C; CO_2 mass content: 39%).

The pressure profile obtained from simulation and experimental data for OP3, where the steam mass flow rate is reduced compared to OP1, is presented in Figure 10.7. The CFD model predicts a relatively constant pressure (approximately 0.95 bar) in the suction chamber and at the beginning of the mixing chamber. In contrast, the distribution is more variable for the experiments and varies between 0.91 and 0.97 bar. The computed pressure profile is within the range determined during the experiment in this region. Decreasing the mass flow rate causes the pressure curves to shift toward lower pressure.

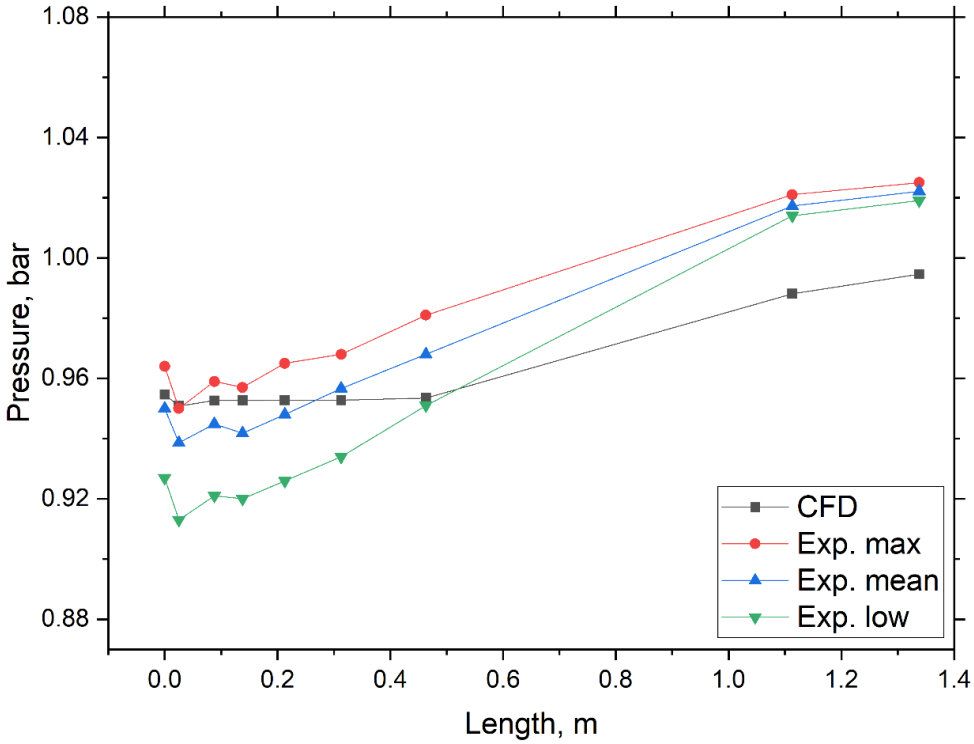

Figure 10.7. Pressure distribution along the flow path obtained from CFD and experimental measurements for OP3 (exhaust gas mass flow: 8.8 g/s; gas temperature: 112.8°C; CO_2 mass content: 21%).

Figure 10.8 presents the temperature distribution along the flow path obtained from CFD and experimental measurements for OP3. The trend of the computed profile is similar to that observed for the other operating points. In the case of experimental data, only slight deviations from the mean values are observed, indicating more stable operating conditions and less pronounced fluctuations. For OP3, the agreement between CFD and experimental results can be considered moderate.

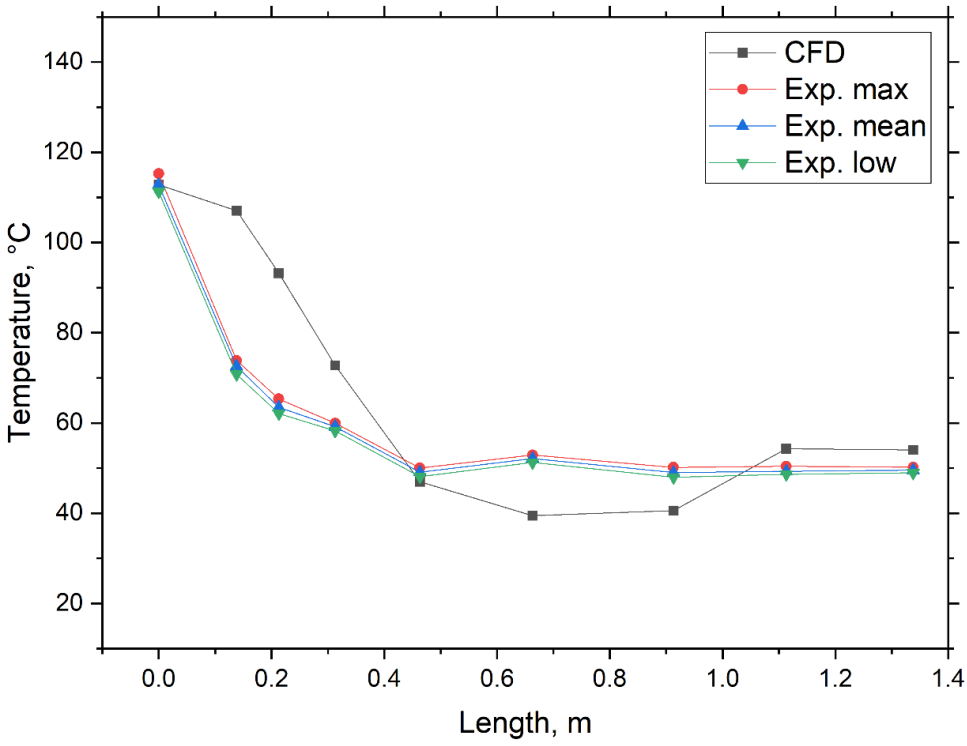

Figure 10.8. Temperature distribution along the flow path obtained from CFD and experimental measurements for OP3 (exhaust gas mass flow: 8.8 g/s; gas temperature: 112.8°C; CO_2 mass content: 21%)

A summary of the ejector performance results is provided in Table 10.2, which presents the computed values of suction pressure, outlet temperature, and non-dimensional parameters for all operating points (OP1–OP3), comparing them with the experimental data. The corresponding relative errors between CFD-predicted and experimentally determined values are listed in Table 10.3. A moderate suction effect was achieved, indicated by the suction pressure in the range of 0.95 to 0.97 bar and a compression ratio between 1.03 and 1.05. The differences between the performance parameters for the three operating points are relatively small. The experimental results generally indicate that the CFD model slightly underestimates the performance for OP1 and OP3, and overestimates for OP2.

Good accuracy is achieved for the suction pressure, outlet temperature, and compression ratio with relative errors below 3.7%. The relative error for the expansion ratio varies from 12.0% to 15.6%. The mass error is near 0% because the mass flow was applied as a boundary condition. Due to the variation in agreement across different parameters, it is difficult to identify which operating point best matches the experimental data.

Table 10.2. Summary of CFD and experimental performance parameters for three ejector operating scenarios (operating points OP1–3).

Operating point		Suction pressure p_{suc}, bar	Outlet temperature T_{out}, K	Compression ratio *CR*	Expansion ratio ξ	Mass entertainment ratio *ER* ($\times 10^{-3}$)
CFD	OP1	0.97	328.3	1.03	13.93	29.52
	OP2	0.95	321.0	1.06	14.20	29.39
	OP3	0.95	327.2	1.05	13.92	25.70
EXP.	OP1	0.95	321.6	1.07	16.49	29.52
	OP2	0.97	319.7	1.04	16.13	29.43
	OP3	0.95	322.7	1.07	16.46	25.70

Table 10.3. The relative error between CFD results and experimental data for performance parameters for three ejector operating scenarios (operating points OP1–3) .

Operating point	Relative error, %				
	Suction pressure p_{suc}	Outlet temperature	Compression ratio *CR*	Expansion ratio ξ	Mass entertainment ratio *ER*
OP1	2.2	2.1	3.7	15.6	0.0
OP2	2.2	0.4	1.9	12.0	0.1
OP3	0.5	1.4	1.9	15.4	0.0

The pressure and temperature distribution along the flow path, together with key performance parameters, indicate that the developed model successfully reproduces the expected behavior of a liquid-driven ejector operating in direct contact condensation mode. The ejector generates the anticipated moderate suction effect under nominal operating conditions, as well as in cases with the highest CO_2 mass content and reduced exhaust gas flow rate.

Considering the complexity of the physical phenomena, the agreement between the simulation results and experimental data is reasonably good. For two-phase ejector models, deviations reported in the literature for mass flow rates, pressure, temperature, and non-dimensional parameters typically remain within 20% [43,54,68,70,86], although in cases accounting for phase change, higher deviations have also been observed [66,87]. The level of accuracy achieved by the developed CFD model of the spray-ejector condenser falls within these ranges. The agreement is considered satisfactory, and the model can be regarded as reliable for further analysis.

10.2. Steam condensation efficiency

From the perspective of operating a gas power plant with negative CO_2 emission, the ejector's ability to condense steam from the exhaust gas mixture is crucial. Figure 10.9 presents the cross-sectional averaged steam mass flow along the flow path and the resulting condensation efficiency for operating points OP1–OP3. A gradual reduction in steam flow is observed along the ejector, with a more pronounced decline in the diffuser section. The lowest condensation efficiency (61.6%) occurs under nominal conditions (OP1), while the highest (83.9%) is observed for OP3, where the exhaust mass flow rate is reduced. When the CO_2 mass fraction is doubled (at the expense of steam), the condensation efficiency increases to 72.8%. Even though the presence of CO_2 weakens the condensation intensity, the effect of reduced steam mass flow rate appears to be dominant.

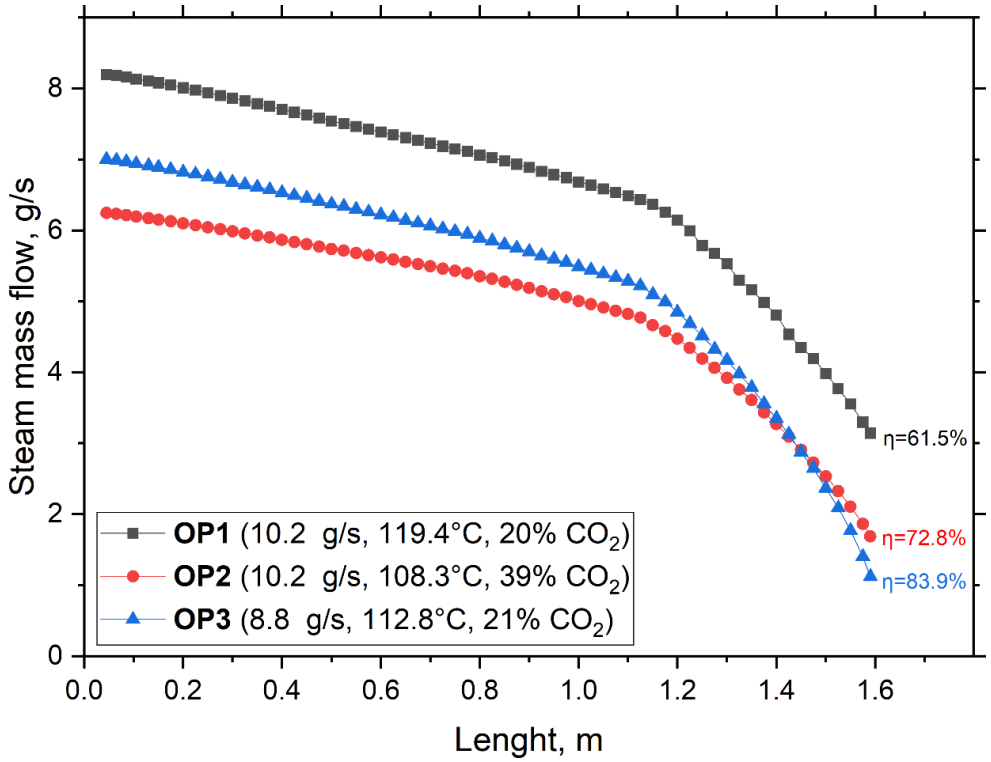

Figure 10.9. The cross-sectional steam mass flow along the flow path for different operating conditions OP1–OP3 (exhaust gas mass flow rate, temperature, CO_2 mass content).

The distribution of condensation rate for different operating conditions (OP1–OP3) is presented in Figure 10.10. The highest condensation rates are observed at the interface between the water jet and the surrounding exhaust gases, indicating that condensation predominantly occurs in this region. The maximum calculated condensation rate reaches approximately 100 kg/m^3. Significantly lower values are observed for the OP2 case, which is attributed to the presence of CO_2. Figure 10.11 shows the steam volume fraction

scalar field for OP1-OP3. The steam volume fraction gradually increases within the water jet region along the length of the ejector. In the diffuser section, the steam volume fraction fluctuates and decreases considerably near the walls. For OP2, the steam volume fraction is lower overall due to the increased CO_2 content, and the decrease of the volume fraction in the diffuser is more gradual. Additional scalar fields of water and CO_2 volume fractions for OP1–OP3 are included in Appendix A (Figure A. 4 and Figure A. 5, respectively).

The determined condensation efficiency ranges from 61.5% to 83.9%, with the lower value corresponding to the nominal point (OP1). While these results are encouraging, they remain insufficient to meet the expected performance targets. Therefore, Further analysis focused on improving the geometrical model is necessary to achieve the desired thermal performance.

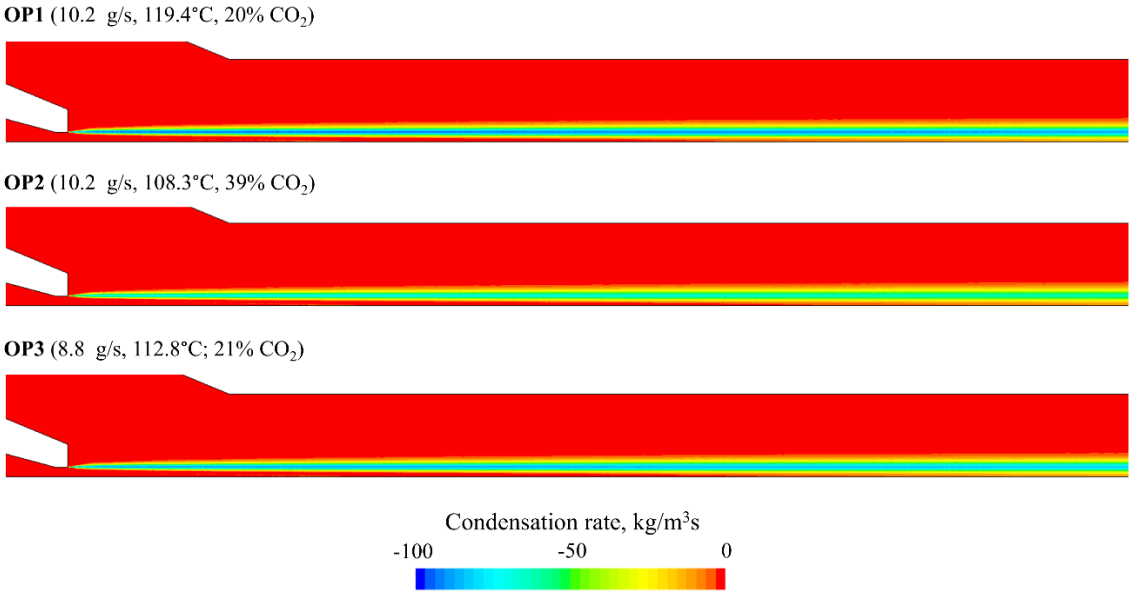

Figure 10.10. Distribution of condensation rate for different operating conditions OP1–OP3 (exhaust gas mass flow rate, temperature, CO2 mass content).

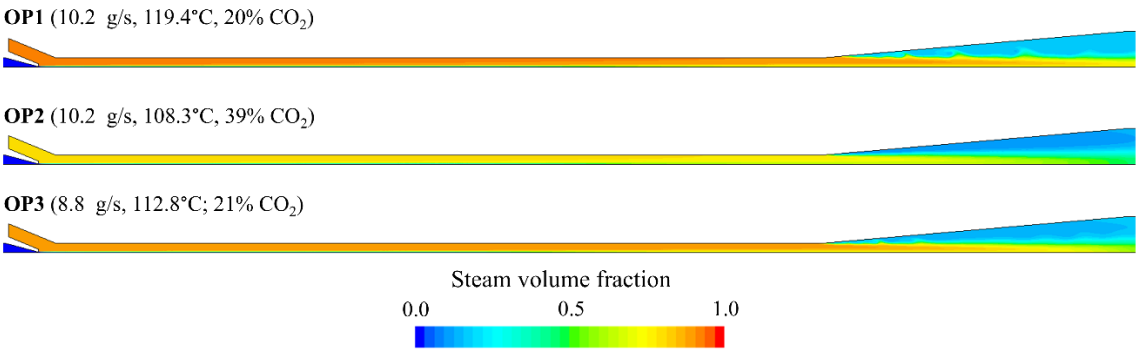

Figure 10.11. Distribution of steam volume fraction for different operating conditions OP1–OP3 (exhaust gas mass flow rate, temperature, CO2 mass content).

11. Study of the impact of selected geometric parameters on the spray-ejector condenser performance

To evaluate the influence of geometry modification on the thermal–flow performance of the ejector condenser, several key geometrical parameters were varied and analysed: mixing chamber diameter D_{MIX}, mixing chamber length L_{MIX}, the motive nozzle diameter D_{MN_2}, outer nozzle diameter D_{TIP}, nozzle exit position L_{MCH}. The impact of employing a modified motive nozzle configuration with a secondary (double) nozzle was evaluated. Section 7.1 provides a more detailed description of the modification, and the schematic drawings of the design changes are presented in Figure 7.3 and Figure 7.4. The exact values of the modified dimensions are listed in Table 7.1 (p. 50).

For each analyzed case, the results are presented as cross-sectionally averaged profiles of key flow properties along the flow path, complemented by scalar field distributions. Each section is summarised by a table comparing the overall performance based on generated suction pressure and non-dimensional performance parameters.

11.1. Analysis of motive nozzle diameter

The investigation concerns the motive nozzle diameter D_{MN_2}, where velocity or pressure was specified at the water inlet. The analysis was divided into independent parts, as the imposed boundary condition type significantly influenced both the local field distributions and the overall trends in performance parameters.

11.1.1. Velocity boundary conditions at the motive inlet

Specifying the constant velocity at the water inlet causes the pressure at the motive inlet to vary with changes in the nozzle diameter, as shown in Figure 11.1. While for the basic motive nozzle diameter (3.0 mm), the pressure at the motive inlet is approximately 13.2 bar, varying the diameter results in pressure values ranging from 7 bar to 23 bar.

The cross-sectional averaged pressure along the flow path for different motive nozzle diameters is presented in Figure 11.2. The nozzle diameter significantly influences the pressure distribution. Reducing the diameter leads to a decrease in pressure within the suction chamber. When the nozzle diameter is reduced to 2.6 mm, the suction chamber pressure reaches approximately 0.9 bar. Increasing the diameter causes the opposite effect, and for the 3.6 mm diameter, the overall pressure increase is almost entirely suppressed.

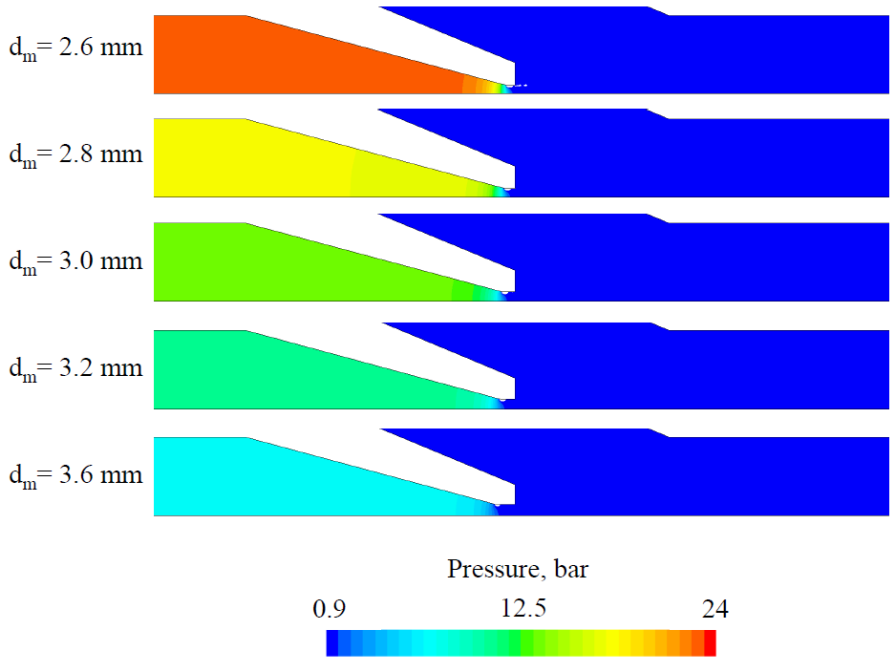

Figure 11.1. The influence of motive nozzle diameter D_{MN_2} on the pressure distribution in motive nozzle (velocity b.c. at the water inlet)

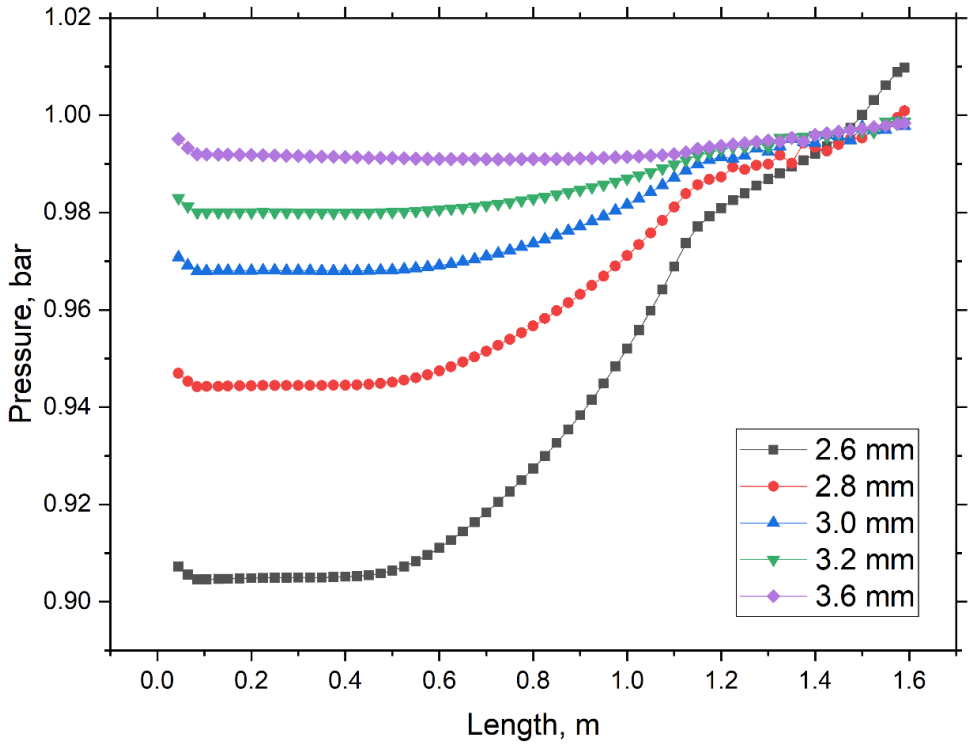

Figure 11.2. The influence of motive nozzle diameter D_{MN_2} on the cross-sectional averaged pressure along the flow path (velocity b.c. at the water inlet).

Figure 11.3 presents the influence of motive nozzle diameter on the cross-sectional averaged velocity along the flow path. While the velocity variations are less pronounced than those observed in the pressure distribution, they are still noticeable, especially at the diffuser outlet. Both increasing and decreasing the diameter result in lower outlet velocities. For the basic case 3.0 mm, the outlet velocity is 2.4 m/s, whereas for the 2.6 mm and 3.6 mm diameters, the velocity decreases to 0.76 and 1.37 m/s, respectively.

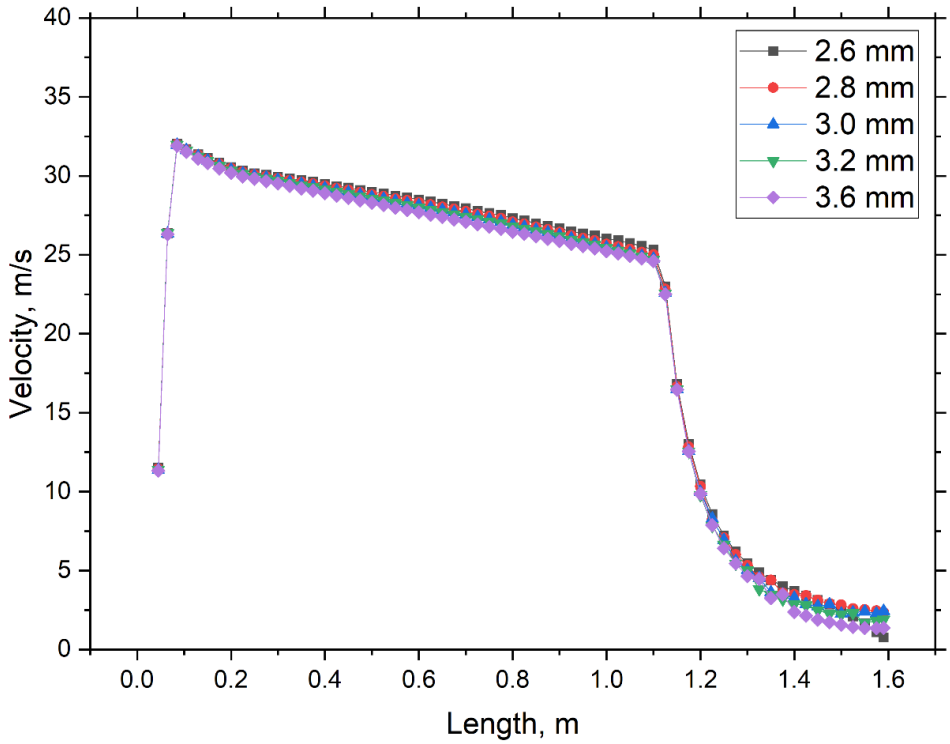

Figure 11.3. The influence of motive nozzle diameter D_{MN_2} on the cross-sectional averaged velocity along the flow path (velocity b.c. at the water inlet).

The cross-sectional mass-averaged temperature along the flow path for different motive nozzle diameters is presented in Figure 11.4. Increasing the motive nozzle diameter results in lower temperatures in the diffuser region, accompanied by more substantial fluctuations. Reducing the diameter leads to a higher outlet temperature, which is associated with more intensive condensation, as shown in Figure 11.5, presenting the cross-sectional averaged steam mass flow along the flow path for different motive nozzle diameters. Increasing the nozzle diameter causes the steam mass flow to decrease slightly faster in the mixing chamber. However, this trend strongly reverses in the diffuser, resulting in an overall less favorable condensation effect.

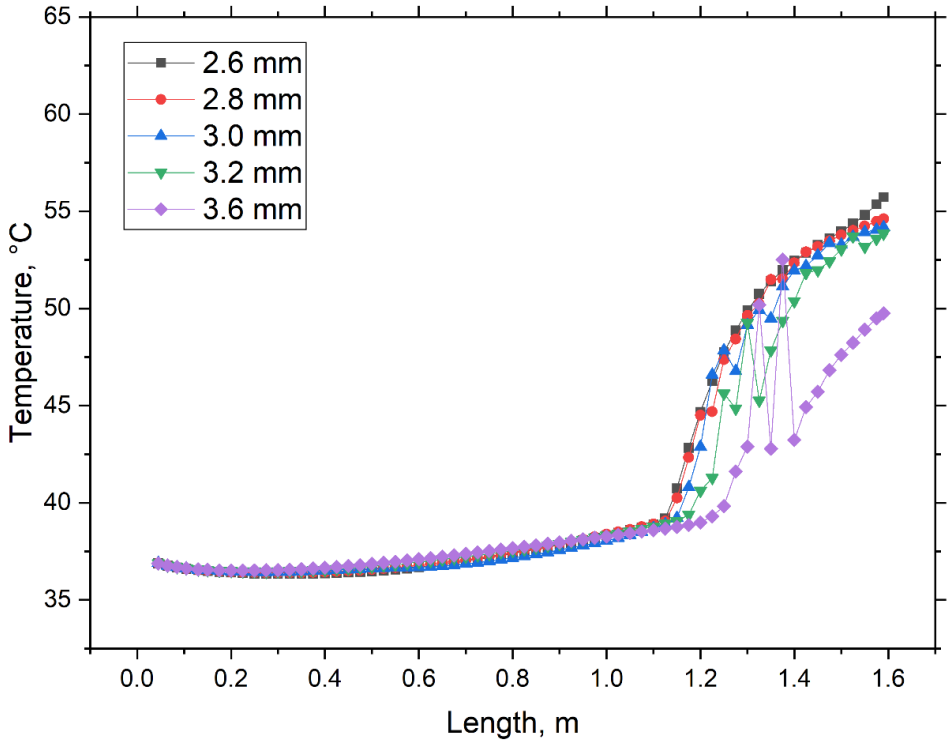

Figure 11.4. The influence of motive nozzle diameter D_{MN_2} on the cross-sectional mass-averaged temperature along the flow path (velocity b.c. at the water inlet).

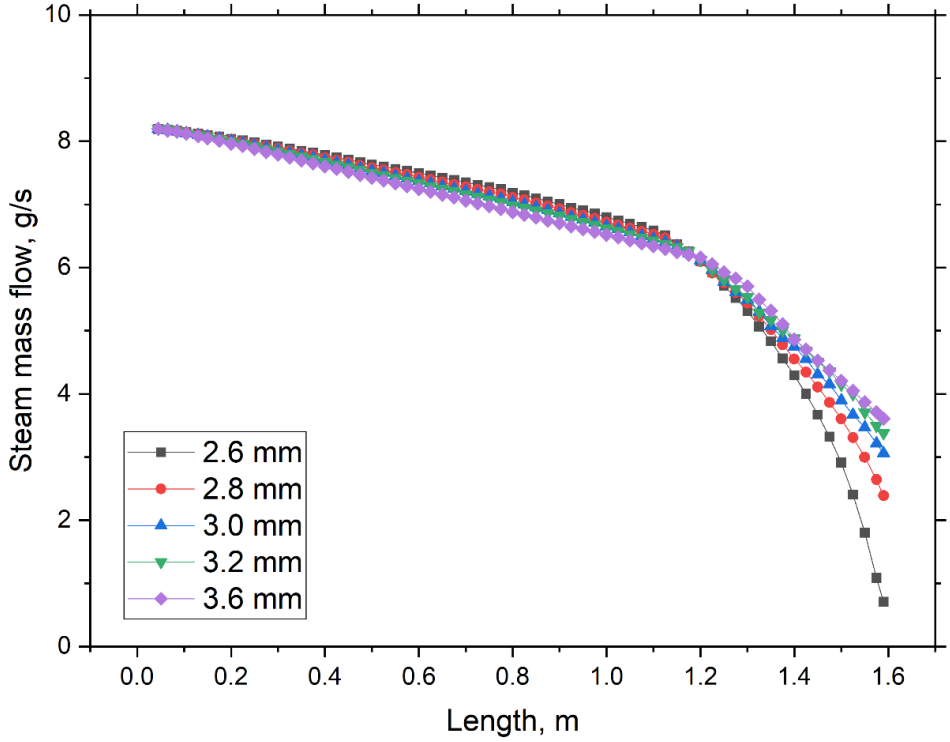

Figure 11.5. The influence of motive nozzle diameter D_{MN_2} on the cross-sectional averaged steam mass flow along the flow path (velocity b.c. at the water inlet).

The pressure scalar field for different motive nozzle diameters is presented in Figure 11.6. While the pressure remains nearly uniform in the radial direction within the mixing chamber in all considered cases, noticeable differences appear in the diffuser region.

Pressure fluctuations in the radial direction are significantly reduced for the increased diameter, which may be attributed to a minimal pressure lift effect.

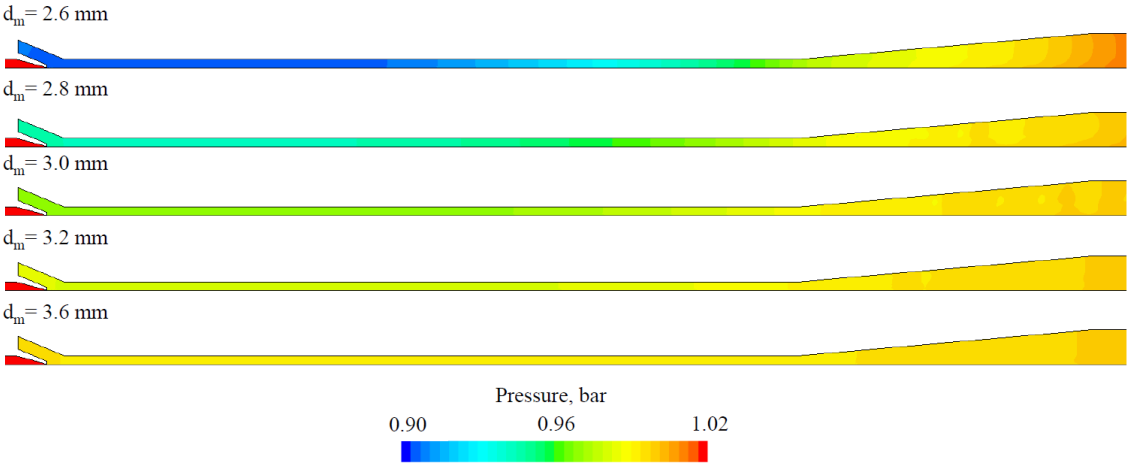

Figure 11.6. The influence of motive nozzle diameter D_{MN_2} on the pressure distribution (velocity b.c. at the water inlet)

Figure 11.7 presents the influence of motive nozzle diameter on the steam volume fraction distribution for velocity boundary conditions at the water inlet. Lower steam volume fractions are observed within the water jet region, particularly for larger nozzle diameters. Moreover, the steam distribution in the diffuser region appears more diffuse for smaller diameters, which may indicate improved mixing and, consequently, more effective condensation.

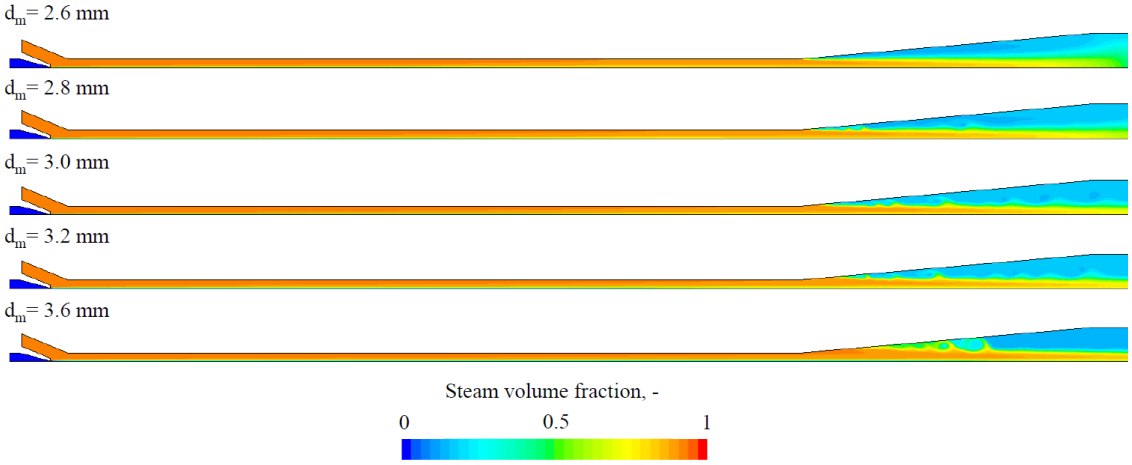

Figure 11.7. The influence of motive nozzle diameter D_{MN_2} on the steam volume fraction distribution (velocity b.c. at the water inlet)

The effect of motive nozzle diameter on the distribution of velocity, temperature, and condensation rate under the velocity boundary conditions at the water inlet is provided in the attachments (Figure A. 6, Figure A. 7, and Figure A. 8, respectively).

The results of the analysis concerning the influence of the motive nozzle diameter on ejector performance, with velocity specified at the water inlet, are summarised in Table 11.1. The nozzle diameter significantly affects both the condensation efficiency and the pressure-related parameters. As the diameter decreases, compression ratio and condensation efficiency increase, reaching 1.11 and 91.4 %, respectively, for the 2.6 mm nozzle diameter. Increasing the diameter deteriorates the performance, resulting in insufficient compression and suction of the exhaust gas, as well as a low condensation efficiency (56.0%).

Table 11.1. Comparison of the ejector condenser performance based on non-dimensional parameters and generated suction pressure for various motive nozzle diameters D_{MN_2} (velocity b.c. at the water inlet)

	Nozzle diameter D_{MN_2}, mm	Suction pressure p_{suc}, bar	Compression ratio CR	Expansion ratio ξ	Mass entertainment ratio ER ($\times 10^{-3}$)	Condensation efficiency η, %
Velocity b.c.	**2.6**	0.91	1.11	25.51	29.51	91.4
	2.8	0.95	1.06	18.48	29.51	70.9
	3.0	**0.97**	**1.03**	**13.91**	**29.51**	**62.7**
	3.2	0.98	1.02	10.87	29.51	58.8
	3.6	1.00	1.00	7.13	29.51	56.0

11.1.2. Pressure boundary conditions at the motive inlet

When the pressure at the water inlet is fixed, changing the motive nozzle diameter results in varying mass flow rates of motive water, as presented in Table 11.2. The mass flow rate increases with nozzle diameter, and for the 3.6 mm diameter, it reaches almost twice the value observed for the 2.6 mm.

Table 11.2. The influence of motive nozzle diameter D_{MN_2} on the water mass flow rate for an assumed constant pressure at the water inlet.

Motive nozzle diameter	Mass flow rate of motive water
d_m= 2.6 mm	0.259 kg/s
d_m= 2.8 mm	0.301 kg/s
d_m= 3.0 mm	0.346 kg/s
d_m= 3.2 mm	0.393 kg/s
d_m= 3.6 mm	0.498 kg/s

The cross-sectional averaged pressure along the flow path for the analyzed motive nozzle diameters is presented in Figure 11.8. When the motive nozzle diameter is reduced, the pressure in the suction chamber is closer to ambient. For the 2.6 mm diameter, the suction pressure is approximately 0.98 bar, while for the 3.6 mm diameter, it is about 0.94 bar. Minor differences in outlet pressure, slightly favoring reduced diameter, are observed, but they do not significantly affect the overall evaluation due to the pronounced variation in suction pressure.

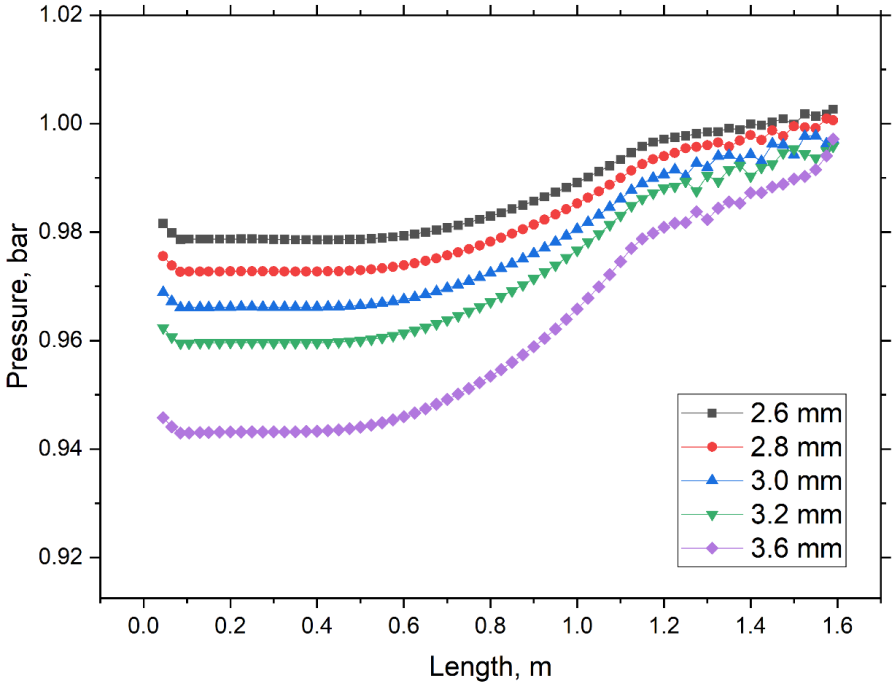

Figure 11.8. The influence of motive nozzle diameter D_{MN_2} on the cross-sectional averaged pressure along the flow path (pressure b.c. at the water inlet).

The cross-sectional averaged velocity along the flow path for the analyzed motive nozzle diameters is presented in Figure 11.9. Under constant pressure at the water inlet, the motive nozzle diameter does not considerably affect the velocity in the diffuser. In particular, the outlet velocity values remain nearly the same. The highest average velocity values for the reduced motive nozzle diameters are observed in the mixing chamber.

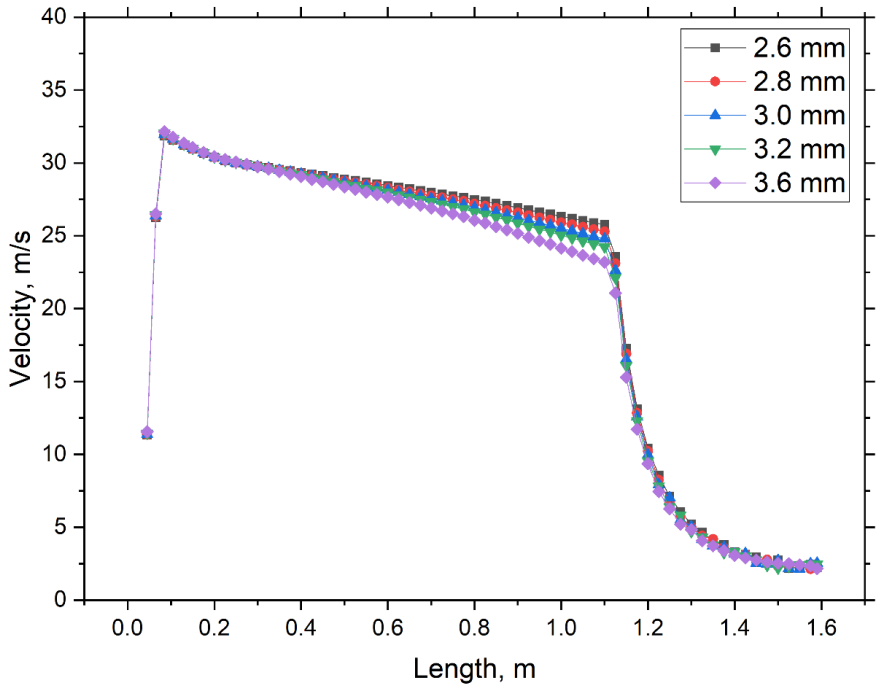

Figure 11.9. The influence of motive nozzle diameter D_{MN_2} on the cross-sectional averaged velocity along the flow path (pressure b.c. at the water inlet).

The cross-sectional mass-averaged temperature along the flow path for various motive nozzle diameters is shown in Figure 11.10. Lower temperatures are observed in the mixing chamber and the diffuser part for the increased diameters. This effect is primarily due to the higher water mass flow rate than less intensive condensation, which is confirmed by Figure 11.11 presenting the cross-sectional steam mass flow along the path for various motive nozzle diameters. Steam mass flow decreases significantly faster for increased diameter. When the motive nozzle diameters are 3.2 mm and 3.6 mm, the steam mass flow at the outlet is 1.3 and 2.5 g/s, respectively, while for a basic diameter of 3.0 mm it is 3.1 g/s.

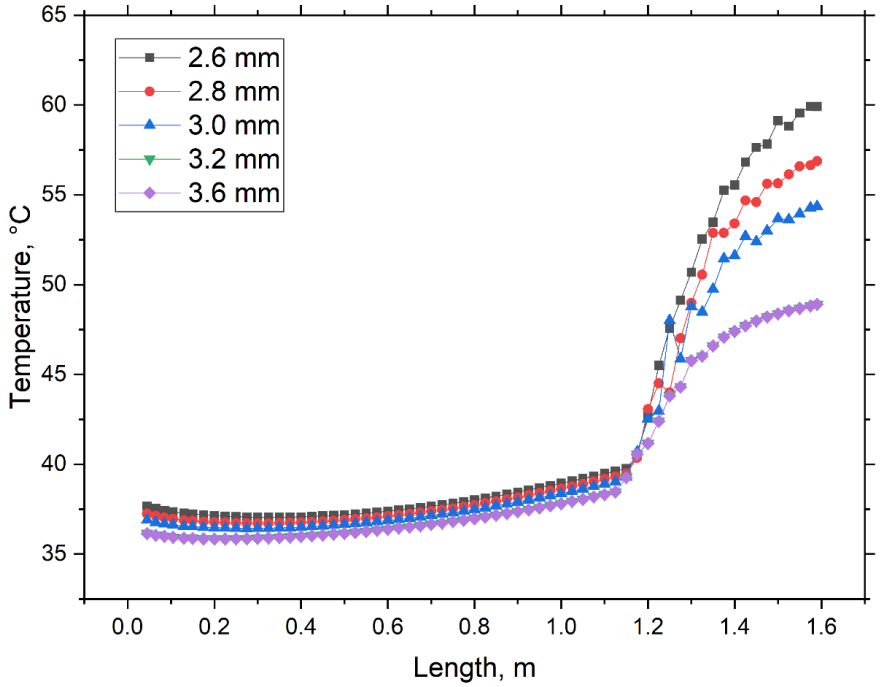

Figure 11.10. The influence of motive nozzle diameter D_{MN_2} on the cross-sectional mass-averaged temperature along the flow path (pressure b.c. at the water inlet).

The influence of motive nozzle diameter on the pressure distribution is presented in Figure 11.12. For the reduced diameters, the axial pressure increase is less pronounced. Additionally, the pressure field in the diffuser becomes more non-uniform, particularly in the radial direction. Figure 11.13 shows the steam volume fraction field for various motive nozzle diameters. Although increasing the diameter results in a higher water mass flow rate, the steam volume fraction within the mixing chamber remains nearly unchanged. The most noticeable differences occur in the diffuser region, where areas of high and low steam volume fractions regions are clearly distinguishable. For the reduced diameters, the steam content in the diffuser is significantly higher.

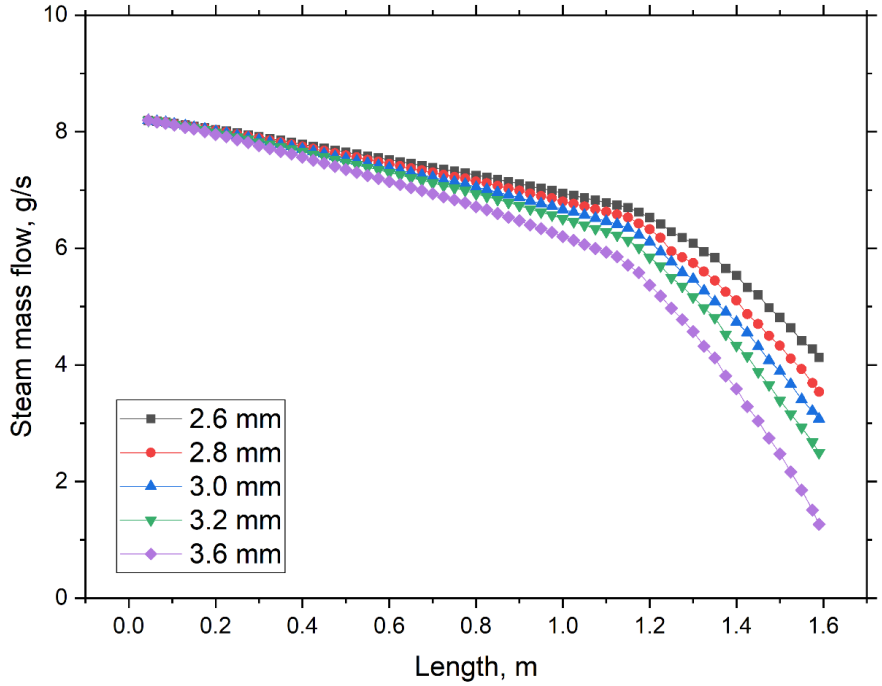

Figure 11.11. The influence of motive nozzle diameter D_{MN_2} on the cross-sectional averaged steam mass flow along the flow path (pressure b.c. at the water inlet).

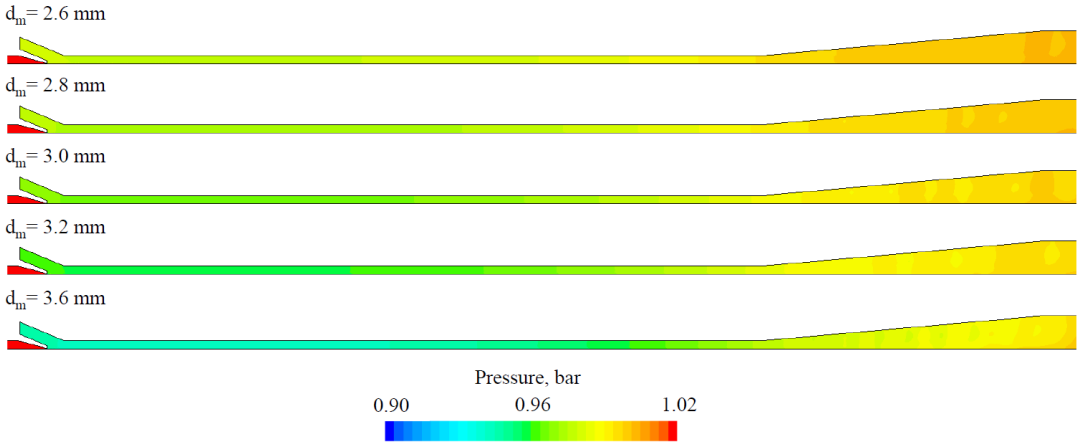

Figure 11.12. The influence of motive nozzle diameter D_{MN_2} on the pressure distribution (pressure b.c. at the water inlet).

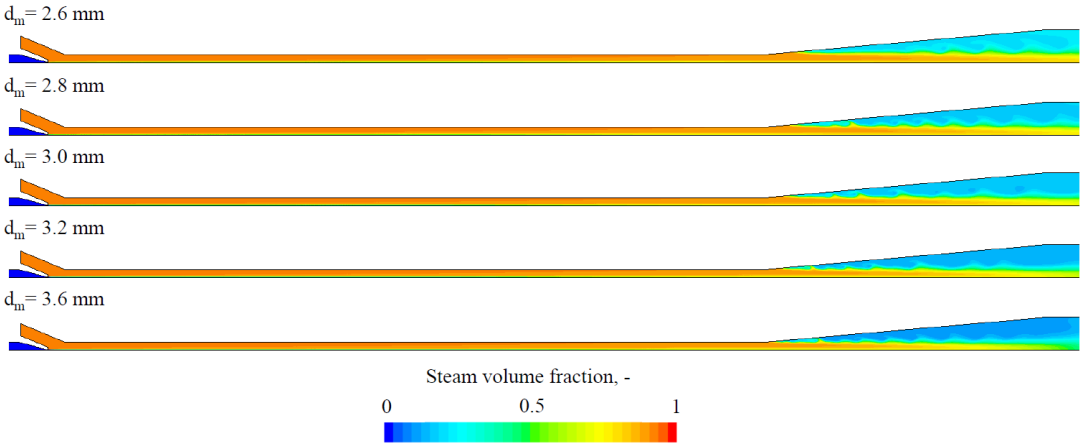

Figure 11.13. The influence of motive nozzle diameter D_{MN_2} on the steam volume fraction distribution (pressure b.c. at the water inlet).

The attachments (Figure A. 9, Figure A. 10, and Figure A. 11) illustrate the effect of motive nozzle diameter on velocity, temperature, and condensation rate distributions under the pressure boundary conditions at the water inlet.

Non-dimensional performance parameters and generated suction pressure for different motive nozzle diameters, assuming constant pressure at the water inlet, are presented in Table 11.3. Increasing the nozzle diameter results in a higher compression ratio and condensation efficiency, but a reduced mass entrainment ratio. For a 3.6 mm diameter, the compression ratio is 1.05 at a suction pressure of 0.97 bar, whereas for a 2.6 mm diameter, it is 1.02 at 0.98 bar. Due to the increased motive nozzle diameter, condensation efficiency improves significantly, rising by approximately 22 percentage points compared to the basic configuration.

Table 11.3. Comparison of the ejector condenser performance based on non-dimensional parameters and generated suction pressure for various motive nozzle diameters D_{MN_2} (pressure b.c. at the water inlet).

	Nozzle diameter D_{MN_2}, mm	Suction pressure p_{suc}, bar	Compression ratio *CR*	Expansion ratio ξ	Mass entertainment ratio *ER* ($\times 10^{-3}$)	Condensation efficiency η, %
Pressure b.c.	**2.6**	0.98	1.02	13.76	39.38	49.6
	2.8	0.98	1.03	13.84	33.94	56.8
	3.0	**0.97**	1.03	13.94	29.50	62.5
	3.2	0.96	1.03	14.03	25.93	69.5
	3.6	0.95	1.05	14.28	20.49	84.5

11.2. Analysis of outer nozzle diameter

The influence of outer nozzle diameter on the cross-sectional averaged pressure and steam mass flow along the flow path is presented in Figure 11.14, and Figure 11.15, respectively. The pressure and steam mass flow distributions are largely unaffected. It can be concluded that, within the investigated range, the outer nozzle diameter has a negligible impact on ejector performance. This observation is further supported by the performance parameters presented in Table 11.4, where no meaningful changes are observed.

Table 11.4. Comparison of the ejector condenser performance based on non-dimensional parameters and generated suction pressure for various outer nozzle diameters D_{TIP}.

Outer nozzle diameter D_{TIP}, mm	Suction pressure p_{suc}, bar	Compression ratio *CR*	Expansion ratio ξ	Mass entertainment ratio *ER* ($\times 10^{-3}$)	Condensation efficiency η, %
5	0.97	1.03	13.93	29.51	63.2
10	0.97	1.03	13.91	29.51	62.7
15	0.97	1.03	13.95	29.51	63.2

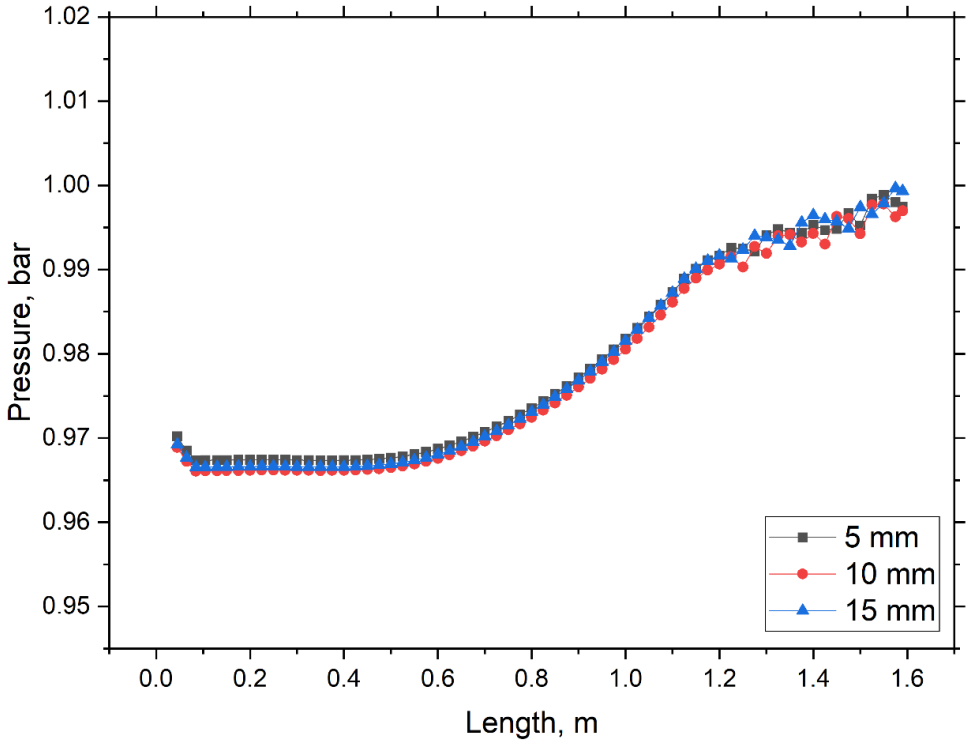

Figure 11.14. The influence of outer nozzle diameter D_{TIP} on the cross-sectional averaged pressure along the flow path.

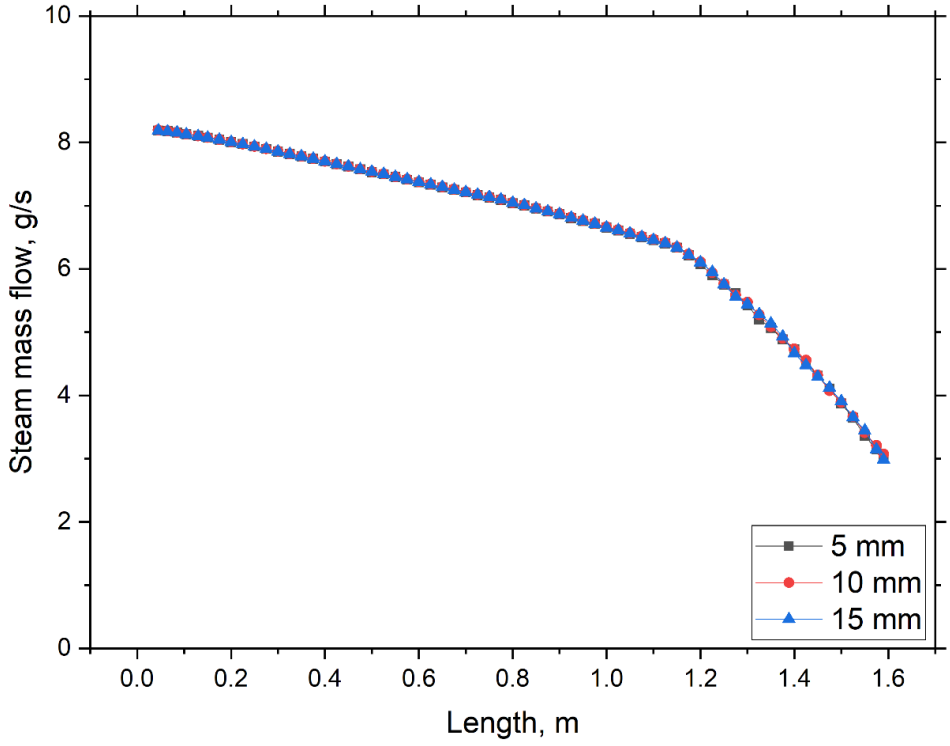

Figure 11.15. The influence of outer nozzle diameter D_{TIP} on the cross-sectional averaged steam mass flow along the flow path.

11.3. Analysis of nozzle exit position

The influence of nozzle exit position on the cross-sectional averaged pressure and steam mass flow along the flow path is presented in Figure 11.16 and Figure 11.17, respectively. No significant differences are observed in the pressure and steam mass flow distributions along the flow path under the analyzed operating conditions.

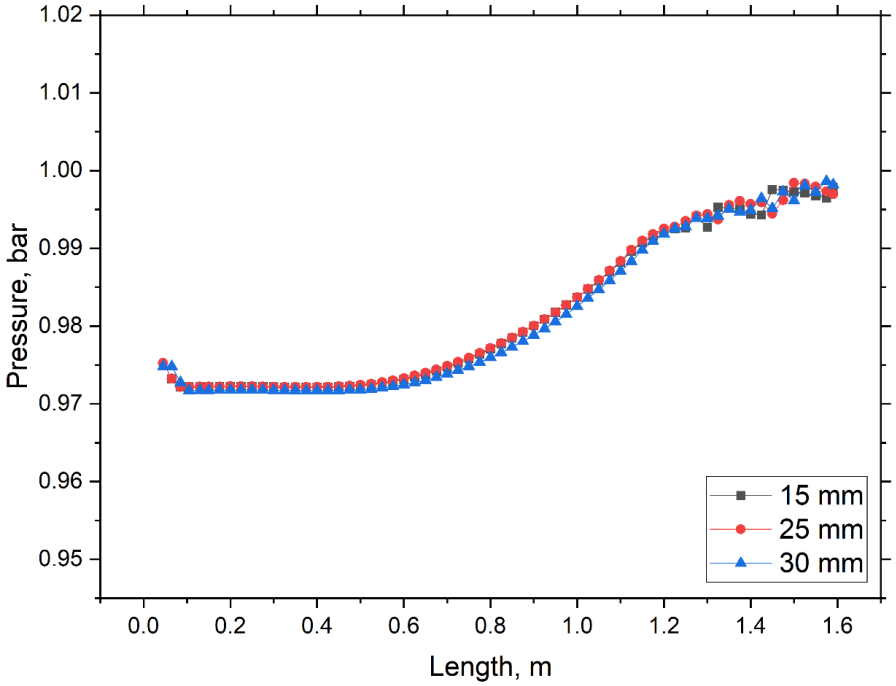

Figure 11.16. The influence of nozzle exit position L_{MCH} on the cross-sectional averaged pressure along the flow path.

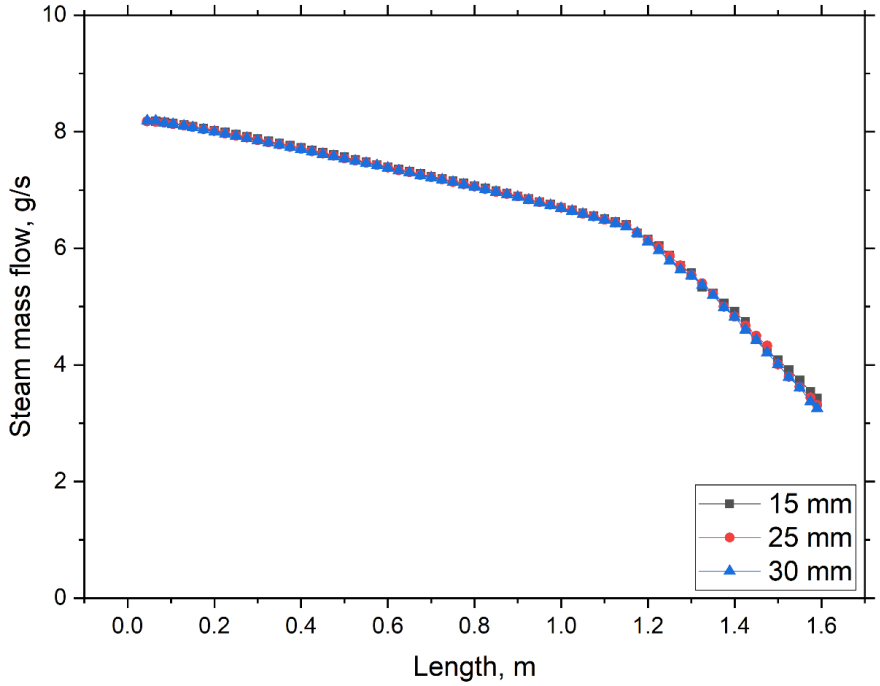

Figure 11.17. The influence of nozzle exit position L_{MCH} on the cross-sectional averaged steam mass flow along the flow path.

A summary in the form of non-dimensional parameters and generated suction pressure for various nozzle exit positions is presented in Table 11.5. A slight decrease in compression ratio and condensation efficiency is observed due to the change in nozzle exit position. However, these differences are minimal and can be considered negligible within the tested parameter range.

Table 11.5. Comparison of the ejector condenser performance based on non-dimensional parameters and generated suction pressure for various nozzle exit positions L_{MCH}.

Nozzle exit position L_{MCH}, mm	Suction pressure p_{suc}, bar	Compression ratio CR	Expansion ratio ξ	Mass entertainment ratio ER ($\times 10^{-3}$)	Condensation efficiency η, %
15	0.98	1.02	13.08	29.51	58.2
25	0.97	1.03	13.93	29.51	62.7
30	0.98	1.02	13.09	29.51	60.3

11.4. Analysis of nozzle configurations

Cross-sectional averaged pressure along the flow path for various configurations of the motive nozzle is presented in Figure 11.18. The application of the double-stage nozzle has a limited impact on the pressure distribution along the flow path. For the configuration with a longer distance between nozzles (v1), the pressure profile appears flatter, which may indicate reduced flow performance.

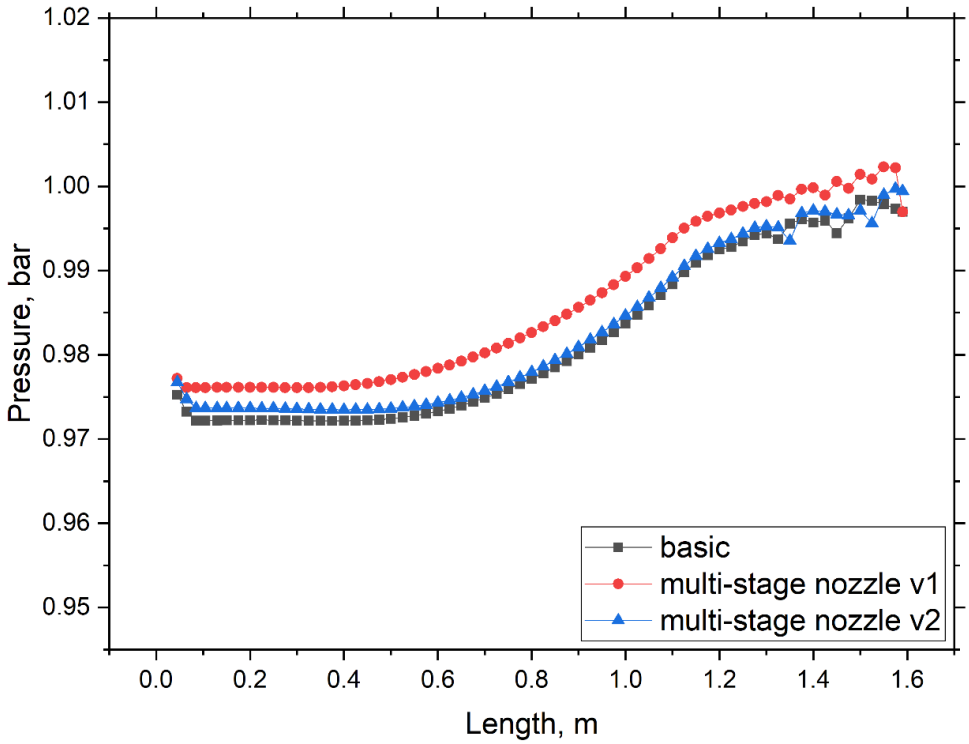

Figure 11.18. The influence of nozzle configuration on the cross-sectional averaged pressure along the flow path.

The influence of nozzle configuration on the cross-sectional averaged velocity along the flow path is presented in Figure 11.19. The velocity distributions in the suction chamber and diffuser are nearly identical. A difference in the average velocity for the multi-stage configuration with a longer distance between nozzles (v1) is observed in the mixing chamber, but it remains small and does not affect the outlet velocity.

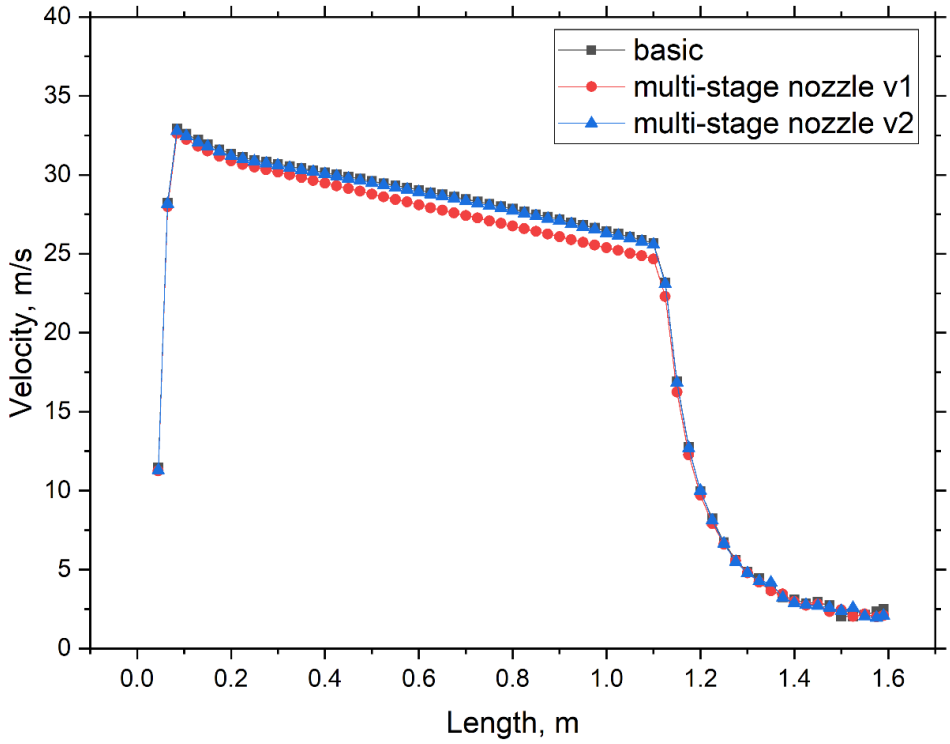

Figure 11.19. The influence of nozzle configuration on the cross-sectional averaged velocity along the flow path.

The condensation rate scalar field for various nozzle configurations is presented in Figure 11.20. Double-nozzle modification causes the condensation process to start earlier, which is visible through higher condensation rate values occurring in the channel between the nozzles for both multi-nozzle configurations. The highest condensation rates are observed for the configuration with a longer distance between nozzles (v1). These values occur inside the second nozzle, particularly near its inner wall, as well as in the region of the water jet downstream of the nozzle exit.

Differences in the condensation rate scalar field do not directly affect the overall performance of the spray-ejector condenser, as confirmed by Table 11.6, which compares the ejector condenser performance based on non-dimensional parameters and generated suction pressure for various nozzle configurations. The minor performance differences further argue against using a multi-stage nozzle in the analyzed configurations.

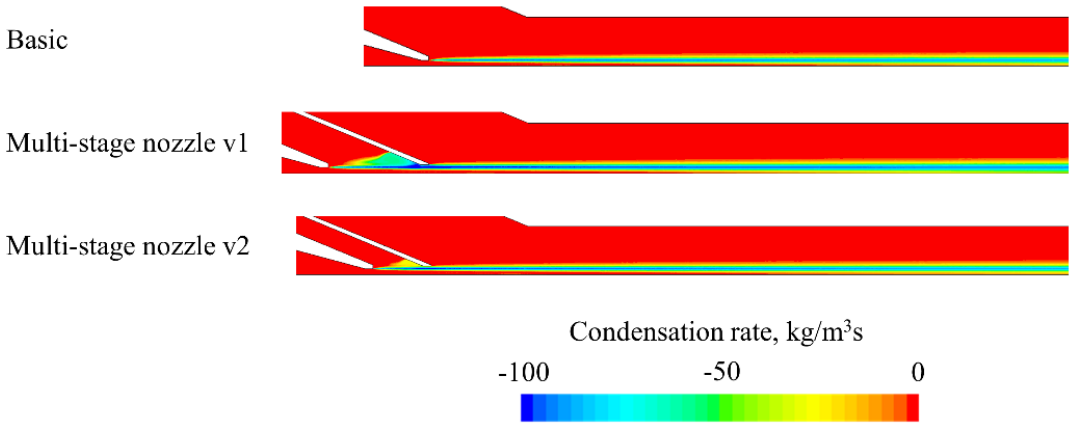

Figure 11.20. The influence of nozzle configuration on the condensation rate distribution.

Table 11.6. Comparison of the ejector condenser performance based on non-dimensional parameters and generated suction pressure for various nozzle configurations.

Nozzle configuration	Suction pressure p_{suc}, bar	Compression ratio CR	Expansion ratio ξ	Mass entertainment ratio ER ($\times 10^{-3}$)	Condensation efficiency η, %
Single (basic)	0.97	1.03	13.93	29.51	62.7
Multi-stage nozzle v1	0.98	1.02	13.07	29.51	60.0
Multi-stage nozzle v2	0.98	1.02	13.05	29.51	59.8

11.5. Analysis of the mixing chamber length

The cross-sectional averaged pressure along the flow path for various mixing chamber lengths is presented in Figure 11.21. The mixing chamber length significantly affects the pressure distribution across all ejector parts. Increasing the mixing chamber length results in lower pressure generated in the suction chamber and, consequently, a greater pressure rise along the flow path. Removing the diffuser causes the pressure in the suction chamber to be close to the ambient level, and the pressure recovery effect is essentially lost.

The influence of mixing chamber length on the cross-sectional averaged velocity along the flow path is presented in Figure 11.22. Changes in the mixing chamber length affect the mixture velocity at the diffuser outlet. Despite this, the velocity trends in the diffuser region remain quite similar, and the outlet velocity values are comparable across the cases.

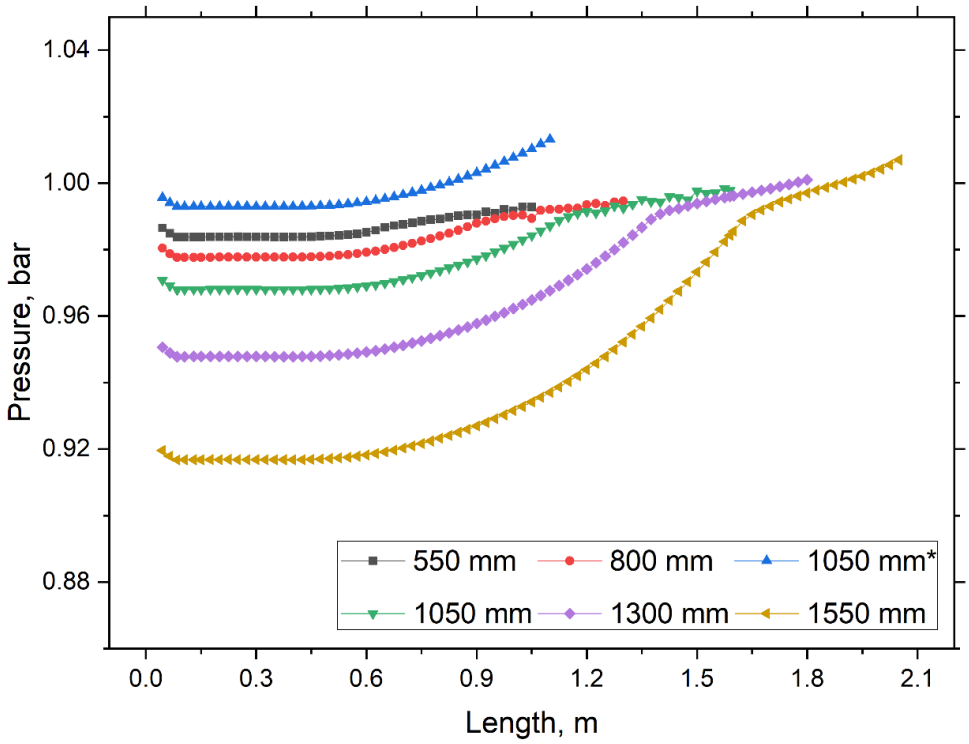

Figure 11.21. The influence of mixing chamber length L_{MIX} on the cross-sectional averaged pressure along the flow path.

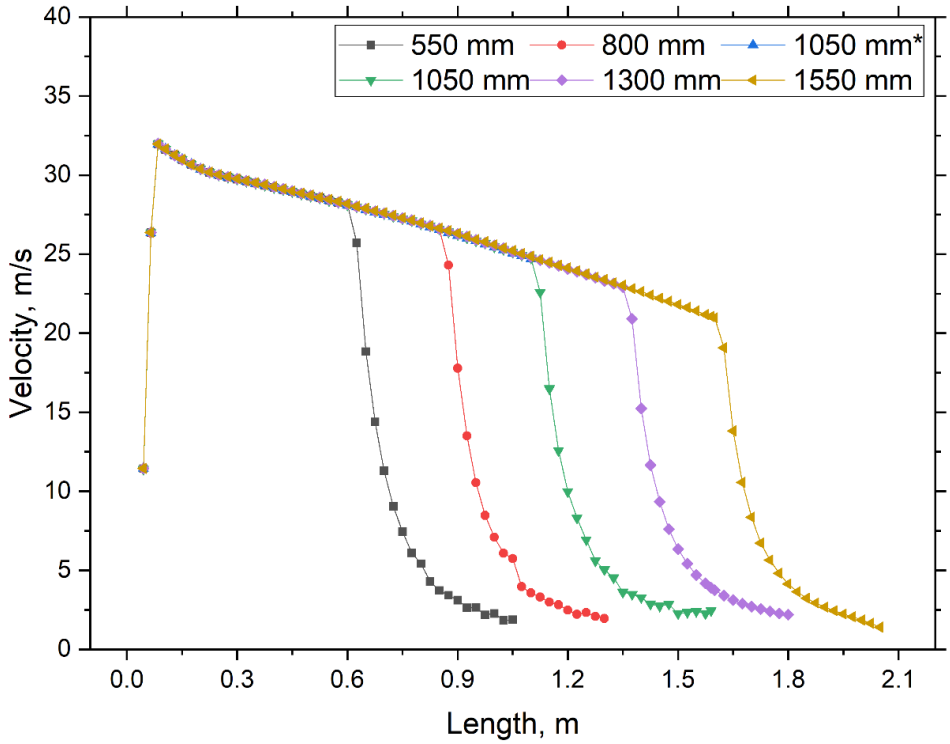

Figure 11.22. The influence of mixing chamber length L_{MIX} on the cross-sectional averaged velocity along the flow path.

The cross-sectional mass-averaged temperature along the flow path for various mixing chamber lengths is presented in Figure 11.23. Lengthening the mixing chamber leads to significantly higher outlet temperatures. For a length of 1550 mm, the outlet temperature reaches 56.5°C, while for 550 mm it is only 49.4°C. The most tremendous temperature increase occurs in the diffuser, therefore removing the diffuser results in only a minor temperature rise of the mixture (approximately 1.9°C).

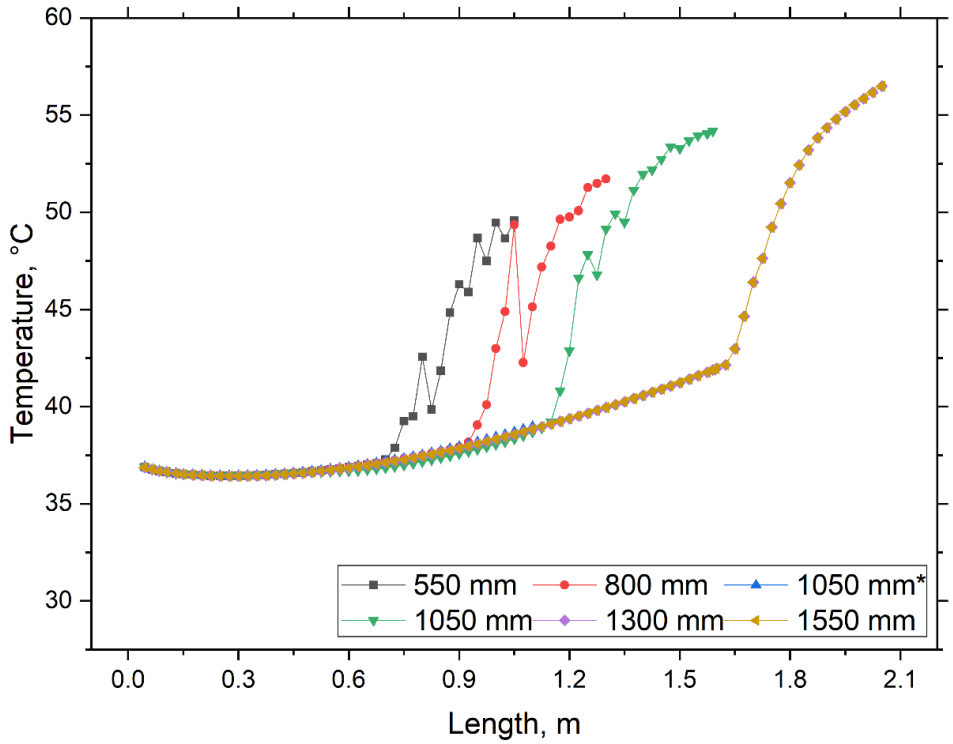

Figure 11.23. The influence of mixing chamber length L_{MIX} on the cross-sectional mass-averaged temperature along the flow path.

The impact of mixing chamber diameter on the cross-sectional averaged steam mass flow along the flow path is presented in Figure 11.24. Reducing the mixing chamber length shortens the contact time, resulting in a higher steam mass flow rate at the ejector outlet. Increasing the mixing chamber diameter leads to enhanced steam condensation not only within the mixing chamber itself, but also further downstream in the diffuser region.

The velocity scalar field for various mixing chamber lengths is presented in Figure 11.25. Lengthening the mixing chamber leads to a more homogenous velocity profile in the diffuser. A high-velocity region along the axis remains visible in the diffuser for shorter lengths. Significantly lower velocities in both the water jet and exhaust gas regions are observed in the configuration without a diffuser.

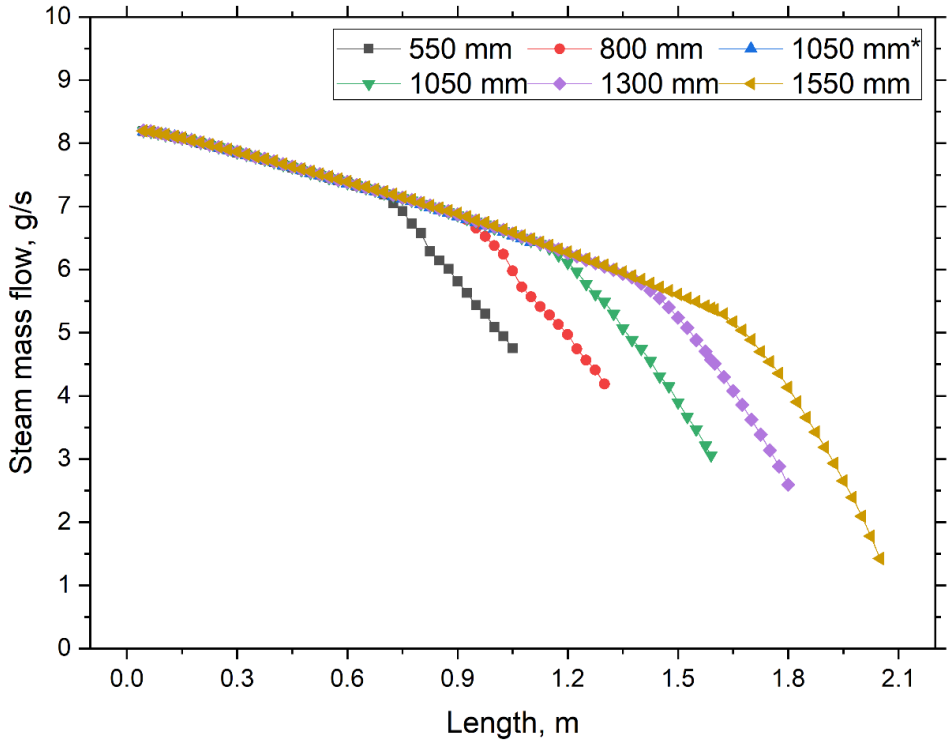

Figure 11.24. The influence of mixing chamber diameter L_{MIX} on the cross-sectional averaged steam mass flow along the flow path.

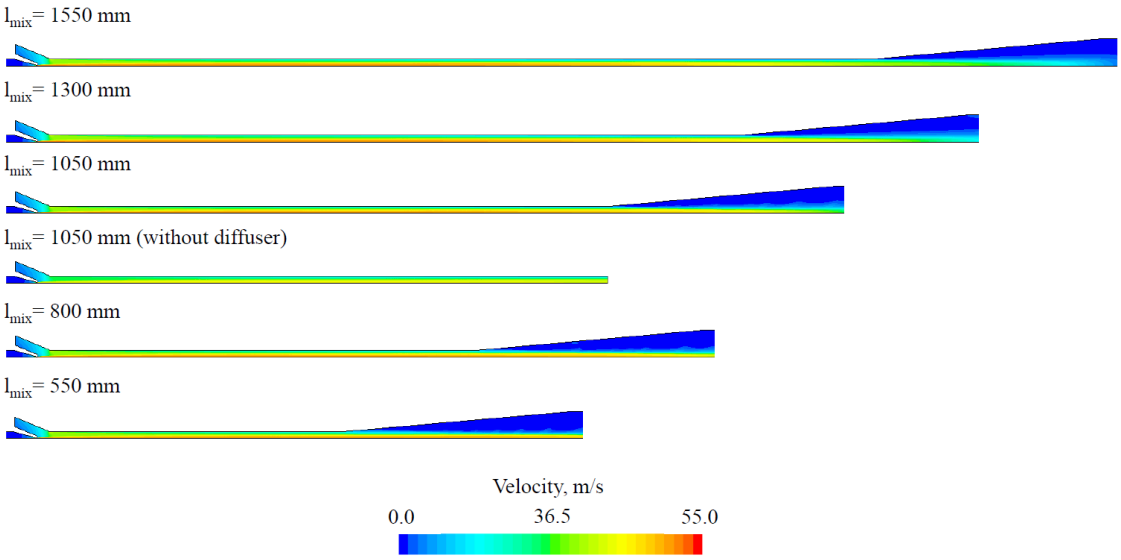

Figure 11.25. The influence of mixing chamber length D_{MIX} on the velocity distribution.

The influence of mixing chamber length on the steam volume fraction distribution is presented in Figure 11.16. Lower values are observed at both the mixing chamber and diffuser outlets as the mixing chamber length increases. Moreover, with increased length, steam volume fraction distribution becomes more dispersed in the diffuser, which may indicate improved mixing and more intensive condensation.

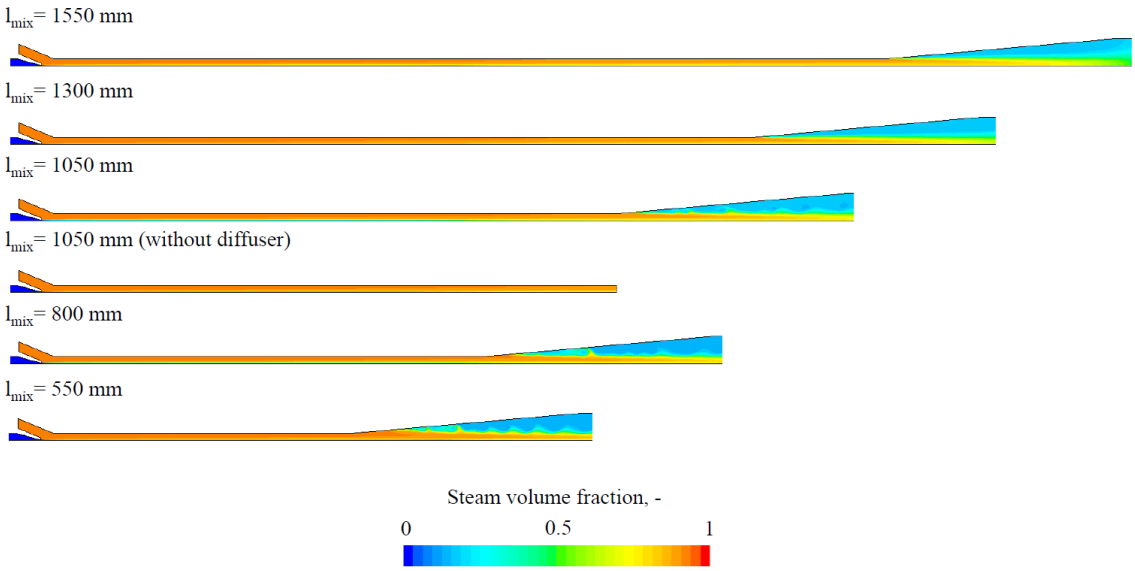

Figure 11.26. The influence of mixing chamber length L_{MIX} on the steam volume fraction distribution.

The influence of mixing chamber length on the pressure and temperature distributions is presented in the Appendix (Figure A. 12 and Figure A. 13).

A summary of the conducted research on the impact of mixing chamber length on thermal–flow performance is presented in Table 11.7, which shows non-dimensional parameters and generated suction pressure for analyzed cases. Shortening the mixing chamber length or removing the diffuser negatively affects condensation efficiency, generated suction pressure, and compression ratio. Reducing the length by 500 mm decreases condensation efficiency by 20.7 percentage points, whereas increasing it by a similar amount improves efficiency by 28 percentage points.

Table 11.7. Comparison of the ejector condenser performance based on non-dimensional parameters and generated suction pressure for various mixing chamber lengths L_{MIX}.

Mixing chamber length L_{MIX}, mm	**Suction pressure p_{suc}, bar**	**Compression ratio CR**	**Expansion ratio ξ**	**Mass entertainment ratio ER($\times 10^{-3}$)**	**Condensation efficiency η, %**
550	0.99	1.01	13.71	29.51	42.0
800	0.98	1.01	13.79	29.51	52.4
1050*	1.00	1.02	13.56	29.51	22.0
1050	0.97	1.03	13.91	29.51	62.7
1300	0.95	1.05	14.21	29.51	74.4
1550	0.92	1.10	14.65	29.51	90.7

11.6. Analysis of mixing chamber diameter

The cross-sectional averaged pressure along the flow path for various mixing chamber diameters is presented in Figure 11.27. A reduction in the mixing chamber diameter leads to a noticeable deterioration in the pressure recovery of the ejector. In particular, significant pressure losses are observed within the mixing chamber for 20 mm diameters. Increasing the mixing chamber diameter slightly elevates the pressure profiles in the suction and mixing chambers. Significant differences between various mixing chamber diameters are observed in Figure 11.28, which presents the influence of mixing chamber diameter on the cross-sectional averaged velocity along the flow path. Reduced mixing chamber diameters are associated with a considerable increase in the average velocity of the two-phase mixture. For the 20 mm diameter, the velocity in the mixing chamber reaches values between 45 m/s and 50 m/s, in contrast to 25–30 m/s observed for the basic diameter of 25 mm. Increasing the mixing chamber diameter reduces the mixture velocity, although the magnitude of this change is less significant than in the case of diameter reduction. Velocity distribution within the diffuser is largely unaffected, particularly in its second half.

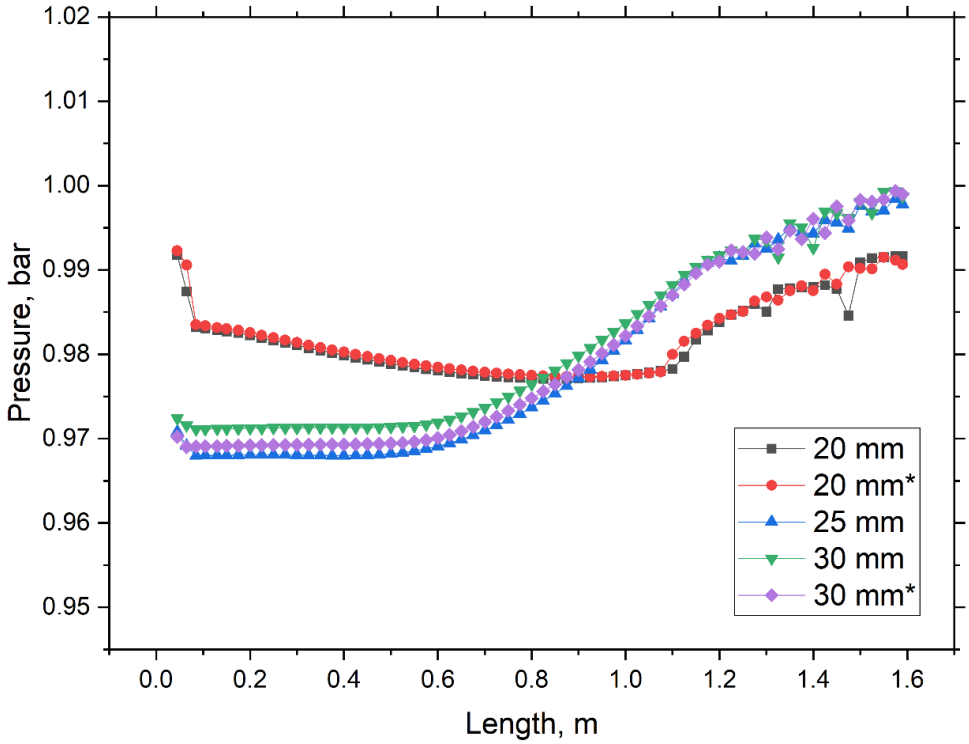

Figure 11.27. The influence of mixing chamber diameter D_{MIX} on the cross-sectional averaged pressure along the flow path.

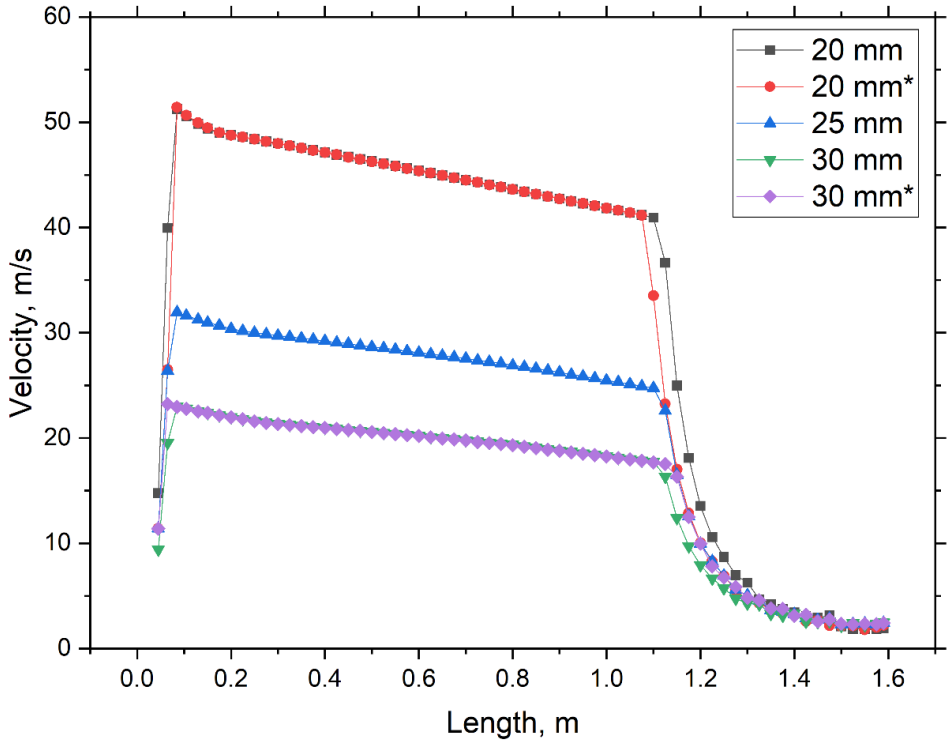

Figure 11.28. The influence of mixing chamber diameter D_{MIX} on the cross-sectional averaged velocity along the flow path.

The cross-sectional mass-averaged temperature along the flow path for various mixing chamber diameters is presented in Figure 11.29. The lowest temperatures in the diffuser region are observed for the 20 mm configurations, with outlet values around 50°C. Increasing the diameter has only a minor impact on the cross-sectional averaged temperature distribution. The outlet temperatures for the basic case (25 mm) and the configurations with larger diameters are nearly the same, approximately 54.6°C.

The cross-sectional averaged steam mass flow along the flow path for various mixing chamber diameters is presented in Figure 11.30. Even though the change in the mixing chamber diameter does not directly affect the steam mass flow rate within the mixing section, noticeable differences are observed at the diffuser outlet. Increasing the diameter results in less steam in the outlet mixture. The steam mass flow for the increased diameters ranges from 2.6–2.7 g/s, whereas for the reduced diameters, it is between 3.3 and 3.5 g/s. For the basic design (25 mm), the outlet steam mass flow is approximately 3.1 g/s, suggesting improved thermal performance for the configurations with increased diameters. This improvement occurs mainly in the final part of the mixing chamber and in the diffuser region, where the influence of the geometric modifications is most evident.

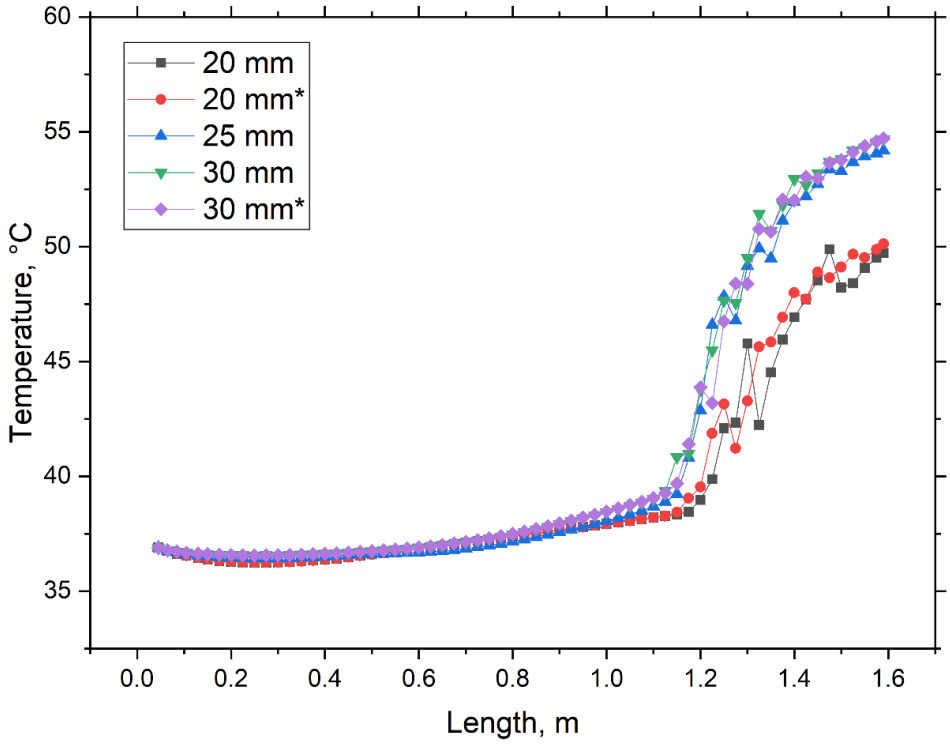

Figure 11.29. The influence of mixing chamber diameter D_{MIX} on the cross-sectional mass-averaged temperature along the flow path.

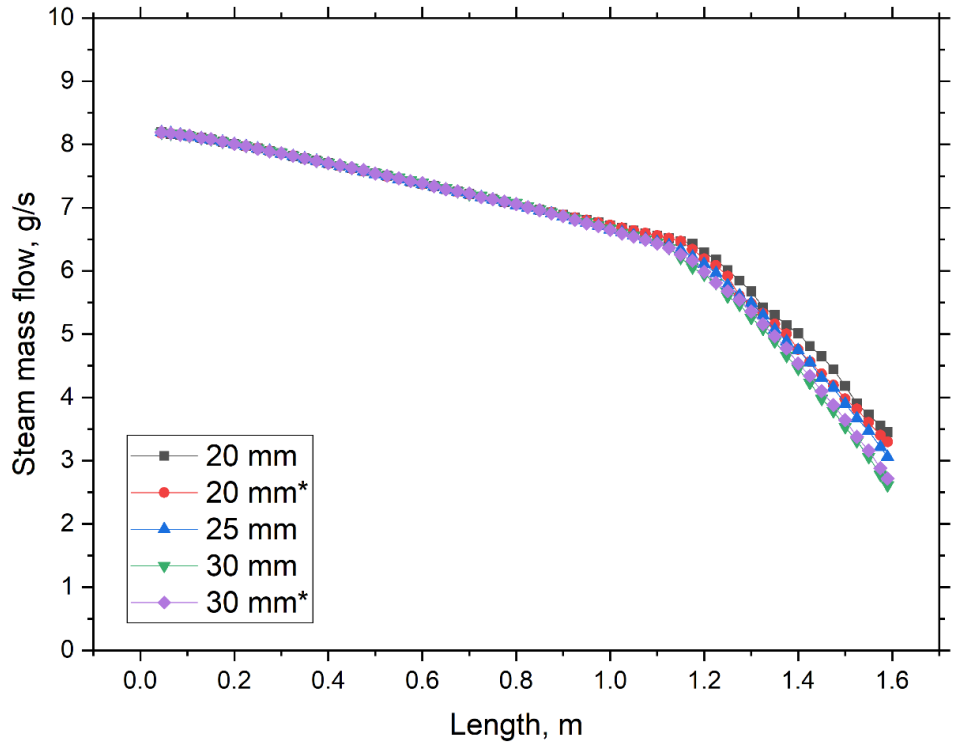

Figure 11.30. The influence of mixing chamber diameter D_{MIX} on the cross-sectional averaged steam mass flow along the flow path.

The velocity distribution for various mixing chamber diameters is presented in Figure 11.31. In the basic design and in the cases with increased diameter, a typical velocity contour for liquid-driven ejector operation is observed, with the highest velocity

occurring along the axis where the liquid jet is present. In contrast, for the reduced diameters, the velocity distribution becomes more uniform, with generally higher values across the entire cross-section.

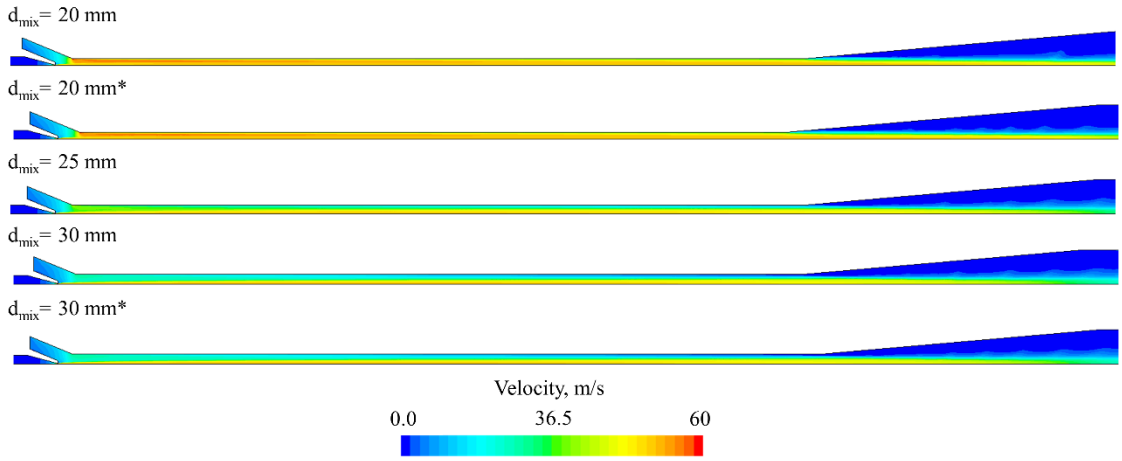

Figure 11.31. The influence of mixing chamber diameter D_{MIX} on the velocity distribution.

The influence of mixing chamber diameter on the temperature distribution is presented in Figure 11.32. When the mixing chamber diameter increases, the temperature difference between the hot gases and the cooling water persists over a longer distance. For the reduced diameter, the mixing process occurs significantly faster. Despite these differences, in the second half of the mixing chamber, all configurations reach a homogeneous temperature profile of similar value.

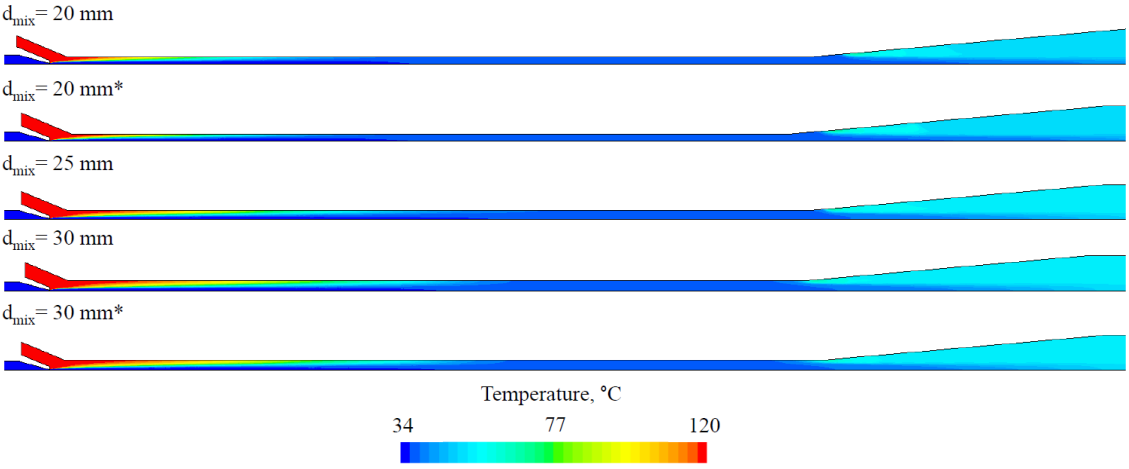

Figure 11.32. The influence of mixing chamber diameter D_{MIX} on the temperature distribution.

The figures illustrating the influence of mixing chamber diameter on the pressure, steam volume fraction, and condensation rate distributions are provided in the Appendix (Figure A. 14, Figure A. 15, and Figure A. 16, respectively).

The investigation of the influence of mixing chamber diameter on the overall performance of the ejector is summarized in Table 11.8, based on a comparison between non-dimensional parameters and the generated suction pressure. Increasing the diameter from 25 mm to 30 mm improves condensation efficiency by 4.1 to 5.4 percentage points, depending on the specific configuration. Reducing the diameter deteriorates both thermal and flow performance.

Table 11.8. Comparison of the ejector condenser performance based on non-dimensional parameters and generated suction pressure for various mixing chamber diameters D_{MIX}.

Mixing chamber diameter D_{MIX}, mm	**Suction pressure p_{suc}, bar**	**Compression ratio *CR***	**Expansion ratio ξ**	**Mass entertainment ratio *ER* ($\times 10^{-3}$)**	**Condensation efficiency η, %**
20	0.99	1.00	13.65	29.51	57.9
20*	0.99	1.00	13.65	29.51	59.8
25	0.97	1.03	13.91	29.51	62.7
30	0.97	1.03	13.89	29.51	68.1
30*	0.97	1.03	13.93	29.51	66.8

12. Analysis of the modeling results for the final geometrical model

Based on the results from numerical investigations, insights from experimental research, and constraints related to the operating environment in the negative CO_2 emission gas power plant, the final nLPL geometrical model was developed. The corresponding dimensions are provided in Table 4.1 (page 29).

Similar submodels and model settings, selected based on literature review and previous numerical analyses, were applied in computational models using the newly developed geometry. The boundary conditions applied in the analysis of nLPL geometrical model are specified in Table 7.3 (page 55). A mesh independence study was conducted to ensure that the solution was independent of mesh density. The properties of the investigated meshes and the final selected mesh are presented in Table 7.2 (page 52). The results, expressed as the relative change in non-dimensional performance parameters and outlet temperature due to mesh refinement, are summarized in Table 12.1. The number of mesh elements was increased by a constant factor of 1.6. The mesh with 860784 elements was selected, as the variation in parameters due to further refinement was below 2% compared to the previous mesh.

Table 12.1. Mesh independence study for the nLPL geometrical model: relative variation of non-dimensional performance parameters and outlet temperature due to mesh refinements.

Number of elements	Relative variation due to mesh refinements, %			
	Compression ratio ξ	Expansion ratio θ	Mass entertainment ratio ω_m	Outlet temperature T_o
80205	-	-	-	-
130016	2.9	2.9	0.6	0.0
208323	3.7	3.7	0.1	0.0
335754	9.7	19.8	0.5	0.1
537990	3.8	3.8	0.3	0.0
860784	**1.7**	**1.7**	**0.4**	**0.0**
1376335	1.4	1.3	0.1	0.1

The final results for the developed nLPL geometry, compared with experimental data, are summarized in Table 12.2. The obtained compression ratio of 1.13 at a suction pressure of 0.94 bar indicates satisfactory flow performance. The calculated error is 6.3% for the mass entrainment ratio and below 1% for the remaining parameters, confirming

that the model accurately predicts the operation of ejector with the nLPL geometrical configuration.

Table 12.2. Performance results of the nLPL geometrical model predicted by the CFD analysis, with reference values from the experiment.

Case	Suction pressure p_{suc}, bar	Outlet temperature T_{out}, K	Compression ratio *CR*	Expansion ratio ξ	Mass entertainment ratio ω_m ($\times 10^{-3}$)
CFD	0.94	312.6	1.13	16.99	18.8
Exp.	0.95	315.2	1.14	16.84	20.0
Error, %	**0.9**	**0.8**	**0.2**	**0.9**	**6.3**

The thermal performance of the developed model can be evaluated by analyzing steam mass flow and the corresponding condensation efficiency along the flow path, as presented in Figure 12.1. The results confirm that the steam is fully condensed at the ejector outlet. Similarly to the LPL geometrical model, the most intensive condensation occurs in the diffuser region.

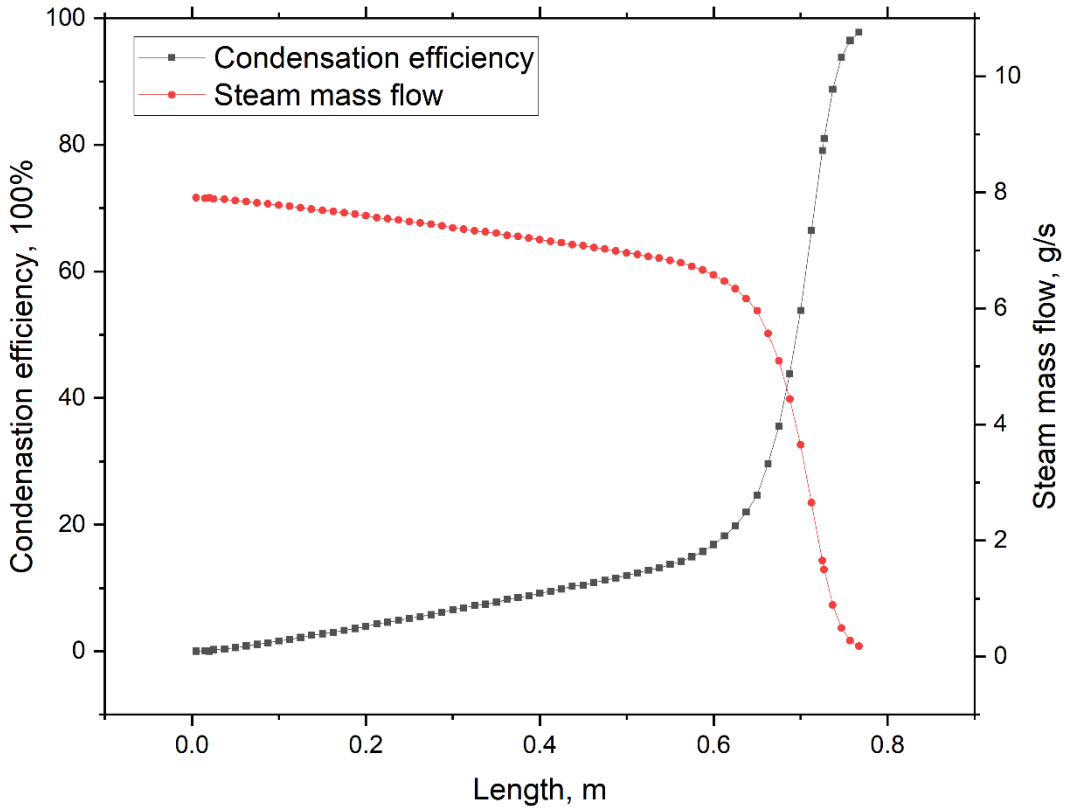

Figure 12.1. Steam mass flow and condensation efficiency along the flow path for the nLPL geometrical model.

The velocity scalar field for the final geometrical model is presented in Figure 12.2. region. A high-velocity region (40–60 m/s) is observed along the axis, reaching peak values within the diffuser. This region forms a jet and expands downstream, spreading radially as it progresses through the mixing chamber. Figure 12.3 shows the temperature distribution for the nLPL geometrical model. Although the gas experiences limited cooling through most of the mixing chamber, a uniform temperature distribution is achieved near the diffuser outlet, indicating effective mixing and condensation.

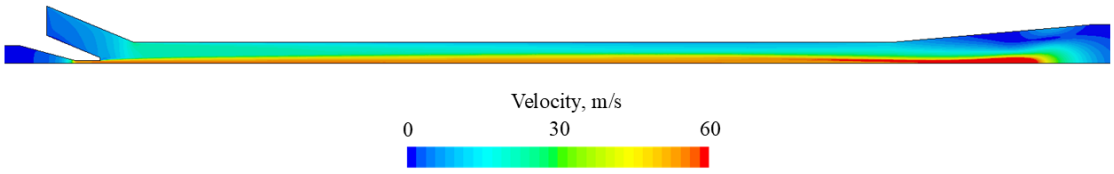

Figure 12.2. Velocity distribution for the nLPL geometrical model.

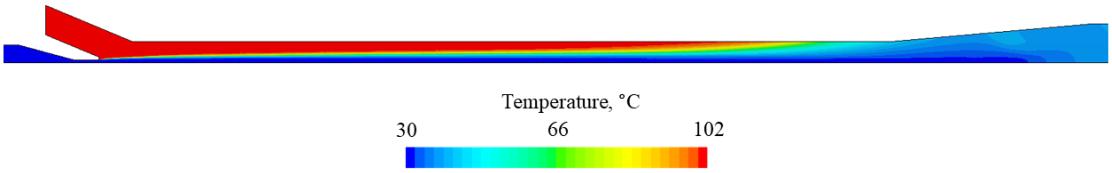

Figure 12.3. Temperature distribution for the nLPL geometrical model.

The condensation rate distribution presented in Figure 12.4 indicates, that condensation occurs mainly along the axis region and in the second half of the diffuser. The highest condensation rates are observed near the axis, where the water jet is present, while in the diffuser, moderate values are reached but over a larger volume. The water and CO_2 volume fraction distributions are presented in the Appendix (Figure A. 17 and Figure A. 18).

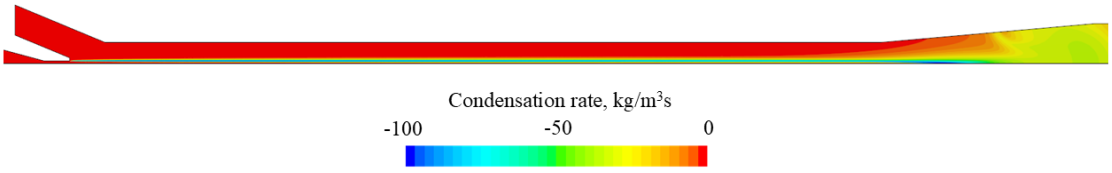

Figure 12.4. Condensation rate distribution for the nLPL geometrical model.

13. Summary

The thesis concerns the numerical investigation of multiphase, turbulent flow with heat transfer and condensation in a spray-ejector condenser. The ejector is one of the key components of a negative CO_2 emission gas power plant, responsible for entraining exhaust gases and condensing the steam. The study aimed to develop a reliable numerical model of a liquid-driven, two-phase ejector, incorporating the effects of direct contact condensation in the presence of an inert gas (CO_2). The model provides insight into the thermal and flow phenomena and enables the evaluation of condensation efficiency under various operating conditions. Finally, the modeling results supported the refinement of the ejector geometry to enhance steam condensation performance.

The literature review on ejector operation and modeling techniques highlighted gaps in understanding physical phenomena and limitations of existing computational models. Currently, most studies focus on gas-driven, two-phase ejectors operating in supersonic regimes with spontaneous condensation, typically applied in refrigeration systems. While the available modeling techniques are well established for such applications, they are not tuned for liquid-driven, two-phase ejectors with direct contact condensation occurring in the presence of CO_2. The review enabled the identification of promising models that, after appropriate calibration, can accurately capture the complex phenomena in the spray-ejector condenser.

The axisymmetric, steady-state CFD model was developed using Simcenter Star-CCM+ software, based on the Finite Volume Method. The two-phase, three-component flow was simulated using the Mixture model based on the Euler–Euler approach. The Realizable k-ε model was applied to account for turbulence. Direct contact condensation was computed using the thermally-driven model, in which the condensation mass flow rate is determined from the local heat balance. A modified Armenante–Kirwan formulation of the Ranz–Marshall correlation for the Nusselt number was employed to reflect the effects of turbulent heat transfer on water droplets. The impact of carbon dioxide on the condensation intensity was considered indirectly by reducing the local heat transport coefficient as a function of CO_2 volume fraction.

The impact of boundary conditions, including both their type and specified values, on ejector performance and model robustness was examined. The assumed pressure at the gas inlet strongly affects the exhaust gas flow rate and, consequently, pressure performance and condensation intensity. The presence of CO_2 in the exhaust gas mixture

delays the condensation process. Several combinations of pressure and velocity boundary conditions were tested at the gas and water inlets. Under the examined operating conditions, model predictions were most affected by the gas inlet specification. Applying a velocity boundary condition at the gas inlet provided more physically consistent results.

To calibrate the developed model, a sensitivity analysis of the key submodels and model settings was performed. The study was preceded by a comprehensive mesh independence analysis, which included evaluating flow variable profiles, non-dimensional performance parameters, and mesh quality indicators. The assumed droplet diameter and the applied Nusselt Number significantly influenced the condensation efficiency. Several RANS-based turbulence models were tested, and their impact was primarily limited to the pressure distribution. Applying a third-order discretization scheme for the temperature solver led to more reliable thermal predictions.

The performance of the spray-ejector condenser for the basic geometrical configuration was evaluated using the calibrated CFD model, and the results were verified against experimental data. Three operating scenarios were considered, including nominal conditions, increased CO_2 mass content, and reduced exhaust gas flow rate. Good agreement with the experimental results was observed, with the relative errors below 16% for the expansion ratio and below 4% for the remaining parameters. The determined condensation efficiency ranges from 61.5% to 83.9%, with the lowest value corresponding to the nominal point.

To improve the condensation efficiency, an analysis of the influence of selected geometrical parameters of the motive nozzle and mixing chamber on scalar fields and overall performance indicators was conducted. Lengthening the mixing chamber and increasing its diameter significantly improved both condensation efficiency and the achieved compression ratio. A similar effect was observed when the motive nozzle diameter was increased under constant water pressure at the motive inlet. For the remaining parameters and configurations, the impact on performance was negligible.

The final geometrical model was developed based on numerical results, experimental insights, and operational constraints. The improved ejector geometry ensures complete steam condensation and generates moderate suction pressure (0.94 bar). The relative error of predicted parameters did not exceed 6.3 %. As the achieved performance met the requirements, the developed solution was implemented in a gas power plant with negative CO_2 emissions.

14. Literature

[1] Spalart, P. R., and Rumsey, C. L., 2007, “Effective Inflow Conditions for Turbulence Models in Aerodynamic Calculations,” AIAA Journal, **45**(10), pp. 2544–2553.

[2] Fetting, C., 2020, *The European Green Deal*, Vienna.

[3] Nematollahi, M. H., Dehaghani, A. H. S., Pirouzfar, V., and Akhondi, E., 2016, “Mixed Matrix Membranes Comprising PMP Polymer with Dispersed Alumina Nanoparticle Fillers to Separate CO2/N2,” Macromol Res, **24**(9), pp. 782–792. https://doi.org/10.1007/s13233-016-4113-6.

[4] Org, W., 2023, “State and Trends of Carbon Pricing 2023.” https://doi.org/10.1596/978-1-4648-2006-9.

[5] International Energy Agency, 2020, *The Role of CCUS in Low-Carbon Power Systems*, Paris.

[6] International Energy Agency, 2023, *CO2 Emissions in 2022*, Paris. [Online]. Available: www.iea.org.

[7] International Energy Agency, 2024, *CO2 Emissions in 2023*, Paris. [Online]. Available: www.iea.org.

[8] Crippa, M., Guizzardi, D., Pagani, F., Banja, M., Muntean, M., Schaaf, E., Becker, W., Monforti-Ferrario, F., Quadrelli, R., Risquez Martin, A., Taghavi-Moharamli, P., Köykkä, J., Grassi, G., Rossi, S., Brandao De Melo, J., Oom, D., Branco, A. , San-Miguel, J., and Vignati, E., 2023, *GHG Emissions of All World Countries*, Luxembourg. https://doi.org/10.2760/235266.

[9] International Energy Agency, 2020, *Energy Technology Perspectives 2020, Special Report on Carbon Capture Utilisation and Storage CCUS in Clean Energy Transitions*, Paris. [Online]. Available: www.iea.org/t&c/.

[10] Kuś, T., Subramanian, N., Madejski, P., and Karch, M., 2023, “Assessment of the Potential for Capture Using Post-Combustion Methods,” Mining – Informatics, Automation and Electrical Engineering , pp. 19–34.

[11] Ministerstwo Gospodarki, 2009, *Polityka Energetyczna Polski Do 2030 Roku*, Warszawa.

[12] Madejski, P., Chmiel, K., Subramanian, N., and Kuś, T., 2022, “Methods and Techniques for CO2 Capture: Review of Potential Solutions and Applications in Modern Energy Technologies,” Energies (Basel), **15**(3). https://doi.org/10.3390/en15030887.

[13] Strušnik, D., Marčič, M., Golob, M., Hribernik, A., Živić, M., and Avsec, J., 2016, “Energy Efficiency Analysis of Steam Ejector and Electric Vacuum Pump for a Turbine Condenser Air Extraction System Based on Supervised Machine Learning Modelling,” Appl Energy, **173**, pp. 386–405. https://doi.org/10.1016/j.apenergy.2016.04.047.

[14] Trela, M., Kwidzinski, R., Butrymowicz, D., and Karwacki, J., 2010, “Exergy Analysis of Two-Phase Steam-Water Injector,” Appl Therm Eng, **30**(4), pp. 340–346. https://doi.org/10.1016/j.applthermaleng.2009.09.011.

[15] Śmierciew, K., Butrymowicz, D., Przybyliński, T., and Pawluczuk, A., 2017, “Investigations of Heat and Momentum Transfer in Two-Phase Injector Operating with Isobutane,” Appl Therm Eng, **127**, pp. 1495–1505. https://doi.org/10.1016/j.applthermaleng.2017.08.160.

[16] Śmierciew, K., Butrymowicz, D., Kwidziński, R., and Przybyliński, T., 2015, "Analysis of Application of Two-Phase Injector in Ejector Refrigeration Systems for Isobutane," Appl Therm Eng, **78**, pp. 630–639. https://doi.org/10.1016/j.applthermaleng.2014.11.064.

[17] Koirala, R., Linh Ve, Q., Date, A., Inthavong, K., and Akbarzadeh, A., 2023, "Influence of Inlet Pressure and Geometric Variations on the Applicability of Eductor in Low Temperature Thermal Desalinations," Journal of King Saud University - Engineering Sciences, **35**(2), pp. 137–147. https://doi.org/10.1016/j.jksues.2021.03.012.

[18] Mazzelli, F., and Milazzo, A., 2015, "Performance Analysis of a Supersonic Ejector Cycle Working with R245fa," International Journal of Refrigeration, **49**, pp. 79–92. https://doi.org/10.1016/j.ijrefrig.2014.09.020.

[19] Memet, F., and Preda, A., 2015, "An Analysis of the Performance of an Ejector Refrigeration Cycle Working with R134a," *IOP Conference Series: Materials Science and Engineering*, Institute of Physics Publishing. https://doi.org/10.1088/1757-899X/95/1/012035.

[20] Croquer, S., Poncet, S., and Galanis, N., 2016, "Comparison of Ejector Predicted Performance by Thermodynamic and CFD Models," International Journal of Refrigeration, **68**, pp. 28–36. https://doi.org/10.1016/j.ijrefrig.2016.04.026.

[21] Atmaca, A. U., Erek, A., and Ekren, O., 2020, "Investigation of the Liquid–Vapor Separator Efficiency on the Performance of the Ejector Used as an Expansion Device in the Vapor-Compression Refrigeration Cycle," ASME Journal of Energy Resources Technology, **142**(1). https://doi.org/10.1115/1.4044354.

[22] Khaliq, A., Almohammadi, B. A., Alharthi, M. A., Siddiqui, M. A., and Kumar, R., 2021, "Investigation of a Combined Refrigeration and Air Conditioning System Based on Two-Phase Ejector Driven by Exhaust Gases of Natural Gas Fueled Homogeneous Charge Compression Ignition Engine," J Energy Resour Technol, **143**(12). https://doi.org/10.1115/1.4052248.

[23] Seckin, C., 2020, "Effect of Operational Parameters on a Novel Combined Cycle of Ejector Refrigeration Cycle and Kalina Cycle," ASME Journal of Energy Resources Technology., **142**(1). https://doi.org/10.1115/1.4044220.

[24] Chowdhury, Md. T., and Mokheimer, E. M. A., 2022, "Performance Assessment of Solar Parabolic Trough Collector-Assisted Combined Organic Rankine Cycle and Triple Pressure Level Ejector-Absorption Refrigeration Cycle," ASME Journal of Energy Resources Technology, **144**(11). https://doi.org/10.1115/1.4053893.

[25] Aronson, K. E., Ryabchikov, A. Yu., Kuptsov, V. K., Murmanskii, I. B., Brodov, Yu. M., Zhelonkin, N. V., and Khaet, S. I., 2017, "Ejectors of Power Plants Turbine Units Efficiency and Reliability Increasing," J Phys Conf Ser, **891**, p. 012249. https://doi.org/10.1088/1742-6596/891/1/012249.

[26] Wang, C., Wang, L., Wang, X., and Zhao, H., 2017, "Design and Numerical Investigation of an Adaptive Nozzle Exit Position Ejector in Multi-Effect Distillation Desalination System," Energy, **140**, pp. 673–681. https://doi.org/10.1016/j.energy.2017.08.104.

[27] Dong, J., Hu, Q., Yu, M., Han, Z., Cui, W., Liang, D., Ma, H., and Pan, X., 2020, "Numerical Investigation on the Influence of Mixing Chamber Length on Steam Ejector Performance," Appl Therm Eng, **174**, p. 115204. https://doi.org/10.1016/j.applthermaleng.2020.115204.

[28] Sokolov, E., and Zinger, N., 1989, "Jet Devices (in Russian)," Moscow: Energoatomizdat.

[29] Grazzini, G., Milazzo, A., and Mazzelli, F., 2018, *Ejectors for Efficient Refrigeration: Design, Applications and Computational Fluid Dynamics*, Springer International Publishing. https://doi.org/10.1007/978-3-319-75244-0.

[30] Elbel, S., and Lawrence, N., 2016, "Review of Recent Developments in Advanced Ejector Technology," International Journal of Refrigeration, **62**, pp. 1–18. https://doi.org/10.1016/j.ijrefrig.2015.10.031.

[31] Croquer, S., Poncet, S., and Aidoun, Z., 2016, "Turbulence Modeling of a Single-Phase R134a Supersonic Ejector. Part 1: Numerical Benchmark," International Journal of Refrigeration, **61**, pp. 140–152. https://doi.org/10.1016/j.ijrefrig.2015.07.030.

[32] Aidoun, Z., Ameur, K., Falsafioon, M., and Badache, M., 2019, "Current Advances in Ejector Modeling, Experimentation and Applications for Refrigeration and Heat Pumps. Part 1: Single-Phase Ejectors," Inventions, **4**(1), p. 15. https://doi.org/10.3390/inventions4010015.

[33] Schillaci, E., Vera, J., Oliet, C., Vemula, J. B., Duponcheel, M., and Bartosiewicz, Y., 2024, "Numerical Modeling of Air Ejectors Covering Supersonic, Subsonic and Closed-Port Operations," Energy, **302**, p. 131627. https://doi.org/10.1016/j.energy.2024.131627.

[34] Croquer, S., Poncet, S., and Galanis, N., 2016, "Comparison of Ejector Predicted Performance by Thermodynamic and CFD Models," International Journal of Refrigeration, **68**, pp. 28–36. https://doi.org/10.1016/j.ijrefrig.2016.04.026.

[35] Kumar, N. S., and Ooi, K. T., 2014, "One Dimensional Model of an Ejector with Special Attention to Fanno Flow within the Mixing Chamber," Appl Therm Eng, **65**(1–2), pp. 226–235. https://doi.org/10.1016/j.applthermaleng.2013.12.055.

[36] Jorge de Oliveira Marum, V., Reis, L. B., Maffei, F. S., Ranjbarzadeh, S., Korkischko, I., Gioria, R. dos S., and Meneghini, J. R., 2021, "Performance Analysis of a Water Ejector Using Computational Fluid Dynamics (CFD) Simulations and Mathematical Modeling," Energy, **220**, p. 119779. https://doi.org/10.1016/j.energy.2021.119779.

[37] Chen, W., Liu, M., Chong, D., Yan, J., Little, A. B., and Bartosiewicz, Y., 2013, "A 1D Model to Predict Ejector Performance at Critical and Sub-Critical Operational Regimes," International Journal of Refrigeration, **36**(6), pp. 1750–1761. https://doi.org/10.1016/j.ijrefrig.2013.04.009.

[38] Mastrowski, M., Smolka, J., Butrymowicz, D., Antczak, Ł., Gagan, J., and Śmierciew, K., 2024, "Experimental Validation of the Theoretical Ejector Model in a Low-Grade Waste Heat Refrigeration System Using R1233zdE as a Working Fluid," Appl Therm Eng, **236**, p. 121716. https://doi.org/10.1016/j.applthermaleng.2023.121716.

[39] Śmierciew, K., Gagan, J., and Butrymowicz, D., 2019, "Application of Numerical Modelling for Design and Improvement of Performance of Gas Ejector," Appl Therm Eng, **149**, pp. 85–93. https://doi.org/10.1016/j.applthermaleng.2018.12.030.

[40] Xiao, J., Wu, Q., Chen, L., Ke, W., Wu, C., Yang, X., Yu, L., and Jiang, H., 2022, "Assessment of Different CFD Modeling and Solving Approaches for a Supersonic Steam Ejector Simulation," Atmosphere (Basel), **13**(1), p. 144. https://doi.org/10.3390/atmos13010144.

[41] Hemidi, A., Henry, F., Leclaire, S., Seynhaeve, J.-M., and Bartosiewicz, Y., 2009, "CFD Analysis of a Supersonic Air Ejector. Part II: Relation between Global Operation and Local Flow Features," Applied Thermal Engineering, **29**(14–15), pp. 2990–2998. https://doi.org/10.1016/j.applthermaleng.2009.03.019.

[42] Ringstad, K. E., Allouche, Y., Gullo, P., Ervik, Å., Banasiak, K., and Hafner, A., 2020, "A Detailed Review on CO2 Two-Phase Ejector Flow Modeling," Thermal Science and Engineering Progress, **20**. https://doi.org/10.1016/j.tsep.2020.100647.

[43] Taslimi Taleghani, S., Sorin, M., and Poncet, S., 2018, "Modeling of Two-Phase Transcritical CO2 Ejectors for on-Design and off-Design Conditions," International Journal of Refrigeration, **87**, pp. 91–105. https://doi.org/10.1016/j.ijrefrig.2017.10.025.

[44] Banasiak, K., and Hafner, A., 2011, "1D Computational Model of a Two-Phase R744 Ejector for Expansion Work Recovery," International Journal of Thermal Sciences, **50**(11), pp. 2235–2247. https://doi.org/10.1016/j.ijthermalsci.2011.06.007.

[45] Atmaca, A. U., Erek, A., and Ekren, O., 2020, "One-Dimensional Analysis of the Convergent-Divergent Motive Nozzle for the Two-Phase Ejector: Effect of the Operating and Design Parameters," Applied Thermal Engineering, **181**, p. 115866. https://doi.org/10.1016/j.applthermaleng.2020.115866.

[46] Śmierciew, K., Pawluczuk, A., Gagan, J., and Butrymowicz, D., 2019, "Thermodynamic Analysis of Two-Phase Injector for Various Working Fluids," Appl Therm Eng, **157**, p. 113713. https://doi.org/10.1016/j.applthermaleng.2019.113713.

[47] Wang, N., Bhushan, S., Cho, H., and Li, L., 2022, "Modeling of Vapor-Liquid Interactions in Condensing Ejectors," Appl Therm Eng, **206**, p. 118111. https://doi.org/10.1016/j.applthermaleng.2022.118111.

[48] Abu Khass, O., Tran, A. P., Klöppel, S., Stathopoulos, P., and Nicke, E., 2024, "1D Modelling of a Water-Steam Ejector as a Compression Step in High-Temperature Heat Pumps," *Volume 5: Cycle Innovations*, American Society of Mechanical Engineers. https://doi.org/10.1115/GT2024-124983.

[49] Palacz, M., Smolka, J., Fic, A., Bulinski, Z., Nowak, A. J., Banasiak, K., and Hafner, A., 2015, "Application Range of the HEM Approach for CO2 Expansion inside Two-Phase Ejectors for Supermarket Refrigeration Systems," International Journal of Refrigeration, **59**, pp. 251–258. https://doi.org/10.1016/j.ijrefrig.2015.07.006.

[50] Smolka, J., Bulinski, Z., Fic, A., Nowak, A. J., Banasiak, K., and Hafner, A., 2013, "A Computational Model of a Transcritical R744 Ejector Based on a Homogeneous Real Fluid Approach," Appl Math Model, **37**(3), pp. 1208–1224. https://doi.org/10.1016/j.apm.2012.03.044.

[51] Kandakure, M. T., Gaikar, V. G., and Patwardhan, A. W., 2005, "Hydrodynamic Aspects of Ejectors," Chem Eng Sci, **60**(22), pp. 6391–6402. https://doi.org/10.1016/j.ces.2005.04.055.

[52] Hassani, M., and Kouhikamali, R., 2024, “Investigation of Two Phase Liquid Jet Ejector with Simultaneous Air and Water Suction in Fresh Water Distillation System,” Energy, **301**, p. 131662. https://doi.org/10.1016/j.energy.2024.131662.

[53] Haida, M., Smolka, J., Hafner, A., Ostrowski, Z., Palacz, M., Nowak, A. J., and Banasiak, K., 2018, “System Model Derivation of the CO2 Two-Phase Ejector Based on the CFD-Based Reduced-Order Model,” Energy, **144**, pp. 941–956. https://doi.org/10.1016/j.energy.2017.12.055.

[54] Palacz, M., Smolka, J., Nowak, A. J., Banasiak, K., and Hafner, A., 2017, “Shape Optimisation of a Two-Phase Ejector for CO 2 Refrigeration Systems,” International Journal of Refrigeration, **74**, pp. 212–223. https://doi.org/10.1016/j.ijrefrig.2016.10.013.

[55] Chen, C., Liu, H., and Duan, P., 2025, “Research on the Ejection Performance of an Ejector with Low Pressure and Back Pressure,” Sci Rep, **15**(1), p. 15970. https://doi.org/10.1038/s41598-025-99722-1.

[56] Saeid, O., Hashem, G., Etaig, S., Belgasim, B., and Sagade, A., 2024, “Performance Assessment of Ammonia Base Solar Ejector Cooling System Emphasizing Ejector Geometries: A Detailed CFD Analysis,” Energy, **301**, p. 131770. https://doi.org/10.1016/j.energy.2024.131770.

[57] Ahmadiani, M., Riahi, A., Payamiazad, P., Minaei, M., and Shafii, M. B., 2024, “Investigation and Numerical Simulation of Two-Phase Ejectors for Use in the Water Desalination Cycle,” Case Studies in Thermal Engineering, **54**, p. 104050. https://doi.org/10.1016/j.csite.2024.104050.

[58] Prosperetti, A., 2000, *Computational Methods for Multiphase Flow*, Cambridge University Press.

[59] Jadhav, A. J., and Barigou, M., 2022, “Eulerian-Lagrangian Modelling of Turbulent Two-Phase Particle-Liquid Flow in a Stirred Vessel: CFD and Experiments Compared,” International Journal of Multiphase Flow, **155**, p. 104191. https://doi.org/10.1016/j.ijmultiphaseflow.2022.104191.

[60] Chen, W., Huang, C., Bai, Y., Chong, D., Yan, J., and Liu, J., 2020, “Experimental and Numerical Investigation of Two Phase Ejector Performance with the Water Injected into the Induced Flow,” International Journal of Advanced Nuclear Reactor Design and Technology, **2**, pp. 15–24. https://doi.org/10.1016/j.jandt.2020.01.001.

[61] Chen, W., Shi, C., Hu, M., Chong, D., Wang, J., and Yan, J., 2014, “Numerical and Experimental Analysis of Two Phase Flow in Ejector,” Energy Procedia, **61**, pp. 1298–1301. https://doi.org/10.1016/j.egypro.2014.11.1085.

[62] Biglarian, M., Najafi, A., Larimi, M. M., and Parhizkari, M., 2023, “Multiphase Modeling of Powder Flow in an Ejector of Solar-driven Refrigeration System by Eulerian-Lagrangian Approach,” *Nanotechnology Applications for Solar Energy Systems*, Wiley, pp. 313–336. https://doi.org/10.1002/9781119791232.ch13.

[63] Assari, M. R., Tabrizi, H. B., Jafar Gholi Beik, A., and Shamesri, K., 2022, “Numerical Study of Water-Air Ejector Using Mixture and Two-Phase Models,” International Journal of Engineering, **35**(2), pp. 307–318. https://doi.org/10.5829/IJE.2022.35.02B.06.

[64] Yuan, G., Zhang, L., Zhang, H., and Wang, Z., 2011, “Numerical and Experimental Investigation of Performance of the Liquid–Gas and Liquid Jet Pumps in Desalination Systems,” Desalination, **276**(1–3), pp. 89–95. https://doi.org/10.1016/j.desal.2011.03.029.

[65] Balamurugan, S., Gaikar, V. G., and Patwardhan, A. W., 2008, “Effect of Ejector Configuration on Hydrodynamic Characteristics of Gas–Liquid Ejectors,” Chem Eng Sci, **63**(3), pp. 721–731. https://doi.org/10.1016/j.ces.2007.10.002.

[66] Giacomelli, F., Mazzelli, F., Banasiak, K., Hafner, A., and Milazzo, A., 2019, “Experimental and Computational Analysis of a R744 Flashing Ejector,” International Journal of Refrigeration, **107**, pp. 326–343. https://doi.org/10.1016/j.ijrefrig.2019.08.007.

[67] Zheng, P., Li, B., and Qin, J., 2018, “CFD Simulation of Two-Phase Ejector Performance Influenced by Different Operation Conditions,” Energy, **155**, pp. 1129–1145. https://doi.org/10.1016/j.energy.2018.04.066.

[68] Kanbur, B. B., Busch, A., Kriezi, E. E., Markussen, W. B., Kærn, M. R., Kristófersson, J., and Walther, J. H., 2024, “Multiphase Mixture Simulations of a Specific Two-Phase R-744 Ejector Geometry,” pp. 456–465. https://doi.org/10.1007/978-3-031-66609-4_42.

[69] Yazdani, M., Alahyari, A. A., and Radcliff, T. D., 2012, “Numerical Modeling of Two-Phase Supersonic Ejectors for Work-Recovery Applications,” Int J Heat Mass Transf, **55**(21–22), pp. 5744–5753. https://doi.org/10.1016/j.ijheatmasstransfer.2012.05.071.

[70] Lee, M. S., Lee, H., Hwang, Y., Radermacher, R., and Jeong, H.-M., 2016, “Optimization of Two-Phase R600a Ejector Geometries Using a Non-Equilibrium CFD Model,” Appl Therm Eng, **109**, pp. 272–282. https://doi.org/10.1016/j.applthermaleng.2016.08.078.

[71] Pangarkar, V. G., 2015, *Design of Multiphase Reactors*, John Wiley and Sons: Hoboken, New York.

[72] Cramers, P. H. M. R., and Beenackers, A. A. C. M., 2001, “Influence of the Ejector Configuration, Scale and the Gas Density on the Mass Transfer Characteristics of Gas–Liquid Ejectors,” Chemical Engineering Journal, **82**(1–3), pp. 131–141. https://doi.org/10.1016/S1385-8947(00)00363-6.

[73] Sharma, D., Patwardhan, A., and Ranade, V., 2018, “Effect of Turbulent Dispersion on Hydrodynamic Characteristics in a Liquid Jet Ejector,” Energy, **164**, pp. 10–20. https://doi.org/10.1016/j.energy.2018.08.171.

[74] Dirix, C. A. M. C., and van der Wiele, K., 1990, “Mass Transfer in Jet Loop Reactors,” Chem Eng Sci, **45**(8), pp. 2333–2340. https://doi.org/10.1016/0009-2509(90)80113-S.

[75] Zhang, G., Wang, X., Chen, J., Tang, S., Smołka, K., Majkut, M., Jin, Z., and Dykas, S., 2023, “Supersonic Nozzle Performance Prediction Considering the Homogeneous-Heterogeneous Coupling Spontaneous Non-Equilibrium Condensation,” Energy, **284**, p. 129274. https://doi.org/10.1016/j.energy.2023.129274.

[76] Edathol, J., Brezgin, D., Aronson, K., and Dong Kim, H., 2020, “Prediction of Non-Equilibrium Homogeneous Condensation in Supersonic Nozzle Flows Using Eulerian-Eulerian Models,” Int J Heat Mass Transf, **152**, p. 119451. https://doi.org/10.1016/j.ijheatmasstransfer.2020.119451.

[77] Zhang, G., Yang, Y., Chen, J., Jin, Z., and Dykas, S., 2024, “Numerical Study of Heterogeneous Condensation in the de Laval Nozzle to Guide the Compressor Performance Optimization in a Compressed Air Energy Storage System,” Appl Energy, **356**, p. 122361. https://doi.org/10.1016/j.apenergy.2023.122361.

[78] Zhang, G., Li, Y., Jin, Z., Dykas, S., and Cai, X., 2024, "A Novel Carbon Dioxide Capture Technology (CCT) Based on Non-Equilibrium Condensation Characteristics: Numerical Modelling, Nozzle Design and Structure Optimization," Energy, **286**, p. 129603. https://doi.org/10.1016/j.energy.2023.129603.

[79] Lei, Y., Li, S., Lu, J., Xu, Y., Yong, Y., and Xing, D., 2023, "Numerical Analysis of Steam Ejector Performance with Non-Equilibrium Condensation for Refrigeration Applications," Buildings, **13**(7), p. 1672. https://doi.org/10.3390/buildings13071672.

[80] Madejski, P., Kuś, T., Michalak, P., Karch, M., and Subramanian, N., 2022, "Direct Contact Condensers: A Comprehensive Review of Experimental and Numerical Investigations on Direct-Contact Condensation," Energies (Basel), **15**(24), p. 9312. https://doi.org/10.3390/en15249312.

[81] Safavi Nic, S. S., Kuipers, T. E., Buist, K. A., Verdurmen, R. E. M., and Kuipers, J. A. M., 2023, "A Transient Mechanistic Two-Fluid Model for Direct Contact Condensation," Chem Eng Sci, **281**, p. 119153. https://doi.org/10.1016/j.ces.2023.119153.

[82] Safavi Nic, S. S., 2023, "Capturing the Dynamics of Direct Contact Condensation: A Numerical and Experimental Study," Eindhoven University of Technology.

[83] Janfada, T. S., Kasiri, N., and Dehghani, M. R., 2022, "Modeling of Direct Contact Condensation in the Water-Saturated Zone of the Soil Exposed to Steam Injection," Iranian Journal of Chemistry and Chemical Engineering, **41**(3), pp. 1003–1021.

[84] Qu, X., Sui, H., and Tian, M., 2016, "CFD Simulation of Steam–Air Jet Condensation," Nuclear Engineering and Design, **297**, pp. 44–53. https://doi.org/10.1016/j.nucengdes.2015.11.011.

[85] Shah, A., Chughtai, I. R., and Inayat, M. H., 2010, "Numerical Simulation of Direct-Contact Condensation from a Supersonic Steam Jet in Subcooled Water," Chin J Chem Eng, **18**(4), pp. 577–587. https://doi.org/10.1016/S1004-9541(10)60261-3.

[86] Zhou, Y., Liu, J., Mo, Y., Chen, W., Xiao, Q., Li, Y., and Yan, J., 2023, "Numerical Simulation on the Direct Contact Condensation in a Steam-Water Two-Phase Ejector with Non-Condensable Gas," International Journal of Thermal Sciences, **185**, p. 108030. https://doi.org/10.1016/j.ijthermalsci.2022.108030.

[87] Koirala, R., Inthavong, K., and Date, A., 2022, "Numerical Study of Flow and Direct Contact Condensation of Entrained Vapor in Water Jet Eductor," Exp Comput Multiph Flow, **4**(3), pp. 291–303. https://doi.org/10.1007/s42757-021-0118-2.

[88] Vieira, C. B., de Ghelin, O. F., Goffaux, C., Nicolle, T., and Dupont, V., 2024, "Numerical Challenges of CFD Simulations of Two-Phase Injectors Working in the Direct Contact Condensation Mode," Exp Comput Multiph Flow, **6**(3), pp. 214–228. https://doi.org/10.1007/s42757-024-0194-1.

[89] Apriyanti, V., Adriansyah, W., Abdurrachim, and Pasek, A. D., 2018, "A Review of Direct Contact Condensation of Steam on Water Droplets," p. 020035. https://doi.org/10.1063/1.5046619.

[90] Ma, X., Xiao, X., Jia, H., Li, J., Ji, Y., Lian, Z., and Guo, Y., 2021, "Experimental Research on Steam Condensation in Presence of Non-Condensable Gas under High Pressure," Ann Nucl Energy, **158**, p. 108282. https://doi.org/10.1016/j.anucene.2021.108282.

[91] Wang, L., Chen, P., Zhou, Y., Li, W., Tang, C., Miao, Y., and Meng, Z., 2018, "Experimental Study on the Condensation of Steam With Air Out of the Vertical Tube Bundles," Front Energy Res, **6**. https://doi.org/10.3389/fenrg.2018.00032.

[92] Mikielewicz, D., Amiri, M., Klugmann, M., and Mikielewicz, J., 2023, "A Novel Concept of Enhanced Direct-Contact Condensation of Vapour- Inert Gas Mixture in a Spray Ejector Condenser," International Journal of Heat and Mass Transfer, **216**, p. 124576. https://doi.org/10.1016/j.ijheatmasstransfer.2023.124576.

[93] Zhang, J., Li, Y., Zhong, J., and Wang, Z., 2024, "Effect of Non-Condensable Gas on the Direct-Contact Condensation Heat Transfer of Vapor in a Convergent Tube," Chemical Engineering Research and Design, **203**, pp. 640–650. https://doi.org/10.1016/j.cherd.2024.01.046.

[94] Ziółkowski, P., Stasiak, K., Amiri, M., and Mikielewicz, D., 2023, "Negative Carbon Dioxide Gas Power Plant Integrated with Gasification of Sewage Sludge," Energy, **262**, p. 125496. https://doi.org/10.1016/j.energy.2022.125496.

[95] Ziółkowski, P., Madejski, P., Amiri, M., Kuś, T., Stasiak, K., Subramanian, N., Pawlak-Kruczek, H., Badur, J., Niedźwiecki, Ł., and Mikielewicz, D., 2021, "Thermodynamic Analysis of Negative CO2 Emission Power Plant Using Aspen Plus, Aspen Hysys, and Ebsilon Software," Energies (Basel), **14**(19), p. 6304. https://doi.org/10.3390/en14196304.

[96] Madejski, P., Banasiak, K., Ziółkowski, P., Mikielewicz, D., Mikielewicz, J., Kuś, T., Karch, M., Michalak, P., Amiri, M., Dąbrowski, P., Stasiak, K., Subramanian, N., and Ochrymiuk, T., 2023, "Development of a Spray-Ejector Condenser for the Use in a Negative CO2 Emission Gas Power Plant," Energy, **283**, p. 129163. https://doi.org/10.1016/j.energy.2023.129163.

[97] Madejski, P., Michalak, P., Karch, M., Kuś, T., and Banasiak, K., 2022, "Monitoring of Thermal and Flow Processes in the Two-Phase Spray-Ejector Condenser for Thermal Power Plant Applications," Energies (Basel), **15**(19), p. 7151. https://doi.org/10.3390/en15197151.

[98] Madejski, P., Karch, M., Michalak, P., and Banasiak, K., 2024, "Conceptual Design of Experimental Test Rig for Research on Thermo-Flow Processes During Direct Contact Condensation in the Two-Phase Spray-Ejector Condenser," J Energy Resour Technol, **146**(3). https://doi.org/10.1115/1.4064194.

[99] Madejski, P., and Karch, 2023, "Use of Optical Methods in the Study of Tidal Phenomena in a Two-Phase Streamer," *XXV Jubileuszowy Zjazd Termodynamików - Book of Abstract*, J. Cieśliński, D. Mikielewicz, and J. Wajs, eds., Wydawnictwo Politechniki Gdańskiej, Gdańsk, pp. 195–198.

[100] Goliński, J., and Troskolański, A., 1979, *Strumienice Teoria i Konstrukcja*, WNT, Warszawa.

[101] Ziółkowski, P., Madejski, P., Amiri, M., Kuś, T., Stasiak, K., Subramanian, N., Pawlak-Kruczek, H., Badur, J., Niedźwiecki, Ł., and Mikielewicz, D., 2021, "Thermodynamic Analysis of Negative CO2 Emission Power Plant Using Aspen plus, Aspen Hysys, and Ebsilon Software," Energies (Basel), **14**(19). https://doi.org/10.3390/en14196304.

[102] Madejski, P., Banasiak, K., Ziółkowski, P., Mikielewicz, D., Mikielewicz, J., Kuś, T., Karch, M., Michalak, P., Amiri, M., Dąbrowski, P., Stasiak, K., Subramanian, N., and Ochrymiuk, T., 2023, "Development of a Spray-Ejector Condenser for the Use in a Negative CO2 Emission Gas Power Plant," Energy, **283**. https://doi.org/10.1016/j.energy.2023.129163.

[103] Bogusławski, A., Drobniak, S., and Tyliszczak, A., 2008, *Turbulencja - Od Losowości Do Determinizmu*.

[104] Paszko, M., and Łygas, K., 2016, *Współczesne Metody Modelowania Przepływów Turbulentnych w Otoczeniu Poruszuszającego Się Autobusu Miejskiego*.

[105] Schiestel, R., and Chaouat, B., 2024, "Turbulence Modeling and Simulation Advances in CFD during the Past 50 Years," Comptes Rendus. Mécanique, **350**(S1), pp. 23–51. https://doi.org/10.5802/crmeca.114.

[106] Rodriguez, S., 2019, *Applied Computational Fluid Dynamics and Turbulence Modeling*, Springer International Publishing, Cham. https://doi.org/10.1007/978-3-030-28691-0.

[107] Shih, T.-H., Liou, W. W., Shabbir, A., Yang, Z., and Zhu, J., 1995, "A New K-ϵ Eddy Viscosity Model for High Reynolds Number Turbulent Flows," Comput Fluids, **24**(3), pp. 227–238. https://doi.org/10.1016/0045-7930(94)00032-T.

[108] SIEMENS, 2020, *Simcenter STAR-CCM+ Documentation - Version 2020.2*.

[109] Jongen, T., 1998, "Simulation and Modeling of Turbulent Incompressible Flows," EPFL.

[110] Liao, Y., Krepper, E., and Lucas, D., 2019, "A Baseline Closure Concept for Simulating Bubbly Flow with Phase Change: A Mechanistic Model for Interphase Heat Transfer Coefficient," Nuclear Engineering and Design, **348**. https://doi.org/10.1016/j.nucengdes.2019.04.007.

[111] Sun, Y., Guan, Z., and Hooman, K., 2017, "A Review on the Performance Evaluation of Natural Draft Dry Cooling Towers and Possible Improvements via Inlet Air Spray Cooling," Renewable and Sustainable Energy Reviews, **79**. https://doi.org/10.1016/j.rser.2017.05.151.

[112] Höhne, T., Gasiunas, S., and Šeporaitis, M., 2017, "Numerical Modelling of a Direct Contact Condensation Experiment." https://doi.org/10.11159/icmfht17.102.

[113] Hughes, E. D., and Duffey, R. B., 1991, "Direct Contact Condensation and Momentum Transfer in Turbulent Separated Flows," International Journal of Multiphase Flow, **17**(5). https://doi.org/10.1016/0301-9322(91)90027-Z.

[114] Ranz, W., and Marshall, W., 1952, "Evaporation from Drops," Chem Eng Prog, **48**, pp. 141–146.

[115] Hughmark, G. A., 1967, "Mass and Heat Transfer from Rigid Spheres," AIChE Journal, **13**(6). https://doi.org/10.1002/aic.690130638.

[116] Jo, J.-C., Lee, S.-K., and Shin, W.-K., 1991, "Heat Transfer of a Spray Droplet in a PWR Pressurizer," KSME Journal, **5**(2). https://doi.org/10.1007/BF02953612.

[117] Kvlic, E., and Rhodes, E., 1977, "Direct Contact Condensation from Air-steam Mixtures on a Single Droplet," Can J Chem Eng, **55**(2). https://doi.org/10.1002/cjce.5450550205.

[118] Li, J., Zhang, Q., and Zhai, Z., 2019, "An Efficient Segregated Algorithm for Two-Dimensional Incompressible Fluid Flow and Heat Transfer Problems with Unstructured Grids," Int J Heat Mass Transf, **133**, pp. 1052–1064. https://doi.org/10.1016/j.ijheatmasstransfer.2018.12.039.

[119] Alonzo-García, A., Gutiérrez-Torres, C. del C., and Jiménez-Bernal, J. A., 2016, "Computational Fluid Dynamics in Turbulent Flow Applications," *Numerical Simulation - From Brain Imaging to Turbulent Flows*, InTech. https://doi.org/10.5772/63831.

[120] Versteeg, H. K., and Malalasekera, W., 2007, *An Introduction to Computational Fluid Dynamics*, Pearson Education, Harlow, England.

[121] Czajka, I., and Gołaś, A., 2017, *Inżynierskie Metody Analizy Numerycznej i Planowanie Eksperymentu*, Wydawnictwo AGH, Kraków.

[122] Wagner, W., and Kretzschmar, H.-J., 2008, *International Steam Tables - Properties of Water and Steam Based on the Industrial Formulation IAPWS-IF97*, Springer, New York.

[123] Linstrom, P. J., and Mallard, W. G., 2001, "The NIST Chemistry WebBook: A Chemical Data Resource on the Internet," Journal of Chemical & Engineering Data, **46**(5), pp. 1059–1063. https://doi.org/10.1021/je000236i.

[124] Hua, L., Jiang, Y., Li, H., and Qin, L., 2022, "Effects of Different Nozzle Orifice Shapes on Water Droplet Characteristics for Sprinkler Irrigation," Horticulturae, **8**(6). https://doi.org/10.3390/horticulturae8060538.

[125] Fleming, R. P., 2002, "Automatic Sprinkler System Calculations," *SFPE Handbook of Fire Protection Engineering*, P.J. DiNenno, D. Drysdale, C.L. Beyler, W. Douglas Walton, R.L.P. Custer, J. John R. Hall Jr, and J. M. Watts Jr., eds., National Fire Protection Association, Quincy.

[126] Atkinson, D. S. F., and Strauss, W., 1978, "Droplet Size and Surface Tension in Venturi Scrubbers," J Air Pollut Control Assoc, **28**(11). https://doi.org/10.1080/00022470.1978.10470714.

[127] Wolfshtein, M., 1969, "The Velocity and Temperature Distribution in One-Dimensional Flow with Turbulence Augmentation and Pressure Gradient," Int J Heat Mass Transf, **12**(3), pp. 301–318. https://doi.org/10.1016/0017-9310(69)90012-X.

[128] Armenante, P. M., and Kirwan, D. J., 1989, "Mass Transfer to Microparticles in Agitated Systems," Chemirol Engineerrng Science, **44**(12), pp. 2781–2796.

[129] Borishanskiy, V. M., 1977, "Effect of Uncondensable Gas Content on Heat Transfer in Steam Condensation in a Vertical Tube.," Heat Transfer Sov. Res., **9**(2), pp. 35–42.

Appendencies

Appendix A: Supplementary scalar fields

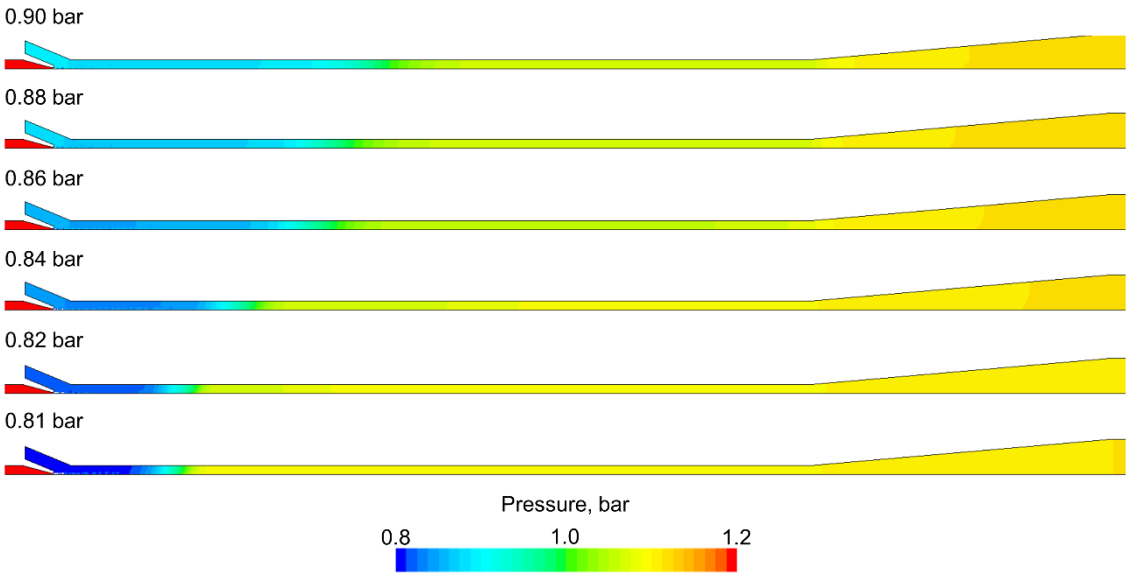

Figure A. 1. The influence of suction pressure on the pressure distribution in the spray-ejector condenser.

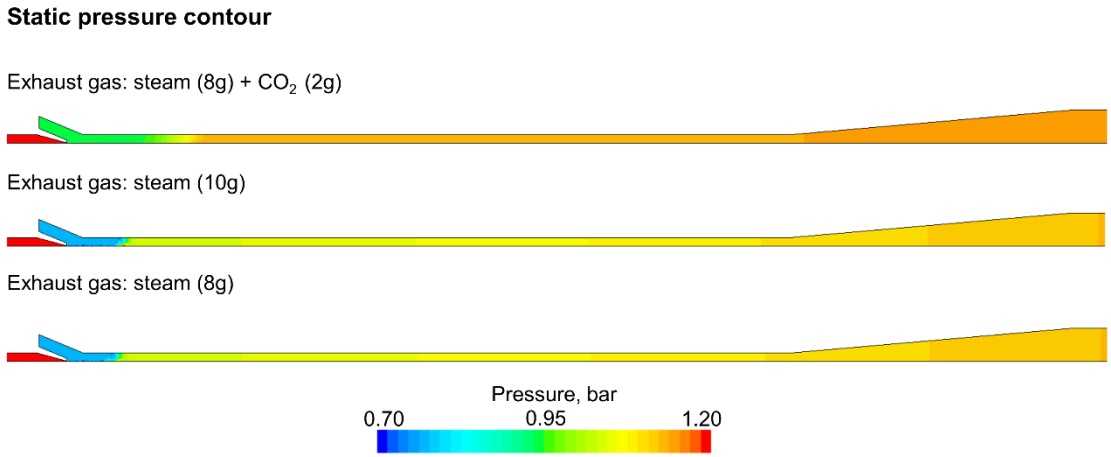

Figure A. 2. Pressure distribution at different exhaust gas contents.

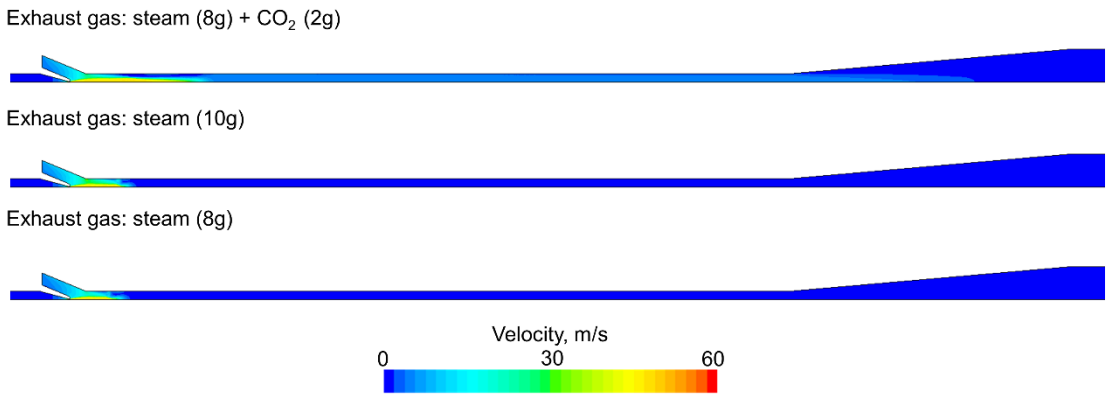

Figure A. 3. Velocity distribution at different exhaust gas contents.

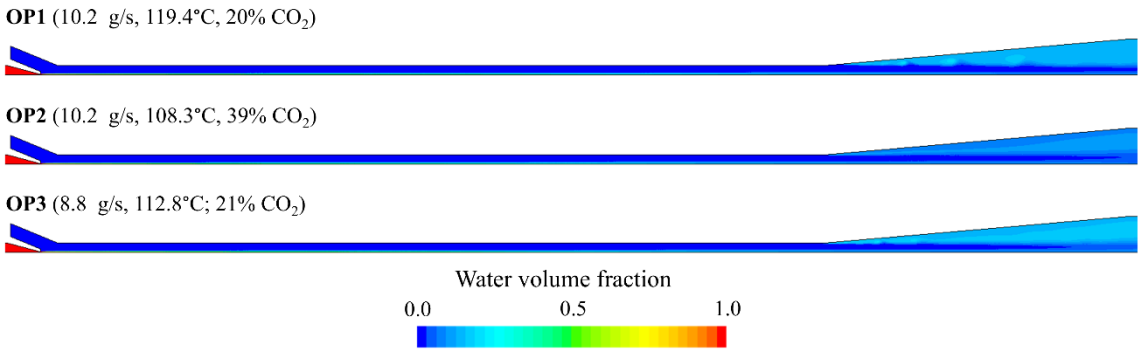

Figure A. 4. Distribution of water volume fraction for different operating conditions OP1–OP3 (exhaust gas mass flow rate, temperature, CO_2 mass content).

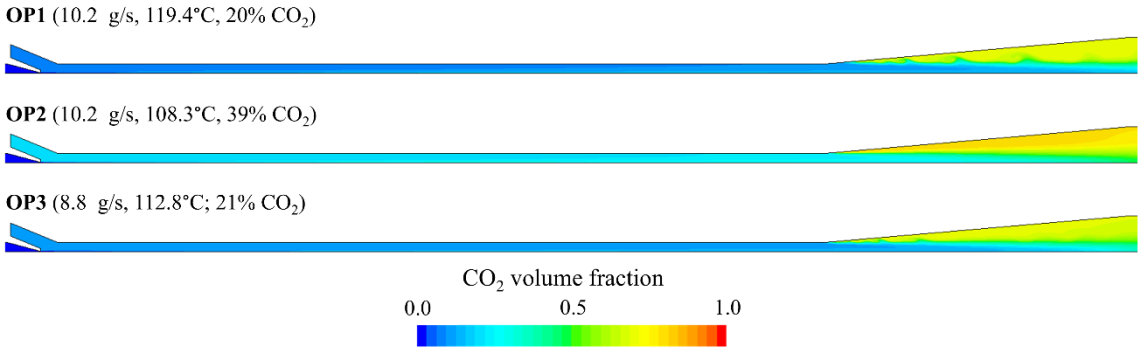

Figure A. 5. Distribution of CO_2 volume fraction for different operating conditions OP1–OP3 (exhaust gas mass flow rate, temperature, CO_2 mass content).

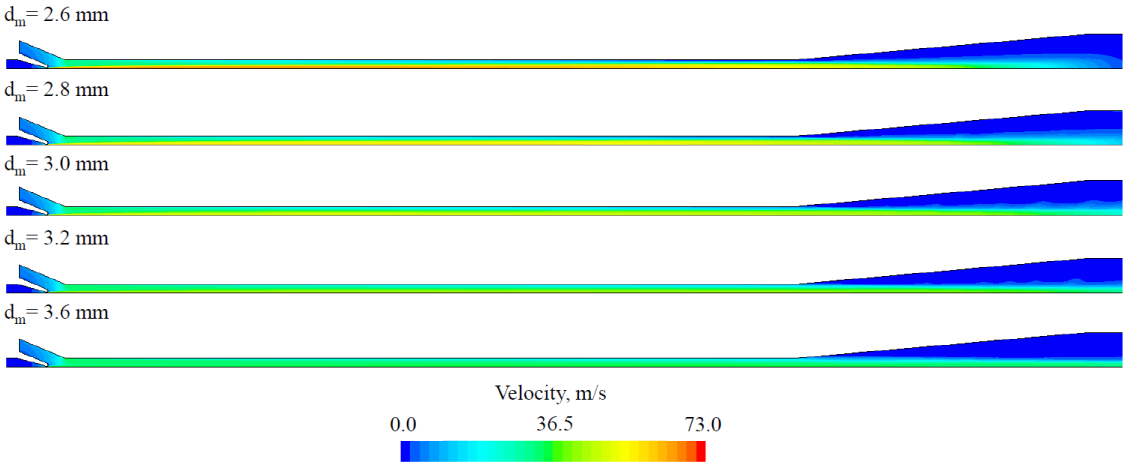

Figure A. 6. The influence of motive nozzle diameter D_{MN_2} on the velocity distribution (velocity b.c. at the water inlet).

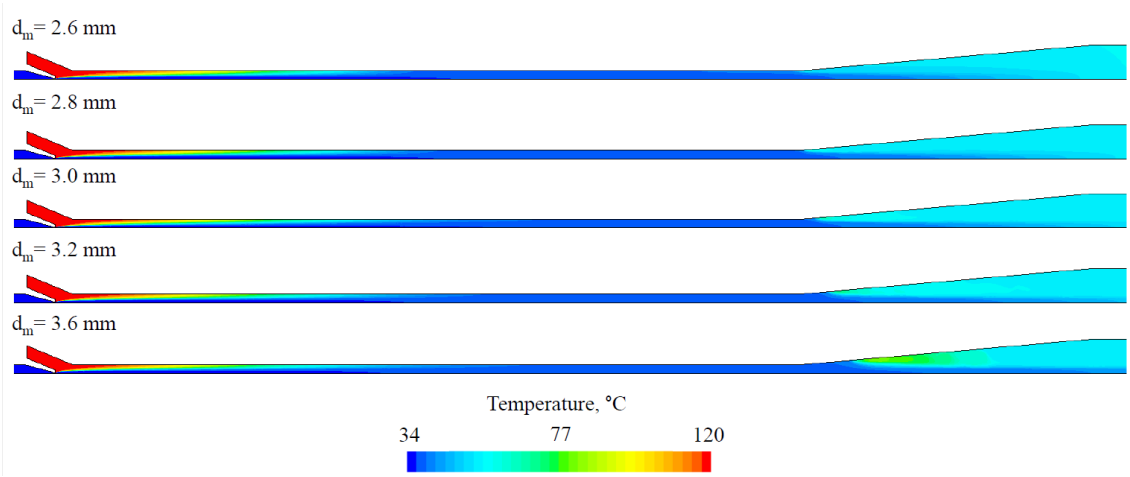

Figure A. 7. The influence of motive nozzle diameter D_{MN_2} on the temperature distribution (velocity b.c. at the water inlet).

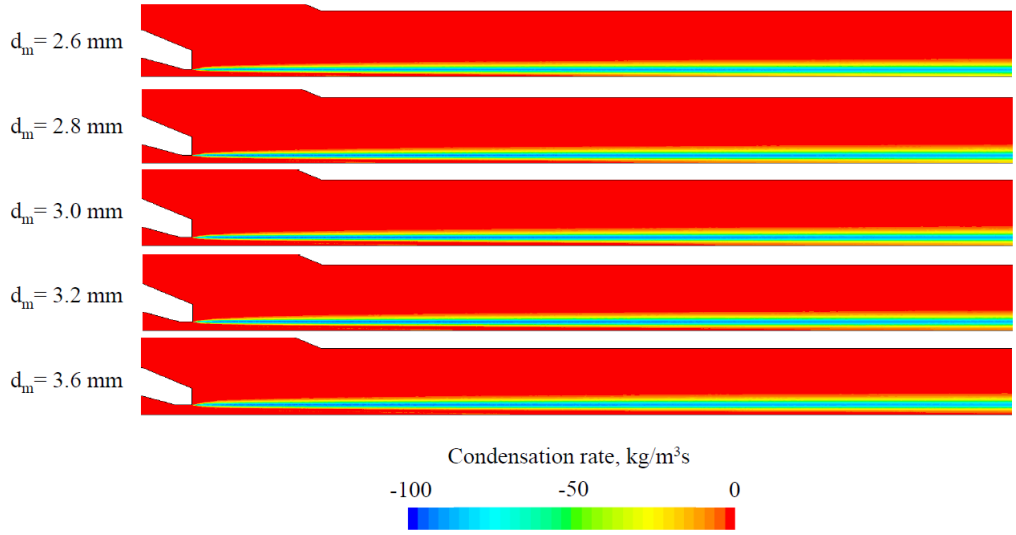

Figure A. 8. The influence of motive nozzle diameter D_{MN_2} on the condensation rate distribution (velocity b.c. at the water inlet).

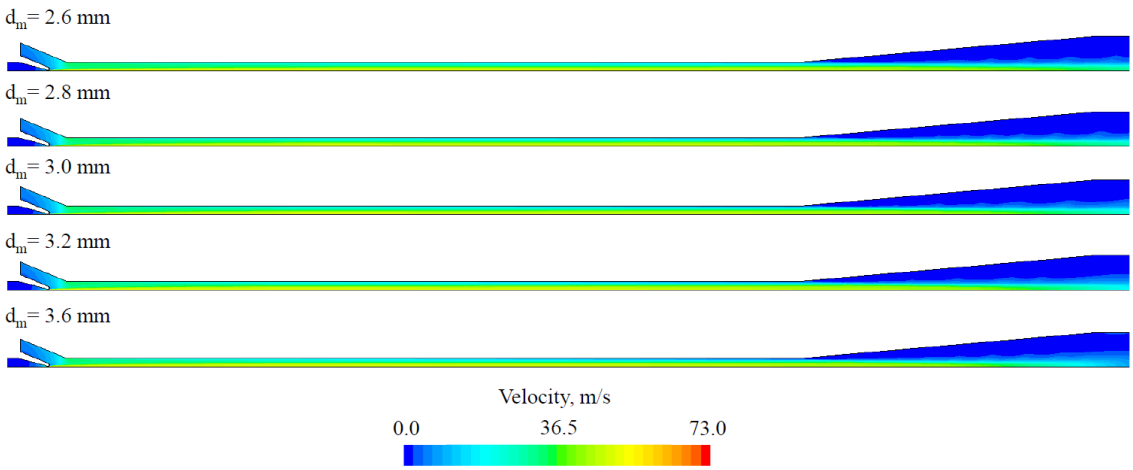

Figure A. 9. The influence of motive nozzle diameter D_{MN_2} on the velocity distribution (pressure b.c. at the water inlet).

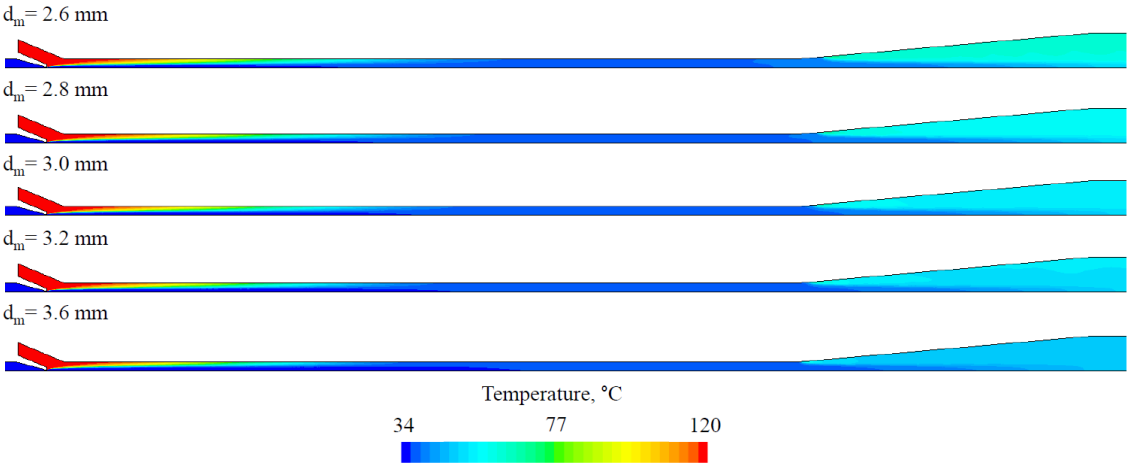

Figure A. 10. The influence of motive nozzle diameter D_{MN_2} on the temperature distribution (pressure b.c. at the water inlet).

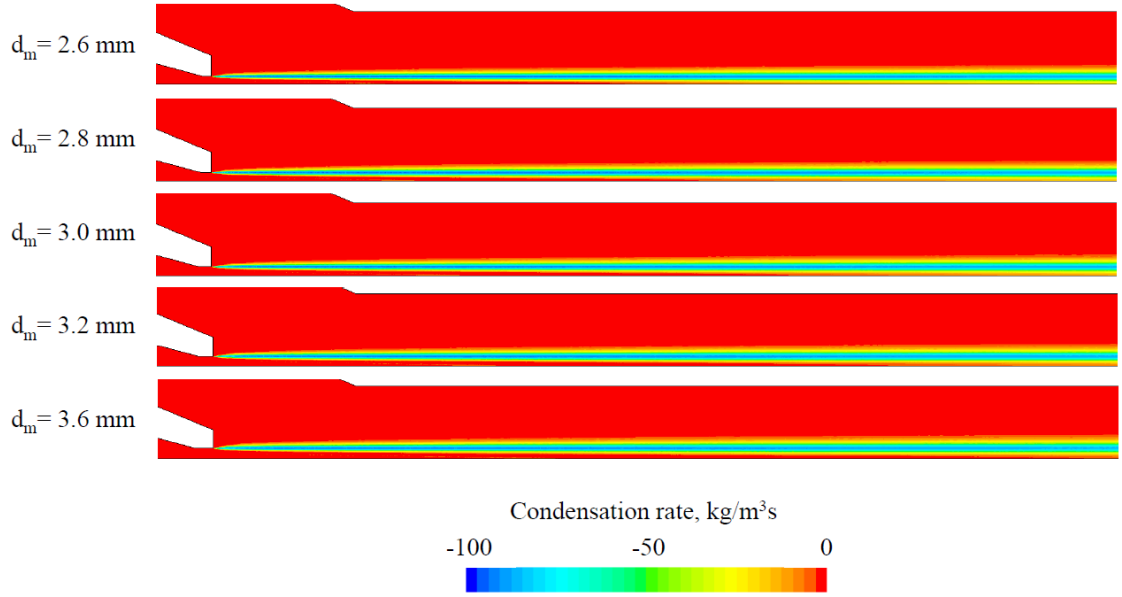

Figure A. 11. The influence of motive nozzle diameter D_{MN_2} on the condensation rate distribution (pressure b.c. at the water inlet).

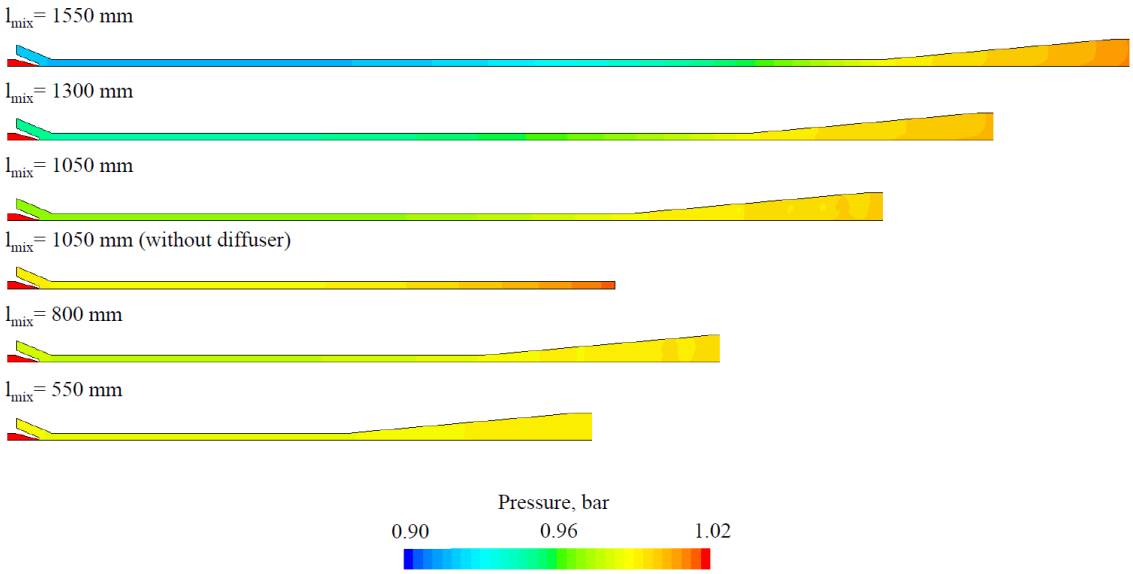

Figure A. 12. The influence of mixing chamber length L_{MIX} on the pressure distribution.

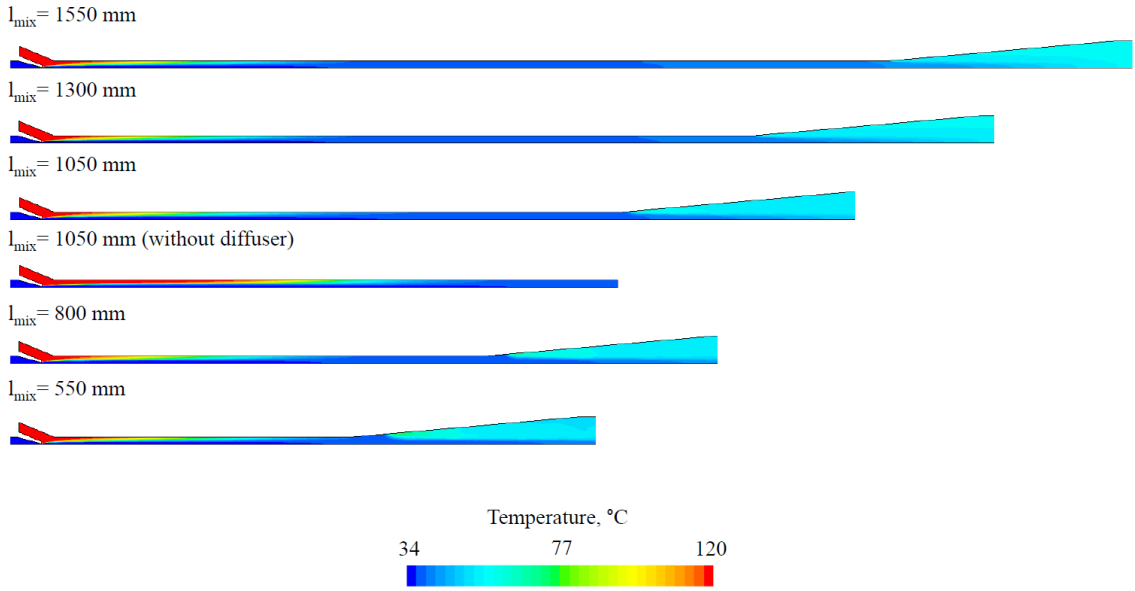

Figure A. 13. The influence of mixing chamber length L_{MIX} on the temperature distribution.

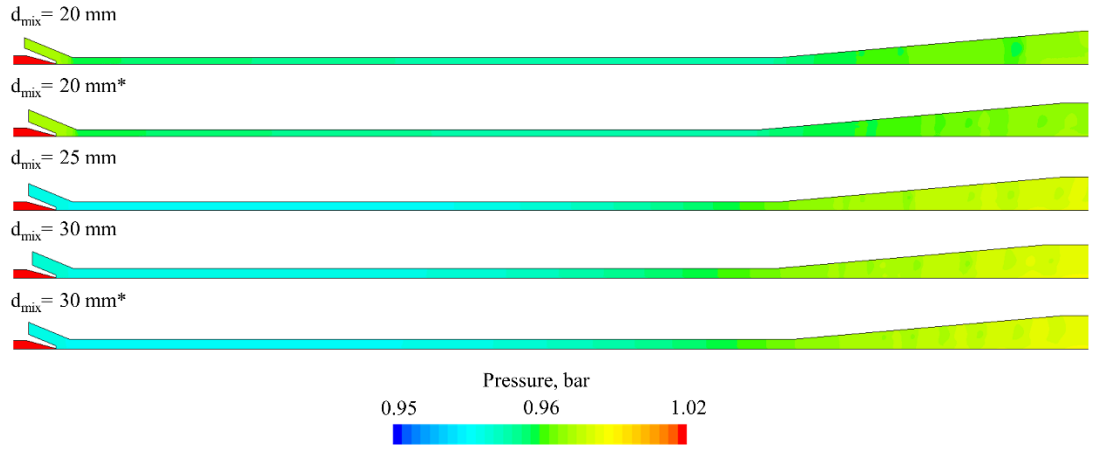

Figure A. 14. The influence of mixing chamber diameter D_{MIX} on the pressure distribution.

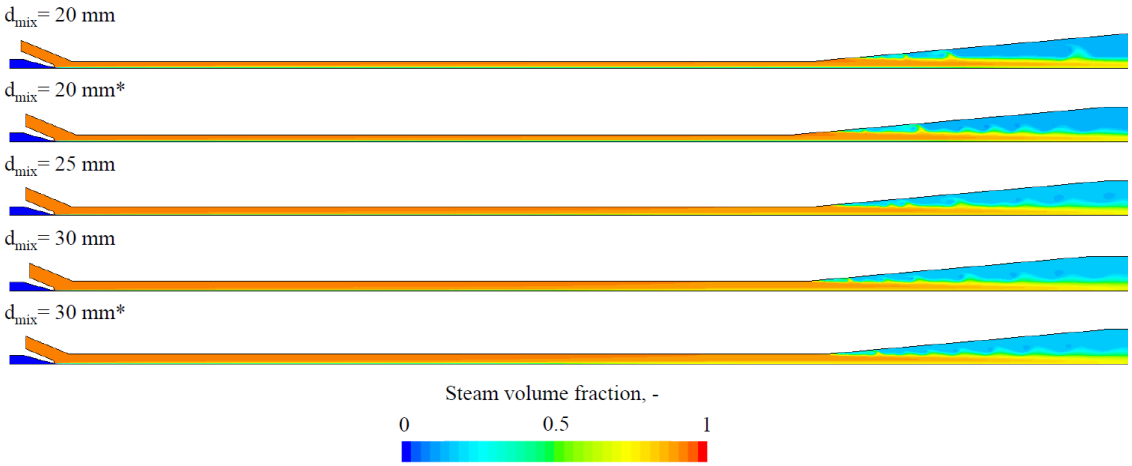

Figure A. 15. The influence of mixing chamber diameter D_{MIX} on the steam volume fraction distribution.

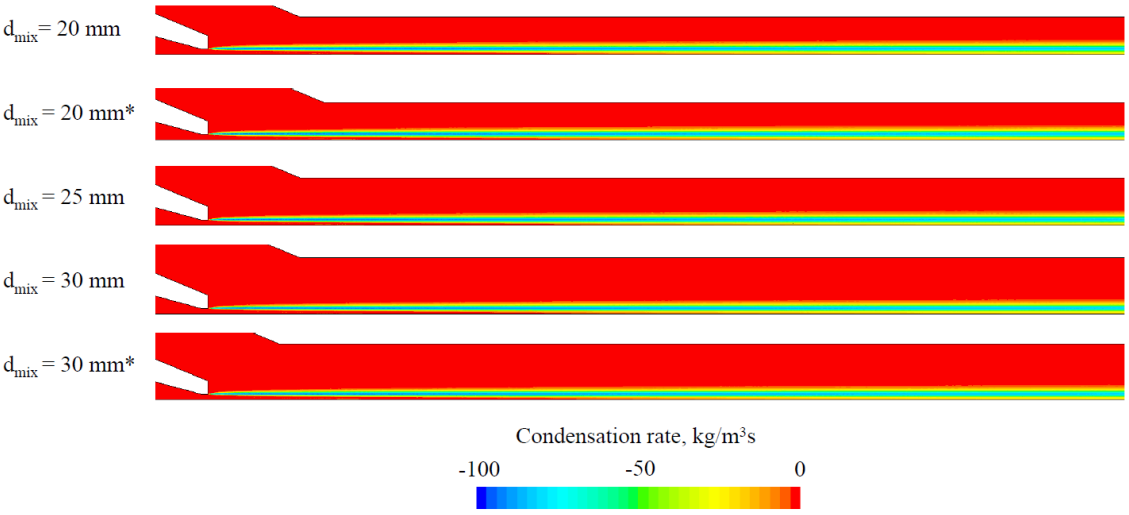

Figure A. 16. The influence of mixing chamber diameter D_{MIX} on the condensation rate distribution.

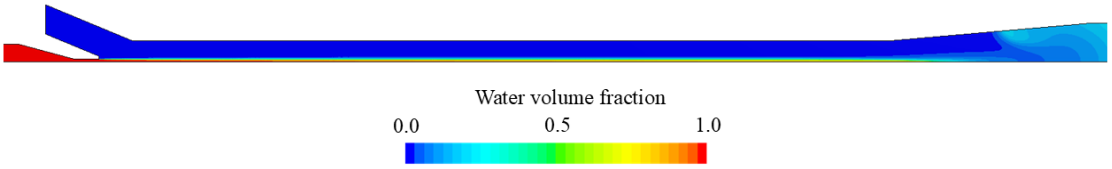

Figure A. 17. Water volume fraction distribution for the nLPL geometrical model.

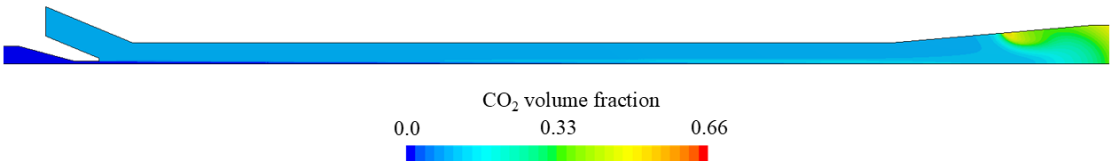

Figure A. 18. CO_2 volume fraction distribution for the nLPL geometrical model.

Appendix B: Additional axial profiles

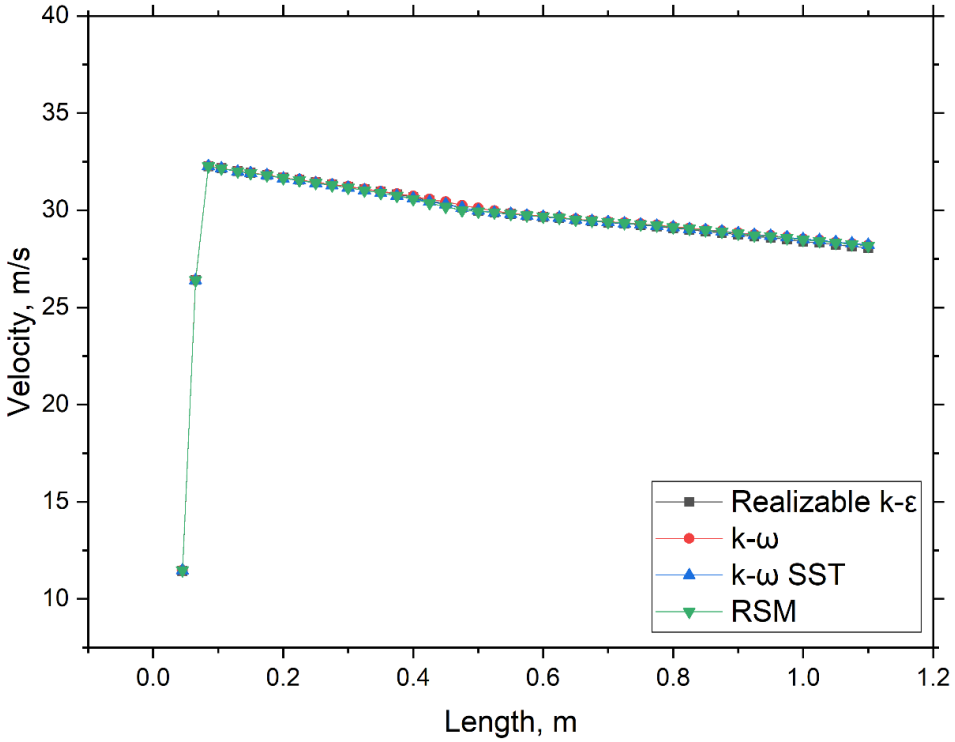

Figure B. 1. The influence of the turbulence model on the cross-sectional velocity along the flow path.

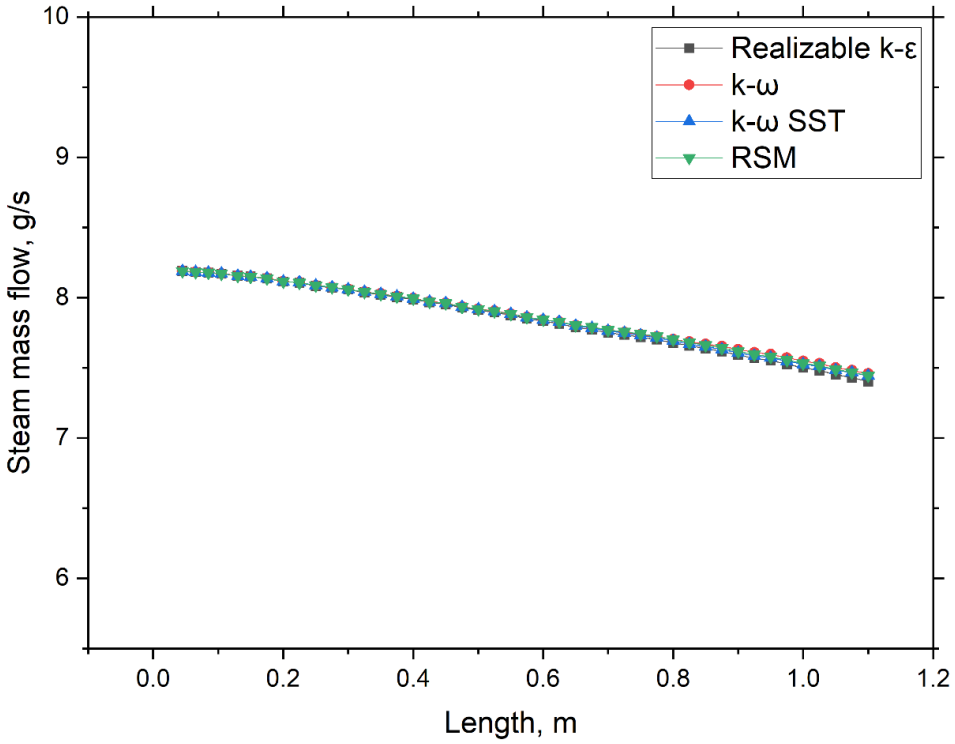

Figure B. 2. The influence of the turbulence model on the cross-sectional steam mass flow along the flow path.

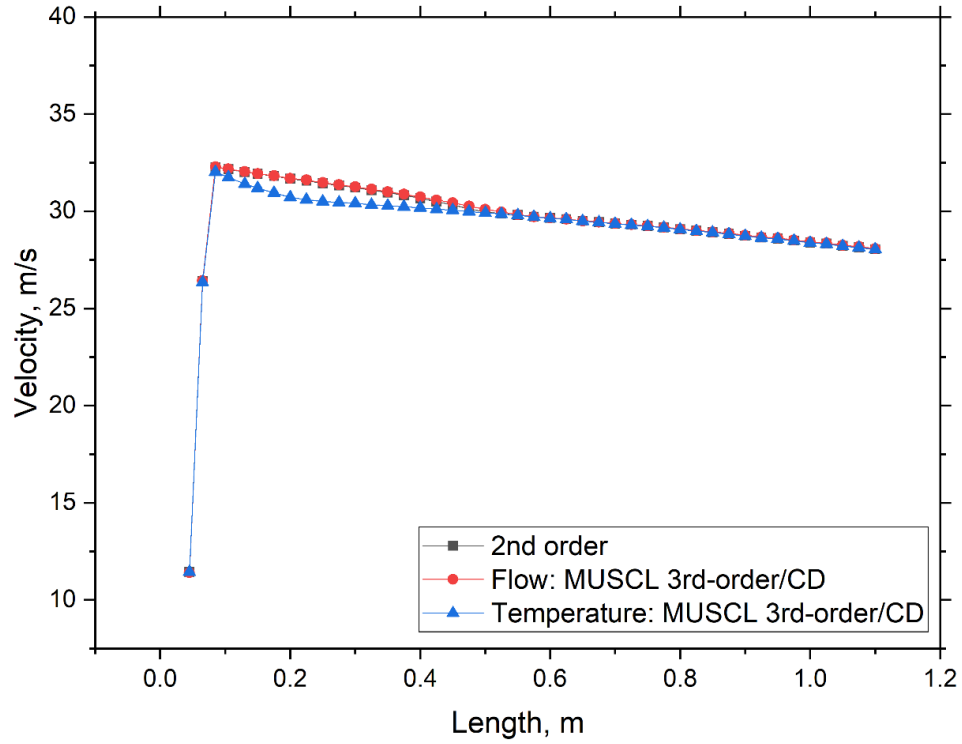

Figure B. 3. The influence of the numerical convection scheme on the cross-sectional velocity along the flow path.

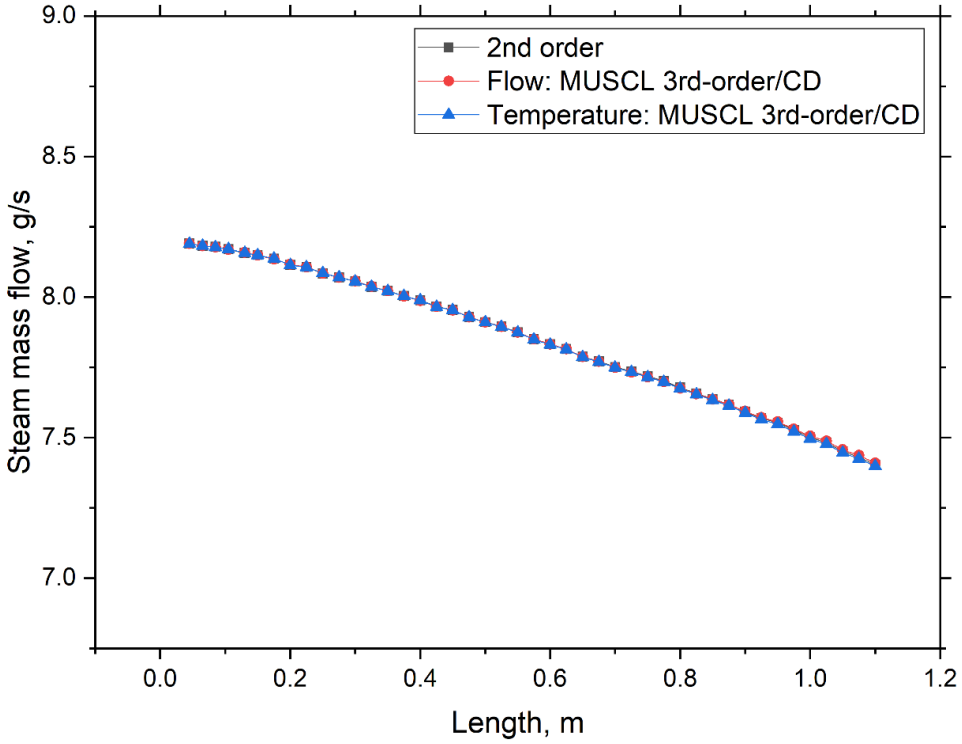

Figure B. 4. The influence of the numerical convection scheme on the cross-sectional steam mass flow along the flow path.

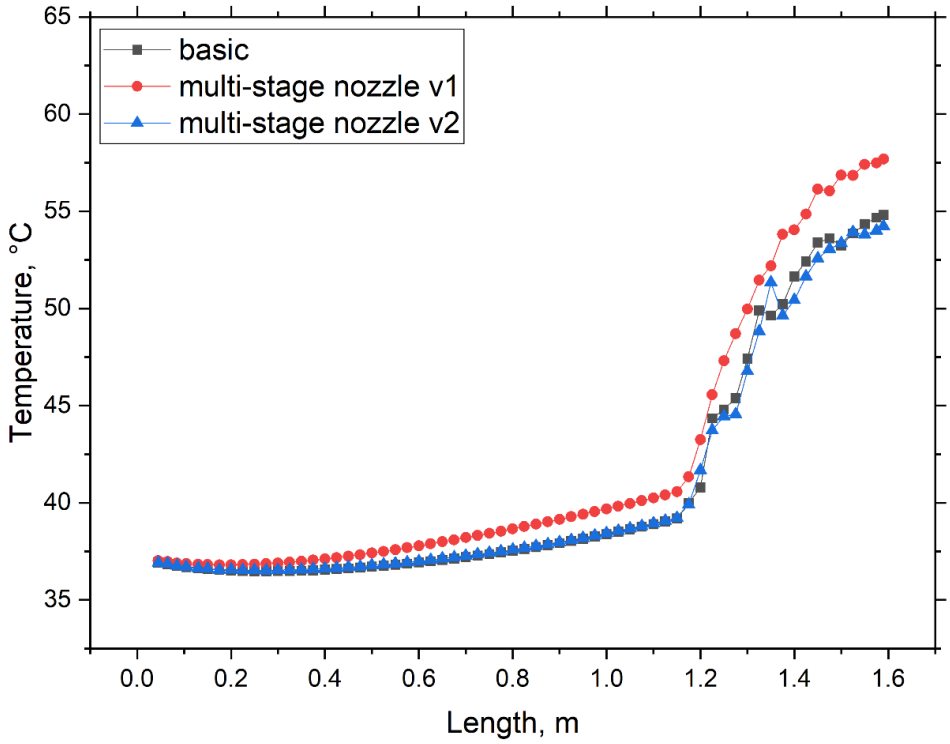

Figure B. 5. The influence of nozzle configuration on the cross-sectional mass-averaged temperature along the flow path.

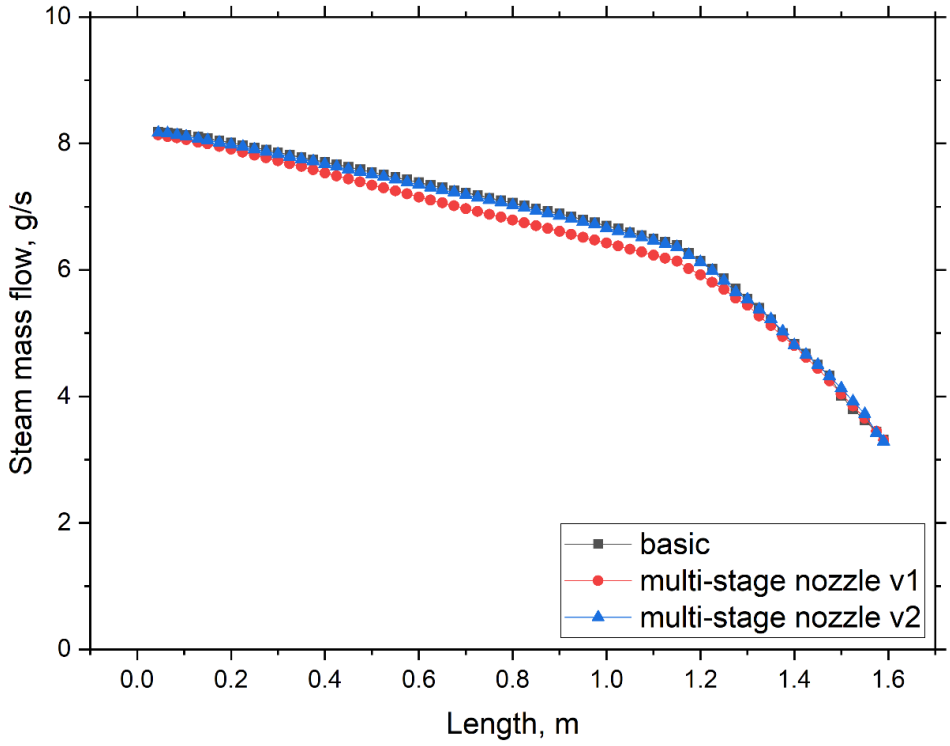

Figure B. 6. The influence of nozzle configuration on the cross-sectional averaged steam mass flow along the flow path.